Interaction of Surface Hydroxyls with Supported Metal Particles: A Combined Vibrational and Electron Spectroscopic Investigation of Au and Pd on MgO(001) Model Surfaces

Dissertation

zur Erlangung des Akademischen Grades

Doktor der Naturwissenschaften (Dr. rer. nat.)

im Fach Chemie

eingereicht im Fachbereich Biologie, Chemie, Pharmazie

der Freien Universität Berlin

von

M. Sc. Yuichi FUJIMORI

aus Kanagawa/Japan

Berlin 2015

Diese Arbeit wurde von Oktober 2010 bis September 2014 am Fritz-Haber-Institut der Max-Planck-Gesellschaft in der Abteilung Chemische Physik unter Anleitung von Prof. Dr. Hans-Joachim Freund angefertigt.

1. Gutachter: Prof. Dr. Hans-Joachim Freund
2. Gutachter: Prof. Dr. Thomas Risse

Disputation am 13.4.2015

Acknowledgments

This research in which I have been involved from May 2010 to December 2014 at the Department of Chemical Physics in the **Fritz-Haber-Institut der Max-Planck-Gesellschaft**, a *utopia* for scientists, would not be realized without numerous supports and encouragement. It is of great difficulty to mention all of them, but I am especially grateful to the following people.

First of all, I genuinely express my sincere appreciation to **Herrn Prof. Dr. Hans-Joachim Freund** for not only providing me with the opportunity to tackle a challenging Ph.D. research project in a state-of-art scientific environment at his department, but also encouraging me since the beginning of my stay in Germany. With supernatural patience, he has allowed me to make countless mistakes and has waited for me until I drew a conclusion after thinking on my own.

I am profoundly grateful to **Herrn Prof. Dr. Martin Sterrer** for his invaluable supports, and his utmost generosity for providing me with freedom of research in his group.

Herrn Prof. Dr. Thomas Risse is greeted not only for reviewing my thesis very closely, but also for suggesting me future plans.

All the members of the Catalysis/Laser Spectroscopy group during my stay—**Dr. Matthew Brown**, **Dr. Franziska Ringleb**, **Dr. Rhys Dowler**, **Prof. Dr. William Kaden**, **Dr. Florencia Calaza**, **Dr. Hei-Feng Wang**, **Dr. Hiroko Ariga**, **Dr. Andreas Aumer**, **Dr. Janaina F. Gomes**, **Dr. Ahmed Ghalgaoui**, **Prof. Dr. Beatriz Roldan-Cuenya**, **Sacha Pomp**, **Peter Siedel**, and, last but not least, **Herrn Dipl.-Phys Burkhard Kell**—are deeply acknowledged.

I appreciate the contributions from the scientific collaborators of mine during the study, which has frequently made me understand what *we* can achieve.

The secretaries to the Department, **Frau Manuela Misch**, **Frau Gabi Mehnert** and **Frau Daniela Nikolaus**, are greatly thanked for their kind support to facilitate processing.

Unforgettable time spent with friends of mine in Japan (one month per year) and Berlin (the rest) was invaluable.

I greatly thank to all the members of the department for having wonderful and exciting time during my stay. Conversations and consultation with them greatly helped me.

Financial support, **TAKATA-DAAD Postgraduate Scholarship** provided by **Co. Ltd. TAKATA** for 4 years, including one year for my master study, and a fellowship by the **Max-Planck-Gesellschaft** for more than one year is greatly acknowledged.

In closing, my appreciation goes to my family and closest friends of mine for their understanding on my decisions in the last decade. Your presence has made me what I am today.

Abstract

One of the primary objectives in current catalysis research is to comprehend and point out the critical factors that determine the activity and selectivity of catalysts. During the past decades the surface science approach to catalysis, which allows chemical reactions on morphologically well-defined model systems to be studied down to the atomic level, has greatly contributed to the fundamental understanding of catalysis. Shortcomings of this approach, such as the well-known materials and pressure gap, have recently been overcome by the development of improved methodological approaches and more sophisticated analytical methods. The goal of this thesis was to determine how environmental parameters, in particular the effect of water under elevated pressure conditions, influence the properties of model catalysts. By using complex model systems, this study aims to come one step closer to a realistic description of catalyst surfaces by surface science models.

Clean and hydroxylated MgO(001) thin films grown on Ag(001) were used as substrates for Au and Pd nanoparticles. The properties of the oxide films and of the supported model catalyst systems were investigated with infrared reflection absorption spectroscopy, X-ray based electronic structure determination techniques, and thermal desorption spectroscopy. The main focus of this thesis was placed on a comparison of the nucleation/sintering behavior and the electronic properties of metal nanoparticles on clean and functionalized oxide surfaces. In addition, the chemical interaction between hydroxyl groups and metals received particular consideration.

At first, the nucleation behavior of gold on pristine MgO thin film surfaces was studied in order to determine the nature and film thickness-dependent distribution of defects. In particular, the formation of cationic gold species was explained by the presence of grain boundaries and anion vacancies on the pristine films. Hydroxylation of the MgO surfaces was achieved by exposing the freshly prepared thin film samples to water at elevated pressure conditions (10^{-3} – 1 mbar). Hydroxyl groups exhibiting different acidity could be prepared by variation of the dosing conditions. Low-temperature deposition of gold and palladium on the hydroxylated MgO surfaces containing the more acidic hydroxyls led to the formation of small oxidized clusters via a specific interaction of the metals with hydroxyl groups. By contrast, gold showed almost no interaction with the normal hydroxyl groups and chemical interaction of palladium with these hydroxyls was observed only at elevated temperature. However, a general effect noticed for hydroxylated MgO was the improved thermal stability of metal nanoparticles on these surfaces compared to non-hydroxylated ones.

Two principal types of reactions between palladium and hydroxyl groups were revealed from detailed investigations of their chemical interaction: the Redox reaction: Pd + OH $\rightarrow$ PdO + $1/2H_2$; and the water-gas-shift (WGS) reaction, which involves the participation of CO adsorbed on the Pd particles: Pd-CO + OH $\rightarrow$ Pd + CO_2 + $1/2H_2$. The significance of hydroxyl groups located in the peripheral region around the Pd particles for the WGS reaction could be verified via variation of the Pd coverage. Comparative studies with clean and oxidized Pd(111) surfaces served to underline the importance of the oxide substrate for the reactions described above, as well as to determine the effect of water on the surface properties of oxidized Pd surfaces.

Finally, water adsorption and dissociation on MgO(001) and CaO(001) was compared. These studies confirmed the difference in the reactivity of the two surfaces toward water. It could be shown that hydroxyls formed on CaO at low temperature inhibit the crystallization of ice layers grown on top. In addition, Mo dopants present in ultrathin CaO layers were found to limit the maximum hydroxylation level of the surfaces, thus contributing to the stabilization of CaO toward water-induced disintegration.

Zusammenfassung

Eine der fundamentalen Zielsetzungen der Grundlagenforschung zur Katalyse ist es, kritische Faktoren, welche die Aktivität und Selektivität von Katalysatoren bestimmen, aufzudecken und zu verstehen. Die Oberflächenwissenschaften mit ihren Modellsystemen, die es ermöglichen, chemische Reaktionen auf wohl-definierten, einkristallinen Oberflächen unter Ultrahoch-Vakuum (UHV)-Bedingungen bis ins kleinste Detail zu erforschen, haben in den vergangenen Jahrzehnten entscheidend zum grundlegenden Verständnis von katalytischen Prozessen beigetragen. Die oft genannten Schwächen dieses Modellansatzes, nämlich die zu starke Vereinfachung der Systeme hinsichtlich Materialeigenschaften und Reaktionsbedingungen, wurden in den letzten Jahren durch verbesserte methodische Ansätze sowie neue Analysenmethoden bis zu einem gewissen Grad überwunden. Die vorliegende Arbeit beschäftigt sich mit dem Thema, wie Umgebungsparameter, vor allem der Einfluss von Wasser unter erhöhten Druckbedingungen, die Eigenschaften von Katalysator-Modellsystemen beeinflussen und zielt daher im Besonderen darauf ab, der Beschreibung von realen Katalysatoroberflächen mit Hilfe von komplexen Modellsystemen einen Schritt näher zu kommen.

Es wurden dünne, auf Ag(001) aufgewachsene einkristalline MgO(001)-Schichten verwendet, die entweder im sauberen Zustand oder nach Funktionalisierung der Oberfläche mit Hydroxyl-Gruppen als Substrat für die Bildung von Au und Pd Nanopartikeln dienten. Die Eigenschaften der Oxid-Filme sowie der geträgerten Modellkatalysator-Systeme wurden mit Infrarot-Absorptions-Reflexions-Spektroskopie, Röntgen-spektroskopischen Untersuchungsmethoden, und Thermischer Desorptions-Spektroskopie untersucht. Das Hauptaugenmerk wurde auf vergleichende Studien über das Nukleations- und Sinterungsverhalten und die elektronischen Eigenschaften von den Metallen auf den sauberen und funktionalisierten Oxid-Oberflächen gelegt, wobei bei letzteren auch die chemische Wechselwirkung zwischen den Hydroxyl-Gruppen und den Metallen berücksichtigt wurde.

Studien zum Nukleationsverhalten von Gold auf frisch präparierten MgO-Filmen dienten zunächst dazu, die Art und MgO-Schichtdicken-abhängige Verteilung von Defekten auf der MgO-Oberfläche zu bestimmen, wobei die Bildung von kationischen Gold-Spezies auf das Vorhandensein von Korngrenzen im Film und Anionen-Fehlstellen zurückgeführt wurde. Die Hydroxylierung der MgO-Oberflächen wurde durch Exponieren der frisch präparierten Proben gegenüber Wasser bei erhöhten Drucken (im Bereich von 10^{-3} bis 1 mbar) erreicht. Durch Variation der Dosierungsparameter konnten Hydroxylgruppen unterschiedlicher Acidität auf der

MgO-Oberfläche erzeugt und hinsichtlich ihrer Wechselwirkung mit den Metallen untersucht werden. Auf den mit Hydroxylgruppen höherer Acidität funktionalisierten MgO-Oberflächen wurden direkt nach der Deponierung bei niedrigen Temperaturen durch die selektive Wechselwirkung mit acidischen Hydroxylgruppen oxidierte Gold- und Palladium-Spezies gebildet. Im Gegensatz dazu war mit den unter normalen Hydroxylierungsbedingungen gebildeten Hydroxylgruppen nahezu keine Wechselwirkung mit Gold, und Oxidation von Palladium erst bei höheren Temperaturen zu beobachten. Generell konnte jedoch festgestellt werden, dass die Funktionalisierung der Oberflächen zu einer Verbesserung der thermischen Stabilität von den Metall-Partikeln auf der MgO-Oberfläche führt.

Durch detaillierte Untersuchungen zur chemischen Wechselwirkung zwischen Palladium und Hydroxylgruppen konnten zwei prinzipielle Wechselwirkungsmechanismen bestimmt werden: die Redox-Reaktion: Pd + OH $\rightarrow$ PdO + 1/2 H_2; sowie die Wassergas-Shift (WGS)-Reaktion unter Beteiligung von adsorbiertem CO: Pd-CO + OH $\rightarrow$ Pd + CO_2 + 1/2H_2. Über Studien zur Pd-Bedeckungsabhängigkeit konnte die Signifikanz der an der Peripherie der Pd-Partikel gebundenen Hydroxylgruppen für die WGS-Reaktion herausgearbeitet werden. Vergleichende Experimente mit sauberen und oxidierten Pd(111)-Einkristall-Oberflächen dienten dazu, einerseits die besondere Rolle des Oxid-Substrats in den oben genannten Reaktionen zu unterstreichen, und andererseits den Einfluss von Wasser auf die Oberflächeneigenschaften von oxidierten Palladiumoberflächen zu bestimmen.

Zuletzt wurde die Adsorption und Dissoziation von Wasser auf MgO(001)/Ag(001) und CaO(001)/Mo(001)-Filmen verglichen. Die in dieser Arbeit vorgestellten Ergebnisse sind im Einklang mit der erwarteten höheren Reaktivität von CaO gegenüber MgO. Die Präsenz von dissoziiertem Wasser auf CaO(001) bei niedrigen Temperaturen führt zu einer starken Wechselwirkung mit darüber liegenden Eisschichten, die hauptverantwortlich dafür ist, dass es, im Gegensatz zu MgO, zu keiner beobachtbaren Kristallisation von amorphem Eis kommt. Zudem konnte gezeigt werden, dass die bei ultradünnen CaO-Schichten auftretende Mo-Dotierung zu einer deutlichen Reduktion des maximal erreichbaren Hydroxylierungsgrades von CaO führt, was sich positiv auf die Stabilität der Schichten auswirkt.

Contents

Acknowledgments **i**

Abstract **iii**

Zusammenfassung **v**

1 Heterogeneous Catalysis and Surface Science **2**

1.1 Motivation of Fundamental Catalyst Research 2

1.2 Surface Science: An Extremely Deductive Approach 4

1.3 Supported Catalysis with Water and Hydroxyls 7

1.4 Organization of the Dissertation 8

2 Experimental Methodology **10**

2.1 Low Energy Electron Diffraction (LEED) 10

2.1.1 Theoretical Principles 10

2.2 X-ray Photoelectron Spectroscopy (XPS) 13

2.2.1 Principles of XPS 14

2.2.2 Inelastic Mean Free Path and Quantification of Signal Intensity 16

2.2.3 Quantification of Binding Energy 17

2.2.4 Initial State Effect 18

2.2.5 Final State Effect 20

2.2.6 Line Shapes 22

2.2.7 Auger Parameter Analysis 23

2.3 Infrared Reflection Absorption Spectroscopy (IRAS) 24

2.3.1 Interaction of Infrared Light with Matter 25

2.3.2 Infrared Reflection Absorption Spectroscopy (IRAS) 27

2.3.3 Fourier-Transform Infrared Spectroscopy 29

2.4 Temperature Programmed Desorption (TPD) 30

2.4.1 Adsorption 30

2.4.2 Desorption and Analysis of TPD Spectra 32

3 Machinery and Experimental **36**
3.1 Overview of the Apparatus . . . 36
3.1.1 Preparation Chamber . . . 36
3.1.2 High-Pressure Cell . . . 39
3.2 Preparation of Samples . . . 41
3.2.1 Preparation of MgO(001) Films on Ag(001) and Hydroxylated MgO Films 42
3.2.2 Preparation of a Pd(111) Surface . . . 42

4 Properties of the MgO & MgO(001) Films on Ag(001) **44**
4.1 General Properties of MgO . . . 44
4.2 Characteristics of the MgO Surfaces and the MgO(001) Films on Ag(001) . . . 45

5 Growth of MgO(001)/Ag(001) Films and Their Hydroxylation **50**
5.1 Introduction . . . 50
5.2 Results . . . 51
5.2.1 Growth of MgO(001)/Ag(001) Films with Different Thicknesses . . . 51
5.2.2 Hydroxylation of MgO(001) Films . . . 53
5.3 Discussion . . . 57
5.3.1 Differences between MgO_{hydr} and MgO_{hg} in Electronic States and the Influence of the Ion Gauge . . . 57
5.3.2 Comparison of Hydroxylating MgO by Water (MgO_{hydr}) and Hydrogen (MgO_{hg}) . . . 59
5.3.3 Effects of MgO Film Thickness for MgO_{hydr} . . . 60
5.4 Summary . . . 61

6 Formation of Positively Charged Au Species on MgO Films **62**
6.1 Introduction . . . 62
6.2 Results and Discussion . . . 64
6.2.1 Au Coverage Dependence on Thick MgO Films . . . 64
6.2.2 Thermal Stability of Au-Carbonyl Clusters and Au Sintering . . . 65
6.2.3 Morphological Aspects . . . 68
6.2.4 DFT Calculations for Free $[Au_nCO]^+$ and Supported $[Au_nCO]$ Complexes 69
6.3 Discussion . . . 71
6.3.1 Origins of the Positively Charged Au on MgO Surfaces . . . 71
6.4 Conclusions . . . 72

7 Interactions of Au and Pd with Active Hydroxyls on MgO(001) **74**
7.1 Introduction . . . 74
7.2 Results . . . 75
7.2.1 Differences in the Reactivity of Metals with Reactive Hydroxyls . . . 75
7.2.2 Interactions of Au with MgO_{hi} . . . 76

7.2.3 Interactions of Pd with MgO_{hi} . . . 79
7.3 Discussion . . . 83
7.3.1 Specific Depletion of Surface Hydroxyls upon Metal Deposition . . . 83
7.3.2 Chemical States of Au/MgO_{hi} . . . 83
7.3.3 Pd on MgO_{hi} . . . 85
7.4 Conclusions . . . 88

8 Metal-Redox and Water-Gas Shift Reaction of Pd with Hydroxyls 90
8.1 Introduction . . . 90
8.2 Results . . . 92
8.2.1 Reactivity of Pd with Surface Hydroxyls on MgO_{hydr} . . . 92
8.2.2 Modification of Pd Electronic Structure by Surface Hydroxyls at Elevated Temperatures . . . 94
8.2.3 The Water-Gas Shift Reaction over Various Size Pd Particles on MgO_{hydr} 97
8.2.4 Interactions of Au with MgO_{hydr} . . . 102
8.3 Discussion . . . 105
8.3.1 Metal-Redox Process of the Pd Particles with Surface Hydroxyls at Elevated Temperatures . . . 105
8.3.2 Mechanistic Insight for the WGS Reaction over Pd/MgO_{hydr} . . . 106
8.3.3 Deactivation Mechanisms of Pd Particles in the WGS reaction . . . 108
8.3.4 Electronic Structure of Au Weakly Interacting with Surface Hydroxyls . . 110
8.4 Conclusions . . . 112

9 Oxidation of Pd, and the Reduction with Water 114
9.1 Introduction . . . 114
9.2 Results . . . 116
9.2.1 Oxidation of Pd Particles and Pd(111) Surfaces and Their Hydroxylation 116
9.2.2 Thermal Reduction of Hydroxylated PdO_{hev} Surfaces . . . 118
9.2.3 Thermal Reduction of Hydroxylated PdO-MgO . . . 121
9.3 Discussion . . . 123
9.3.1 Activation of PdO by Hydroxylation . . . 123
9.4 Conclusions . . . 127

10 Interaction of Water with the CaO Films Grown on Mo(001) 130
10.1 Introduction . . . 130
10.2 Experimental . . . 132
10.3 Results . . . 132
10.3.1 Growth of Thin and Thick CaO Films . . . 132
10.3.2 Characterization of CaO(001) Interacting with Water . . . 133
10.3.3 Ice Desorption and its Phase Transition over CaO(001) . . . 137
10.3.4 Effect of Film Thickness on Hydroxyls . . . 138

10.4 Discussion 139
10.4.1 Characterization of Surface Hydroxyl Groups 139
10.4.2 Mechanisms behind Hydroxylation and the Effect of Films Thickness . . . 144
10.4.3 ASW → CI Transition and Surface Hydroxyls 145
10.5 Conclusions 146

11 Conclusions and Outlook **148**

Abbreviations **152**

Appendix **154**
A Infrared Spectra of CO Adsorbed on Supported Au under Various Conditions 154
B O_2 Adsorption on Ultra-Thin MgO/Mo(001) Films 155
C Auger Parameter Analysis for Au/MgO 156

References **162**

Chapter 1

Heterogeneous Catalysis and Surface Science

The great importance of catalysis is reflected by the fact that it is involved in the production of almost 90 % of fundamental materials, and, furthermore, heterogeneous catalysts are employed in 85 % of catalytic processes [1]. Metal particles supported on oxide supports as one type of catalyst used in heterogeneous catalysis have received considerable attention both in industrial and fundamental research, but mechanistic understanding of the surfaces processes occurring during reactions is limited due to the high complexity of these systems. *Surface science* is a fundamental-oriented approach which can be applied to better understand chemical reactions occurring on catalyst surfaces. Within the realm of surface science research of single-crystalline oxides, epitaxially grown oxide thin-films have been utilized for convenience as well as controllability, instead of single-crystalline bulk oxides, owing to their ability to avoid charging problems, uncontrollable bulk contamination, etc. This study, carried out using oxide thin-films as supports for metal nanoparticles, aims to gain fundamental understanding of the catalytic reactivity of supported metal/oxide catalysts.

1.1 Motivation of Fundamental Catalyst Research

A catalyst, discovered by Döbereiner two centuries ago, is a material which selectively accelerates a specific chemical reaction [1, 2]. This promotional effect is achieved by the reduction of free enthalpy (or Gibbs function), $\Delta G^{\ddagger}$, which is given in units of joules per mole [J/mol], for a specific reaction and by suppressing the production of by-products. Fig. 1.1 displays energy diagrams corresponding to reaction pathways for the reaction A + B $\rightarrow$ AB with or without catalyst. Without catalyst, the reaction proceeds via the direct collision of the two molecules with each other which may be characterized by a free enthalpy of the corresponding transition state (indicated by ‡) $\Delta G_1^{\ddagger}$. In the catalytic reaction, the reactants A and B can adsorb on a catalyst surface, and subsequently react to form the product AB, which desorbs into the gas-phase. This energetically favored path brings about the same product and the same change in the enthalpy

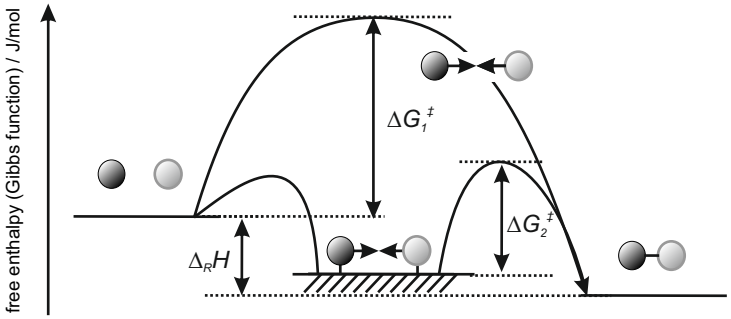

Figure 1.1: An energy diagram of the chemical reaction (A + B → AB) without a catalyst ($\Delta G_1^{\ddagger}$), and with a catalyst ($\Delta G_2^{\ddagger}$). A catalyst can change the reaction path, by which the free enthalpy (Gibbs function) of activation drops from $\Delta G_1^{\ddagger}$ to $\Delta G_2^{\ddagger}$, but the enthalpy of reaction, $\Delta_R H$, remains the same.

of reaction, $\Delta_R H$, but requires a much smaller free enthalpy, $\Delta G_2^{\ddagger}$, compared to the simple gas-phase collision reaction. The different reaction path with the smaller $\Delta G^{\ddagger}$ in the presence of a catalyst can account for the acceleration of a specific reaction. The enthalpy of reaction, however, remains the same, because only thermodynamic parameters such as temperature and pressure affect the chemical potential of the contributing species. This means that the presence of catalysts does not change the chemical equilibrium.

In order to highlight important aspects of catalysis, artificial nitrogen fixation, known as the "Haber-Bosch" process, is taken as an example [1]. The successful industrial scale nitrogen fixing reaction achieved by this process enabled human beings for the first time to produce chemical nutrition for the production of nitrogen-containing molecules in plants. This process proceeds as $N_2 + 3H_2 \rightarrow 2NH_3$ with a negative reaction enthalpy, ΔH° of -92.4 kJ/mol [3]. As this reaction is exothermic, thermodynamics favors the formation of the product at low temperatures. However, there is a high free enthalpy, ΔG, required to break the strong nitrogen triple bond. As a result, the reaction rate becomes too low to be practically used. This kinetically unfavorable situation can be overcome by raising the temperature, which is, however, thermodynamically unfavorable, as demonstrated by the van't Hoff equation. Hence, its successful operation demands the following compromised conditions: high temperature (> 600 K) to enhance the reaction rate, and high pressure (> 100 bar) to shift the equilibrium to the product by increasing the entropy contribution according to the Le Chatelier's principle. This relatively harsh experimental condition consumes a lot of energy, as evidenced by the fact that 1 % of energy consumption in the world is spent for this process. These facts fruitfully illustrate why both kinetic and thermodynamic factors significantly matter for successful catalytic reactions, and, moreover, why it is of crucial importance to develop superior catalysts.

Regarding the catalyst material, the Haber-Bosch process proceeds over solid Fe, to which Al_2O_3, K_2O, etc., are added as promoters (their functions are briefly mentioned in the next section) [4]. This solid material is exposed to N_2 and H_2 gases during the catalytic process. Pro-

cesses where the catalyst and reactants are present in different phases belong to the category of heterogeneous catalysis, whereas in homogeneous catalysis, both the catalyst and the reactants are present in the same phase. The advantages of heterogeneous catalysts are their insolubility, robustness, re-usability, and easy separation of catalyst material from reactants/products [1]. The disadvantages of heterogeneous catalysts are the difficulties in controlling reactions and identifying active local sites, structures and surface compositions. These difficulties, which mainly arise from the extraordinary complexity of the catalytically most active materials and materials combinations, limit the possibilities for a rational catalyst design. Fundamental research into catalysis using specifically designed and less complex model systems has the potential to reveal basic physical and chemical properties of catalytically active surface ensembles and may thus allow deeper insight into catalytic processes to be obtained.

1.2 Surface Science: An Extremely Deductive Approach

Catalysts composed of metal nano-particles supported on oxides are a typical and widely utilized class of material in heterogeneous catalysis (Fig. 1.2) [1]. The catalytically active sites are presumed to be the surface sites of the metal particles or specific metal/oxide interface sites. Hence, different combinations of metals and oxides exert distinct catalytic activity. For instance, dispersed Pt and Rh particles in the automotive three-way catalyst are mainly involved in CO oxidation and NO_x reduction, respectively. Moreover, the choice of the oxide support can also dramatically influence the reactivity (for example, CO oxidation over supported Au nano-particles is strongly promoted over reducible oxides such as TiO_2 [5, 6]). A summary of the properties of different oxides is given elsewhere [7].

Heterogeneous catalysts exhibit a high level of complexity, for which few details are known about the relationship between the structure and the catalytic activity. A first issue concerns the inhomogeneous distribution of particles sizes and the uncontrollable presence of specific local structures. Well prepared supported catalysts should be in the thermodynamically most stable state. This fact, however, does not necessarily assure that all the microscopic structures are in the thermodynamically equilibrated state; there might be specific local configurations far from equilibrium with dominant catalytic activity. Therefore, dominant surface morphological features as identified by microscopic techniques must not necessarily be the sites with superior catalytic activity. The second area devoid of information is the influence of impurities such as K, Li, Mg, Ca [8]. These alkaline(earth) elements often act as promoters in catalytic reactions by modifying the electronic and conformational structures of the supported metals or of the oxide surfaces [9,10], or by accommodating key molecules or functional groups, which are subsequently provided for chemical reactions [11]. A notable example is found for the Fe catalyst used in the Haber-Bosch process, whose activity is enhanced by using Al_2O_3 as a structural promoter, and K_2O as an electronic promoter [12]. The last challenge lies in the lack of information about the elementary catalytic steps responsible for reaction under working conditions, where dissipative structures at elevated chemical potentials could change catalytic reactivities, as illustrated below

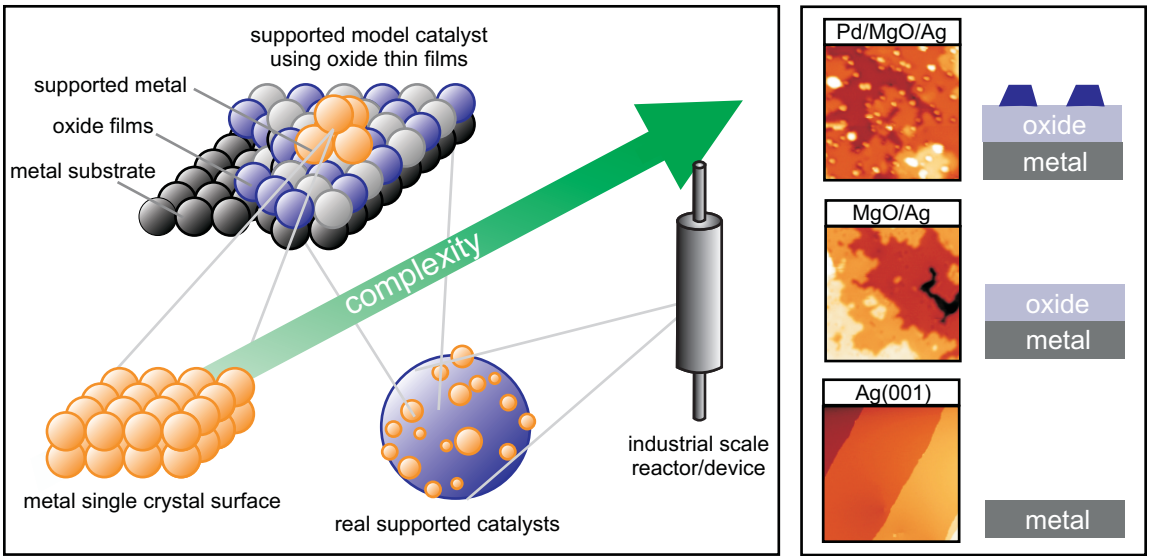

Figure 1.2: Left panel; Material gap. Catalysts of interest with different complexity are displayed; metal single crystal (left), supported model catalyst (middle left), powder catalyst (middle right), and industrial catalysts/devices (right). Right panel; the preparation procedure of a model supported oxide catalyst using metal oxide films grown over a metal substrate. The STM images correspond to (i) clean an Ag(001) substrate (200 × 200 nm^2), (ii) 8 ML MgO(001) films on the Ag(001) substrate (40 × 40 nm^2), (iii) Pd on the MgO(001) films (30 × 30 nm^2). The cartoons correspond to the next STM images, respectively.

regarding the influence of pressure.

Within the realm of *surface science*, which uses UHV technology and sophisticated methods of surface physics, a bottom-up approach has been extensively applied in the last decades in order to tackle these challenges on the basis of model systems [13]. The simplest model systems conceivable for heterogeneous catalysts are well-defined surfaces of metal single-crystals (see Fig. 1.2). In these models the complexity is reduced to only one specific type of metal surface species (as present, for example, on low Miller-index planes), and the influence of particle size or the presence of oxide supports and metal/oxide interfaces is not taken into account. Nevertheless, these simplest models have succeeded in providing atomic scale understanding of surface processes. A representative system is the CO oxidation reaction on Pt(110) and Pt(111) surfaces [2]. Using these systems, Ertl and his co-workers demonstrated that it is possible not only to reveal reaction mechanisms and sites, but also to control entire surface catalytic reactions.

The transfer of knowledge obtained from the metal single-crystal surface science models to real catalysis is, however, still a long-term goal, primarily because of the following aspects [14].

1. The material gap

2. The pressure gap

The material gap refers to issues caused by (i) the presence of the oxide support, and (ii) those of

complicated local structures on the surface of metal particles or at metal/oxide interfaces, which cannot be studied with the simple single-crystalline metal surface models described above.

One of the approaches to partially fill the material gap is to study supported model catalysts consisting of metal clusters deposited onto well-defined, single-crystalline oxide surfaces (see Fig. 1.2) [7, 15]. This approach has been successfully applied to single-crystalline "reducible" oxide surfaces such as rutile-TiO_2(110) [16], where sufficient electrical sample conductivity, which is required to allow techniques such as electron spectroscopy to be utilized without accompanying problems relating to sample charging, can be achieved by thermal reduction. However, thermal reduction typically does not work, at least without sample damage, for insulator materials. Therefore, studies using insulating bulk metal-oxides such as MgO or Al_2O_3 are forced to be carried out under severe restrictions, and only a few analytical methods (e.g., AFM, IRAS and TPD) can be applied.

A circumventive method is to grow well-defined films of insulators or semiconductors on single crystalline metal surfaces, via, for example, reactive deposition of metal in an oxygen atmosphere (see the right panel in Fig. 1.2). This *thin film* approach was pioneered by Somorjai and followed by Goodman and Freund [17–19]. Typical problems such as charging and surface contamination (for example by thermal induced segregation of bulk impurities) encountered with insulating oxide samples, are avoidable with this approach [20]. The surface properties of the oxide films were found to correspond to those of bulk single-crystal oxide surfaces when the thickness of the films was sufficiently large [20]. Hence, the oxide films provide a unique opportunity not only to study stoichiometric supported systems, but also to tune critical parameters of the oxide supports for catalytic activity, such as the number of defects [21], the amount of dopants [10], or the degree of reduction or oxidation [22]. Moreover, owing to the strong interactions with the metal substrate underneath, thin oxide films may even be responsible for a new catalytically active phase formed under ambient environments [23]. While covering of metal particles with thin oxide layers, which may be caused by strong metal support interaction (SMSI) effect [24], does often lead to catalyst deactivation, recent studies found specific metal/oxide combinations to be catalytically much more active than the pure metal substrate [25].

The other gap, the *pressure gap*, indicates that the relevance of the behavior of atoms or molecules under UHV conditions could be questioned because the pressure-induced chemical potentials are overlooked in surface science studies, despite its importance in, for instance, the ethylene epoxidation over Ag [26]. The chemical potential for an ideal gas reads,

$$\mu = \mu^\circ + RT \ln(\frac{p}{p^\circ}) \tag{1.1}$$

where μ is the chemical potential, μ° is its standard state chemical potential, R is the gas constant, T is the temperature, and p and p° are relevant pressure and the standard state pressure, respectively. Upon increasing the pressure from 10^{-10} mbar (UHV condition) to 1 mbar (typical ambient environment) at 300 K, the chemical potential increases by $\sim$ 57 kJ/mol. This chemical potential difference is large enough to induce differences in adsorption states and chemical reactivity on the surface. A classical example to demonstrate how pressure matters

Table 1.1: Surface sensitive techniques operating under ambient conditions.

Name	working principle	environment	Information	Resolution	ref.
AP-XPS	phototelectron by x-ray	gas & liquid	chemical state	$\sim$ meV	[30, 31]
PM-IRAS	IR absorption	gas & liquid	vibration at interface	1 cm^{-1}	[32]
SFG	IR generation by IR + visible	gas & liquid	vibration at interfaces	1 cm^{-1}	[33, 34]
XAS	x-ray absorption, fluorescence	gas & liquid	structure, chemical state	0.02 Å	[35]
STM	tunneling electron	gas & liquid	structure, density of states	1 Å	[36, 37]
AFM	van-der Waals force	gas & liquid	structure, atomic force	1 Å	[38, 39]
GISAXS	Bragg diffraction	gas	structure	1 Å	[40]
E-TEM	Electron energy loss	gas	structure, chemical states	1 Å	[41, 42]

is found in CO adsorption on Rh/Al_2O_3. Whereas an infrared spectroscopic study indicated the formation of isolated Rh-carbonyl clusters [27], TEM under UHV conditions suggested the preservation of large Rh clusters [28]. Later on, this puzzle was solved in terms of the pressure gap, namely, CO-induced Rh dispersion occurs at elevated pressures, while CO free Rh particles experience energetically-favored agglomeration [29]. This non-negligible pressure-induced dynamic Rh clustering has clearly made *in-situ* observation today's provocative theme, leading to the development and usage of *i*n-situ surface sensitive analytical techniques, which are summarized in Tab. 1.1.

1.3 Supported Catalysis with Water and Hydroxyls

What happens if supported systems experience environmental conditions? This question is of particular interest since oxide surfaces can be decorated by surface functional groups, which might affect surface reactivity under relevant environmental conditions. The simplest and probably most abundant species on oxides surfaces in ambient atmosphere are hydroxyls. Surface hydroxyls play numerous roles on the surface of heterogeneous catalysts. They can act as a promoter in chemical reactions by their direct or subsequent involvement in reactions such as CO oxidation, probably through the formation of intermediates [5], be directly involved in the chemical reactions, such as in water-gas shift [43], or may indirectly be involved, for example, by inhibiting the agglomeration of supported metals [44, 45]. Moreover, surface hydroxyls present at oxide/liquid interfaces during catalyst preparation (e.g., by impregnation of metal-complexes onto oxide surfaces from the aqueous phase) can control the properties of supported metal catalysts [46]. It has been generally accepted that the properties of surface hydroxyls in catalyst preparation can be tuned by the solution pH, which consequently determines the fate of metal-complexes upon their adhesion onto oxide surfaces, or even their activation by the removal of ligands.

From a fundamental point of view, the interaction of metals with surface hydroxyls has been studied using well-defined hydroxylated oxide surfaces, and several changes to the properties of

the supported metals could clearly be ascribed to their interaction with hydroxyls: the transient or permanent formation of corrosive oxygen, i.e., the oxidation of metals [47–52]; or the accommodation of protons by supported metals such as Pt, Pd, Rh [53]. Despite their paramount importance, few surface science studies or atomic scale investigations have appeared that reveal the effects of "genuine" surface hydroxyls on supported metals, owing to the necessity of exposure of oxide surfaces to water vapor at elevated pressure and to the difficulties in analyzing the changes induced by surface hydroxyls [45, 47–49, 51, 53–60]. The development today in closing both the material and pressure gaps has started to allow overcoming the gaps so that we can take advantage of the ability to prepare well-defined hydroxyl-covered oxide surfaces, and apply sophisticated surface science techniques to obtain atomic-level understanding of their rich chemistry. This is the theme of this dissertation.

1.4 Organization of the Dissertation

The specific aims of this thesis are to reveal chemical interactions between supported metals and hydroxyls on oxide surfaces. In particular, the reactivity and electronic structure of both the oxide surfaces and the supported metals are focused on. To this end, both clean and hydroxylated oxide surfaces are prepared and investigated, taking advantage of the capabilities of our combined UHV/elevated pressure chamber system. Conventional surface science techniques such as low energy electron diffraction (LEED), infrared reflection absorption spectroscopy (IRAS), x-ray photoelectron spectroscopy (XPS) and temperature-programmed desorption (TPD) are employed to characterize and monitor the sample surfaces. The present work treats mainly the stoichiometric MgO(001) film grown on an Ag(001) substrate [18]. The properties of the MgO films are tuned by changing the film thickness [25, 61], or by functionalizing the surface with hydroxyls [46]. First, the characterization of MgO films with different thicknesses and hydroxylated MgO films prepared by different procedures is performed. Subsequently, the interaction of metals (Au and Pd) with these surfaces and the chemical reactions occurring in the systems are investigated. Since Pd is found to strongly interact with surface hydroxyls, a study on the interaction of metallic and oxidized Pd particles and surfaces with water molecules is comprehensively conducted, in order to determine the particle size and oxidation state effects. Finally, the interaction of water with CaO(001) films grown on Mo(001), as a comparison to the MgO(001) films, is documented. CaO exhibits the same crystal structure but a much higher basicity, as compared to MgO. Therefore, it provides an excellent example to reveal the significance of surface basicity in the interactions of oxides with water at UHV as well as elevated pressures. The details of the above mentioned topics are provided in the following.

- Details about the experimental methodology (LEED, XPS, IRAS and TPD), the machinery and the procedures to prepare samples employed in this study follow in the next chapters (Chapter 2 and Chapter 3). Regarding photoelectron spectroscopy, Chapter 2 includes a detailed explanation of electron binding energy shifts observed in XPS of

supported systems as well as a method called *Auger parameter analysis*, which allows additional information about the origin of electron binding energy shifts to be obtained.

- The properties of the bulk MgO material, the MgO surface, and the MgO(001) films prepared on an Ag(001) substrate are explained in Chapter 4.

- The characterization and preparation of pristine MgO(001) films as well as the hydroxylated MgO(001) surfaces functionalized under various conditions are subsequently documented in Chapter 5. In particular, two different hydroxylated MgO surfaces covered with normal and active hydroxyls are presented. Their relevance to the realistic hydroxylated MgO is discussed.

- Results from the nucleation of Au on clean surfaces of MgO(001)/Ag(001) films as investigated by IRAS using CO as a probe molecule and interpreted with support by DFT calculations are presented in Chapter 6.

- Chapter 7 includes the results of the interaction of metals (Au and Pd) with active surface hydroxyls and their influence on the sintering of the supported particles. The deposited metals are shown to have distinct interactions with these hydroxyl groups.

- The main topic of this thesis, interaction of Pd and Au with the hydroxylated MgO(001) surface relevant to the realistic case, is presented in Chapter 8. A rich chemistry concerning interactions of Pd with surface hydroxyls is demonstrated: (i) small Pd particles strongly react with hydroxyls to evolve hydrogen molecules via the metal-redox process; (ii) the adsorbed CO on the Pd particles also contributes to the formation of hydrogen molecules via the water-gas shift reaction at the periphery of the Pd particles. Compared to Pd, the supported Au clusters show rather weak interaction with surface hydroxyls.

- A comparison of the reactivity of water with oxidized Pd(111) surfaces as well as supported PdO particles on the MgO(001) surface is presented (Chapter 9). A notable material gap within the regime of surface science is highlighted by comparing these two model systems. The influence of water on catalyst deactivation is discussed.

- The hydroxylation of the CaO(001)/Mo(001) films with different thicknesses is investigated (Chapter 10). This strongly basic oxide is proven to be easily hydroxylated and hydrated under UHV and ambient environments, respectively. Furthermore, different to MgO, the dewetting of the amorphous solid ice is found not to occur on the CaO surface because of the presence of interfacial hydroxyls. Lastly, the influence of dopants in CaO films on water adsorption is discussed.

- Chapter 11 summarizes the results of the dissertation, and provides an outlook for future research in this area.

Chapter 2

Experimental Methodology

This study employs the following four experimental methods: low energy electron diffraction (LEED), X-ray photo-electron spectroscopy (XPS), infrared reflection absorption spectroscopy (IRAS), and temperature programmed desorption (TPD). This chapter provides canonical information of the methods.

2.1 Low Energy Electron Diffraction (LEED)

When well-ordered surfaces are studied, the electron diffraction by periodic surfaces is very often utilized to reveal their two-dimensional spatial distribution with high surface sensitivity. The present section introduces this method, called *Low Energy Electron Diffraction* (LEED).

2.1.1 Theoretical Principles

For the determination of periodicity of surfaces under UHV environment the diffraction of low-energy electrons by surface atoms, called *low-energy electron diffraction* (LEED), is most widely utilized [62]. The reason why low energy electrons in the range of tens or hundreds eV are employed lies in their short de Broglie wavelength relevant to atomic scale. Indeed, electron's kinetic energy and its de Broglie wavelength hold the following relation.

$$\lambda \approx \frac{12.3}{\sqrt{E_{eV}}}\text{Å}. \tag{2.1}$$

The electrons in this energy range has a relatively short inelastic mean free path (see Section 2.2.2), by which LEED can be used as a highly surface sensitive tool. When an electron with a de Broglie wavelength of λ propagates in a direction described by the spherical coordinates (θ, ϕ), its wave vector $\boldsymbol{k}$ is described as:

$$\boldsymbol{k} = (k_x, k_y, k_z) = \frac{2\pi}{\lambda}(\sin\theta\cos\phi, \sin\theta\sin\phi, \cos\theta) = \frac{2\pi}{\lambda}\boldsymbol{n}, \tag{2.2}$$

where $\boldsymbol{n}$ is a unit vector.

Let us consider electron diffraction at a surface, as schematically described in real space (Fig. 2.1a), where an electron with $\boldsymbol{k}^0$ impinges on a surface at an angle of ϕ between the

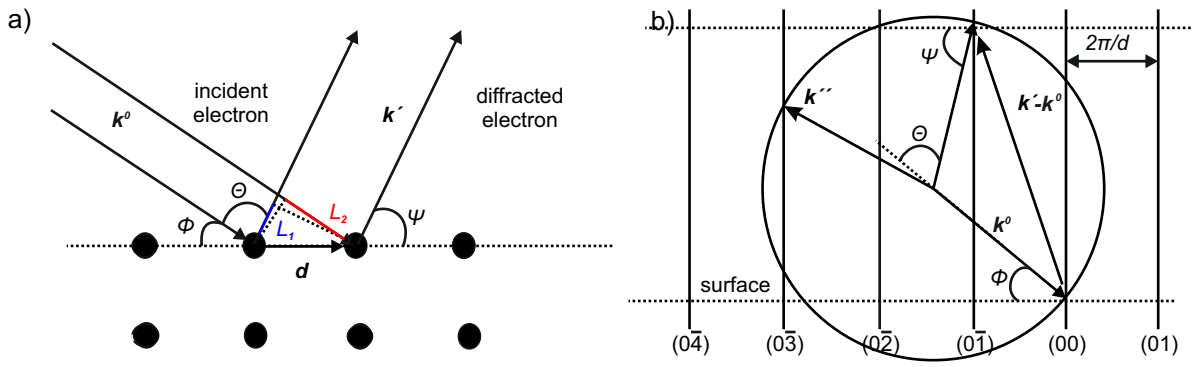

.

Figure 2.1: a) A real space representation of electron diffraction. The incident beam impinges onto the surface at an angle of ϕ between the incident beam and the row of the scatters, and the diffracted beam leaves the surface at an angle of ψ between the diffracted beam and the row of the scatters. b) The corresponding diffraction event in reciprocal space (k-space). The circle represents the so-called *Ewald Sphere*, which indicates the following electron beams: an incident electron, $\boldsymbol{k}^0$, and elastically diffracted electrons, $\boldsymbol{k}'$ and $\boldsymbol{k}''$

incident beam and the row of the scatters, and the elastically scattered electron with $\boldsymbol{k}'$ leaves the surface at an angle of ψ between the diffracted beam and the row of the scatter [62,63]. The path difference between the two routes, L_1 and L_2, is found:

$$L_1 - L_2 = |\boldsymbol{d}| \cdot (\cos\psi - \cos\phi) = \boldsymbol{d} \cdot (\boldsymbol{n}' - \boldsymbol{n}^0), \tag{2.3}$$

where $\boldsymbol{d}$ is the displacement vector of scatters, and $\boldsymbol{n}^0$ and $\boldsymbol{n}'$ the unit vectors of $\boldsymbol{k}^0$ and $\boldsymbol{k}'$, respectively. The constructive interference between these two beams at different atoms could basically be achieved when the path difference is equal to $m\lambda$ for integer m:

$$\boldsymbol{d} \cdot (\boldsymbol{n}' - \boldsymbol{n}^0) = m\lambda. \tag{2.4}$$

This condition, called the Laue condition, is rewritten in the following expression with $\boldsymbol{k}$-vectors.

$$\boldsymbol{d} \cdot (\boldsymbol{k}' - \boldsymbol{k}^0) = 2\pi m. \tag{2.5}$$

As evident from Eq. 2.5, diffraction is conveniently treated using wave vectors. To this end, let us describe two dimensional periodic systems in k-space (reciprocal space). The translational periodicity of the surface allows defining a primitive unit cell, which is a unit cell built on the primitive basis of the direct lattice. This means that the same point in different unit cells are connected by so-called lattice vectors, which can be described as a linear combination of the two basis vectors, $\boldsymbol{a}_i$ and $\boldsymbol{a}_j$ of the lattice for integers n and m such that:

$$\boldsymbol{R} = n\boldsymbol{a}_i + m\boldsymbol{a}_j. \tag{2.6}$$

Two dimensional systems have five Bravais lattices: oblique, rectangular, rhombic, square and hexagonal. The reciprocal lattice vectors, $\boldsymbol{b}_i$ and $\boldsymbol{b}_j$, are defined by basis vectors:

$$\boldsymbol{b}_i = 2\pi \frac{Q(\theta_0)\cdot \boldsymbol{a}_j}{\boldsymbol{a}_i \cdot \boldsymbol{a}_j}, \tag{2.7}$$

$$\boldsymbol{b}_i \cdot \boldsymbol{a}_j = 2\pi\delta_{ij}, \tag{2.8}$$

where $Q(\theta_0)$ is the 90 degrees rotation matrix. Note that $\boldsymbol{b}_i$ is perpendicular to $\boldsymbol{a}_j$. If we define $\boldsymbol{k}_{xy}$ as the orthogonal projection of $\boldsymbol{k}$ onto the xy-plane, $\boldsymbol{k}_{xy}$ and $\boldsymbol{b}_i$ share the same unit. Each lattice point in reciprocal space refers to a set of lattice lines (planes for three-dimensional systems) in real space, and the corresponding unit cells are separated with a distance of $2\pi/a_i$ in the b_i axis. At a surface, the periodicity is broken in the perpendicular direction, so that only the two dimensional periodicity in parallel to the surface remains (i.e., there are rods normal to the surface). This is why we need to construct only two dimensional reciprocal space to consider diffraction at surfaces.

Let us find a condition for constructive diffraction from a surface. Eq. 2.5 is the condition for constructive interfere among two electron beams. However, in order to observe diffraction, not only just two beams, but also a set of all beams at the sites of a Bravais lattice must constructively interfere. This means that the condition given in Eq. 2.5 needs to be held for all $\boldsymbol{R}$ that are Bravais lattice vectors, instead of a specific $\boldsymbol{R}$:

$$\boldsymbol{R}\cdot(\boldsymbol{k}'_{xy} - \boldsymbol{k}^0_{xy}) = 2\pi(np + mq) = 2\pi l, \tag{2.9}$$

for $\boldsymbol{k}'_{xy} - \boldsymbol{k}^0_{xy} = p\boldsymbol{b}_i + q\boldsymbol{b}_j$ with coefficients p, q and integers m, l. Provided that Eq. 2.9 must be fulfilled for any $\boldsymbol{R}$, the change in wave vector, $\boldsymbol{k}'_{xy} - \boldsymbol{k}^0_{xy}$, should be a vector of the reciprocal lattice with *integers* coefficients. This constructive interference is instructively described in reciprocal space (Fig. 2.1b), in accord with the scheme shown in Fig. 2.1a. There is an incident beam, $\boldsymbol{k}_0$, pointing to a reciprocal lattice point (0, 0). The wave vector of the diffracted beam, $\boldsymbol{k}'_{xy}$, points to (0, −1). Note that $\boldsymbol{k}'_{xy}$ has the same kinetic energy, and that $\boldsymbol{k}'_{xy} - \boldsymbol{k}^0_{xy}$ is a vector pointing from (0, 0) to (0, −1): $\boldsymbol{k}'_{xy} - \boldsymbol{k}^0_{xy} = -\boldsymbol{b}_j$. Because the coefficients of this wave vector are integers, the constructive interference occurs between the waves in accord with Eq. 2.9. There are also other possible constructive diffraction between, for example, $\boldsymbol{k}^0_{xy}$ and $\boldsymbol{k}''_{xy}$ for $\boldsymbol{k}''_{xy} - \boldsymbol{k}^0_{xy} = -3\boldsymbol{b}_j$.

There is a simple scheme to schematically draw how the diffraction spots appear. Since the elastic electron diffraction proceeds without the loss of electron kinetic energy, the energy conservation rule allows drawing a sphere of the electrons centered on the origin of the incident wave vector $\boldsymbol{k}_0$ in reciprocal space. This sphere (or circle in two dimensional) intersects with several reciprocal lattice rods. As discussed above, these intersection points allow constructing the wave vector of the outgoing electrons which fulfill the Laue condition. Therefore, this sphere (or circle) can be used to visualize the diffraction spots or peaks for specific crystal structures. This sphere is specifically called the *Ewald Sphere*.

Briefly, the electron diffraction from single crystalline surfaces are illustrated. For regular surfaces with the rectangular symmetry such as Pt(110) or the hexagonal one such as Pt(111),

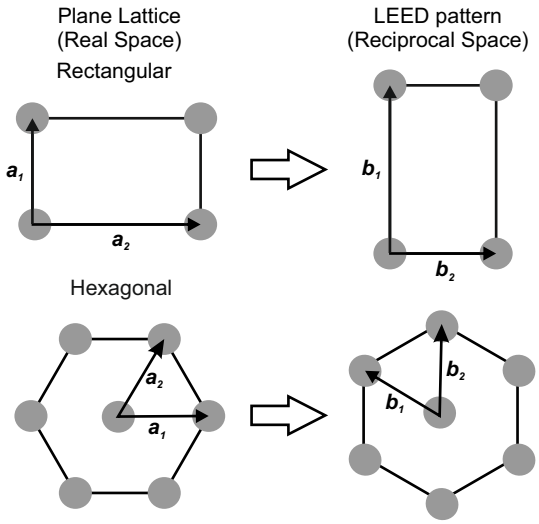

Figure 2.2: Bravais lattices of surfaces with the rectangular symmetry (top) and the hexagonal one (bottom) in real space and the corresponding diffraction patterns in reciprocal space.

Fig. 2.2 displays their real space lattices (left) and the corresponding reciprocal space (right). For the surface unit cell with D_{2h} symmetry, the diffraction spots in the $\boldsymbol{a}_1$ and $\boldsymbol{a}_2$ axes are placed in a distance of $2\pi C_0/\boldsymbol{a}_1$ and $2\pi C_0/\boldsymbol{a}_2$ for constant C_0. The surface unit cell with D_{6h} symmetry, however, exhibits complexity. The reciprocal space basis vectors are no longer co-linear with the corresponding real space basis vectors due to the orthogonality requirement stated in Eq. 2.8.

Lastly, it is emphasized that the LEED pattern itself only contains information on the lattice, hence, the geometric properties of the unit cell. The atom positions also called the basis are encoded in the intensities of the diffraction spots. In order to obtain the quantitative information of atomic positions within a surface unit cell, the energy-dependence of LEED spot intensities (the geometrical structure factor) need to be analyzed. This method is called the LEED-IV [62].

2.2 X-ray Photoelectron Spectroscopy (XPS)

The determination of chemical composition, the chemical states of the elements and their concentrations are important information needed for a meaningful discussion of surface properties. X-ray photoelectron spectroscopy (XPS) is utilized as a non- destructive analytical method to determine these quantities. This analytical method takes advantage of the photoelectric effect, for which x-rays are employed as an excitation source. Here, its theoretical foundations and considerations for interpreting the data are provided. Furthermore, the so-called Auger parameter analysis is explained, which takes advantage of both photoelectrons and X-ray excited Auger electrons for better understanding of the photoelectron spectra.

2.2.1 Principles of XPS

Photoelectron Spectroscopy (PES) is a technique to observe electrons ejected from a surface after irradiation with photons of sufficient energy to overcome the work function of the surface. This photoinduced electron ejection, called the *photoelectric effect*, was discovered by Herz, and later Einstein. When x-rays are employed as the excitation source, this technique is specifically called X-ray Photoelectron Spectroscopy (XPS). The development of this method was attempted even in 1930's by de Broglie, but Siegbahn was the first who succeeded in constructing a sophisticated electron analyzer to obtain highly resolved XPS spectra in the mid 1960's [64, 65]. This achievement has enabled XPS to be a widely used technique today to characterize chemical compounds.

The photoemission process satisfies the following energy conservation relation;

$$E_k = h\nu - E_B - \phi, \tag{2.10}$$

where E_k, ν, E_B, and ϕ indicate the kinetic energy of an ejected electron, the frequency of an impinging photon, the binding energy for the ejected electron, and the work function of the surface, respectively. The binding energy of core levels is an atomic property, which allows the identification of elements present at or close to the surface of the material under consideration. However, the binding energy is also sensitive to the details of the electronic structure such as atomic charge states or the environment of the element. Therefore, the following information can be obtained using XPS:

- Determination of elements–elemental analysis of materials is possible, by measuring electron binding energies specific to element.
- Quantification of elements—The number of photoelectrons acquired from a material with an element-specific binding energy is ideally proportional to the concentration of the species. This quantification, however, must be carefully carried out with the consideration of electron inelastic mean free path (IMFP) and the cross sections of atomic orbitals for the photoemission process, as discussed later [66].
- Determination of chemical states via binding energy shifts—E_B of atoms is sensitive to their chemical states as well as their chemical environments. For instance, a negatively charged atom is surrounded by more electrons than a neutral one. This electron-rich environment results in the surrounding electrons being weakly bound to the nucleus, because there is weaker Coulomb interaction and stronger electron-electron repulsive forces. As a result, the orbital energies experience upward shifts toward the Fermi edge. In other words, electrons ejected from a reduced atom have higher kinetic energies (i.e., lower binding energies), compared to those from a neutral one. This crude consideration indicates that a correlation should be able to be made between the charge states of atoms and the binding energies of the photoelectrons [65]. In particular, the binding energy difference of a sample of interest and a reference is termed as the *binding energy shift*, whose details are provided in the next section.

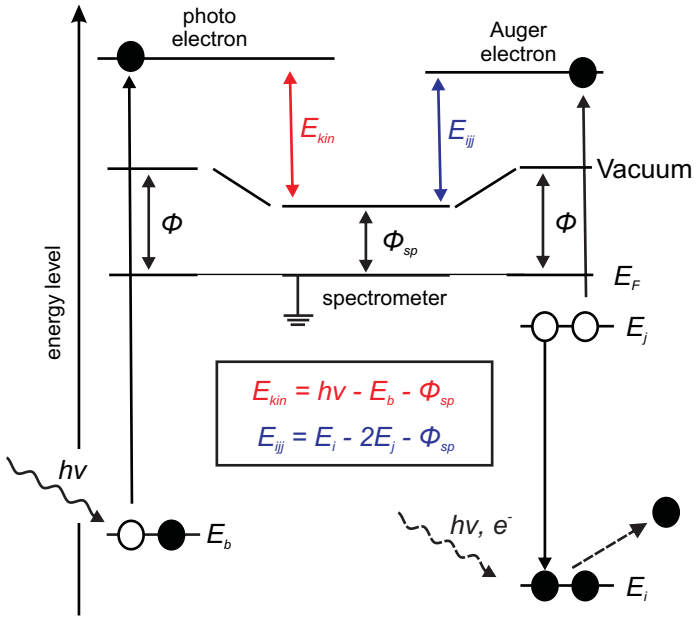

Figure 2.3: The schematics of the energy diagram for the photoemission process (left side), the ijj Auger process (right side), and the detection of these electrons by a spectrometer with a work function of ϕ_{sp}.

Prior to providing a detailed explanation about binding energy shift, the measurement principle of XPS is presented in an energy diagram (Fig. 2.3). Consider the typical photoemission event as described in Eq. 2.10 (Fig. 2.3, left). This ejected electron is monitored by an electron spectrometer (Fig. 2.3, middle). Both the sample and the spectrometer are grounded, which allows the Fermi edge of the sample to be in equilibrium with that of the spectrometer, unless the sample is an insulator or not grounded such as gas molecules [67]. The analyzer has a work function, ϕ_{sp}, and the work function difference between the sample and the spectrometer is called the contact potential, $\Delta\phi = \phi - \phi_{sp}$. $\Delta\phi$ becomes either positive ($\phi > \phi_{sp}$) or negative ($\phi < \phi_{sp}$), which increases or decreases measured kinetic energies of electrons, respectively [68]. The presence of the contact potential might require the modification of Eq. 2.10 to extract real kinetic energies of electrons detected by the spectrometer, reading:

$$E_k = h\nu - E_B - \phi_{sp}. \tag{2.11}$$

In an analogous way, the energetic diagram of the Auger process is provided in the right panel of Fig. 2.3. The Auger process begins with the creation of a core hole in an orbital i. Subsequent decay of one electron in an orbital j, with a higher orbital energy to the vacancy in the orbital i occurs. This decay is accompanied by a simultaneous electron ejection from orbitals with an orbital energy above E_i. Let a final state after the Auger decay have two core holes in the same orbital, j, after the Auger process. According to the energy conservation, the ejected electron,

called the *Auger electron*, has a kinetic energy of:

$$E_k = E_i - 2E_j - \phi_{sp}. \tag{2.12}$$

Note the fact that the kinetic energy of Auger electrons is independent of the energy of incident photon. It is emphasized that the diagram described above is valid only if the specimen's Fermi edge is in equilibrium with the analyzer and the sample is electronically neutral. For insulators, irradiated samples cannot be electronically neutral due to low conductivity (charging).

2.2.2 Inelastic Mean Free Path and Quantification of Signal Intensity

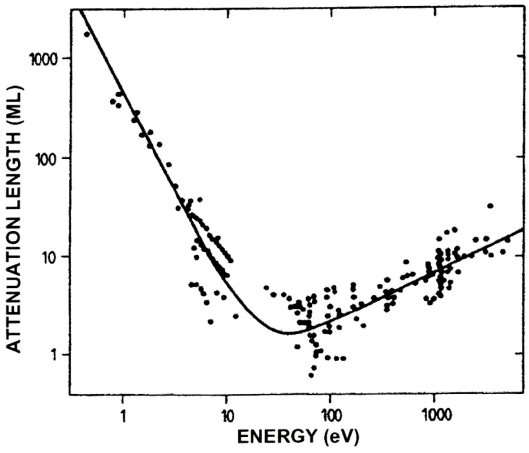

Figure 2.4: Inelastic mean free path of electrons as a function of electron's kinetic energy. The figure was taken from [69].

There is a detailed explanation concerning the quantification of peak intensity of XPS spectra [66], thus, we provide a brief account. Let us define the intensity of an XPS peak acquired at an angle of θ with respect to the surface, $I(\theta)$, acquired from a atomically flat semi-infinite specimen:

$$I(\theta) = I_\theta \Omega_\theta(E_k) A_\theta(E_k) \rho (d\sigma_k/d\Omega) \lambda_e(E_k), \tag{2.13}$$

where I_θ is the strength of x-ray beam, $\Omega_\theta(E_k)$ is the acceptance solid angle of analyzer, $A_\theta(E_k)$ is the effective specimen area, ρ is the density of the specimen, $d\sigma_k/d\Omega$ is the differential cross section, λ_e is termed the inelastic mean free path (IMFP), whose definition is provided next.

When an electron penetrates a material, its transmission probability varies as a function of its kinetic energy. Based on the Lambert-Beer rule, the transmission probability of electrons through a material, P, is given:

$$P = \exp(-d/\lambda_e), \tag{2.14}$$

where d is the effective path length of the electrons. This formula indicates that the longer λ_e is, the deeper electrons can penetrate a material. The IMFP is dominantly determined by kinetic energy, and IMFP as a function of the energy is displayed in Fig. 2.4. It is noticeable that the IMFP is in the range of 1–10 ML in an electron kinetic energy region of 10–1000 eV. This

relatively short IMFP due to strong interaction of electrons with matter makes XPS a powerful surface sensitive tool.

One useful application of the IMFP is the quantification of film thickness grown on a metal substrate. When electrons ejected from a substrate covered with an epitaxially grown film with a thickness of l are collected, at an electron emission angle of θ, the effective thickness of film, d, for the electrons to escape from the substrate to the vacuum is:

$$d = l \cdot \cos\theta. \tag{2.15}$$

According to the definition given in Eq. 2.14, the phototelectron count ratio of the samples with and without the overlayers, I_d/I_0, leads to the following relation:

$$P = \frac{I_d}{I_0} = \exp\left(-d \cdot \cos\theta/\lambda_e\right). \tag{2.16}$$

A simple mathematical transformation of Eq. 2.16 yields:

$$d = -\frac{\lambda_e}{\cos\theta} \cdot \ln\left(\frac{I_d}{I_0}\right). \tag{2.17}$$

The thickness of the overlayers can be quantified using Eq. 2.17 by measuring the number of photoelectrons ejected from a buried substrate before and after the film preparation, with the knowledge of the IMFP dependent on electron kinetic energy and the film's materials. Numerical data sets of IMFPs are found elsewhere [69, 70].

2.2.3 Quantification of Binding Energy

Here, a quantum mechanical approach for the quantification of binding energies is provided [71]. Within an adiabatic approximation (Koopmans' theorem), the binding energy defined by Eq. 2.11 is equal to the energy gain of the system of interest upon photoemission, because the creation of one core hole destabilizes the system. This energy gain, $-\varepsilon_k$, reads:

$$-\varepsilon_k = \langle \Psi_k^{N-1} \mid H^{N-1} \mid \Psi_k^{N-1} \rangle - \langle \Psi^N \mid H^N \mid \Psi^N \rangle, \tag{2.18}$$

where k is an orbital from which a photoelectron is ejected, H^N the Hamiltonian with N electrons, H^{N-1} the Hamiltonian with $N-1$ electrons. In this scheme, the frozen-core orbital wave-functions have been employed, i.e., all energy levels are fixed. Therefore, whereas Ψ^N is the eigenfunction of H^N, Ψ_k^{N-1} is not the eigenfunction of the $N-1$ electron Hamiltonian. For the calculation of the first term, $\langle \Psi_k^{N-1} \mid H^{N-1} \mid \Psi_k^{N-1} \rangle$, we need to do the eigenfunction expansion of Ψ_k^{N-1}:

$$\Psi_k^{N-1} = \sum_i c_i \psi_i \tag{2.19}$$

where c_i is a weighting factor, and ψ_i is an eigenfunction. Eq. 2.19 allows calculating $\langle \Psi_k^{N-1} \mid H^{N-1} \mid \Psi_k^{N-1} \rangle$, giving observable energy levels with a probability (intensity in the photoemission peak at the energy) of c_i^2. Thus, it is clear that ε_k is solely determined by the electronic structure of the solid in the absence of a photoemission event, and, hence, this contribution to the observed binding energy is specifically called the *initial state effect*.

There is, however, another contribution to the binding energy. A core hole created by the photoemission event creates local electric fields, which attract electrons to themselves (screening) [63]. Thereby, the electron deficient system is relaxed. The binding energy shift induced by the screening is called the *final state effect*, for which the following definition is given:

$$R_i = \langle \Psi_k^{N-1} \mid H^{N-1} \mid \Psi_k^{N-1} \rangle - \langle \Psi_\alpha^{N-1} \mid H^{N-1} \mid \Psi_\alpha^{N-1} \rangle \geq 0, \tag{2.20}$$

where α indicates that the system of interest is relaxed, i.e., in the lowest energy state with a core hole in k-orbital. Note that Ψ_α^{N-1} is the $N-1$ electron eigenfunction. As evident from this definition, the final state contribution is the extent of relaxation of the system. Using Eq. 2.18 as well as Eq. 2.20, the observed binding energy, $E_B(k)$, is disentangled into these two contributions:

$$\begin{aligned} E_B(k) &= \langle \Psi_\alpha^{N-1} \mid H^{N-1} \mid \Psi_\alpha^{N-1} \rangle - \langle \Psi^N \mid H^N \mid \Psi^N \rangle \\ &= (\langle \Psi_k^{N-1} \mid H^{N-1} \mid \Psi_k^{N-1} \rangle - \langle \Psi^N \mid H^N \mid \Psi^N \rangle) \\ &\quad -(\langle \Psi_k^{N-1} \mid H^{N-1} \mid \Psi_k^{N-1} \rangle - \langle \Psi_\alpha^{N-1} \mid H^{N-1} \mid \Psi_\alpha^{N-1} \rangle) \\ &= -\varepsilon_k - R_k. \end{aligned} \tag{2.21}$$

Lastly, the origin of binding energy shifts for the same element in different chemical states and environments is considered. When a binding energy of a system of interest is compared to that taken from a recognized reference, E_B^{ref}, its binding energy *shift* is defined as:

$$E_B(k) - E_B^{ref} = -\Delta\varepsilon_k - \Delta R_k. \tag{2.22}$$

With the unrealistic assumption that ΔR_k is negligibly small, the binding energy shift is interpreted as the pure difference in the initial state contributions. For example, if the material of interest is oxidized and the reference is a pure bulk metal, $-\Delta\varepsilon_k$ must be positive (thus, $\Delta\varepsilon_k$ is negative), because the oxidized material should have a deeper orbital energy than the corresponding metallic one. This assumption is, however, valid only if the difference in the final state contributions, ΔR_k, is negligible, i.e., screening efficiency of core holes is comparable among the samples. Indeed, bulk metals often employed as references have a superior ability of screening core holes to other samples such as metal particles supported on insulators or semiconductors, or even thin oxide films, because bulk metals have plenty of free electrons available for screening. The present study employs thin oxide films, where the core-hole screening still has a significant impact on binding energy shifts of the films as well as supported metal particles. Therefore, the final state contribution needs to be closely quantified by a method, called the Auger parameter analysis, as detailed in Section 2.2.7.

2.2.4 Initial State Effect

The initial state effect refers to any changes of orbital energies caused by chemical bonding, structural and environmental effects. Mechanisms to cause the shifts in energy levels include: change of oxidation state, called the chemical shift; altered bonding properties at the surfaces causing a surface core level shift; the changes of work function induced by particle's size.

Chemical Shift

The orbital energies of atoms shift upon the formation of chemical bonds or transformation into corresponding ions, which will change the density of electrons surrounding a nucleus, and, thereby, the electron-nucleus interaction (*chemical shift*). For example, oxidized metals donating electrons to oxygen atoms are found at higher binding energy, compared to neutral metals, because of the stronger Coulomb interaction between the electrons surrounding the nucleus as well as reduced electron-electron repulsion causing downward shift of the orbital energies of the oxidized metals, i.e., the increases of the binding energies [72]. Using references of chemical shifts taken from known samples, the oxidation state of atoms can be deduced from the observed chemical shift [64].

Surface Core Level Shift (SCLS) and Particle Size Effect

Surface atoms are less coordinated than bulk atoms; electrons above the surfaces are not spent on the formation of chemical bonds without adsorbates. Particularly, dangling bonds formed by valence electrons not spent on the formation of chemical bonds direct to the vacuum, and the electronic structure of surface atoms might be reorganized as a consequence of intraatomic charge transfer. For instance, in the case of surface gold atoms, the 6s→5d intraatomic charge transfer occurs, by which the 5d-shell is contracted for better screening (bulk configuration $5d^{9.6}6s^{1.4}$). Consequently, the binding energies of surface gold atoms decrease [73]. By contrast, there are also *positive* binding energy shifts of orbitals belonging to surface atoms with respect to those of bulk atoms [74]. Because surface atoms are identified to account for the binding energy shift, this effect is called *Surface core level shift* (SCLS). The degree of SCLS is dependent on metals and orbitals. For example, the SCLS in Ag 3d lines is too small to be resolved [75].

SCLS is of particular importance for small supported metal particles, which contain a high fraction of undercoordinated metal atoms. Thus, their binding energies are expected to be featured by a positive/negative binding energy shift to a bulk metal [76]. Indeed, small supported metal clusters usually exhibit a positive binding energy shift [77]. This tendency, often referred to the *particle size effect*, is explained in conjugation with the work function change [77, 78] as well as the inefficient core hole screening in small metal particles [79]. Let us consider a work function change for small metallic particles upon photoemission. As the photoemission occurs in the system, the ejected electron leaves a positive charge in a particle. This positive charge gives rise to increasing the work function by an energy of e^2/R. For neutral metal particles, their work function reduces by $5e^2/(8R)$ relative to the plane surface due to the smaller Coulomb interaction, where R is the radius of a particle. Consequently, the work function change observed for small metallic particles with respect to bulk metals upon photoemission, $\Delta W(R)$, is increased by:

$$\Delta W(R) = \frac{3e^2}{8R} = \frac{5.40}{R(\text{Å})}\text{eV} \tag{2.23}$$

This simple formula could be further extended by the inclusion of the inter-atomic charge transfer from the substrate to the supported particles [80].

2.2.5 Final State Effect

Here, three important final state effects are treated: spin-orbit coupling (Multiplet splitting), screening and the formation of satellite peaks by plasmon losses and interband transitions.

Spin-Orbit Coupling (Multiplet Splitting)

The *spin-orbit coupling* refers to the interaction of spin of a particle with its motion. In quantum physics, this statement is expressed as: spin-orbit coupling arises when an atom simultaneously possesses non-zero orbital angular momentum, $\boldsymbol{l}$, and spin angular momentum, $\boldsymbol{s}$ [81]. In the case of electrons bound to a nucleus, the motion of electrons produces a magnetic field, with which the electron spin interact via the Zeeman interaction. The Hamiltonian of electrons bound to a nucleus with an atomic number of Z reads:

$$H = \underbrace{\sum_i \big(-\frac{\hbar^2}{2m_e}\Delta_i\big)}_{electron's\ kinetic\ energy} - \underbrace{\sum_i \big(\frac{Ze^2}{r_i}\big)}_{e^- - nucleus\ interaction} + \underbrace{\sum_{i>j} \frac{e^2}{r}_{ij}}_{e^- - e^-\ interaction} + \underbrace{\sum_i \zeta_i l_i s_i}_{spin-orbit\ interaction} \tag{2.24}$$

The Hamiltonian is mainly dominated by the first three terms: the kinetic energy of electrons (the first term) and the Coulomb interaction between the nucleus and electrons (the second term), in addition to the electron-electron interactions (the third term). The last term represents the spin-orbit coupling, where ζ_i is a constant roughly proportional to Z^4. This results in that, for light elements, the spin-orbit contribution is much smaller than the electron-electron interaction. Thus, the spin-orbit contribution can be obtained by a perturbation approach. This approximation is called Russell-Saunders or L-S coupling. For heavy atoms, the spin-orbit coupling becomes as strong as the interactions between individual spins or orbital angular momenta, so that the j-j coupling scheme is employed.

Let us consider the spin-orbit coupling within the L-S coupling. When an electron is ejected from a fully occupied orbital upon photoemission, an electron with either spin up, $\alpha = +1/2$ or spin-down $\beta = -1/2$ remains in the orbital. The calculation of spin-orbit interaction requires the introduction of the total angular momentum, J, defined as $\boldsymbol{J} = \boldsymbol{L} + \boldsymbol{S}$, because neither l nor s is a good quantum number. A state for a total angular momentum J is $(2L+1)(2S+1)$ fold degenerate such that $J = |L+S|, |L+S-1|, ..., |L-S|$. Since in the conventional photoemission process only one core hole per atom is created, the spin state holds $s = \pm 1/2$. Consequently, J becomes either $J = L + 1/2$ or $J = L - 1/2$. Since the degeneracy of J is $2J+1$, the ratio between the two states with α or β spins is

$$\frac{g_\beta}{g_\alpha} = \frac{l}{l+1}, \tag{2.25}$$

where g means degeneracy for each spin state.

This electron-spin induced splitting of degenerate energy levels can be observed in XPS measurements. A Pd 3d spectrum taken from a single crystalline Pd surface is employed as an example (Fig. 9.1a). When an electron is removed from the Pd 3d-orbital, only one L-S-term, ${}^{2S+1}D = {}^2D$, exists with a degeneracy of $(2L+1)(2S+1) = (2\times 2+1)(2\times 0.5+1) = 10$,

corresponding to the number of possible microstates. The presence of up/down electron spin in the Pd 3d orbital could split the ^2D state into two levels.

$$^2D_J = \begin{cases} ^2D_{2+1/2} = {}^2D_{5/2} & (g_\alpha = 6) \\ ^2D_{2-1/2} = {}^2D_{3/2} & (g_\beta = 4) \end{cases} \tag{2.26}$$

Referring to Fig. 9.1a, one finds that the intensity ratio between Pd $3d_{3/2}$/Pd $3d_{5/2}$ is 2:3, which is exactly the same value as theoretically expected using Eq. 2.25. Usually, the intensity ratio of different microstates is fixed, unless the valence band strongly interacts with core orbitals [71,82]. It is also noted that the energy difference between the two spin states might also be changed if the observed orbitals strongly interact with surrounding ligands (e.g., $\Delta 2p$ of Ti^0 = 6.17 eV, $\Delta 2p$ of Ti^{4+} = 5.54 eV) [72].

Core Hole Screening

Core hole screening refers to the attraction of electrons to the holes via the Coulomb interaction due to the potential field created by the positive charges [63, 83]. This phenomenon results in significant upward binding energy shifts, and is especially non-negligible for some systems such as thin films and supported metal particles [71].

With an aim of investigating supported model systems, the utilization of thin insulator films grown on metal substrates was originally invented as a circumventive approach to avoid the charging [17, 71], for which the present study used only these oxide films. The thin oxide films might be able to either increase or reduce the screening efficiency by varying the oxide film' thickness via tuning its conductance [84] or the charge transfer between the metal substrates and supported metals or oxide films [76].

Satellites

Strong asymmetry is recognized for 3d and 4f photoelectron spectra of metals (e.g., Au, Pd, Mo), accompanying tails in lower kinetic energy [72]. The formation of these tails is explained by the excitation of electrons around the Fermi level to the vacant orbitals just above the Fermi edge by the ejected electrons, for which small electron energy loss ($\sim$ hundreds meV) is observed for the photoelectrons. This phenomenon is called the *shake up*. This excitation process also indicates that the metals accompanied by a sharp Fermi edge might exhibit this asymmetrical feature in their photoelectron spectra.

In addition to the small electron energy loss processes discussed above, electron loss process which gives rise to peaks separated from the main photoemission line by several eV or even tens of eV might occur for s part of metals, semiconductors and insulators. Two of these processes are explained in the following: First, electrons ejected from metals are capable of inducing an oscillatory excitation of bulk electrons, called *plasma oscillation* or *plasmon* [63]. In the classical Drude model of metals, plasmons are depicted as an electron gas, which vibrate under the influence of external field against the positively charged ions. Plasmons can oscillatorily

propagate, provided:

$$1 + 4\pi i\sigma(\omega)/\omega = 0, \tag{2.27}$$

$$\epsilon(\omega) = 1 - \omega_p^2/\omega^2, \tag{2.28}$$

where $\sigma(\omega)$ is the frequency-dependent (AC) conductivity, ω is the frequency of electric field, ϵ is the dielectric constant, and ω_p is known as the plasma frequency, which is given by:

$$\omega_p^2 = \frac{4\pi ne^2}{m}, \tag{2.29}$$

where n and m indicate the number of free electrons and the mass of the electron. For positive ϵ, i.e., $\omega > \omega_p$, the stable propagation of the electron gas occurs. Its excitation energy, ΔE_p, is given by:

$$\Delta E_p = h\nu_p = h\frac{\omega_p}{2\pi} = h \times 11.4 \times \left(\frac{r_s}{a_0}\right)^{-\frac{3}{2}} \times 10^{15}, \tag{2.30}$$

where r_s is the radius of free electrons and a_0 is the Bohr radius. Noting that r_s/a_0 is in the range of 2 to 6, the bulk plasmon is in the energy range of several eV (for $r_s/a_0 = 4$, $E_p \sim 6$ eV). Metal surfaces exhibit another plasmon, called the *surface plasmon*, for which there is the solution at a frequency $\omega_s = \omega_p/\sqrt{2}$ [63]. The plasmons are directly observed as electron energy loss in multiplies of $\hbar\omega_p$ or $\hbar\omega_s$ for some metals (see, for example, Pd surfaces in Chapter 9). Further details about surface and bulk plasmons in the photoemission spectroscopy are found elsewhere [64].

In sharp contrast to metals, non-metallic compounds are featured with no vivid plasmon loss due to the absence of free electrons. However, there is another electron energy loss process for photoelectrons among semiconductors, insulators as well as metals, named the *interband transition* [85]. For non-metals, electron energy loss by the interband transition corresponds to the band gaps of materials (e.g., several or tens eV) [86]. Metals also experience electron excitation between specific valence and conduction bands; photoelectrons ejected from Ni show satellites with an energy of 6 eV due to d-band excitation [87,88]. It is noted that quite similar electron energy loss features appear for both the plasmon and the interband transition, but their mechanistic details are hardly distinguished by the appearances of the satellite peaks. Nevertheless, mechanistic perspectives provide that the former should occur only for metals, whereas the latter process could be observed for any substances.

2.2.6 Line Shapes

In experiment, the line shapes of XP peaks are mostly a Gaussian-Lorentzian function [71], which reads:

$$SGL(x, F, E, m) = (1 - m)\exp(-4\ln 2\frac{(x - E)^2}{F^2}) + m(1 + 4\frac{(x - E)^2}{F^2}), \tag{2.31}$$

$$Y(x) = SGL(x) + (1 - SGL(x)) \times T(x), \tag{2.32}$$

where

$$T(x,k,F,E) = \begin{cases} \exp(-k\frac{x-E}{F}) & x \geq E \\ 0 & x < E \end{cases} \tag{2.33}$$

where x is the binding energy of photoelectron, E the binding energy at the maximum, F the full width at the half maximum, m ($0 \leq m \leq 1$) the weighting factor for Lorenzian contribution, and an additive parameter to introduce asymmetry is k. The $Y(x)$ function gives an asymmetrical profile, only if T is non-zero. Intrinsically, the line shape of photoemission spectra is Lorentzian, because Lorentzian function represents the spectral response of an exponential decay of excited core holes. Accompanying contributions to the photoemission process add the Gaussian feature to the Lorentzian, which is mainly caused by various contributions such as phonon vibration, roughness of the surface, analyzer's various parameters such as pass energy, etc.

2.2.7 Auger Parameter Analysis

It is widely accepted to correlate binding energy shifts to their chemical states or atomic charges. As mentioned earlier in Section 2.2.3, this *a priori* interpretation is not justified for systems with inefficient screening (see Eq. 2.22). The separation of the initial and final state contributions is, hence, a crucial issue in order to extract meaningful quantitative information of the orbital energy levels prior to the occurrence of photoemission. To determine the final state contribution, Wagner proposed a so-called Auger parameter analysis [89]. Herein, its brief explanation is provided.

We begin to describe the Auger process, according to Shirley [90]. The final state for a simple Auger decay, which leaves two core holes, yields

$$E_{i*j*} = E_0 - \varepsilon_i - \varepsilon_j - R_{ij} + F(ij,X), \tag{2.34}$$

where E_0 is the energy at the ground state, ε_i and ε_j denote the energy levels of the orbital i and j within the frozen orbital approximation, R_{ij} the relaxation energy in the presence of the two holes, and $F(ij,X)$ the interaction energy of two open shells in the orbitals i and j resulting in a state X. Now, let us consider the electron kinetic energy for kij Auger transition. The Auger electrons' kinetic energy for the kij Auger peak, $E_A(kij,X)$, is the difference between the two final states after the Auger decay, E_{i*j*}, and the photoemission leaving a core hole in the k orbital, $E_B(k) + E_0$:

$$\begin{aligned} (E_B(k) + E_0) - E_{i*j*} &= E_A(kij,X) \\ &= -\varepsilon_k + \varepsilon_i + \varepsilon_j - R_k + R_{ij} - F(ij,X). \end{aligned} \tag{2.35}$$

$E_A(kij,X)$ consists of three orbital energies referring to the initial state of the system, as a result of the separation of the two final state contribution (R_k and R_{ij}) and the hole-hole interaction, $F(ij,X)$.

Let us specifically consider the kii Auger decay [91, 92]. Using Eq. 2.21 and Eq. 2.35, the following relationship among the kii Auger kinetic energy and the orbital energies $E_B(i)$ and

$E_B(k)$ can be formulated:

$$\beta(i,X) = 2E_B(i) - E_B(k) + E_A(kii,X) = -2R_i + R_{ii} - F(ii,X),$$
$$\Delta\beta(i,X) = \Delta[2E_B(i) - E_B(k) + E_A(kii,X)] = -2\Delta R_i + \Delta R_{ii} - \Delta F(ii,X). \quad (2.36)$$

$\Delta\beta(i,X)$ is specifically called *modified Auger parameter* [91,92]. If the Auger transition occurs within the core orbitals (i.e., no valence band states are involved), $\Delta F(ii,X)$ can be neglected. Now, ΔR_{ii} is evaluated. The origin of the relaxation energy is the polarization, induced by the core holes. The polarization energy is proportional to the strength of the electric field, namely, the number of electric charges of interest. Note that R_{ii} is the relaxation energy resulting from the two core holes, while R_i describes the effect of a single vacancy [89]. Hence, the following relation is realized:

$$\Delta R_{ii} = 4\Delta R_i. \quad (2.37)$$

Finally, $\Delta\beta(i)$ is computed as follows:

$$\Delta\beta(i) = \Delta[2E_B(i) - E_B(k) + E_{kin}(kii,X)] = 2\Delta R_i. \quad (2.38)$$

The substitution of $\Delta\beta(i)$ for ΔR_i in Eq. 2.21, finally, leads to the following expression:

$$\Delta\varepsilon_i = -[\Delta E_B(i) + \Delta\beta(i)/2]. \quad (2.39)$$

Note that the pure initial state contribution is successfully obtained by removal of the final state contribution from the binding energy shift.

The modified Auger parameter, $\beta(i)$, can straightforwardly applied for data interpretation. Nevertheless, the modified Auger parameter has low versatility, because it frequently requires probing a very deep core, namely $E_B(k)$. Instead, the original Auger parameter, $\alpha(i)$, introduced by Wagner is more often employed [89,93]:

$$\Delta\alpha(i) = \Delta E_B(i) + \Delta E_{kin}(kii) = 2\Delta R_i. \quad (2.40)$$

The comparison of Eq. 2.38 with Eq. 2.40 easily finds that $\Delta\alpha(i)$ can safely substitute $\Delta\beta(i)$, provided that $\Delta E_B(i)$ is equivalent to $\Delta E_B(k)$. This condition is satisfied if the binding energy shifts of different orbitals for a certain chemical state and the screening efficiency of different core holes remain similar, which might limit the applicability of Eq. 2.40. Again, the substitution of $\Delta\alpha(i)$ for ΔR_i in Eq. 2.21 gives:

$$\Delta\varepsilon_i = -[\Delta E_B(i) + \Delta\alpha(i)/2]. \quad (2.41)$$

2.3 Infrared Reflection Absorption Spectroscopy (IRAS)

Infrared (IR) light is the electromagnetic radiation with λ of 750 nm – 1 mm, corresponding to $\tilde{\nu}$ from 30 to 14000 cm^{-1} [94]. The photon energies correspond to the excitation of vibration and rotation of molecules. This fact makes IR light a tool to determine chemical species and states by observing specific excitation of vibrational- and rotational-modes. The present study employs *total reflection* of infrared light to obtain vibrational spectra. This method is called the *infrared absorption reflection spectroscopy* (IRAS) [95].

2.3.1 Interaction of Infrared Light with Matter

The interaction of an electromagnetic wave with matter is first explained [96]. The Hamiltonian for a particle in the field yields:

$$\begin{aligned} H &= \frac{1}{2m}\left(\boldsymbol{p} - \frac{e}{c}\boldsymbol{A}\right)^2 && (2.42)\\ &= \frac{1}{2m}\left[-i\hbar\nabla - \frac{e}{c}\boldsymbol{A}\right]^2 && (2.43)\\ &= H_0 + V, && (2.44)\end{aligned}$$

where $\boldsymbol{p}$ is the momentum, $\boldsymbol{A}$ is the vector potential of the electromagnetic wave, H_0 and V are the Hamiltonians of non-interaction and interacting terms. Using the relationship $\nabla\cdot\boldsymbol{A} = \boldsymbol{A}\cdot\nabla$, V can be written as:

$$V = \frac{i\hbar e}{mc}(\boldsymbol{A}\cdot\nabla) + \frac{e^2}{2mc^2}\boldsymbol{A}\cdot\boldsymbol{A}. \quad (2.45)$$

The second term, $\boldsymbol{A}\cdot\boldsymbol{A}$, can be neglected within the *weak-field approximation*. The approximation is valid unless intense fields as found e.g., in ultra-short pulse laser are used. Finally, the interaction term is described as:

$$\begin{aligned} V &= -\frac{e}{mc}\boldsymbol{A}\cdot\boldsymbol{p} = -\frac{e}{mc}A_0\cos(\boldsymbol{k}\cdot\boldsymbol{r}-\omega t)\boldsymbol{\varepsilon}\cdot\boldsymbol{p}\\ &= -\frac{e}{2mc}A_0\big\{(\cos(\boldsymbol{k}\cdot\boldsymbol{r}-\omega t) + i\sin(\boldsymbol{k}\cdot\boldsymbol{r}-\omega t)) + (\cos(\boldsymbol{k}\cdot\boldsymbol{r}-\omega t) - i\sin(\boldsymbol{k}\cdot\boldsymbol{r}-\omega t))\big\}\boldsymbol{\varepsilon}\cdot\boldsymbol{p}\\ &= -\frac{e}{2mc}A_0(e^{i(\boldsymbol{k}\cdot\boldsymbol{r}-\omega t)} + e^{-i(\boldsymbol{k}\cdot\boldsymbol{r}-\omega t)})\boldsymbol{\varepsilon}\cdot\boldsymbol{p}\\ &= U(\boldsymbol{k})e^{-i\omega t} + U(-\boldsymbol{k})e^{i\omega t}, && (2.46)\end{aligned}$$

where the Euler's formula, $e^{\pm ix} = \cos(x) \pm i\sin(x)$, is used, and

$$U(\pm\boldsymbol{k}) = -\frac{e}{2mc}A_0 e^{\pm i(\boldsymbol{k}\cdot\boldsymbol{r})}\boldsymbol{\varepsilon}\cdot\boldsymbol{p}. \quad (2.47)$$

The presence of $U(\pm\boldsymbol{k})e^{\mp i\omega t}$ in the interaction potential V indicates that the interaction potential V is composed of two periodic components.

In order to know the transition of quantum state of V, let us consider the evolution of an oscillating Hamiltonian, $H(t) = H_c e^{\pm i\omega t}$. According to the Fermi's golden rule, the transition probability, T_{km}, of $H(t)$ from the initial state m to the final one k per unit of time is computed:

$$T_{km} = \frac{2\pi}{\hbar}\,|\langle k \mid H_c \mid m\rangle|^2\,\delta(E_k - E_m \mp \hbar\omega). \quad (2.48)$$

The $H_0 e^{i\omega t}$ term causes $E_k = E_m - \hbar\omega$, thus, leading to stimulated emission, whereas the $H_0 e^{-i\omega t}$ term causes $E_k = E_m + \hbar\omega$, leading to stimulated absorption. Applying the Fermi's golden rule to Eq. 2.46, the rate of absorption and emission are provided by:

$$\begin{aligned} w_{abs}(m\to k) &= \frac{2\pi}{\hbar}\,|\,U_{km}(\boldsymbol{k})\,|^2\,\delta(E_k - E_m - \hbar\omega), && (2.49)\\ w_{em}(m\to k) &= \frac{2\pi}{\hbar}\,|\,U_{km}(-\boldsymbol{k})\,|^2\,\delta(E_k - E_m + \hbar\omega), && (2.50)\end{aligned}$$

where

$$U_{km}(\pm\boldsymbol{k}) = -\frac{eA_0}{2mc}\langle k \mid e^{\pm i\boldsymbol{k}\cdot\boldsymbol{r}}\boldsymbol{\varepsilon}\cdot\boldsymbol{p} \mid m\rangle. \quad (2.51)$$

A further simplification of Eq. 2.51 can be obtained by assuming that the wavelength of light is long enough compared to the bond lengths of molecules. This approximation, called the *dipole approximation*, yields $e^{\pm i\boldsymbol{k}\cdot\boldsymbol{r}} \sim 1$, because $\boldsymbol{k}\cdot\boldsymbol{r} = 2\pi r/\lambda \to 0$. Hence, the U_{km} term is given by

$$U_{km} = -\frac{eA_0}{2mc}\langle k \mid \boldsymbol{\varepsilon}\cdot\boldsymbol{p} \mid m\rangle. \tag{2.52}$$

Applying the following relationship to Eq. 2.51,

$$\boldsymbol{p} = \frac{im}{\hbar}[H_0, \boldsymbol{r}], \tag{2.53}$$

the following expression for U_{km} is provided:

$$U_{km} = -\frac{eA_0}{2mc}\frac{im}{\hbar}\boldsymbol{\varepsilon}\cdot\langle k \mid [H_0, \boldsymbol{r}] \mid m\rangle = -\frac{ieA_0}{2c\hbar}(E_k - E_m)\langle k \mid \boldsymbol{\varepsilon}\cdot\boldsymbol{r} \mid m\rangle. \tag{2.54}$$

$E_k - E_m = \hbar\omega_{km} = \pm\hbar\omega$ is non-zero in the case of the resonant transition. Finally, the absorption rate, U_{km}, is given by the definition of the transition dipole moment $\boldsymbol{\mu}_{km} = e\langle k \mid \boldsymbol{r} \mid m\rangle$:

$$U_{km} = \frac{\mp iA_0\omega}{2c}\boldsymbol{\varepsilon}\cdot\boldsymbol{\mu}_{km}. \tag{2.55}$$

This expression is specifically called the *electric dipole approximation* for U_{km}. Note that the absorption rate is directly proportional to the square of the transition dipole moment.

Lastly, we describe how the absorption of infrared light appears within this approximation. According to Eq. 2.55, the absorption of light occurs if $\boldsymbol{\mu}_{km}$ is nonzero. When the potential energy of molecules is described by a harmonic potential, which a reasonable approximation close to the near the equilibrium geometry, non-zero $\boldsymbol{\mu}_{km}$ is found for $k - m = \pm 1$ [81]. It is important to look again into the definition of the transition dipole moment $\boldsymbol{\mu}_{km} = e\langle k \mid \boldsymbol{r} \mid m\rangle$. In case of a permanent dipole moment which does not depend on the distance r, it is readily seen that the transition dipole moment is 0, because of the orthogonality of the wavefunctinos k and m. However, a change of the distance r between the atoms may be associated with a change of the permanent dipole moment, which may be described by a series expansion around the equilibrium geometry:

$$\boldsymbol{\mu} \approx \boldsymbol{\mu}_0 + \boldsymbol{r}\left.\frac{\partial\boldsymbol{\mu}}{\partial\boldsymbol{r}}\right|_0, \tag{2.56}$$

where the term $d\boldsymbol{\mu}/d\boldsymbol{r}$ is called dynamic dipole moment. Note that the operator has been switched from $\boldsymbol{\mu}$ to $\boldsymbol{r}$. Its substitution into Eq. 2.54 yields:

$$U_{km} = \frac{\mp iA_0\omega}{2c}\boldsymbol{\varepsilon}\cdot\langle k \mid \boldsymbol{r}\left|\frac{\partial\boldsymbol{\mu}}{\partial\boldsymbol{r}}\right|_0 \mid m\rangle. \tag{2.57}$$

Using Eq. 2.57, the transition probability of the molecular vibration by light, $|U_{km}|^2$, can be obtained, which is proportional to the square of the dynamic dipole moment. The overtone absorption ($\Delta n \geq 2$) needs the presence of the anharmonic potentials.

2.3.2 Infrared Reflection Absorption Spectroscopy (IRAS)

As described above, infrared light is *absorbed* by matter for vibrational and rotational excitation. In particular, metals are not transparent to infrared light, which renders transmission experiment impossible. Hence, to acquire the absorption spectra of adsorbates on single crystalline surfaces, infrared light is introduced to a surface at a high angle of incidence and the reflected light which is partially absorbed by surface species is collected by a detector. This method, called the *infrared reflection absorption spectroscopy* (IRAS), is performed [95], according to the scheme shown in Fig. 2.5. Note that a non-polarized infrared light contains both p-polarized (perpendicular to the surface) and s-polarized (parallel to the surface) components. The absorption of infrared light by adsorbates occurs in the presence of transition dipole moment parallel to the electromagnetic field of the infrared light. On the surfaces, the absorption of s-polarized infrared light by adsorbate does not occur, because electric field component parallel to the surface is canceled by the image dipole induced in the metal surface, as shown in Fig. 2.5. On the other hand, the absorption of p-polarized light is enhanced almost by a factor of two, because both the dipole moment of adsorbate and the corresponding image dipole in the surface contribute to the absorption of the incoming p-polarized light. The term, *metal surface selection rule*, was coined for the selectivity of infrared absorption on metal surfaces to the perpendicular component of the dynamic dipole moment of vibrations [95]. The opposite interfacial absorption properties of the s and p components indicate, if an absorption spectrum of p-polarized is subtracted from the corresponding s-polarized one, the resulting spectrum contains only the absorption of adsorbates, while isotropic adsorption e.g., by molecules in the gas phase are subtracted out. This technique is called *polarization modulation IRAS* (PM-IRAS), frequently used in environmental surface science studies [32, 95].

The fact that the surface dipole of adsorbates is quite influenced by substrates, while the molecules in gas phase freely rotate and vibrate, indicates that the vibrational spectra acquired by IRAS might be quite different as compared to the corresponding gas-phase spectra [95]. Ideally, isolated adsorbates should exhibit only the interaction with the surfaces. The pure adsorbate-surface interactions are categorized in the following types.

Polarization effect indicates the changes of the vibrational frequency of adsorbates induced by the dipole-dipole interaction between them and the surface [95]. The vibrational frequency of adsorbates is blue shifted (red shifted) as the two dipoles are finally aligned in a parallel (an anti-parallel) manner. The dynamic dipole of molecules adsorbed on metal surfaces induces the formation of the corresponding image dipole in the metals, resulting in lowering the vibrational frequency.

Wall effect refers that the vibrational frequency of adsorbates can be blue-shifted due to a strong repulsive force between them and a rigid surface (e.g., CO adsorbed on the MgO(001) surface) [97]. In the case of the Mg^{2+}-CO system, there is a strong electrostatic interaction between CO and Mg^{2+}. This brings CO closer to the surface, because of little deformation of the MgO surface. This short distance between CO and the MgO surface

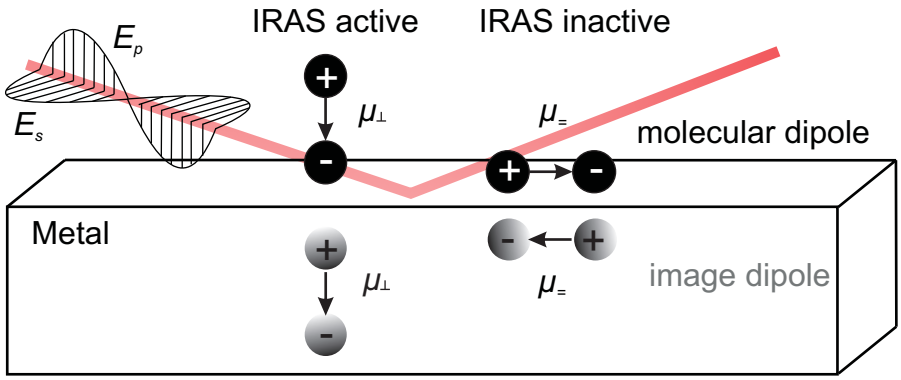

Figure 2.5: Metal surface selection rule; a schematic representation as a molecule adsorbed on a metal surface is observed via infrared reflection absorption spectroscopy. The molecule with a dipole $\mu_\perp$ perpendicular to the surface is observable. The molecule lying on the surface with a dipole parallel to the surface, $\mu_=$, is unobservable, due to the formation of the oppositely directed image dipole.

results in the enhanced repulsion due to the overlapping of the electron cloud of C and surface O^{2-} ions. This repulsive force restricts the CO vibration in the direction of C, so that the potential well of CO becomes steeper, which increases the vibrational frequency of CO.

Interatomic charge transfer corresponds to the charge transfer between an adsorbate and surfaces. A well-known example is CO adsorption on transition metals, which was successfully explained by Blyholder [98]. In the Blyholder model, CO adsorption on metal surfaces proceeds upon an electron donation from the d-orbital of surfaces to the $2\pi^*$ orbital of CO molecules, accompanied by an opposite electron transfer from the 5σ orbital of CO to the surface. Populating the anti-bonding orbitals of CO decreases the C-O bond strength, which results in the red shift of the stretching frequency. For example, there is a solid relation between the vibrational frequency of CO molecules and their adsorption sites: (atop) 2100–2000 cm^{-1}, (bridge) 2000–1900 cm^{-1}, (3-fold) 1900–1800 cm^{-1} [95].

Chemical state of the substrate can also induce the frequency shifts of adsorbate. For instance, the vibrational frequency of CO adsorbed on Au has a clear dependence on the charge state of Au clusters [99,100], where the electron extraction from/to an adsorbate corresponds to the removal/donation of electrons from/to the HOMO/LUMO of the adsorbate, resulting in blue-/red-shift, respectively.

All interaction except for the Wall effect usually decreases the bond strength of adsorbates for adsorbate/metal systems, as evidenced by the occurrence of red-shift [95]. This tendency is not surprising, because the dangling bonds at metal surfaces (see Ref. [101]) could be inserted into the LUMO of adsorbate upon adsorption. Hence, the dissociation and chemical reaction of adsorbate are enhanced on the metal surfaces.

Different to the isolated adsorbate, as the coverage of adsorbate increases, the following adsorbate-adsorbate interaction start to be noticeable [95].

Static dipole-dipole interaction, the so-called *intermolecular repulsion*, refers to the strong static dipole coupling between adjacent species. This phenomenon is evident if the coverage of adsorbate becomes high and the intermolecular distance decreases. The coupling occurs when they are parallel or anti-parallel. In the former case, the repulsive interaction makes the bond weaker, as evidenced by red shifts.

Coverage dependent chemical shift means that the effect of Blyholder mechanism is affected by the coverage of adsorbate. At a high coverage of adsorbates such as CO, less electrons are inserted into the LUMO of the adsorbates, because the number of electrons in the *d*-orbitals is limited. Hence, this leads to a smaller red-shift.

2.3.3 Fourier-Transform Infrared Spectroscopy

There are two widely-available types for infrared measurement: dispersive and Fourier-Transform (FT) modes [95]. The dispersive IR utilizes monochromatized white light to record absorption spectra as a function of wavelength, resulting in a serial measurement of the spectrum. The other method is called the FT infrared spectroscopy [95]. Suppose that a non-monochromatic beam is divided into two beams by a beam splitter, where one of them is reflected by a fixed mirror with an optical path $l_1/2$ and the other one is reflected by a movable mirror. The variable position of the second mirror produces a path difference of $l_1 - l_2$ between the two refracted beams recombined by the beam splitter (see Fig. 2.6a). Their superposition either constructively or destructively interferes with each other as a function of path difference (Fig. 2.6b), in accordance with the Young's law. Light usually contains various wavelength, and their total interference and subsequent absorption of light by molecules yields the observed beam intensity. Thus, the decomposition of each signal to obtain an absorption spectrum is possible by calculating the contribution of each wavelength. This is achieved by Fourier transformation, as detailed below [102].

There is the following relation between an interferogram, $I(x)$, and the corresponding absorption spectrum (called the power spectrum), $G(k)$:

$$
\begin{aligned}
I(x) &= \int_0^\infty (1 + \cos kx) G(k) dk && (2.58)\\
&= \int_0^\infty G(k) dk + \int_0^\infty G(k) \frac{e^{ikx} + e^{-ikx}}{2} dk && (2.59)\\
&= \frac{1}{2}\{I(0) + \int_0^\infty G(k) e^{ikx} dk + \int_0^{-\infty} G(k) e^{ikx} (-dk)\}. && (2.60)
\end{aligned}
$$

where k is the wavenumber, holding the following relation with the frequency ω: $\omega = ck$. It follows:

$$
W(x) = \frac{1}{\sqrt{2\pi}}(2I(x) - I(0)) = \int_{-\infty}^{\infty} e^{ikx} G(k) dk \frac{1}{\sqrt{2\pi}}. \qquad (2.61)
$$

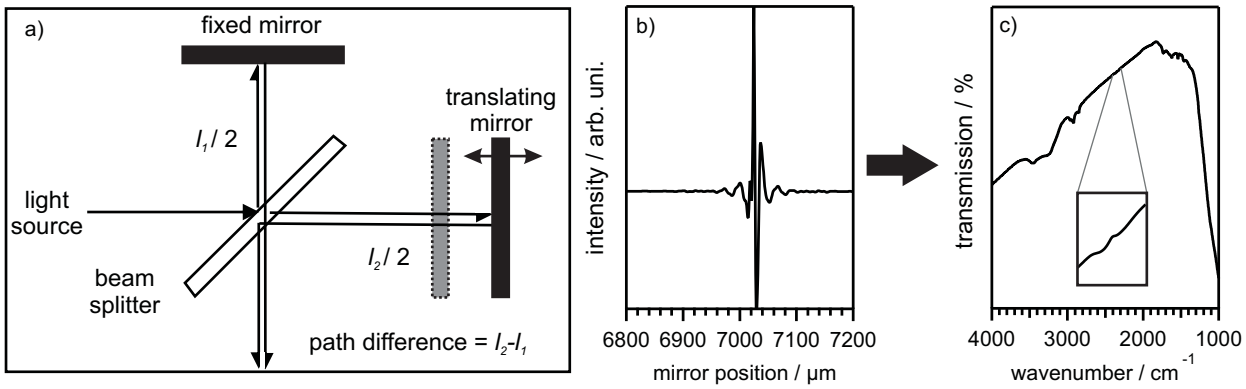

Figure 2.6: a) A schematic of the Michelson's interferometer. b) An interferogram (x-axis is the mirror position, and y-axis is the total light intensity.) of 5 mbar CO. c) The corresponding power function (spectrum) via transmission FT-IR, where the absorption peaks of IR by gas-phase CO molecules are zoomed in.

Its Fourier transformation pair is written as follows

$$G(k) = \frac{1}{\sqrt{2\pi}} \int_{-\infty}^{\infty} W(x) e^{-ikx} dx. \tag{2.62}$$

Eq. 2.62 is the Fourier transformation of $W(x)$, and note the fact that the absorption spectrum can be calculated only by using $I(x)$ and $I(0)$. In other words, an interferogram is sufficient to determine the corresponding power function (spectrum). Fig. 2.6b and Fig. 2.6c are an interferogram and the corresponding spectrum for gas-phase CO at a pressure of 5 mbar. Since FT-IR utilizes the white light instead of monochromatic light to obtain a spectrum, this method not only reduces the acquisition time, but also improves the spectral quality, compared to the dispersive IR.

2.4 Temperature Programmed Desorption (TPD)

A way to characterize adsorbates is to measure their masses after desorption. *Temperature programmed desorption* (TPD) is a method to measure desorbing species from a surface, which is heated in a controlled manner. In addition to the characterization and quantification of adsorbates, theoretical consideration can provide insight into the desorption mechanisms and interactions of adsorbates with the surfaces and adjacent species.

2.4.1 Adsorption

Adsorption is a phenomenon in which atoms or molecules are bound to a surface. Adsorption accompanied by the formation of chemical bond between adsorbates and a surface is called *chemisorption*, while much weaker adsorption achieved by the van der Waals interaction is termed *physisorption* (see pp. 1375–1415 of Ref. [1]). The threshold between chemisorption and physisorption is artificially determined as an adsorption energy (∼40 kJ/mol) [1].

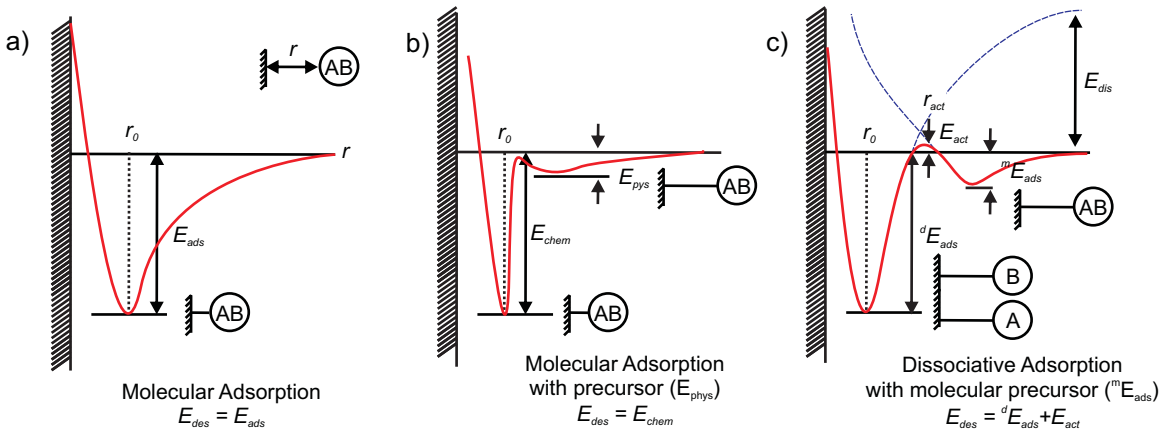

Figure 2.7: Schematic energy diagram for adsorption: a) associative chemisorption; b) associative chemisorption with precursor; c) dissociative chemisorption with an activation barrier and precursor, taken from p. 1382 [1].

Investigation of molecular adsorption was experimentally and theoretically pioneered by Langmuir [103] and Lennard-Jones [104], respectively. Langmuir claimed that adsorbed species, *adsorbates*, could feel a strong attractive force to a surface with patchwork-like structure, and that adsorption (desorption) occurs upon cooling (annealing). Lennard-Jones proposed a model to describe the adsorption of noble gas atoms on a surface, as schematically shown in Fig. 2.7a [1]. His model depicts the interaction of an adsorbate with a substrate as a function of their separation. The potential energy of this model system consists of two components: short range repulsive force, ascribed to the overlap of the occupied orbitals, and long range attractive force, due to the van der Waals interaction:

$$E_i(r) = -Ar^{-6} + Br^{-12}. \tag{2.63}$$

This quasi-1D potential energy diagram has a minimum, at which distance a noble gas atom is stabilized (adsorbed) by the van der Waals interaction. Though the original model was developed for the adsorption of noble gas atoms, this idea can be extended to describe non-dissociative or even dissociative molecular adsorption (the panels (b) and (c) of Fig. 2.7). Fig. 2.7b depicts non-dissociative molecular adsorption with two minimums. As a molecule approaches a surface, there is a first minimum at a longer distance with a smaller adsorption energy of ${}^1E_{ads}$, corresponding to molecular physisorption. At a closer distance, the molecule finds a barrier. After overcoming this barrier, the molecule can find the second minimum with a shorter distance from the surface and with a larger adsorption energy of ${}^2E_{ads}$, because a strong chemical bond between the adsorbate and the surface is formed. The energetic scheme of dissociative molecular adsorption is more complicated (Fig. 2.7c). With a longer bond length, metastable non-dissociative adsorption of the molecule on a substrate occurs with an adsorption energy of ${}^mE_{ads}$. As the molecule approaches the surface, the molecule encounters an activation barrier for the dissociation of the molecule. Thermodynamically, this dissociation is explained such that the formation of

two chemical bonds between the substrate and the separated species is energetically favored compared to the formation of a single chemical bond between the molecule and the surface. It must be kept in mind that the desorption energy, E_{des}, could be inequivalent to E_{ads}, if an additional activation energy, E_{act}, is necessary to cause the desorption. For instance, as shown in Fig. 2.7c, the dashed line corresponds to the imaginary energetic diagram of two isolated atoms. Comparison of the dashed and solid lines suggests that the desorption energy for this dissociative molecular adsorption is equivalent to the sum of the adsorption energy and the activation energy of desorption; $E_{des} = E_{ads} + E_{act}$ (see Fig. 2.7c).

2.4.2 Desorption and Analysis of TPD Spectra

Desorption can be approximated as the inverse of adsorption. The theoretical justification for the use of this idea is provided by microscopic reversibility, which indicates that each trajectory is exactly the same upon reversing individual trajectories in time and space [13]. In other words, this microscopic reversibility makes the assumption that the desorption process is completely equivalent to the backward process of adsorption possible, irrespective of the direction of the process. As detailed below, this enables a correlation between desorption spectra and adsorption as well as recombination. One might question whether or not the reversibility is always valid. These exceptional cases are mentioned at the end of this section.

With the principle of the microscopic reversibility, when the products and transition states are assumed to be in a thermally equilibrium, the well-known *transition state theory* can be applied to the desorption of materials from surfaces, developed mainly by Eyring, Wigner and Polanyi [105]. The Polanyi-Wigner model assumes that the desorption rate of a species in a state i from a surface is expressed as

$$r_d = -dN_i/dt = \nu_i N_i^{x_i} \exp(-E_i/RT), \tag{2.64}$$

where r_d is the desorption rate, x_i is called the reaction order, ν_i is the frequency factor, E_i is the desorption energy, and N_i is the population in state i [105]. At a fixed ramp rate, $\beta = dT/dt$, Eq. 2.64 yields

$$-dN_i/dT = \nu_i N_i^{x_i} \exp(-E_i/RT)/\beta. \tag{2.65}$$

As the desorption maximum is found at T_m, one has

$$0 = d^2N_i/dT^2 = x_i\nu_i N_i^{x_i-1}\frac{dN}{dT} + N_i^{x_i}\frac{E_i}{RT_m^2}. \tag{2.66}$$

For the first order desorption phenomenon, the combination of Eq. 2.64 and Eq. 2.66 yields

$$\ln\frac{T_m^2}{\beta} = \frac{E_i}{RT_m} + \ln E_i\nu_i R. \tag{2.67}$$

Analysis and more detailed information about desorption events with other orders are found elsewhere [105]. ν_i, the pre-exponential factor, is indicative of the probability of how often the desorption is attempted to occurs per unit time. The usage of $\nu_i = 10^{13}$/sec is frequently justified,

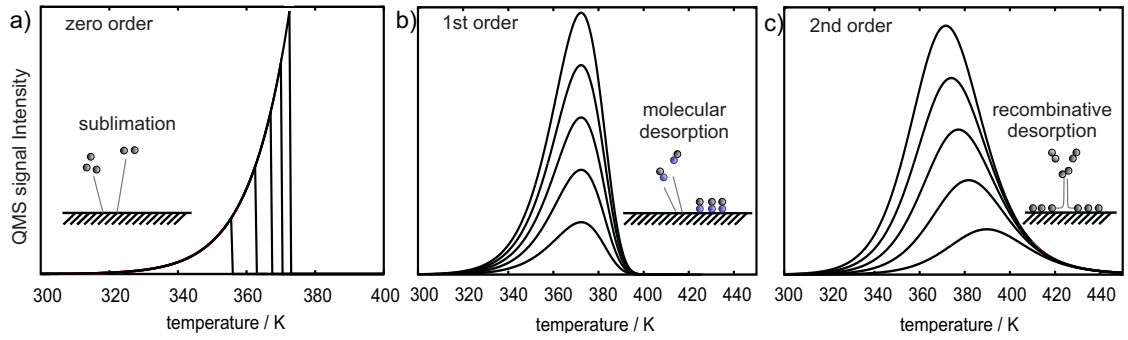

Figure 2.8: Numerically calculated TPD spectra, according to Eq. 2.65, for $n = 0$, 1, 2, and N_i = 0.2, 0.4, 0.6, 0.8, 1.0, E_i = 100 [kJ/mol], $\nu = 1.0\times10^{13}$/s, and β = 10 [K/s].

because this value, called the general frequency factor, corresponds to vibrational frequency of the bonds formed between adsorbates and surfaces [105].

Analyzing desorption spectra on the basis of desorption kinetics makes it possible to discard certain mechanisms and provide insight into the possible microscopic desorption processes by x_i . According to Eq. 2.64, simulated TPD spectra are provided for different $x_i = 0, 1, 2$ in Fig. 2.8. For very simple systems, each spectral feature can be explained in the following manner.

- zero-order: The intensity of a desorbing species is independent of the coverage (e.g., sublimation of surface atoms)
- first-order: The intensity of a desorbing species depends simply on its coverage (e.g., CO/Pt $\rightarrow$ CO↑)
- second-order: The intensity of a desorbing species is equivalent to meet two adsorbates on the surface (recombination, e.g., 2O $\rightarrow$ O_2 ↑)

Eq. 2.67 is a quite simple equation, although it is not simple enough to determine the activation energy for desorption without the aid of numerical calculations. The simplest analysis proposed by Redhead found the following correlation between the desorption temperature with the maximum desorption intensity and the activation energy for desorption for the first order desorption [106].

$$E_i = RT_i[\ln(\nu_i T_i/\beta) - 3.46] \quad [\text{kJ/mol}] \tag{2.68}$$

Using the general frequency factor, $\nu = 10^{13}$, one directly obtains the activation energy E_i. The Redhead analysis can be further simplified, which was proposed by Masel [107].

$$E_i = 0.25 \times T_m \quad [\text{kJ/mol}], \tag{2.69}$$

with the assumption that the surface is fully covered with the desorbing species. This formula can provide the activation energy of desorbing species in the accuracy of $\pm$20 %.

Lastly, let us provide a concrete example where the microscopic reversibility is broken. For the recombinative oxygen desorption from Ag surfaces [108], the oxygen desorption occurs readily at the edges of oxygen islands. The site specific desorption leads to the violation of the

assumption for the 2nd order desorption, in which no site specific desorption is considered. Hence, an analysis on the basis of the simple 2nd order desorption yields notable deviation. Problems arising from dynamic events could, for example, theoretically be overcome by kinetic Monte Carlo simulation [109]. It is noted that another possible scenario is that the chemical reaction does not occur reversibly, when, for example, a permanent structural deformation of surfaces occurs upon adsorption.

Chapter 3

Machinery and Experimental

This chapter is devoted to introducing the UHV chamber system where all experiments reported in this thesis were carried out. To prepare and characterize samples under both UHV and ambient conditions, this machine consists of two parts: a preparation chamber designed for working only under UHV conditions, and a custom-built high-pressure cell operating at UHV as well as elevated pressures. Facilities for LEED, XPS and TPD are installed on the preparation chamber. Infrared measurements are carried out in the high pressure cell.

3.1 Overview of the Apparatus

3.1.1 Preparation Chamber

The whole apparatus is schematically depicted in Fig. 3.1. A disc-shaped, single-crystal sample is attached to two Mo rods via sport-welded Ta wires and held by a manipulator (`UI4204L`, VG-Scienta), which allows the sample to be rotated and moved vertically and horizontally inside the UHV chamber. The preparation chamber is used for: (i) cleaning metal single-crystal samples; (ii) preparing metal-oxide films; (iii) characterizing these surfaces; and (iv) doing reactivity studies under UHV conditions. Sample cleaning is achieved by noble gas sputtering using a standard sputtering gun (`IQE 11`, Specs) attached to a flange, which is ∼25 degrees off-angle to the horizontal line. The samples are usually sputtered at a beam voltage of 1.5 kV in 1×10^{-5} mbar Ar^+ with a typical sputter current of 4 μA. Subsequent annealing of the samples to create large flat terraces is achieved either by resistive heating via the Ta wires, controlled by a PID controller (`HA 901`, RKC), or by electron bombardment. Electrons for the latter method are emitted from a hot W-filament and accelerated across a potential difference of 0–2000 V. This method is specially applied for samples that require $T > 1300$ K for annealing. The W-filament is located opposite to the sputter gun. Furthermore, its application requires surrounding the sample with a floating stainless steel shield, in order to avoid contamination of other facilities by evaporated species upon high-temperature flashing. It is noted that annealing a sample to temperatures higher than 900 K requires cooling the manipulator with liquid nitrogen in order to protect the ceramic feedthroughs. Physical vapor deposition of materials is performed

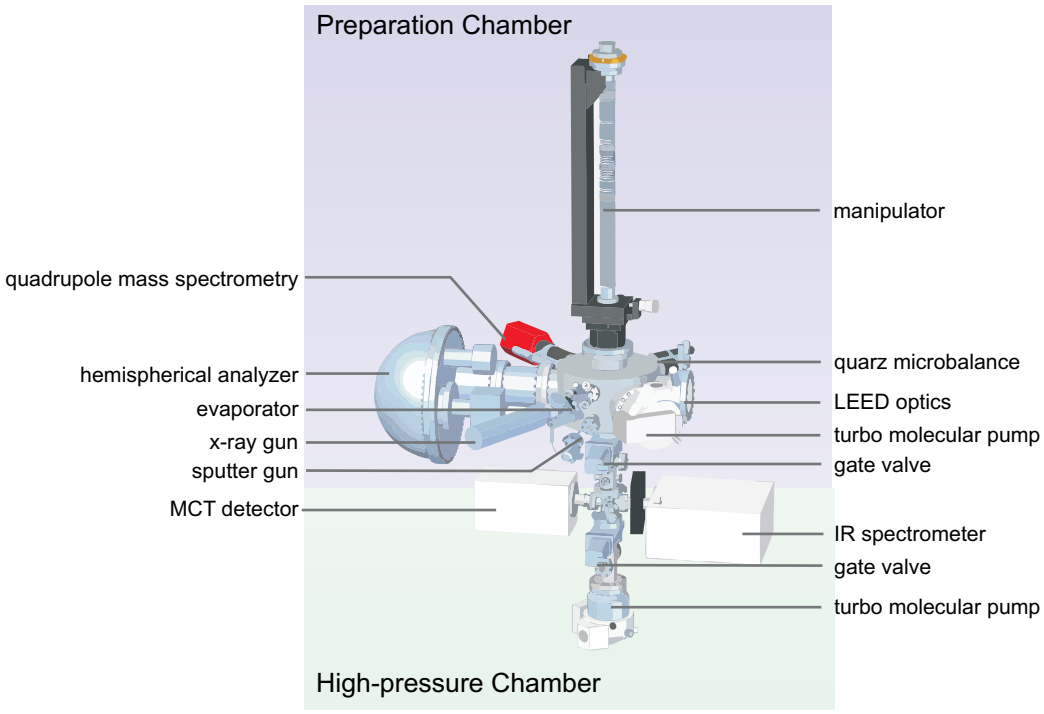

Figure 3.1: A drawing of the whole chamber. The upper part is named the "preparation chamber", and the other part "high-pressure cell". Positions for the facilities are pointed.

with an e-beam evaporator (`EFM-3T`, Omicron), which is mounted off-angle to the horizon by 25 degrees. Deposition rates are quantified with the help of a quartz microbalance (`SQM-160`, Sigma). XPS measurements are carried out using a dual anode x-ray gun (`XRC 1000`, Specs) and a hemispherical electron energy analyzer (`Phoibos 150`, Specs). Typically, the photoemitted electrons are detected at an exit angle of 60 degrees with respect to the surface normal. A standard four-grid LEED optics (`ErLEED 1000-A`, Specs) is located opposite to the analyzer. A thoria coated filament is employed as anode. A QMS (`Smart-IQ+`, Thermo), with a cone, is also horizontally attached.

X-ray Gun and Concentric Hemispherical Analyzer

XPS measurements demand two facilities: an x-ray source and an electron analyzer. Amongst several principles for x-ray emission (e.g., characteristic X-ray, synchrotron radiation, high harmonic generation [110]), the characteristic x-rays of Al Kα ($h\nu$ = 1486.6 eV) and Mg Kα ($h\nu$ = 1253.6 eV) are utilized in the present set-up by a dual-anode x-ray gun (`XRC 1000`, Specs). Characteristic x-rays are produced by an electron beam impinging on an anode from a cathode with high energy ($\sim$ 5–20 kV). The created core holes in the target anode are screened by the electron transition, by which fluorescent x-rays with specific energies such as Al Kα and Mg Kα are emitted. The x-ray light utilized in the present machine is non-monochromatized, for the sake of preserving the Bremsstrahlung background, by which the charging of insulating films is alleviated. Another reason lies in the fact that the excitation of core orbitals with

binding energies higher than the photon energy of Al Kα (e.g., Pd 2p) is accessible only to the Bremsstrahlung excitation in our setting, by which Auger parameter analysis is made possible.

A concentric hemispherical analyzer (CHA) is used for energy-resolved measurements of ejected electrons from a sample (`Phoibos 150`, Specs). The analyzer consists of one concave and one convex shaped hemisphere. The two hemispheres are positioned such that their centers of curvature are coincident. Different voltages can be applied to each hemisphere to produce an electric field. Electrons with a specific kinetic energy have a stable trajectory within the analyzer and thus pass through to the detector, while electrons with higher or lower kinetic energies will hit the outer and inner curved walls. At the end of the detector, the electrons hit channeltrons, by which the number of electrons is counted and converted into a signal. There are several important parameters characterizing the analyzer. The potential difference between the hemispheres, ΔV_{io}, determines energy range of electrons passing through the analyzer. This energy is called the pass energy, E_{pass}, reading

$$E_{pass} = (-q)k\Delta V_{io} \tag{3.1}$$

where q is the charge of an electron and k is a calibration constant. The higher the value of E_{pass} is, the more electrons are detected and the worse the energy resolution becomes. In the present study, E_{pass} was typically set to 10–20 eV, which results in a FWHM of $\sim$1 eV for the Ag 3d line.

Quadrupole Mass Spectrometer (QMS)

A quadrupole mass spectrometer (QMS) is employed to detect desorbing species during TPD experiments. QMSs are small, robust, capable of working from rough to ultra-high vacuum, and allow the simultaneous observation of different species [111]. The QMS consists of four electrode rods positioned in a radial array (left, Fig. 3.2). Species (atoms, molecules) entering the spectrometer are positively ionized by a hot filament located in front of the aperture. The electrons ejected from the filament need to have an energy above the first ionization potential of the species. The trajectory of a charged species inside the quadrupole is determined by the two electric fields in the dimension of x and y

$$E_x = U - V\cos(\omega t)\tfrac{x}{r^2} \tag{3.2}$$

$$E_y = -[U - V\cos(\omega t)\tfrac{y}{r^2}], \tag{3.3}$$

where U is the DC part, and $V\cos(\omega t)$ is the AC part. These electric fields work in the following mechanisms. Given V is zero, a positively charged ion is stabilized by the strong repulsion in the x axis, but it will hit the rods in the y axis. As V increases, the number of ions stabilized in the x axis decreases, because of the reduced repulsion between the positive electric field and the positively charged species. In contrast, the positive ions become more stabilized in y axis. This operational principle means that E_x works as a *low pass filter*, whereas the E_y has a function of a *high pass filter*. For a certain U/V value, the transmission probability of ionized species

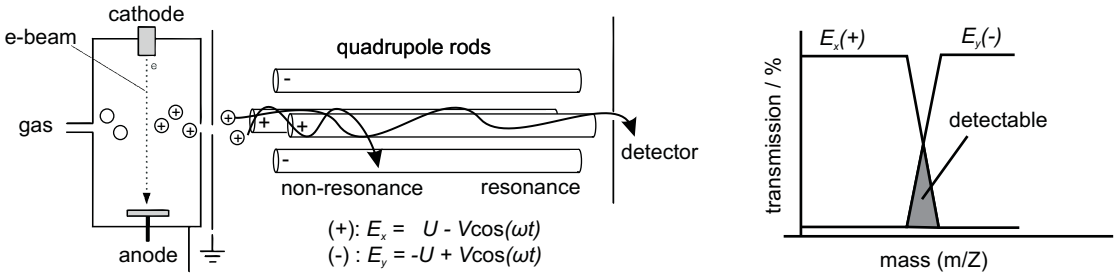

Figure 3.2: (Left): Schematics of QMS, where species are positively ionized by electrons and ions with specific masses and charges successfully travel to the detector through the electric fields between the two pairs of rods. (Right): Transmission probability of ions as a function of mass. The quadrupole works as a bandpass mass filter; the high pass mass filter in the x axis, and the low pass mass filter in the y axis.

with a specific mass is depicted in the right panel of Fig. 3.2. Indeed, when an ionized species satisfies the following relation, it can selectively arrive at the end of the electrodes to give the corresponding current at the detector:

$$\frac{m}{Z} = K\frac{V}{r^2\omega^2} \tag{3.4}$$

where K is a parameter. This function, called the Mathieu's equation, indicates that observing a wide range of ion masses is achieved by increasing V with a fixed parameter of U/V.

Our preparation chamber is equipped with a QMS (`Smart-IQ`$^+$, Thermo) with a home-made conic shield at the entrance of the spectrometer to avoid detection of species desorbed from the sample holder.

3.1.2 High-Pressure Cell

The UHV and high-pressure compatible cell attached underneath the preparation chamber is schematically depicted in Fig. 3.3. The volume of this cell is ∼400 cm^3. Its base-pressure is kept at $\sim 1\times10^{-10}$ mbar. This part has the following two functions: (i) allowing exposure of sample surfaces to gas at varying pressures in the range of UHV to 1 bar without breaking the vacuum of the preparation chamber; and (ii) measuring IRA spectra under UHV and high-pressure conditions. The first aim is achieved by a special sealing mechanism consisting of spring-loaded Teflon rings mounted on a flange between the preparation chamber and the high pressure cell. By inserting the sample into the high-pressure cell, the sample-holder (cold-finger) slides through the arrangement of Teflon rings. Thereby, an internal seal between preparation chamber and high-pressure cell is established. For the second purpose, the high-pressure cell is equipped with two CaF_2 windows, which allow light in the mid-IR range to be transmitted. In order to measure a wide range of pressure, this cell is equipped with two gauges: at low pressures (UHV conditions) an ion gauge (`SenTorr`, Varian) located below the gate valve is used, and for elevated pressures two aneroid gauges (`Baratron`, MKS) placed opposite to a leak valve are

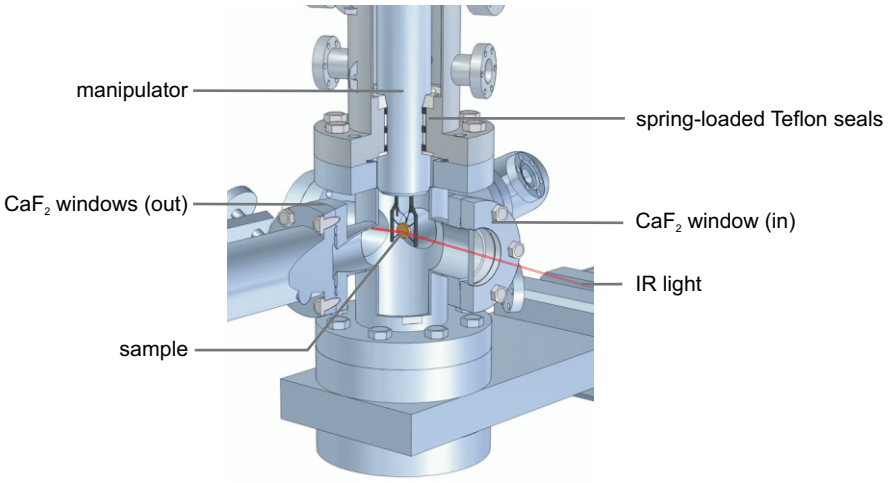

Figure 3.3: Schematics of the high-pressure cell. CaF_2 windows (in) (and (out)) are for IR light impinges onto (from) a sample surface.

employed. One of the baratrons operates up to 10 mbar, and the other one up to 1 bar. The baratrons are classified as aneroid gauge, which means that they sense mechanical deflection in response to the pressure. Hence, the pressure output is independent of the gas composition.

For reactivity studies, the high-pressure cell is equipped with two oppositely placed ports, and is transformed into a batch reactor by connecting these ports from the outside. This closed system must be circulated by a pump during reactivity experiments (`MB-41E`, ansycol).

IRAS Measurement

The high-pressure cell serves also as IRAS measurement chamber. Infrared light in the mid-IR region is emitted from a Globar (silicone carbide) stored in the Bruker IFS 66v/S spectrometer. The emitted infrared light from the spectrometer is introduced into the chamber at an incident angle of 83° via a CaF_2 window. The CaF_2 window is necessary to separate the UHV environment from the rough vacuum region, where the spectrometer and a detector are placed. The light reflected by a sample is detected by a Mercury-cadmium-telluride (MCT) detector through another CaF_2 window and a lens made of ZnSe. The MCT detector can operate only at liquid nitrogen temperature because of its low band gap of 0 to 1.5 eV. This low band gap allows electrons in the valence band to be excited by infrared light. A photoelastic modulator (`PEM90`, Hinds) can be placed between the spectrometer and the sample. This photoelastic modulator enables polarization-modulation IRAS measurements for in-situ vibrational studies at elevated pressures [32]. The system described above has a spectral range of 1000–5000 cm^{-1}.[1]

IRA spectra are typically acquired by accumulating 1000 scans with a resolution of 4 cm^{-1}. Enormously sensitive measurements are required for the detection of surface deutrium-substituted hydroxyl groups with a stretching frequency around ∼2700 cm^{-1} [112]. A reasonable

[1] IR light with a frequency below 1000 cm^{-1} is accessible when KBr windows are used instead of the CaF_2 windows. However, KBr windows are easily damaged by moisture.

signal-to-noise ratio is achieved if both the spectrometer and the MCT detector are under perfect conditions. To this end, the MCT detector was typically cooled overnight, and the spectrometer was also left to run. Great care must be taken to measure all the spectra at exactly the same sample coordinates.

Preparation of Gases and Liquids for the High-Pressure Experiments

Gases (e.g., CO (Linde AG, 99.999 %)) are introduced to the chamber via variable leak valves. Prior to gas introduction, contamination is aimed to be removed by cold traps. The removal of Ni-carbonyl, which is produced when CO gets in contact with stainless steel, is achieved by a Ni remover. Further efforts are made to avoid contamination in cases where samples are exposed to high-pressure gas. Gas lines connecting the high-pressure cell and gas bottles or glass tubes are baked while leak valves are kept open to achieve UHV-level vacuum ($\sim 1 \times 10^{-9}$ mbar) even in the gas lines. The gas lines are sealed after introducing the gases.

This above mentioned protocol is inapplicable to liquids (e.g., D_2O (Merck, 99.75 %)), stored in glass tubes, because liquids have always to be degassed prior to their introduction. Multiple freeze-pump-thaw cycles must be performed to remove residual gases in liquid materials. In this treatment, liquids are frozen by liquid nitrogen while being exposed to the vacuum of a turbo-molecular pump for minutes. Subsequently, the reactant is melted autonomously. In order not to break glass tubes, one must remove condensed liquid water on glass tubes, and wait until the tubes are free of frozen materials.

Furthermore, once the inner surface of the high-pressure cell is contaminated by sticky molecules such as thiol, carbonate or methanol, they must be washed away by repeated cycles of baking and the introduction and evacuation of exchangeable molecules such as water at elevated pressures.

The ion gauge must be turned off upon gas introduction. Otherwise, the ejected electrons from the filament induce the formation of radical species and contamination with carbon-related species, resulting in sample surfaces that are covered with carbon related species.

As explained above, the high-pressure cell can also be used as a batch reactor [113]. Its operation demands that the mixed reactants are balanced by He to keep the total pressure in the chamber at 1 bar. This reaction mixture is circulated by the circulation pump.

3.2 Preparation of Samples

Two different oxide films are prepared in the present study: MgO films on an Ag(001) surface and CaO(001) films on a Mo(001) substrate. Furthermore, a Pd(111) sample is used to compare the properties of supported Pd particles with those of extended single-crystal surfaces. Here, the preparation procedures of the MgO films and Pd(111) surface as well as the hydroxylated MgO surfaces are described. Details about the preparation of the CaO films are described in Chapter 10.

3.2.1 Preparation of MgO(001) Films on Ag(001) and Hydroxylated MgO Films

MgO(001) films are prepared on an Ag(001) single-crystal sample. The Ag(001) sample is connected to two Mo rods via Ta-wires for resistive heating, and a type-K thermocouple is spot-welded to the sample to monitor and control the temperature of the sample. The Ag(001) surface is cleaned by repeated cycles of Ar^+ sputtering (typically 1×10^{-5} mbar for 0.5–1 h) and annealing (673 K for 20 min). After the formation of a clean, well-ordered Ag(001) surface is confirmed by LEED and XPS, MgO(001) films are grown on the Ag surface by physical vapor deposition of Mg (Goodfellow, 99.9 %) in an oxygen environment of 1×10^{-6} mbar and at a substrate temperature of 573 K. The deposition rate is adjusted to be 1 ML (2.1 Å)/min. During deposition, the crystal was biased with a retarding voltage in order to avoid ion acceleration towards the sample (point defect creation). Subsequent annealing to 673 K for 5 min is performed to remove residual hydroxyls, which are formed during the sample preparation. The quality of the MgO films is checked using LEED and XPS.

Hydroxylation of the MgO Films

Three methods are employed to hydroxylate MgO(001) surfaces: exposure to 0.05 mbar D_2O for 3 min; exposure to 0.001 mbar D_2O for 3 min with the ion gauge filament turned on; and exposure to 100 mbar D_2 for 40 min. As well-defined MgO(001) films are exposed to 0.05 mbar D_2O vapor or 100 mbar D_2, their surfaces are covered mainly with surface hydroxyls, and the amount of carbon contamination is negligible. An enhancement of hydroxylation is achieved with the aid of electrons emitted from the ion gauge. In this situation, D_2O vapor at a pressure of 1×10^{-3} mbar is sufficient to produce the same coverage of surface hydroxyls as exposure to 0.05 mbar D_2O vapor without the ion gauge filament turned on. However, this procedure leads to contamination of the surface by carbon-related species (see Chapter 5) [112].

Deposition of Au or Pd

Au and Pd are deposited onto the MgO films at substrate temperatures of 100 or 300 K by physical vapor deposition. During deposition, the crystal was biased with a retarding voltage in order to avoid ion acceleration towards the sample (point defect creation). The deposition rate is usually fixed at 0.1 Å. During the deposition, the background pressure of the preparation chamber typically increased to $\sim8\times10^{-10}$–1×10^{-9} mbar.

3.2.2 Preparation of a Pd(111) Surface

A Pd(111) sample is connected to two Mo-rods via Ta-wires for resistive heating, and a type-K thermocouple is spot-welded to the backside of the crystal for temperature control. The Pd(111) surface is cleaned by repeated cycles of Ar^+ sputtering (typically: 1×10^{-5} mbar for 20 min) and annealing (1023 K for 3 min). The quality of the surface order and purity of the sample is confirmed with LEED and XPS.

Chapter 4

Properties of the MgO & MgO(001) Films on Ag(001)

This chapter provides a brief explanation about magnesium oxide and the MgO(001) films grown on an Ag(001) substrate. Information about their electronic and geometric structures is comparably presented.

4.1 General Properties of MgO

Magnesium oxide (MgO) is an insulating ionic oxide. Fig. 4.1a presents the conventional and the primitive unit cells (shaded) of MgO. The formation of this ionic oxide, MgO, is driven by the strong difference in Pauling's electronagetivities of Mg(1.31) and O(3.44) [114], inducing the interatomic charge transfer. This charge transfer oxidizes $Mg(1s^2 2s^2 2p^6 3s^2)$ to $Mg^{2+}(1s^2 2s^2 2p^6)$, and reduces $O(1s^2 2s^2 2p^4)$ to $O^{2-}(1s^2 2s^2 2p^6)$. Every Mg^{2+} and O^{2-} ion is surrounded by six counter ions in a cubic fashion at an equilibrium distance of 2.1 Å. The strong ionic character is responsible for the high melting point of MgO, 3125 K. As is readily expected from the oxidation states of Mg and O ions, the valence band is predominantly dominated by the O 2p orbital and the conduction band mainly by O 3s and Mg 3s states [7]. A main contribution to stabilize MgO is, hence, the Coulomb interaction over long distance. Calculations based only on the *Madelung potential* [63] of MgO yield a band-gap of 23.9 eV [7]. This band gap is clearly overestimated compared to the experimental band-gap of 7.8 eV [115]. This overestimation emerged due to the assumption that each ion is placed in an equilibrium position. For ionic crystals, this static situation does not hold as realistic, because there is a non-negligible contribution of dipole moment. There is a fluctuation of the electronic fields resulting from the displacement of charged ions (displacement polarization) [63]. The finite distribution of charge instead of a point charge alleviates the Coulomb interaction, and, thereby, the calculated band gap decreases. A closer theoretical value can be obtained if we allow each orbital to interact with each other, using a better wave functional than the tight-binding theory [7,63]. The inclusion of the orbital overlap reduces the bulk band gap of MgO to 7.8 eV (Fig. 4.1c).

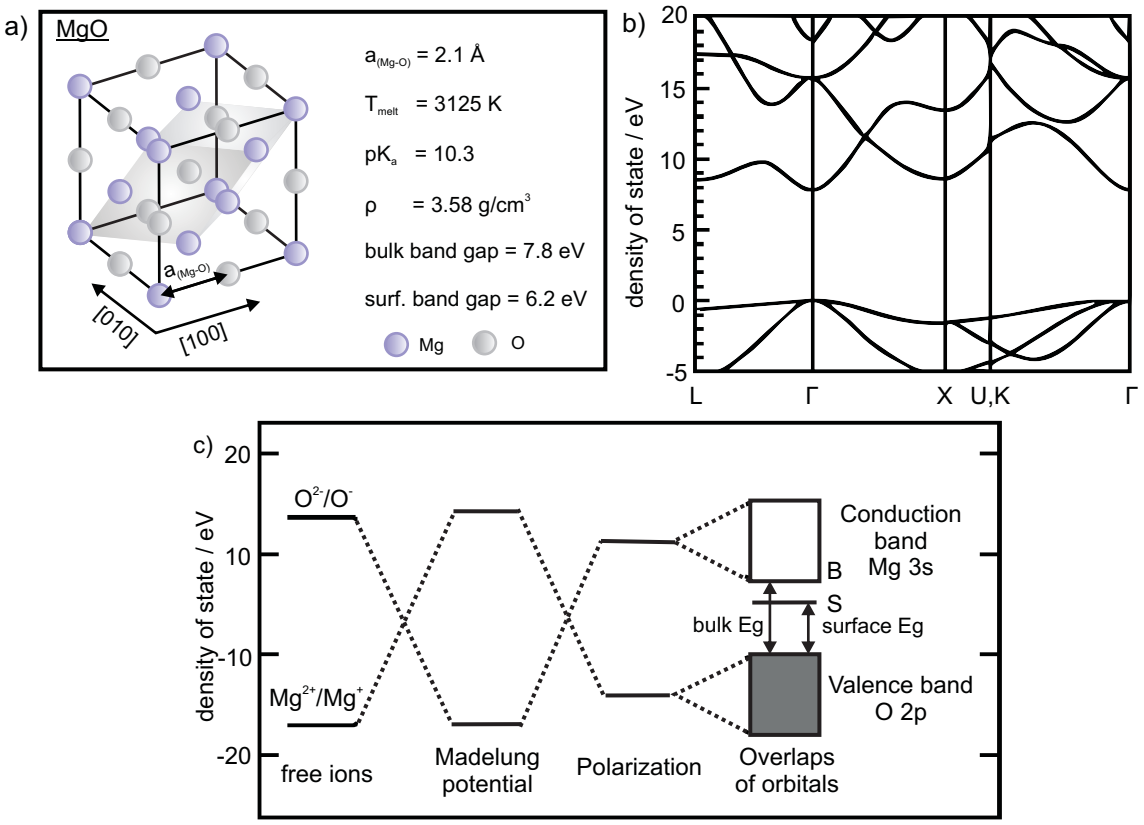

Figure 4.1: a) Schematic representation of MgO using a conventional unit cell, and the primitive unit cell (shaded). Fundamental properties of MgO are also given [114]. b) Calculated band structure of bulk MgO [116]. c) The energy diagram of Mg and O ions consisting of MgO with different levels of theoretical approximation [7]. E_g indicates the band gap for bulk MgO and E_s means that for the MgO(001) surface [115].

Compared to bulk MgO, the surface band gap corresponding to the most stable facet of MgO, {001}, has a slightly reduced value of 6.2 eV, because of the emergence of the surface specific energy state [117]. This empty energy states largely shifted compared to that of bulk MgO results from the admixture of the Mg 3s and 3p components induced by the polarization effect due to the strong electric field at the surface. It is noted that the anion-cation distance at the MgO surface is contracted for better overlapping of the orbitals, and the rumpling is 1.07 ± 0.5 % [118]. This inward displacement induces a reinforcement of the Madelung potential at the surface, which causes the Stark effect (the formation of static electric field (polarization)) to stabilize the Mg 3s surface state [119].

4.2 Characteristics of the MgO Surfaces and the MgO(001) Films on Ag(001)

In line with the explanation of bulk MgO given in the previous section, the nature of the MgO surface and MgO(001) films grown on the Ag(001) surface is shortly introduced (Fig. 4.2). For

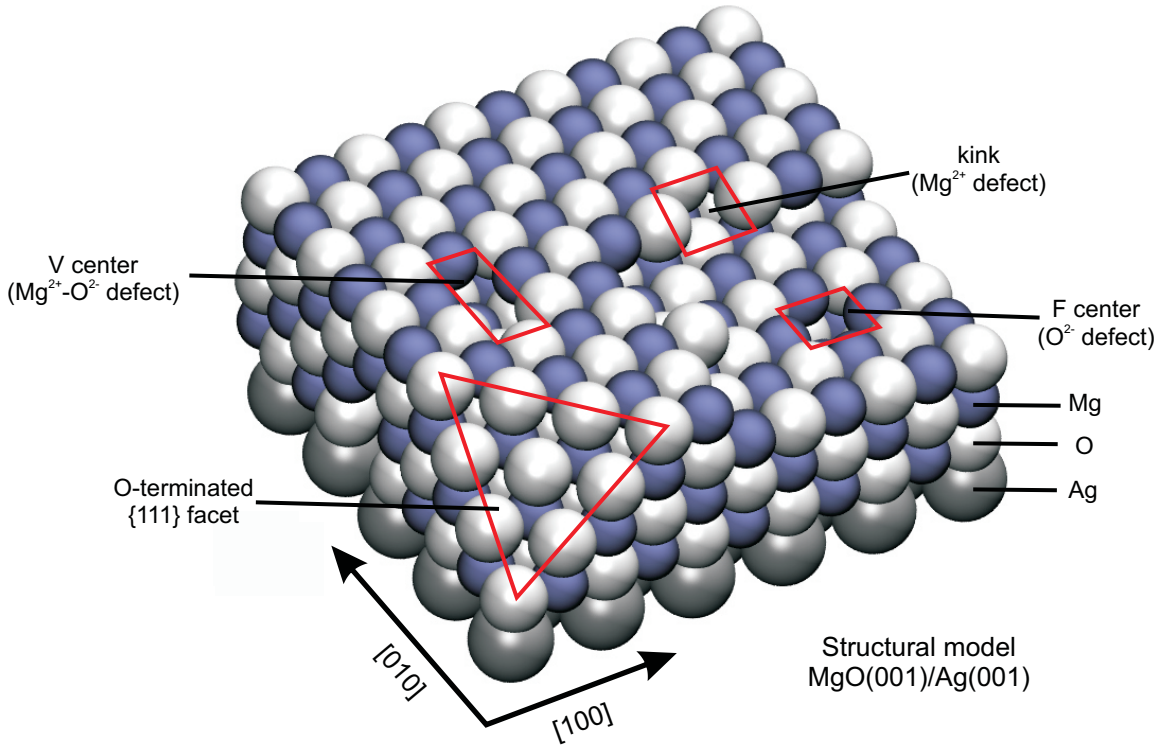

Figure 4.2: A schematic model of the MgO(001) surface with various surface defects, O-terminated polar facet, and the MgO(001) films supported on Ag(001) substrate.

the ease of the qualitative description of the surface states, a short description regarding surface thermodynamics is provided [120, 121]. The generalized Gibbs energy of a system with surfaces is written as

$$\mathrm{d}G = -S\mathrm{d}T + V\mathrm{d}P + \sum_i \gamma_i \mathrm{d}A_i + \sum_i \mu_i \mathrm{d}n_i, \tag{4.1}$$

where γ, A, μ and n indicate the surface tension, the surface area, the chemical potential and the constituent concentration for the species i. For a pure system at a constant temperature and pressure, note that $\mathrm{d}G$ is equal to γ of a value above zero. This indicates that the formation of surfaces is thermodynamically unfavored. The thermodynamic property including only the surface contribution is provided by the Gibbs surface energy. This surface energy and its differential form are given:

$$G^s = H^s - TS^s = \textstyle\sum_i \mu_i n_i^s \tag{4.2}$$

$$\mathrm{d}G^s = -S^s\mathrm{d}T - A\mathrm{d}\gamma + \textstyle\sum_i \mu_i \mathrm{d}n_i^s \tag{4.3}$$

where $\mathrm{d}G^s$ indicates the change of Gibbs free energy per unit area to form a specific state, and $\mathrm{d}S^s$ corresponds to the change of entropy. These quantities are more closely examined. G^s is always positive according to the definition, which is microscopically interpreted as the formation of chemical bonds to stabilize the system, i.e., the presence of surface destabilizes the system. Furthermore, $\mathrm{d}G^s$ indicates the non-zero quantity of the entropy term, $S^s\mathrm{d}T$, which can

stabilize the surface on a specific facet. Microscopically, the increase in surface entropy means that the surface becomes covered with various defects and grain boundaries. The entropy term is, for example, expected to S = 0.18 mJ/m^{2}K for conventional grain boundaries [122]. An ideally ordered surface is characterized by S^s of zero, so that dG^s increases, i.e., the formation of a defect free surface is not thermodynamically favored. Hence, the entropic contribution in Eq. 4.3 inevitably works to create surface defects.

The MgO(001) surface is the most stable facet under UHV conditions, because this surface is non-polar, and all the surface Mg and O ions are coordinated by as many as five counter ions, i.e., only a single bond breaking occurs. Note that the ionic bond is rather strong compared to other bonds, so that the amount of bond breaking associated with faceting critically determines the stability of each facet of magnesium oxide. Nevertheless, the MgO(001) surface contains various defect sites: kink at boundary, V-center (a neutral vacancy formed by the removal of Mg-O ion pair), and F center (oxygen vacancy with trapped electron(s)) (Fig. 4.2) [121]. These defects have special structural and electronic properties and are potential metal nucleation sites or catalytically highly active sites (*cf.* [9,123]). It is also noted that, at non-equilibrium condition, polar {111} terraces terminated by O-atoms can be formed [124, 125]. However, these surfaces are unstable and the polarity is compensated either by reconstruction (e.g., the MgO {111} facet exposing {001}-type nano-facet) or adsorption of hydrogen [126, 127].

Several limitations exist for the application of conventional surface science techniques to single-crystalline MgO bulk: the uncontrollable amount of surface defects and bulk contamination (dopants), and surface charging. To avoid these problems, MgO films grown epitaxially on a metal substrate with a suitable lattice constant are used, instead (see the MgO films on the Ag(001) surface in Fig. 4.2). MgO(001) films can be epitaxially grown on Ag(001) [128], Fe(001) [129] and Mo(001) [18]. The lattice mismatch of these metals compared to MgO(001) is, respectively, +2.9 %, +3.7 %, and −5.4 %. In the present study, Ag(001) was used as substrate for the growth of MgO(001) thin films. Each O^{2-} and Mg^{2+} ion is positioned on the on-top and the four-fold hollow sites of the Ag(001) substrate. The distance between the first MgO layer and the Ag(001) substrate has been experimentally and theoretically determined to be 2.5–2.6 Å [130]. Compared to the usual Mg-O ion pair distance of 2.1 Å, this elongated state found at the MgO/Ag interface reflects the larger radius of Ag atoms [131]. The layer distance is converged into the bulk Mg-O ion distance of 2.1 Å as the films become thicker [130].

This larger Ag-O distance implies that the thin MgO films with a thickness of, for example, less than 10 ML, might have distinct properties from those of bulk MgO. A reason behind this consideration is, in addition to the lattice mismatch, the hybridization of the valence band of the MgO films, mainly composef of O 2p, with the Fermi edge of the Ag substrate, Ag 5sp, as evidenced by photoemission spectroscopy [132]. This orbital hybridization can cause an upward shift in the O 2p state, often referred as the metal induced gap states (MIGS). This is a generally observed phenomenon for metal-oxide interfaces [133]. If the same charge transfer is present for the thin MgO films, the band gap of the MgO(001) films would increase or decrease [134]. This possibility was negatively proven by a combination of experimental and theoretical works [135],

suggesting that the surface electronic structure of ultra-thin MgO(001) films is similar to that of bulk MgO even at a film thickness of 3 ML. This finding is indicative of a weak orbital overlaps at the MgO/Ag(001) interface, as expected for inert oxide/noble metal junctions [136].

The growth and properties of thin oxide films can be strongly affected by the choice of metal substrate. For instance, the work function of a metal substrate might govern the ability to transfer charge from metal substrates to supported oxide films [137]. Furthermore, in parallel to the charge transfer through the films, migrated metal atoms into the oxide films can change the electronic structure of oxide films, too.

Chapter 5

Growth of MgO(001)/Ag(001) Films and Their Hydroxylation

This chapter is devoted to a spectroscopic study of the growth of clean MgO(001)/Ag(001) films with different thicknesses, and the hydroxylation of the MgO films at ambient pressures. The thickness dependence measurements were carried out to probe the influence of Ag on the film growth as well as hydroxylation. Three methods for hydroxylation are presented: exposure of MgO films to water (D_2O) vapor with the ion gauge turned on and off, or exposure to D_2 gas. It was found that all the procedures were capable of forming hydroxyl groups on the MgO(001) surface. The hydroxyls formed with the aid of the gauge were featured by a lower vibrational frequency compared to those on hydroxylated MgO powder. The MgO films which were hydroxylated without using the electron source yielded almost identical infrared spectra to what has been obtained using hydroxylated MgO powder. The MgO(001) surface exposed to D_2 exhibited a smaller amount of surface hydroxyl groups than the other two surfaces.

5.1 Introduction

The hydroxylation and hydration of metal oxide surface plays a pivotal role in supported-metal catalysts. For example, in the precipitation of metal complexes onto oxide supports, metal-precursors in dilute solutions dynamically react with oxide surfaces, which are possibly covered with hydroxyls at the solid/water interface [46, 138]. In this process, the distinct properties of hydroxyls present on different oxide surfaces might fatefully determine the performance of the prepared catalysts. The functions of surface hydroxyls on oxide surfaces could also tune catalytic performances; e.g., moisture is a notable promoter in CO oxidation [5].

In order to study hydroxylation as well as the hydration of oxide surfaces, MgO has been employed as a model over decades, due to its simple crystal structure and electronic properties [112,139–146]. The complete hydration of MgO leads to the formation of brucite, $Mg(OH)_2$, proceeding as an exothermic process with $\Delta G = -35.6$ kJ/mol at room temperature [145, 147]. Microscopically, the initial event to hydroxylate MgO is the water dissociation over MgO sur-

faces, and its energetic has been known to be dependent on the facet exposed to water molecules. One work demonstrated that MgO smoke initially exposing {001} facet exhibits the growth of a {111} facet by the hydration, as experimentally [126] and theoretically [127,148]. This indicates that the dissociated hydroxyl groups are more stabilized over MgO(111) surfaces. Theoretical works confirmed it; water does not dissociate into two hydroxyls to make a hydroxyl group on a Mg^{2+} ion and a proton on an O^{2-} ion, as this would result in an endothermic reaction with $\Delta H = +62$ kJ/mol [146, 149]. Exceptionally, the hydroxylation of point defects was found to readily proceed [150]. In order to make the energetically unfavorable hydroxylation of MgO(001) occur, the increases of chemical potential by elevating pressures of water vapor or reaction temperature must be necessary. These changes shift the equilibrium of the system, H_2O + MgO $\rightleftharpoons$ $Mg(OH)_2$, toward hydroxylating MgO(001). The hydroxylation of the MgO(001) surface has been studied using MgO smoke [151], single crystalline MgO(001) [144,152,153], and MgO(001) films [112,154]. These works suggest that scissoring a lattice MgO bond at ambient conditions is necessarily accompanied by the accommodation of one dissociated water molecule: $\{$-Mg-O-$\}_n$ + $D_2O \rightarrow \{$-Mg(OD) + O(D)-$\}_n$ [112,150]. Nevertheless, there is little comprehensive information about the vibrational and electronic structures of these systems to correlate hydroxyl's nature to MgO(001) film's thickness.

In this chapter, vibrational and electronic information is provided concerning hydroxylated MgO films by various methods, after calibrating and characterizing the pristine MgO(001) films grown on an Ag(001) single crystal. First, the so-called "normally hydroxylated MgO(001)" films grown on Ag(001) with different thicknesses (3 and 30 ML) were prepared by exposing the surface to D_2O. Thickness of the MgO film was proven to matter the degree of hydroxylation, where a thickness dependence was found for the degree of charge transfer from the OH groups to the films. Second, the influence of dosing water with the aid of electrons emitted from an ion gauge upon the state of surface hydroxyl groups was studied. The emitted electrons from the filament drastically accelerated the reactivity of water molecules in hydroxylating the MgO(001) surfaces. The stretching frequency of the hydroxyls on this surface are red-shifted compared to case, when the MgO films were hydroxylated without the ion gauge, which is indicative of a stronger acidic character of the hydroxyls on the former surface. Furthermore, the hydroxylation of the MgO(001) surface by hydrogen (D_2) gas exposure is presented.

5.2 Results

5.2.1 Growth of MgO(001)/Ag(001) Films with Different Thicknesses

Determination of MgO Film Thickness

The growth of MgO/Ag(001) films with different thicknesses (4, 10, 20 ML) was studied by means of XPS. The MgO films were deposited onto the Ag(001) surface at a rate of 1 ML/min and a substrate temperature of 573 K. For the determination of the MgO film thickness, the attenuation of the Ag 3d XP intensity by MgO films was analyzed using Eq. 2.17. The IMFP

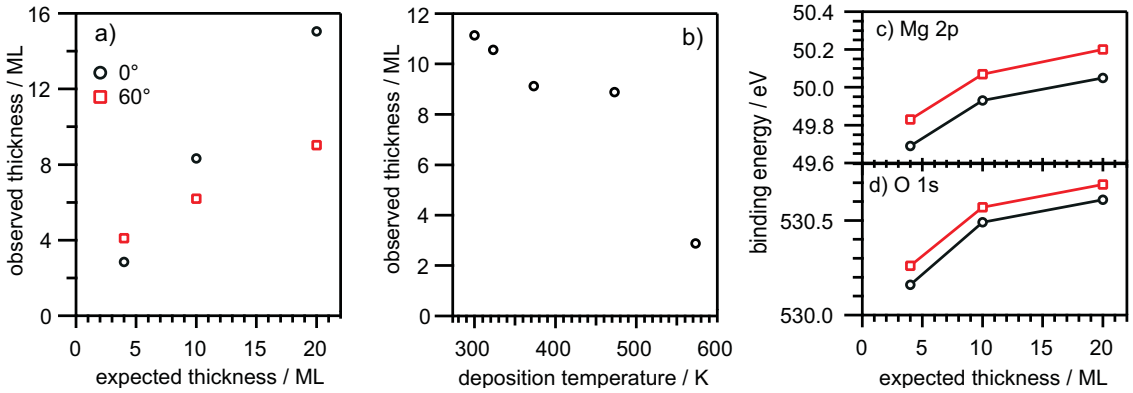

Figure 5.1: a) The MgO(001) film thicknesses at different angles of electron emission (0 and 60°) titrated by Eq. 2.17 on the basis of Ag 3d peak areas. b) The MgO film thickness as a function of annealing temperature, for nominally 4 ML MgO films as measured using a QMB. The thickness was determined by data acquired at an angle of emission of 0 degree. The binding energy shifts of c) Mg 2p and d) O 1s states as a function of expected MgO film's thickness.

for Ag 3d photoelectrons with a kinetic energy of 1118 eV is 23.6 Å according to [70]. The calculated MgO film thicknesses are presented in Fig. 5.1a. At an electron-emission angle of 0 degree, the actual MgO films with expected thicknesses of 4, 10 and 20 ML were found to be 3, 8, and 15 ML, respectively. While these measurements clearly indicated the linear relation between the MgO film thickness and the deposition time, the data acquired from the same samples at an electron emission angle of 60 degrees was found to have an offset of ∼2 ML and yielded smaller MgO thicknesses. This difference reflects the angle dependence of the attenuation length of electrons, which states that attenuation lengths might be longer at high emission angles [155]. The mechanism behind the longer attenuation lengths is the elastic diffraction of electrons emitted from the buried substrate by the oxide overlayers. This results in the overestimation of the contribution of the silver substrate. Secondly, it was recently found that the growth model of MgO film could be deviated from the ideal layer-by-layer growth [156]. This ill-defined growth mode might violate the utility of the model to deduce the film thickness. Thus, the oxide film thickness was determined at an electron emission angle of zero.

Fig. 5.1b displays the actual MgO film thicknesses as a function of substrate temperature, upon depositing nominally 4 ML thick MgO films as expected according to QMB calibration. The calculated thickness decreased from ∼11 to 9 ML in the temperature range of 300–473 K. However, at the most appropriate temperature for the growth of ordered MgO(001)/Ag(001) films [157], ∼573 K, the oxide film thickness was found to be ∼3 ML.

As the MgO film thickness increased from 4 to 20 ML, the Mg 2p and O 1s binding energies increased by 0.35 and 0.5 eV, respectively (Fig. 5.1c). An earlier study observed a similar tendency [134]: as the film thickness increased from 2.7 to 20 ML, $\Delta BE = +0.4$ eV was observed for Mg 2p, and $\Delta BE = +0.8$ eV for O 1s. Auger parameter analysis applied to these MgO/Ag(001) films revealed that the thickness-dependent shifts are mainly caused by differences in the final-

state screening of the core-hole. For the thin MgO films, the presence of an image potential created in the Ag substrate reduces the Coulomb interaction and charge transfer energies, and readily eases the created positive electric fields of the core holes (i.e., better screening) [158,159].

There is another possible mechanism to explain the binding energy shifts in terms of the stoichiometry of the films; the O 1s/Mg 2p intensity ratio decreased from $\sim$ 14 to $\sim$ 12, as the thickness increased from 4 to 10 or 20 MLs. With the assumption that MgO films with a thickness of 20 ML are close to the perfect stoichiometry, the intensity ratio difference indicates 15 % excess of oxygen in the 4 ML thick MgO film. Additionally, there was a larger binding energy shift of the O 1s peak than that of Mg 2p as the film thickness increased. These results are in agreement with the situation that O ions in thicker MgO films became fully oxidized (-2) according to the system's stoichiometry. There were parallel binding energy shifts for the O 1s and Mg 2p peaks, as an electron takeoff angle varied from 0 to 60 degrees. One mechanism to explain this observation is that the longer paths for the electrons results in the strong interaction with the MgO films, accompanied by energy loss processes in the MgO films or by adsorbates. Another possibility is the occurrence of SCLS, as a recent study revealed that even oxide surfaces could experience it [160].

Policy of Using the MgO(001) Film as a Model

It was previously shown that MgO films with a nominal thickness of 3–4 ML are required to cover a large part of the Ag(001) substrate [156]. An ISS experiment has proven that 30 ML MgO films were thick enough to close Ag surfaces (less than $\sim$ 0.1 %) [161]. Hence, all experiments that must not be affected by the properties of thin MgO films (e.g., abundant defect sites, Ag doping, charge transfer from the substrate) employed the 30 ML thick MgO(001) films in this thesis. When the effects of ultra-thin MgO films were aimed to be studied, the MgO film with a thickness of 3–4 ML was employed.

5.2.2 Hydroxylation of MgO(001) Films

Hydroxylating Thick MgO(001) Films using Various Methods

Three different hydroxylation treatments were applied to MgO surfaces: a) 3 min exposure to 0.05 mbar D_2O at RT with the ion gauge filament inside the hydroxylation cell switched off (MgO_{hydr}); b) 3 min exposure to 0.001 mbar D_2O at RT with the ion gauge filament switched on (MgO_{hi}); c) 40 min exposure to 100 mbar D_2 at RT (MgO_{hg}). O 1s XP spectra of clean MgO films and after subsequent hydroxylation using the treatments described above are presented in the panels a–c of Fig. 5.2, respectively. The O 1s binding energy of the 30 ML thick MgO film was shifted from 531.3 to 530.8 eV upon hydroxylation, accompanied by the simultaneous appearance of an O 1s peak at 532.9 eV relating to surface hydroxyl groups. The hydroxyl coverage was calculated to be 0.6 ML [162]. With the aid of the ion gauge during hydroxylation, the O 1s peak position was greatly shifted to 529.5 eV from 530.7 eV. Despite the formation of a comparable amount of hydroxyl groups to MgO_{hydr}, the O 1s binding energy of hydroxyls on

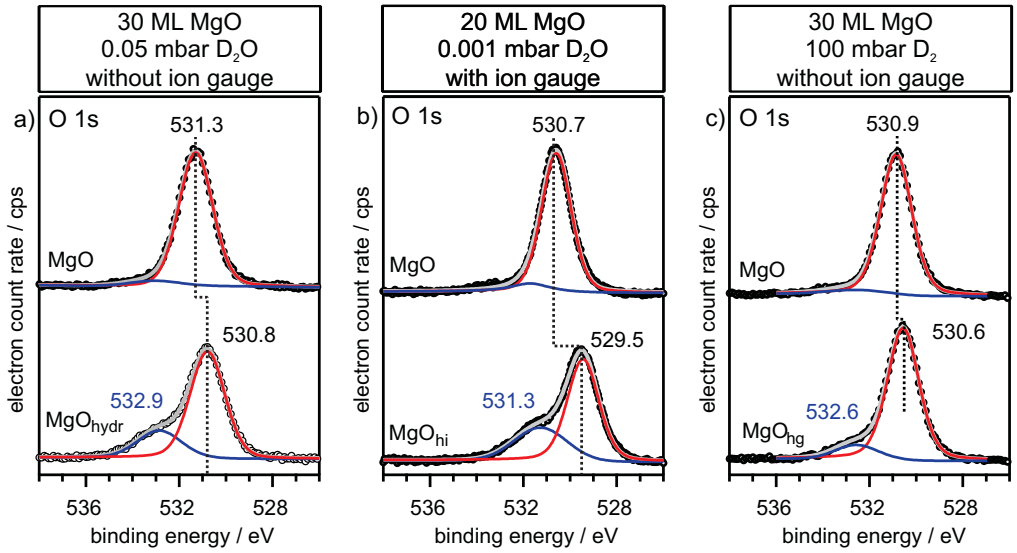

Figure 5.2: O 1s XP spectra of a) 30 ML thick pristine MgO films, and after subsequent hydroxylation at 0.05 mbar D_2O without an ion gauge, b) 20 ML thick MgO pristine films, and after hydroxylation by 1×10^{-3} mbar D_2O with the ion gauge, and c) 30-ML thick MgO films exposed to 100 mbar D_2 for 40 min at room temperature.

MgO_{hi} appeared at 531.3 eV. Furthermore, it is notable that while no change in the region of Mg 1s was observed upon producing MgO_{hydr}, MgO_{hi} exhibited a pronounced negative binding energy shift in the region of Mg 1s (∼1 eV). The exposure of 30 ML MgO film to D_2 yielded a small amount of surface hydroxyl groups. The hydroxyl O 1s binding energy appeared at 532.9 eV and the coverage was estimated to be 0.1 ML. The O 1s peak relating to the oxide was slightly shifted from 530.9 to 530.6 eV.

Infrared spectroscopic measurements were performed in order to characterize the hydroxyl groups formed on the MgO surface. IRA spectra of the hydroxylated films as well as hydroxylated MgO powders (courtesy of Dr. Sterrer) are shown in Fig. 5.3a. Typically, the spectra were featured by one sharp absorption band and a second broad absorption feature. The hydroxylated powder MgO and MgO_{hydr} exhibited almost identical absorption profiles; the sharp band appeared at 2754–2756 cm^{-1} and the maximum of the other broad feature was centered at 2620 cm^{-1}. Previous studies using DFT calculations, NMR and IR assigned the higher vibrational component to isolated hydroxyls and proton-acceptor hydroxyls, and the lower broad signal to proton-donor hydroxyls [143, 144]. Over MgO_{hi}, the sharp signal of surface hydroxyls was shifted to 2734 cm^{-1}, at which neither MgO_{hydr} nor the powder MgO gave an OD signal. Upon exposure of the thick MgO(001) film to 100 mbar D_2 at room temperature, MgO_{hg} exhibited one weak signal centered at 2742 cm^{-1}. This vibrational frequency was slightly lower than that observed for MgO_{hydr}. This observation is in agreement with previous investigations [140, 163]. A noticeable feature specific to MgO_{hi} is the formation of a pronounced band at 2850 cm^{-1}, which can be ascribed to adsorbed formate created during the hydroxylation treatment from

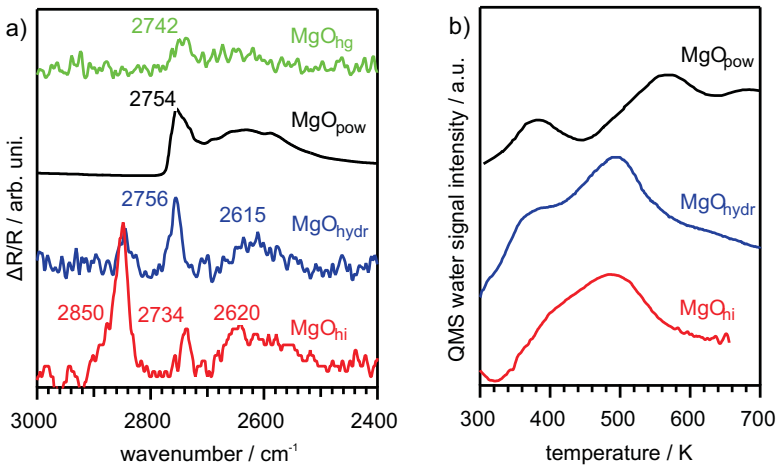

Figure 5.3: a) An IRA spectrum of the hydrogenated MgO(001) film by 100 mbar D_2 (green trace), a transmission IR spectrum of hydroxylated MgO powder (black trace), and IRA spectra of hydroxylated MgO(001) films at 0.05 mbar D_2O without the ion gauge (blue trace), and 1×10^{-3} mbar D_2O with the gauge turned on (red trace). b) Water (D_2O) TPD spectra acquired from hydroxylated MgO powder [141], the hydroxylated MgO films at 0.05 mbar D_2O without the gauge (blue trace) and at 1×10^{-3} mbar D_2O with the gauge turned on (red trace). Ramp rate was 1 K/s.

concomitantly introduced or produced contaminations. A much smaller peak relating to this contamination appeared on MgO_{hydr} as well as MgO_{hg}.

TPD spectra of the MgO films that have been hydroxylated using the different methods and of hydroxylated MgO powder (taken from [141]) are presented in Fig. 5.3b. The desorption of water from MgO_{hi} and MgO_{hydr} results in qualitatively similar TPD profiles with a main desorption peak at 500 K, and a smaller peak at ~400 K. The lower temperature peak is more pronounced in the case of MgO_{hydr}. The peaks can be ascribed to the desorption of physisorbed water (~400 K) and recombinative desorption of OH groups (~500 K) [141]. The powder MgO sample showed a water desorption peak at 380 K, accompanied by the broader water desorption at 550 K. The shift by 50 K compared to the flat MgO samples might be the result of a higher abundance of defects on the powder surface or could be related to the porous nature of the powder.[1] Note that the physisorbed water desorption at 400 K was smaller for MgO_{hi}.

Hydroxylating Thin and Thick MgO(001) Films without the Ion Gauge

The effects of MgO film thickness on hydroxylation without the ion gauge was investigated. The MgO films with 3 ML and 30 ML thick films were hydroxylated at a D_2O pressure of

[1] Once a chemical bond between a water molecule and the MgO(001) surface is broken, the water can leave the surface to the vacuum, where the re-adsorption of water is hardly expected. In contrast, the complexity of MgO powder provides many sites for water molecules to be trapped until they reach the exterior of the powder. This causes the delay in water desorption for the powder.

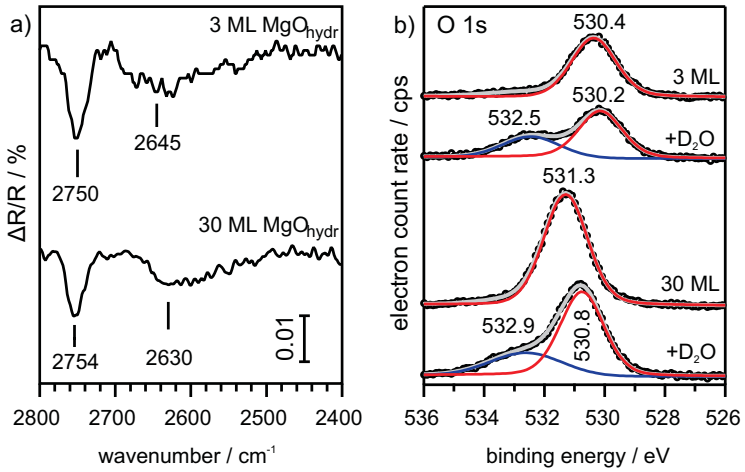

Figure 5.4: a) IRA spectra of 3 ML and 30 ML MgO films after exposure to D_2O at a pressure of 0.05 mbar and a substrate temperature of 300 K for 3 min. b) O 1s XP spectra of pristine and hydroxylated MgO films with a thickness of 3 ML (top two spectra) and those with a thickness of 30 ML (bottom two spectra).

0.05 mbar, and used for the subsequent infrared measurements (Fig. 5.4a). The thin MgO films yielded almost the same vibrational profile as the thick MgO_{hydr}. However, two minor differences appeared: (i) the thin MgO_{hydr} showed a peak centered at 2645 cm^{-1}, but the thick MgO_{hydr} films gave rise to an absorption maximum at a frequency of 2630 cm^{-1}; (ii) the sharp component around 2750 cm^{-1} became more prominent for the thinner MgO films. The corresponding O 1s XP spectra were taken to investigate how hydroxylation affected the electronic structure of these films (Fig. 5.4b). The O 1s peaks appeared at 530.4 and 531.3 eV for the pristine 3 and 30 ML thick MgO films, respectively. As the 3 ML thick MgO film was hydroxylated, the O 1s component experienced a negative shift to 530.2 eV, accompanied by a hydroxyl O1s peak at 532.5 eV. In the case of 30 ML MgO_{hydr}, the O 1s peak relating to the MgO film shifted from 531.3 to 530.8 eV, and the hydroxyl component emerged at 532.9 eV. A general feature among the films was the hydroxylation-induced negative binding energy shifts of the oxide O 1s peaks.

To provide a deeper insight into the thickness-dependent electronic structure of MgO_{hydr}, photoemission spectra of O 1s, Mg 1s, Mg 2s and Auger electron lines corresponding to the Mg KL_1L_1 decay, for the sake of Auger parameter analysis, were acquired, and a summary is tabulated in Tab. 5.1. The initial, $\Delta\varepsilon$, and final, ΔR, state contributions were calculated by Eq. 2.38. The KL_1L_1 Auger transition was chosen in order to exclude the contribution of the valence band to the relaxation of core holes. The presence of surface hydroxyls had no influence on the Mg 1s binding energy, irrespective of the film thickness. In the case of hydroxylation, the 3 ML and 30 ML thick MgO films showed small reduced screening effects for the Mg 2s orbitals, $\Delta R = -0.1$ eV and -0.2 eV, respectively. A distinct difference appeared in the initial state contribution, $\Delta\varepsilon$; the Mg 2s core level of the thicker MgO was upward shifted by ~0.6 eV upon hydroxylation, whereas for the thinner, 3 ML, film, this shift was only +0.3 eV.

Table 5.1: Binding energy shifts (eV) of the O 1s, Mg 1s and Mg 2s peaks, and the Auger kinetic energy of the Mg KL_1L_1 of the clean and hydroxylated MgO films with thicknesses of 3 and 30 ML, and calculated initial state effect ($\Delta\varepsilon$) and final state effect (ΔR)

Sample	O 1s (MgO)	Mg 1s	Mg 2s	Mg KL_1L_1	ΔR	$\Delta\varepsilon$
3 ML MgO	530.4	1305.0	88.8	1103.0		
3 ML MgO_{hydr}	530.1	1305.1	88.6	1103.3	−0.1	+0.3
30 ML MgO	531.3	1305.0	89.6	1101.8		
30 ML MgO_{hydr}	530.8	1305.0	89.2	1102.2	−0.2	+0.6

5.3 Discussion

5.3.1 Differences between MgO_{hydr} and MgO_{hg} in Electronic States and the Influence of the Ion Gauge

An ideal hydroxylation of the MgO(001) facet proceeds with the simultaneous dissociation of the bond between surface Mg and O atoms and one water molecule being accepted: {-Mg-O-}$_n$ + D_2O → {-Mg(OD) + O(D)-}$_n$ [112, 148]. The additive OD groups on surface Mg atoms are considered to work as electron donors for the Mg atoms via forming a chemical bond between Mg^{2+} and OD^-. The hydroxylation of thick MgO(001) films with the ion gauge turned on for electron emission, MgO_{hi}, significantly decreased not only the binding energy of the O 1s state, but also the Mg 2p, Mg 2s as well as Mg 1s binding energies by 1.2 eV (data not shown), whereas MgO_{hydr} exhibited only negative Mg 2s and O 1s binding shifts of 0.5 eV, without any accompanying binding energy shift of Mg 1s (Tab. 5.1). The larger negative binding energy shifts observed for MgO_{hi} than MgO_{hydr} are explained by different degrees of reduction, and the absence of a Mg 1s binding energy shifts for MgO_{hydr} and $MgO_{hg}$is accounted for by the occurrence of *band bending* only over MgO_{hi}, which are separately discussed below.

Band Bending for MgO_{hi}

Along with the reduction of the films, the hydroxylation-induced negative binding energy shifts in the O 1s and Mg 2s lines might be accounted for by a phenomenon, known as the *band bending* [133, 164]. Band bending is a general phenomenon for heterojunctions such as metal-insulator interfaces, where all the interfacial orbital energies corresponding to the non-metallic compounds are continuously shifted in order to align their Fermi-edges at the metal/non-metal interface (see Fig. 5.5). This alignment is induced by a charge transfer, which in turns yields an electron double layer at the interface. An experimental proof of the occurrence of band bending by means of XPS is the identical shifts of *all* the interfacial XP lines [47]. For the hydroxylated MgO films, only MgO_{hi} exhibited simultaneous negative binding energy shifts of all the oxide components, which can be clearly ascribed to the band bending. This indicates

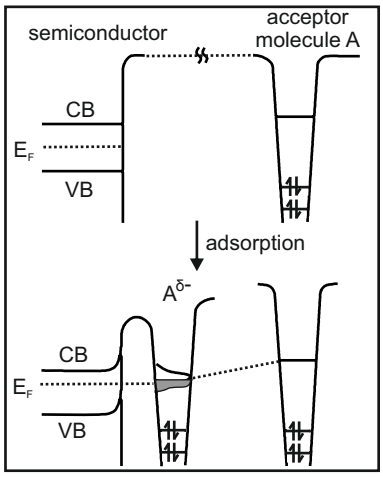

Figure 5.5: Schematics of band bending upon electron acceptor adsorption interacting with insulator or semiconductor surfaces. (taken from [164])

that an electron acceptor adsorbed onto the MgO surfaces so that electrons flow from the oxide support to the supported surface species. On the other hand, for MgO_{hydr}, band bending is no longer responsible for the shifts, as evidenced by the absence of Mg 1s binding energy shift upon hydroxylation of the MgO films (Tab. 5.1). In this case, it is safely maintained that the hydroxylation-induced binding energy shifts in the Mg 2s and O 2s levels were purely ascribed to the changes of the chemical state of the surface Mg and O ions.

It is to be answered how these differences occur. As already discussed, infrared spectroscopy revealed the stronger Lewis acidic properties of the surface hydroxyls on MgO_{hi}, compared to those on MgO_{hydr} (Fig. 5.3). This indicates that the hydroxylation with the ion gauge might specifically populate strongly Lewis acidic hydroxyl groups such as radical-like or highly coordinated ones, which act as electron acceptor.

The invariant nature of the signals of buried layers, such as Ag 3d, is explained as follows. By differentiating Eq. 2.10 with an explicit definition of binding energy with reference to the Fermi edge E_F, it is found that

$$\Delta E_k = -[(\varepsilon_{Ag}^{MgO} - E_F^{MgO}) - (\varepsilon_{Ag}^{ads/MgO} - E_F^{ads/MgO})] - \Delta\phi = 0. \tag{5.1}$$

With the assumption that the work function change is purely induced by the charge transfer to empty orbitals of the adsorbates, the work function change should be exactly the same as the change in the Fermi edge. This relationship yields

$$E_F^{MgO} - E_F^{ads/MgO} = \Delta\phi. \tag{5.2}$$

The combination of Eq. 5.1 and Eq. 5.2 yields the same electron kinetic and orbital energies of Ag 3d, suggesting that they are not affected by the band bending.

Different Properties of Hydroxyl Groups on MgO_{hydr} and MgO_{hi}

The hydroxyl groups on MgO_{hi} are characterized by a stretching frequency of 2734 cm^{-1}, while those on MgO_{hydr} were found at 2754 cm^{-1} [151]. There is a correlation between the frequency of the hydroxyl stretching mode and its Lewis acidity, based upon the net charge on the oxygen atom [165]. According to the electronegativity of the atoms involved, the net charge of the O atom in pure OH^- is -2. For its coordination number n on oxide surfaces such as Al_2O_3, the oxygen net charge is computed as $-2 + n/2$. This situation naturally makes highly coordinated OH groups more electrophilic, i.e., more Lewis acidic. At the same time, from the perspective of molecular vibration, the decrease of the net charge on the O atom indicates that the bonding strength of OH bond is weakened, because the electron donated to form a new bond is provided from the HOMO of the hydroxyls. Thus, as one hydroxyl group is highly coordinated, the hydroxyl vibrational frequency is reduced. This consideration, again, confirms that the hydroxyl groups with lower frequencies observed for MgO_{hi} are more electrophilic than those on MgO_{hydr}. Therefore, the hydroxyl groups on MgO_{hi} should have a superior ability in oxidizing metals and reacting with nucleophilic adsorbates [165]. The high activity of MgO_{hi} is demonstrated in Chapter 7.

It has not yet been mentioned how the electrons emitted from the ion gauge can accelerate the hydroxylation. These electrons can transform normal molecules such as water and concomitant CO, into corresponding positively ionized fragments [166]. This artificial phenomenon could occur for fragile materials (e.g., H_2 or thiol), exposed to electrons emitted from an ion gauge, LEED optics, or even an ion-getter pump. The charged ions and radicals produced in this way could assist in the functionalization of oxide surface with not only hydroxyls, but formate. Our experimental observations indicate that secondary, electron-induced processes indeed contribute to the hydroxylation of the films, but also to its contamination with formates, as suggested by the formation of an infrared band at around 2850 cm^{-1} (Fig. 5.2a).

5.3.2 Comparison of Hydroxylating MgO by Water (MgO_{hydr}) and Hydrogen (MgO_{hg})

Here, a comparison between MgO_{hg} and MgO_{hydr} is provided. The hydroxylation of MgO by either water or hydrogen was investigated using powder MgO [140,163,167]. They found that surface hydroxyl groups at 3734 cm^{-1} for OH (2754 cm^{-1} for OD) appear upon hydroxylating MgO by water, whereas hydrogenating MgO surfaces produces hydroxyl groups with lower stretching frequencies of 3712 cm^{-1} for OH (2737cm^{-1} for OD). The latter signal at 2737 cm^{-1} corresponds to the O-D stretching created by the homolytic hydrogen splitting on MgO surfaces [167]. This reaction is assumed to occur irreversibly only at defect sites, so it gets saturated at 0.1 mbar H_2 (D_2) exposure. Additionally, there is a reversible heterolytic hydrogen splitting path, which leads to the formation of OH band at 3462 cm^{-1}. However, this is observable only in a hydrogen atmosphere, so the present study acquiring *ex-situ* spectra observed no absorption in this region. Both XPS (Fig. 5.2) and IRAS (Fig. 5.3) revealed that the comparative behavior of

MgO_{hg} and MgO_{hydr} is in agreement with the well-established conclusions on the hydroxylation and hydrogenation of MgO powder. It is particularly noted that the small signal intensities of hydroxyls over MgO_{hg} suggest the presence of a small coverage of defect sites on the MgO films.

5.3.3 Effects of MgO Film Thickness for MgO_{hydr}

Auger parameter analysis made it clear that there were negative ΔR of -0.1 and -0.2 eV, and positive $\Delta\varepsilon$ by $+0.3$ and $+0.6$ eV for 3 ML and 30 ML MgO films, respectively, upon hydroxylation (Tab. 5.1), from which several findings are obtained. First, it is noted that positive $\Delta\varepsilon$ means that the orbital energies were reduced upon hydroxylation. The hydroxylation-induced reduction of MgO surfaces is in agreement with a recent theoretical study, which found that the charge transfer from the hydroxyl groups to the MgO support occurs [168]. Second, the negative $\Delta\varepsilon$ observed for both the films suggests that the direction of charge transfer was independent of the film's thickness. Interestingly, the influences of surface hydroxyl groups on the film's electronic state were alleviated for the 3 ML MgO film by a factor of two, compared to the 30 ML MgO film. A convincing mechanism to explain the thickness dependence has not been determined, but there is a possible scheme driven by charge transfer. It is known that thin MgO films mediate the charge transfer between the metal substrate and adsorbates [22, 146, 169]. For gold adsorbed on the thin MgO film, this charge transfer is driven by the fact that Au 6s, the valence band of gold, lies below the Fermi edge of the metal substrates such as Mo(001), so that the gold atoms can be negatively charged. In the present, the opposite might happen to the hydroxylated 3 ML MgO film. A part of charge transferred from the hydroxyl groups to the thin MgO film is subsequently compensated by the Ag substrate, so that the extent of the reduction of 3 ML MgO is decreased compared to that of 30 ML MgO. The charge transfer from the MgO film to the Ag substrate could occur, because the empty states of Ag, 5s, is positioned far below that of the MgO film (the mixture of Mg 3s and O 3s, see Chapter 4) or even the valence band of MgO film (O 2p) [169], and the radius of Ag 5s is rather large ($\sim$1.2 Å). The combination of these two factors and the fact that Ag 5s is well interacted with O 2p orbital [170] might make the escape of electrons stored in the thin MgO film to the Ag substrate energetically favorable. This tunneling does not, of course, happen to 30 ML MgO_{hydr}, because of the short radius of Ag 5s. It is noted that the occurrence of the charge transfer to the Ag substrate is in agreement with a recent theoretical investigation of OH (not OH^-) adsorption on thin MgO films [146].

The stronger positive screening effect by a factor of 2 could be also explained in terms of the film thickness, but its origin has not been determined yet. The negative ΔR, by which the Mg 2s binding energy increases, means the hydroxylation-induced inferior screening efficiency. This is contrary to a simple expectation, where core hole screening is accelerated by the adsorption of electron donor species [76]. One possible explanation is the reduced polarizability of the film after hydroxylation. The reduction in the polarizability results in reduced screening, accompanied by negative binding energy shifts of oxide [47], but the present study does not aim to provide evidence on this issue.

5.4 Summary

An investigation concerning the hydroxylation of MgO films was comprehensively carried out using various methods. The 30 ML thick MgO(001) film was hydroxylated by exposure to 1×10^{-3} mbar D_2O with the ion gauge at a substrate temperature of 300 K. Its IRA spectrum indicates the formation of highly Lewis acidic hydroxyl groups as evidenced by its lower vibrational frequency ($\sim$2734 cm^{-1}), accompanied by a non-negligible amount of formate. Without the ion gauge, increasing the vapor pressure to 0.05 mbar produced the same amount of surface hydroxyls at a frequency of 2754 cm^{-1} on MgO(001), with a negligible amount of formate. Moderate reduction of the oxide due to electron-donor property of surface hydroxyls was present. This MgO film hydroxylated without the ion gauge was found to be relevant to hydroxylated MgO powder prepared under realistic conditions. The band bending occurred only for MgO_{hi}, not for MgO_{hydr}. Hydroxylation of MgO was tried by exposure to 100 mbar D_2 (MgO_{hg}), which resulted in the formation of surface hydroxyls at a coverage of 0.1 ML.

Auger analysis revealed that hydroxylating MgO films caused notable changes of the electronic structure of MgO films. No band bending occurred upon hydroxylation, unless the electron emission from an ion gauge was employed. There were sharp reduction of the outer orbitals' energies of the MgO films via chemical reduction by a partial charge transfer from the hydroxyls to MgO and orbital interaction. The thickness-dependent hydroxylation of MgO_{hydr} demonstrated that the electronic structure of the thicker MgO film was strongly modified compared to the thinner one, but the nature of chemical interaction remained the same. The charge transfer from the hydroxylated thin MgO film to the Ag substrate is proposed to be possible mechanisms to account for the alleviated changes of the electronic structure of the MgO film upon hydroxylation, compared to the 30 ML thick MgO film.

Chapter 6

Formation of Positively Charged Au Species on MgO Films

This chapter is devoted to detailing the interactions of Au with specific adsorption sites on the MgO(001)/Ag(001) surface. The surface properties, in particular the distribution of defects, were tuned by varying the MgO film thickness. IRAS using CO as a probe molecule was employed to determine the charge state of Au clusters. Positively charged and neutral Au clusters appeared after Au deposition at 100 K. The thermal behavior of Au clusters were monitored by means of CO-IRAS and XPS. These experimental data were corroborated with DFT calculations to reveal the origins of various kinds of gold-carbonyl species.

6.1 Introduction

Supported Au clusters have received much attention in the field of heterogeneous catalysis, since the pioneering work which reported high catalytic activity of supported Au particles for low-temperature CO oxidation [171]. However, a number of investigations attempting to explain and improve the activity of Au catalysts have not settled a long-standing debate on the nature of the active sites and states. One of the fundamental questions still remaining is the mechanism behind the changes in the reactivity, for example in CO oxidation, of the catalysts with respect to the Au oxidation state changes.

Information about the electronic properties of the catalysts should provide answers to this question. The electronic structure of supported metal particles can be probed by several different methods, such as x-ray photoelectron spectroscopy (XPS), x-ray absorption near edge spectroscopy (XANES) and x-ray emission spectroscopy (XES). These methods take advantage of electron excitation by photons. In contrast to these rather direct ways, vibrational spectroscopy is capable of an *indirect* determination of the oxidation state of metal using a probe molecule. The adsorption of CO as a probe molecule is frequently taken advantage of to extract electronic and geometric information of metal surfaces. Its extensive application to supported Au clusters in the last 20 years has allowed general conclusions to be drawn [99]. CO stretching

frequencies are found at 2100–2120 cm^{-1} for neutral Au particles, 2130–2180 cm^{-1} for positively charged Au particles and 2040–2080 cm^{-1} for negatively charged Au. The Hückel orbital theory for CO adsorbed on a metal surface, often called the Blyholder model, reasonably accounts for this trend as a function of Au oxidation state based on back-donation of electrons from the metal surface to the CO $2\pi^*$ orbital [98]. An exception to this trend was recently found for CO adsorbed on neutral Au atoms on the MgO(001) surface, which exhibit a stretching frequency of 1850 cm^{-1}, red-shifted by almost 300 cm^{-1} with respect to gas phase CO (2143cm^{-1}) [172]. This large red-shift is induced by a net charge transfer of one electron from the valence orbital of Au 6s to the CO $2\pi^*$ orbital, and is driven by the Pauli repulsion between the neutral Au atom's 6s electron and the closed shell oxygen ion in the oxide surface [173].

Tuning electronic properties of supported particles is often triggered externally [6]. Changing thin oxide film's thickness is one way to achieve this purpose. The electronic properties of metal particles supported on thin oxide films may be influenced by electron transfer through the film, polaronic distortion within the film, and electron polarization effects [174]. Recent examples for effects specifically related to the oxide film thickness are the observation of cationic Au atoms on the ultra-thin FeO(111)/Pt(111) film [175] and anionic Au on ultra-thin MgO(001)/Ag(001) films [172]. In addition to these effects, the nature and abundance of specific defects can critically affect the electronic states of supported metals [7, 123, 174, 176]. In some cases, the latter properties can also be controlled by variation of the oxide film thickness. Therefore, both the contributions ascribed to oxide film thickness and surface morphology must be considered for the supported model systems. The effects mentioned above are considered to be of particular significance for supported clusters containing only a few atoms, whereas their influence could quickly vanish with increasing particle size [177]. Thus, experimental studies to elucidate these effects requires the coverage of adsorbed metals to be kept at a very low level.

This work aims to provide a deeper insight into the initial interactions of gold atoms and clusters with intrinsic surface defects on MgO(001) by means of two spectroscopic methods (IRAS and XPS). MgO(001)/Ag(001) films were employed as a support, and the thickness of the films was varied to configure surface states. Much attention has been paid determining the origin of the observed blue-shift of CO adsorbed on as-deposited Au particles. The results show that a fraction of as-deposited Au at sub-monolayer coverages is cationic at 100 K. These positively charged Au-carbonyl clusters exhibited unusual thermal stability up to 250 K, followed by the formation of flat Au particles. The unexpected formation of cationic Au on MgO indicates a strong interaction of the supported gold with surface defects. Corroborative DFT calculations were carried out to identify the local configuration responsible for the formation of cationic gold species. Since the determination of oxidation states by XPS is not unambiguous, Auger parameter analysis was additionally applied to ascertain the charge states of Au (Section 2.2.7), whose results are presented in Appendix C.

6.2 Results and Discussion

6.2.1 Au Coverage Dependence on Thick MgO Films

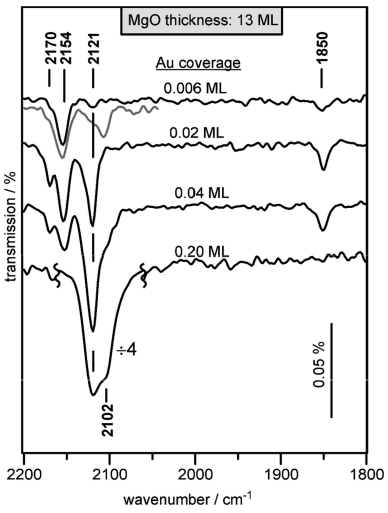

Figure 6.1: IRA spectra of adsorbed CO of Au (0.006–0.20 ML, corresponding to 0.015–0.5 Å) deposited at 90 K on 13 ML thick MgO(001) films. The gray spectrum was taken using a mixture of 67 % ^{12}CO and 33 % ^{13}CO.

The nucleation of gold (0.006–0.20 ML, corresponding to 0.015–0.5 Å) deposited onto 13 ML MgO films at 90 K was studied using CO-IRAS. IRA spectra of CO adsorbed on the Au particles at 90 K were collected (Fig. 6.1). At the lowest Au coverage, 0.006 ML, a band at 2154 cm^{-1} appeared, accompanied by a shoulder at 2170 cm^{-1} and two additional small signals at 2121 cm^{-1} and 1850 cm^{-1}. The gray trace in Fig. 6.1 is the CO-IRAS spectrum of 0.006 ML Au on 13 ML thick MgO films exposed to a ^{12}CO/^{13}CO isotope mixture with a ratio of 2:1. Only one component at 2107 cm^{-1} developed in addition to that at 2154 cm^{-1}. The absence of multiple new bands is evidence for the presence of only mono Au-carbonyl complexes. As the Au coverage was increased to 0.02 ML, all the components developed in intensity. At this coverage, the band at 2170 cm^{-1} was clearly resolved and the signals at 2154 and 2121 cm^{-1} exhibited a similar intensity. For 0.04 ML Au, the bands at 2150–2170 cm^{-1} reduced in intensity, while the one at 2121 cm^{-1} gained intensity. Note that the intensity of the signal at 1850 cm^{-1} reached saturation. At the largest Au coverage of 0.20 ML, the component at 2121 cm^{-1} became the most intense absorption band, accompanied by a shoulder on the lower frequency side, 2102 cm^{-1}. The signal contributions at 2154, 2170 and 1850 cm^{-1} disappeared at this high Au coverage.

The CO bands with frequencies of 2121, 2102 and 1850 cm^{-1} are known from previous studies of Au/MgO(001) systems. The band at 1850 cm^{-1} can be assigned to CO bound to neutral Au atoms adsorbed on the MgO surface [100]. The other two bands are typical for CO adsorption on very small neutral or positively charged Au clusters (2121 cm^{-1}) [5, 178], and on large, neutral Au particles (2102 cm^{-1}) [175]. The bands observed at 2154 cm^{-1} and

2170 cm^{-1} are typical for CO adsorbed on positively charged Au particles [99]. However, CO adsorbed on the low-coordinated cations on the MgO(001) surface can give rise to a band in the same frequency region [179–181]. This exceptionally high vibrational frequency for CO on an oxide surface is due to the wall effect [97]. Since the adsorption energy of CO on the MgO(001) surface is rather small, the origin of the bands at 2154 cm^{-1} and 2170 cm^{-1} can be determined by studying the thermal stability of adsorbed CO, which is presented in Section 6.2.2.

6.2.2 Thermal Stability of Au-Carbonyl Clusters and Au Sintering

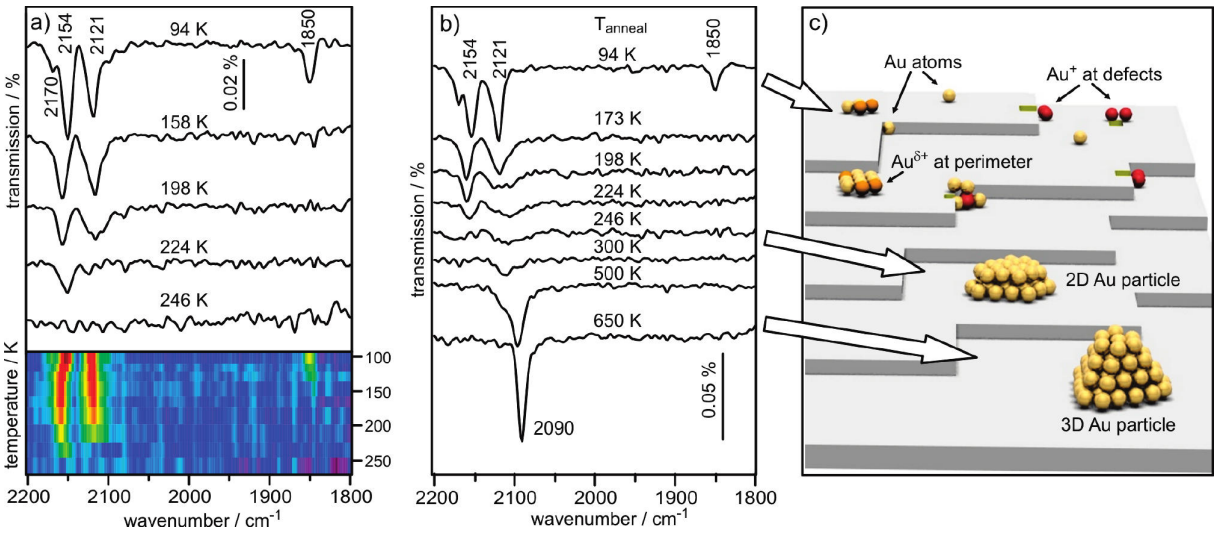

Figure 6.2: a) IRA spectra of CO on 0.02 ML (0.1 Å) Au on 13 ML MgO(001) films taken at the indicated temperatures. Au deposition and CO dosing were carried out at 110 K. All data was collected after annealing to the indicated temperatures without any CO exposure. b) TP-IRA spectra of CO adsorbed on 0.02 ML Au on the MgO films, after Au deposition and exposure to CO at 110 K. All the spectra were collected after annealing to the indicated temperatures. c) Models of the species and progress of Au agglomeration deduced from the IRA spectra shown in the panel b).

The thermal stability of the bands at 2170, 2154, 2120 and 1850 cm^{-1} was investigated by means of temperature dependent infrared spectroscopy. Fig. 6.2a shows selected IRA spectra of CO adsorbed on 0.02 ML (0.1 Å) Au on 13-ML thick MgO(001) films as a function of temperature, where CO was initially adsorbed onto the Au particles at 90 K, and infrared spectra at elevated temperatures were subsequently acquired without additional exposure to CO. To show the data in a more graphical manner, an image plot is provided which includes data taken at all annealing temperatures (typically in steps of 15 K) of this study. Initially, CO adsorption on the Au particles gave rise to IR bands at 2170, 2154, 2121, and 1850 cm^{-1} at 94 K. Annealing the sample to 140 K induced a substantial decrease in intensity of the band at 1850 cm^{-1} in agreement with a previous study [172]. The CO absorption signal at 2121 cm^{-1} is thermally more stable and disappeared only after heating to 220 K. The two signals at 2170

and 2154 cm^{-1} converged into a single band at a frequency of 2160 cm^{-1} after heating to 120 K, which was stable up to 240 K. The observed thermal stability of the CO band corroborates the assignment of this signal to CO adsorbed on positively charged Au clusters, since CO adsorbed on the MgO(001) support desorbs at much lower temperatures [181]. It is notable that the 2120 cm^{-1} component disappeared at 220 K, considerably higher than the typical desorption temperature for CO adsorbed on regular Au clusters on MgO (∼150 K) [178]. The rather high thermal stability is in line with an interpretation of CO adsorption on very small Au clusters or at Au-MgO perimeter sites, where the Au atoms are present in low-coordination environment. Combining the results presented in Fig. 6.1 and Fig. 6.2a leads to the conclusion that the initial nucleation of Au on the surface of the MgO(001) film at 90 K occurs at sites that give rise to positively charged Au species. These sites are almost completely occupied at the smallest Au coverage studied here. Therefore, their abundance is estimated to be below 0.5 % ML. As the coverage is increased, single Au atoms (1850 cm^{-1}) and small Au clusters (2121 cm^{-1}) are stabilized on the surface, and finally, large metallic gold particles (2102 cm^{-1}) are formed.

The IRA spectra shown in Fig. 6.2a reflect the dynamic processes occurring on the surface. These spectra could fail to observe some agglomerated Au species, because the agglomeration process could lead to CO desorption, and afterward there might be no adsorbed CO remaining on the Au particles. In order to understand the thermal-induced nucleation of Au particles in more detail, IRA spectra of CO adsorbed on 0.02 ML Au/MgO(001) were collected after annealing to 173–650 K with subsequent dosing of CO at 94 K after each individual annealing step (Fig. 6.2b). After annealing to 173 K, the band at 1850 cm^{-1}, corresponding to CO adsorbed on neutral Au atoms, as well as the band at 2170 cm^{-1} were not observed. This thermal treatment caused also a broadening of the band at 2121 cm^{-1} with a simultaneous decrease in intensity as well as a slight decrease of the intensity of the high-frequency bands (2160 cm^{-1}). The intensity of these bands continued to decrease until 246 K, at which temperature the IR band at 2154 cm^{-1} disappeared. It is interesting to note that up to an annealing temperature of 200 K the spectra in Fig. 6.2a and Fig. 6.2b share almost identical nature, suggesting that the spectral changes observed at temperatures between 100 K and 200 K can primarily be ascribed to morphological changes caused by thermally-induced diffusion and agglomeration. Upon annealing to 300 K only a very weak CO signal at 2110 cm^{-1} remained. After annealing the Au/MgO(001) system above 500 K, an absorption band at 2090 cm^{-1} appeared, indicative of CO adsorbed on well-faceted 3D Au particles.

The results presented in Fig. 6.2b allow drawing general conclusions about the nucleation and sintering behavior of Au on the MgO(001) surface (Fig. 6.2c). Initially, several different Au species are formed upon deposition of Au at 90 K, which can be distinguished according to distinct stretching frequencies of adsorbed CO. These include neutral Au atoms (1850 cm^{-1}), small Au clusters (2121 cm^{-1}) and positively charged Au species (2150–2170 cm^{-1}). The preferential disappearance of the band at 1850 cm^{-1} after annealing to 170 K means that the thermal stability of neutral Au atoms is the lowest among the initially formed species. Note that single, neutral Au atoms are stabilized on the surface mainly via electrostatic interactions with

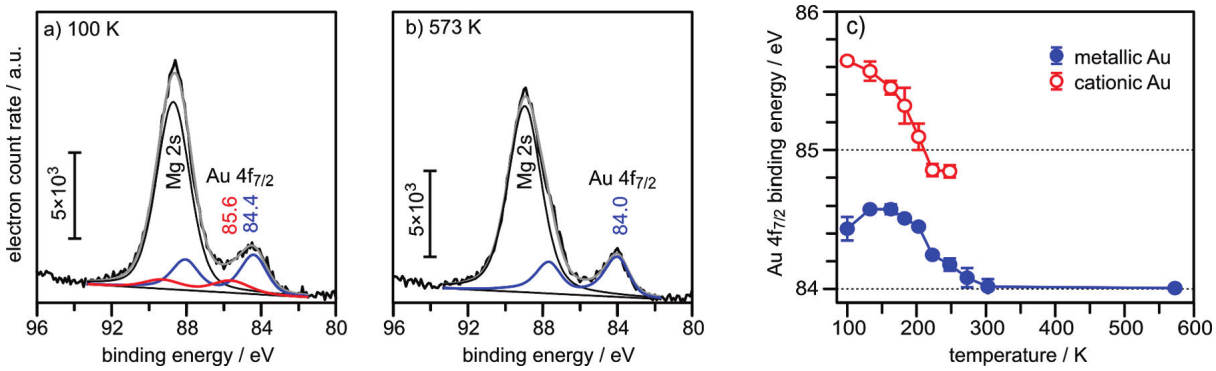

Figure 6.3: O 1s XP spectra of 0.02 ML Au/MgO/Ag(001) film at 100 K a) and of the same sample upon annealing to 573 K b). c) Binding energies of the Au $4f_{7/2}$ components as a function of annealing temperature after initial deposition of 0.02 ML Au at 100 K.

the pristine MgO(001) surface [173]. Therefore, it is not surprising that this weak interaction leads to the disappearance of the signal at 1850 cm^{-1} at as low as 170 K, most likely because of diffusion-induced agglomeration. The positively charged Au species giving rise to a signal at 2150–2175 cm^{-1} showed superior thermal resistance (∼240 K), probably because they were formed and trapped at energetically favored sites (defects).

In the temperature range of 246–300 K, the only signal observed was a weak band at 2110 cm^{-1}, which can be ascribed to CO adsorption on flat Au particles with a height of 2–3 MLs [84]. CO adsorbs on these particles preferentially at the perimeter sites with an expected adsorption angle, and dynamic dipole, oriented almost parallel to the surface [182,183]. The surface selection rule accounts for the low absorption intensity of this signal. If the thermal energy input is large enough (> 300 K), the flat gold clusters were transformed into hemispherical gold particles, which gave rise to the typical frequency of adsorbed CO at around 2100 cm^{-1}.

XPS analysis of the electronic structures of gold for 0.02 ML Au on 13 ML thick MgO films corroborates the infrared data. Fig. 6.3 shows the XP spectra in the region of Au 4f and Mg 2p, for the as-deposited 0.02 ML Au/MgO sample. Since the Mg 2p and Au 4f electron emission partly overlap in energy, the inclusion of Mg 2p component and careful peak fitting were required to extract the individual Au 4f components. In the fitting, the spin orbit coupling of Au 4f was set to 3.67 eV, and the intensity ratio was set to the theoretical value of 3:4. Parameters for the Mg 2p component were extracted from fits of XP spectra taken from a clean MgO(001) film. The XPS analysis revealed that the freshly prepared Au/MgO sample (Au deposition at 90 K) contains two Au species with Au $4f_{7/2}$ binding energies of 85.6 and 84.4 eV, respectively, which were shifted by 1.6 eV and 0.4 eV to higher binding energies relative to the bulk Au reference (84.0 eV) [72]. Referring to the infrared data, the high binding energy component can be ascribed to positively charged Au, and the other one is attributed to neutral Au species. The measured temperature dependence of these components provides an additional proof of this assignment (Fig. 6.3c). In the temperature range of 100–300 K, the Au $4f_{7/2}$ binding energy of the neutral Au species decreased gradually from 84.4 to 84.0 eV. The higher binding energy

signal dropped in intensity and its binding energy decreased rapidly, until it finally disappeared at 250 K. This disappearance is in agreement with the agglomeration-induced loss of the CO-IR signal due to positively charged Au observed in the temperature-dependent IRAS experiment (Fig. 6.2a). At 573 K, there was a single gold species with an Au $4f_{7/2}$ binding energy of 84.0 eV, suggesting the sintering-induced formation of large metallic Au particles.

The observed sintering behavior follows the general trends expected for supported metal particles. However, the observation of positively charged Au species raises some questions about which type of nucleation centers are present on the surface of the MgO thin films. Previous surface science work about Au nucleation on transition metal-oxide and rare-earth metal-oxides such Fe_3O_4 or CeO_2 found indications for the presence of positively charged Au species on these surfaces during the initial nucleation stage [184,185]. While the formation of positively charged Au on these rare-earth oxides can be explained by the redox interaction between the supports and admetals, the observation of positively charged gold on the non-reducible MgO support is hardly accounted for by the same mechanism. Instead, the interaction of Au with particular defects present on the surface of MgO thin films seems to be more likely, as shown further below.

6.2.3 Morphological Aspects

From the results shown in Fig. 6.1 it was deduced that the maximum amount of positively charged Au on the surface of thick MgO films is about 0.5 %. Since the type and abundance of defects on MgO thin films, which lead to the formation of positively charged gold, could vary with MgO film's thickness, the influences of film thickness on the initial interaction of Au with various thick MgO films were clarified via infrared spectroscopy.

Fig. 6.4 displays IR spectra of CO adsorbed on 0.02 ML of Au deposited onto MgO films of different thicknesses (4–28 ML) at 110 K. On the thinnest MgO films (4 ML), positively charged Au giving rise to the CO band at 2154 cm^{-1} was the main species present on the surface, as well as small neutral Au clusters (2121 cm^{-1}). No signal corresponding to CO adsorption on neutral single Au atoms (1850 cm^{-1}) was observed. Furthermore, the CO absorption peak at 2170 cm^{-1} was completely absent. As the MgO film thickness was increased from 4 to 28 ML, the signal for CO molecules adsorbed on small Au clusters (2121 cm^{-1}) and the one relating to neutral Au atoms at 1850 cm^{-1} gained intensity. Characteristic changes were also observed in the spectral region, where CO adsorbed on positively charged Au appears. The signal at 2154 cm^{-1} decreased in intensity, while the band at 2170 cm^{-1} gained intensity. This film thickness dependence provides hints about the type of defects involved in the formation of cationic gold species, as further detailed in Section 6.3.

It should be mentioned that according to previous theoretical and experimental studies, Au atoms adsorbed on ultra-thin MgO films are expected to be negatively charged [169,186]. The IRAS data presented here do not provide evidence for CO adsorption on $Au^{\delta-}$, which is explained by a small adsorption energy of CO bound to negatively charged Au atoms [183,187]. Thus, no observable infrared signals, corresponding to CO adsorbed on anionic gold, appeared at 90 K.

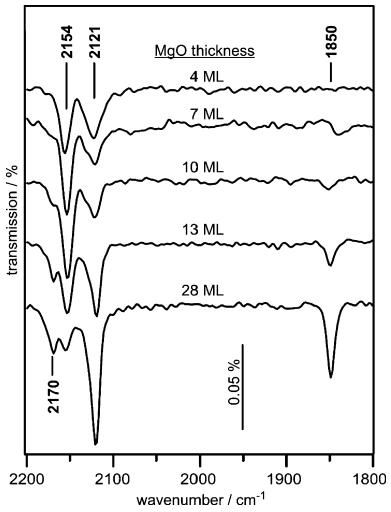

Figure 6.4: IRA spectra of adsorbed CO on 0.02 ML (0.1 Å) of Au deposited on MgO(001) films of different thicknesses (4–28 ML) at 110 K after exposure to CO at 110 K.

The fact that the IRA spectrum of CO adsorbed on Au deposited on 4 ML MgO(001)/Ag(001) lacked the signal of neutral Au atoms provides, however, an indirect support for the presence of anionic Au atoms on this surface.

6.2.4 DFT Calculations for Free $[Au_nCO]^+$ and Supported $[Au_nCO]$ Complexes

The vibrational frequencies and most stable conformations of positively charged Au-carbonyl gas-phase clusters, those supported on MgO surfaces without defects, and neutral Au-carbonyl complexes adsorbed on various sites such as F^{2+} centers on MgO were elucidated by DFT calculations using the B3LYP hybrid functional [188, 189]. The vibrational frequency shifts of the gas-phase $[Au_nCO]^+$ complexes relative to gas-phase CO (2143 cm^{-1}) were calculated as: $n = 1$ ($\Delta\nu = +99$ cm^{-1}), $n = 2$ ($\Delta\nu = +72$ cm^{-1}), $n = 3$ ($\Delta\nu = +57$ cm^{-1}) and $n = 4$ ($\Delta\nu = -4$ or $+2$ cm^{-1} for two different configurations). In line with a previous study [190], the CO stretching frequencies of positively charged $[Au_nCO]$ clusters exhibited considerable blue shifts unless the number of Au atoms per cluster exceeded three. This theoretical conclusion is also supported by experiments, reporting that CO molecules adsorbed on gas-phase Au_5^+–Au_8^+ have vibrational frequencies of 2150–2160 cm^{-1}, blue-shifted with respect to gas-phase CO [191].

The contribution of MgO supports on the CO vibrational frequencies for positively charged Au-carbonyl complexes was studied next. The upper panel of Fig. 6.5 summarizes the stable adsorption geometries and the corresponding vibrational frequency shifts relative to gas-phase CO of the $[AuCO]^+$ complexes supported on various sites of MgO surfaces without charged defects. Only the complexes supported on terrace and edge sites exhibited notable blue-shifts of 60–10 cm^{-1}. In contrast, the interactions of the $[AuCO]^+$ complex with hydroxyls and anionic defects caused notable red-shifts [189].

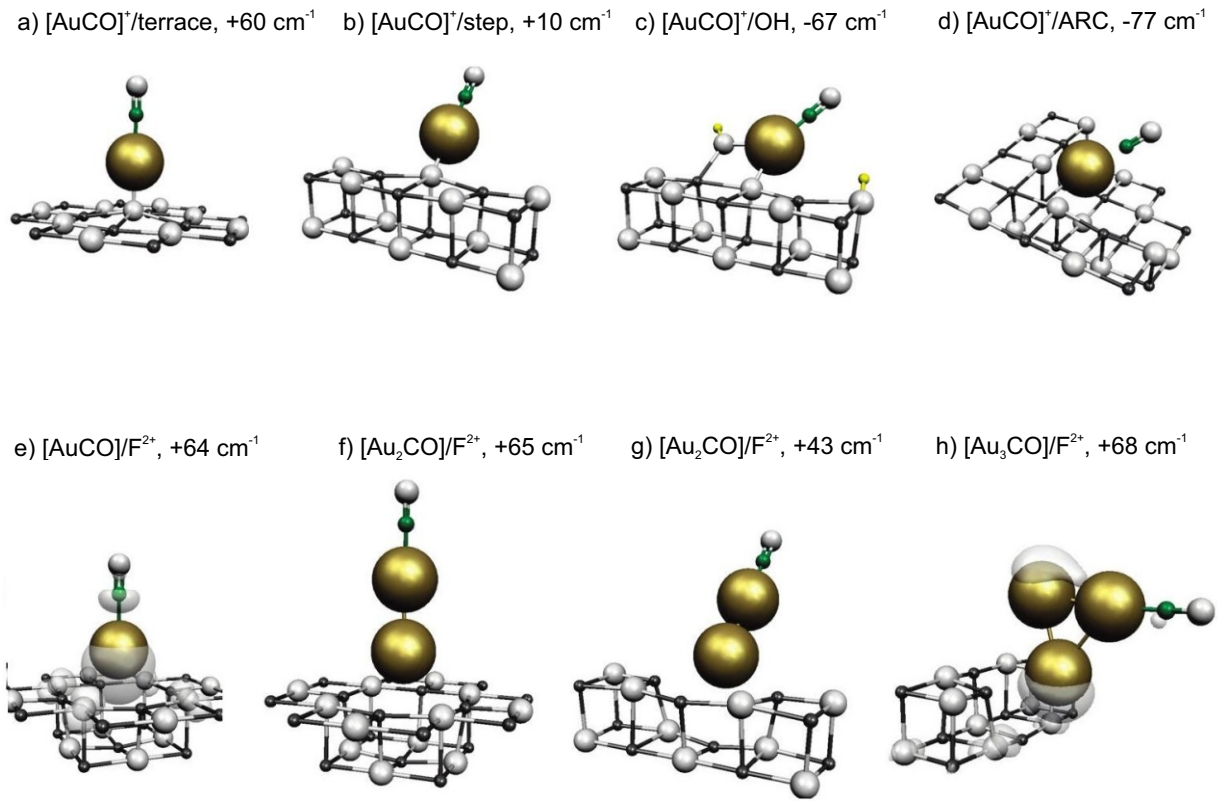

Figure 6.5: Equilibrium states and the vibrational frequency shifts of CO with reference to the gas-phase CO for $[AuCO]^+$ clusters supported on a) a terrace oxygen, b) an edge oxygen, c) an edge oxygen neighbor upon a hydroxyl group, and d) an anionic reverse center (ARC) of MgO surfaces. In the lower panel, neutral Au_n-carbonyl complexes supported on e) and f) a terrace F^{2+} center, g) and h) an edge F^{2+} center of MgO surfaces, according to DFT calculations.

Since the present study did not ionize the Au atoms before the deposition, Au clusters were expected to be neutral prior to their contact to the surfaces. Additionally, the above mentioned results suggest that the observed blue-shifts of the CO molecules are highly due to the interaction of *neutral* Au-carbonyl clusters with specific adsorption sites. The DFT calculations identified some adsorption sites for Au atoms and clusters, which give rise to positive frequency shifts, and their conformation and CO frequency shift relative to the gas-phase CO are summarized in the lower panel in Fig. 6.5. Neither F^0 centers nor pristine step or terrace sites of the MgO surface was found to be responsible for the blue-shifts. Only the neutral small Au-carbonyl clusters adsorbed onto F^{2+} centers on terrace or edge sites were found to contribute to notable blue-shifts of 68–43 cm^{-1} for the adsorbed CO molecules. The bond strength, D_e, of CO was calculated as ∼0.2 eV for the $[Au_1CO]$ complex adsorbed on F^{2+}. This relatively low stability improved by a factor of 6, $D_e \sim 1.2$ eV, if the number of Au atoms constituting the carbonyl-complex increased to 2 or 3. This energetically favored adsorption of the complexes and their vibrational frequencies showed good agreement with the experimental observation.

6.3 Discussion

6.3.1 Origins of the Positively Charged Au on MgO Surfaces

The DFT study found that the positive charge on the small Au clusters (n=1–5) causes blue-shifts of the CO stretching frequency relative to gas-phase CO [190]. A recent theoretical work on gas-phase Au-carbonyl clusters clarified two major contributions leading to either red or blue shift of the CO vibrational frequency as a function of charge states of a gold atom: the electric field induced by the charged particles, called the Stark effect, and π back donation [177]. They concluded that the other contributions are insufficient to induce any notable blue-shifts in the CO vibrational frequency of Au-carbonyl clusters, unless direct charge transfer is involved [187].

In the current study, the interaction of Au-carbonyl clusters with the MgO support was additionally considered. The present DFT calculations proposed that the following adsorption complexes could give rise to blue-shifts in the CO frequency as observed in the IRAS experiments; $[Au_{1-3}CO]^+$ at terrace sites, and $[Au_{1-3}CO]/F^{2+}$ centers located at edge or terrace sites (Fig. 6.5) [189]. Essentially, only the F^{2+} centers located at edge or terrace sites are responsible for the formation of the cationic $[Au_{1-3}CO]$ (Fig. 6.5). The driving force for these adsorption-induced chemical states is ascribed to the significant reduction of gold's ionic potential (IP). The IP is 9.42 eV for bulk metallic Au, however, for Au atoms at edge or anionic sites the IP is reduced to 4.82 and 2.32 eV, respectively. This is even valid for small Au clusters; MgO-supported Au_3 has an IP of 3.46 eV, which is only 50 % of that of the gas-phase Au_3, 7.26 eV [192]. This means that the formation of cationic Au on MgO surfaces could be thermodynamically favorable if strong electron trapping sites are present. In line with electron trapping sites, it has been shown that electrons can be trapped at grain boundaries over MgO particles [193] or on MgO films [194]. Indeed, the lattice mismatch between Ag and MgO results in the formation of misfit dislocations to compensate for the lattice strain already at the early stages of MgO film growth. As the films grow, the tilt angle of the mosaic decreases significantly with increasing film thickness [128]. In other words, the density of this kind of electron-traps drops as the film thickness increases. This tendency allows the infrared absorption at 2154 cm^{-1} to be assigned or strongly related to Au-carbonyl complexes trapped at the grain boundaries.

By a process of elimination, the Au-carbonyl signal at 2170 cm^{-1} is ascribed to resulting from positively charged gold formed by Au nucleated at point defects such as F^{2+} centers. This species developed when the nominal oxide film thickness is more than 10 ML. This could be accounted for by the fact that the defects responsible for this feature are thermodynamically unfavorable on very thin films. Indeed, spectroscopic studies revealed that F^{2+} centers present on thin oxide films get easily reduced by the metal substrate [132, 195]. Recently, experimental evidence for the presence of F^{2+} centers on thin MgO(001) films was demonstrated [123]. Interestingly, the authors noticed the very limited abundance of F^{2+} centers ($\sim$5 % of all defects), reflecting their low stability. If this mechanism dominantly accounts for F^{2+} defect density on MgO(001) film surfaces, the formation of positively charged Au-carbonyl should be favored on thicker MgO films. This scenario agrees with the observation made earlier (see Fig. 6.4), where the signal at

2170 cm^{-1} was found to gain intensity with increasing MgO film thickness.

It is worth noting that the deposition of Mg on MgO films leads to spontaneous oxidation of Mg and trapped electrons at surface defects [196]. The depletion of defects by Mg deposition resulted in the disappearance of the IR band at 2170 cm^{-1} upon deposition (see Appendix A), suggesting a similar role of the underlying defect sites in the activation of Mg and Au.

Finally, some discussion about the differences in the experimentally determined and computed stability of the Au-carbonyl clusters is necessary. The positively charged Au clusters giving rise to the CO signals at 2154 or 2170 cm^{-1} were found to exhibit high thermal stability; they were stable up to 240 K (Fig. 6.2a). The corresponding decomposition energy computed by the Redhead equation is 0.5–0.6 eV, using a general frequency factor of 10^{13} s^{-1} [106]. This bond dissociation energy is, however, much lower than what is calculated for $[AuCO]^+$ clusters (∼2 eV) [189]. Thus, the CO desorption temperature observed via infrared, ∼240 K, seems not to reflect the pure decomposition of $[Au_nCO]^+$ complexes. This difference could be attributed to CO desorption induced by Au cluster aggregation. Indeed, the diffusion barrier of $[AuCO]^+$ is estimated to be 0.6 eV. Therefore, by raising the temperature, $[AuCO]^+$ diffusion will occur and eventually lead to forming larger clusters [192]. CO is much more weakly bound on the larger clusters and thus desorb upon their formation.

6.4 Conclusions

This study has provided information on the initial interactions of atomically dispersed Au on MgO(001) films with various thicknesses. The infrared absorption spectra of CO consisted of bands corresponding to positively charged Au-carbonyl clusters at 100 K on thin and thick MgO/Ag(001) films, accompanied by components corresponding to CO on flat Au clusters as well as neutral Au atoms. The positively charged Au-carbonyl species were found to be stable up to ∼240 K. It was found that altering the surface defect concentration by changing the film thickness could be used to adjust the type and abundance of cationic Au-carbonyl species. With the help of DFT calculations the formation of cationic Au species on MgO was attributed to (i) defect sites such as F^{2+} centers, and (ii) grain boundaries leading to the spontaneous formation of Au^+ or positively charged Au clusters.

Chapter 7

Interactions of Au and Pd with Active Hydroxyls on MgO(001)

This chapter describes a study related to the interactions of metals (Au, Pd) with active surface hydroxyls on MgO_{hi} (see Chapter 5), using XPS, IRAS and TPD in collaboration with STM observations. On the surface of MgO_{hi}, there was a strong interaction between the metals and the hydroxyl groups, which resulted in the formation of oxidized species such as Pd^{4+} and Au^{+}.

7.1 Introduction

It is known that the chemical properties of hydroxyls on oxide surfaces strongly depend on the coordination and chemical environment of the corresponding anchoring sites [165, 197]. The partial charge on the oxygen determines the hydroxyls acidity or basicity, which in turn affects its chemical affinity to adsorbates. Previous studies have shown that the adhesion of metals to oxide surfaces can strongly be affected by the presence of hydroxyl groups. For instance, hydroxyl groups located on the bridging oxygen rows on rutile-TiO_2(110) have been shown to weaken the interaction of the surface to Au atoms and clusters, which results in an enhanced agglomeration and sintering into larger particles as compared to Au deposited on stoichiometric or slightly reduced TiO_2(110) surfaces [51, 58]. On the other hand, calculations have predicted that the interaction of Au with terminal hydroxyls located on the Ti^{4+} rows is strongly enhanced and even leads to partial oxidation of the Au atoms and clusters [57]. Early experimental studies on Rh deposited on non-hydroxylated and hydroxylated alumina thin films have also shown that the hydroxyl groups formed on this surface lead to enhanced binding of the metal particles to the substrate, whereas the opposite trend was predicted from theoretical studies on the adhesion of Pd clusters on dehydrated γ-alumina (100) and hydroxylated γ-alumina (110) surfaces [198].

As detailed in Chapter 5, by exposing the MgO surfaces to water vapor with the filament of an ion gauge either on or off during the hydroxylation, the present work provides two different hydroxylated MgO surfaces, MgO_{hi} and MgO_{hydr}. While the hydroxyl coverage is comparable for the two surfaces ($\sim$0.6 ML), the chemical properties of the hydroxyls are expected to be different,

as evidenced by their different stretching frequencies. The frequency of surface hydroxyl groups on MgO_{hi} is red-shifted to those on MgO_{hydr}, indicating a higher Lewis acidity, and, hence, a superior oxidizing character. This situation, where different hydroxyl species are individually created without changing the supports, provides us with the opportunity to closely investigate the interaction of metals with different hydroxyl groups on MgO (using MgO_{hi} and MgO_{hydr} as supports). The results for MgO_{hydr} will in more detail be presented in Chapter 8. In short, both Au and Pd interact only weakly with MgO_{hydr} at room temperature. At elevated temperatures, Pd is found to interact with the hydroxyls on the MgO_{hydr} surfaces via a redox-process leading to the evolution of hydrogen with simultaneous oxidation of Pd. In addition, evidence for the water-gas shift-type interactions between hydroxyls located at the periphery of the Pd particles and CO adsorbed on the Pd particles will be provided.

In this chapter, a comparative XPS, IRAS and CO-TPD study about the interactions of Au and Pd with MgO_{hi} surfaces is presented. The results indicate that both metals become oxidized (formation of Pd^{4+} and Au^{+} species) by the hydroxyls on MgO_{hi}. In particular, studies of the thermal stability of metals show that surface hydroxyl groups on MgO_{hi} act to enhance the stability of supported metals toward thermal sintering.

7.2 Results

7.2.1 Differences in the Reactivity of Metals with Reactive Hydroxyls

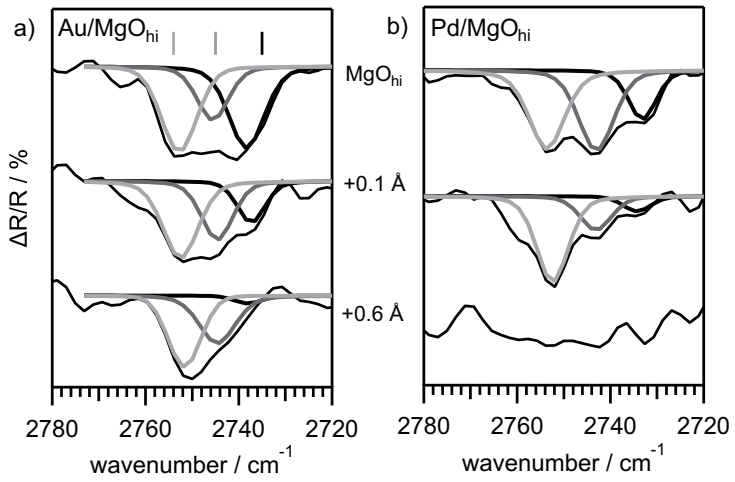

Figure 7.1: IRA spectra in the OD stretching region acquired from the MgO_{hi} surface before and after the deposition of Au or Pd at the indicated coverages. The deposition and data acquisition were done at room temperature.

The interaction of Au and Pd with the surface hydroxyl groups on the MgO_{hi} surface was studied with IRAS by monitoring the changes in the hydroxyl (OD) stretching region at ∼2750 cm^{-1} upon deposition of the metals at room temperature (Fig. 7.1). The OD-IRAS spectrum of the freshly hydroxylated MgO_{hi} surface exhibited signal contributions at 2735, 2745 and 2753

cm^{-1}. Deposition of 0.1 Å Au led to a reduction of the signal intensity of the band at 2735 cm^{-1} (Fig. 7.1a, middle). Further deposition of 0.5 Å Au completed the selective annihilation of this surface OD groups, while the other OD components remained unaffected (Fig. 7.1a, bottom). In the case of the low coverage Pd deposition, a similar preferential depletion of hydroxyls on the lower frequency side was observed (0.1 Å Pd, Fig. 7.1b, middle). But different to gold deposition, all hydroxyls were non-selectively depleted after depositing 0.6 Å Pd (Fig. 7.1b, bottom). It is noted that the present result for Pd deposition on MgO_{hi} is quite comparable to what has been observed for Rh and Co deposited on hydroxylated alumina surfaces [47, 49].

7.2.2 Interactions of Au with MgO_{hi}

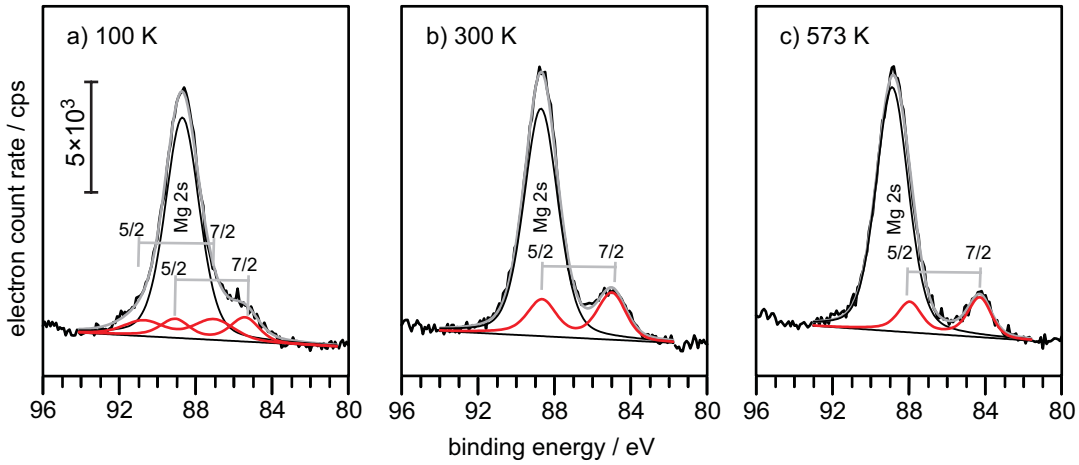

Figure 7.2: XP spectra in the region of Au 4f and Mg 2s for a) 0.1 Å Au deposited onto 13 ML MgO_{hi} at 100 K, and the same sample upon annealing to b) 300 K, and c) 573 K.

The selective depletion of the hydroxyl groups at 2735 cm^{-1} by Au deposition observed with IRAS (Fig. 7.1a) posed a question about the dimension of the interaction between Au and hydroxyls, which should be reflected in the Au electronic structure. To answer this, an Au 4f XP spectrum was collected from 0.1 Å Au deposited onto 13 ML MgO_{hi} at 100 K (Fig. 7.2a). The Mg 2p and Au 4f orbitals overlap in energy, so that careful inclusion of the Mg 2p component was required to obtain a consistent fit. The spin-orbit coupling constant of Au 4f was set to 3.67 eV, and the intensity ratio of Au $4f_{5/2}$ to Au $4f_{7/2}$ was set to 3:4, its theoretical value [72]. A reasonable fit result was obtained for the freshly prepared Au/MgO system only when two Au components were used. The Au $4f_{7/2}$ binding energies of the two components were found at 84.7 and 86.2 eV, shifted by +0.7 and +2.2 eV compared to the bulk gold reference (84.0 eV) [72]. After annealing to 300 K, only one Au component with an Au $4f_{7/2}$ binding energy of 84.5 eV remained (Fig. 7.2b). This single species ended up having the binding energy of 84.3 eV after annealing to 573 K, as shown in Fig. 7.2c. It is noted that the 84.3 eV for 0.1 Å Au on MgO_{hi} is 0.3 eV higher in binding energy than the value recorded for the corresponding annealed Au/MgO(001) sample (Chapter 6). The gold deposition caused a positive binding

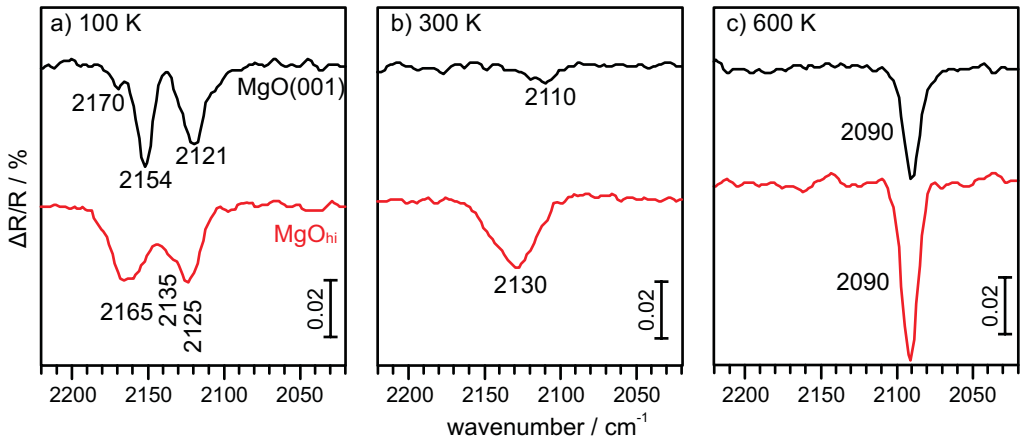

Figure 7.3: IRA spectra of adsorbed CO for 0.1 Å Au deposited at 100 K onto 13 ML MgO films (top , black) and MgO_{hi} (bottom, red) as a function of annealing temperatures to a) 100 K, b) 300 K and c) 573 K. The spectra were taken at 100 K after exposure to 1 L CO at 100 K.

energy shift of the O 1s signals relating to the oxide by 0.2–0.3 eV, arising from the oxide (data not shown). Interestingly, the O 1s signal was oppositely shifted for gold deposition onto the MgO(001) substrate (Appendix C) and MgO_{hydr} (Section 8.2.4), where "negative" O 1s binding energy shifts by 0.3–0.4 eV were observed. As discussed later, this contrasting behavior can be explained in terms of the opposite direction of charge flow [133].

As noted in Section 2.2, core-level binding energy shifts can originate from several, often counterbalancing effects. This leaves some ambiguity in the interpretation of these data if they are not backed up by additional evidence. In addition to XPS, infrared spectroscopy using CO as a probe molecule was employed in the present study to obtain information about the electronic and geometric structure of Au deposited onto differently prepared MgO surfaces. IRA spectra were collected at a substrate temperature of 100 K with 1 L CO exposure at 100 K for the following surfaces: 0.1 Å Au deposited onto MgO(001) (top, black) and MgO_{hi} (bottom, red) in Fig. 7.3. For CO adsorbed on as-deposited Au on the pristine MgO films (black spectrum, Fig. 7.3a) three absorption bands were observed at 2121, 2154 and 2170 cm^{-1}, which are assigned to CO adsorbed on small neutral Au particles (2121 cm^{-1}) and positively charged Au clusters (2154 and 2170 cm^{-1}), respectively (see Chapter 6). After annealing this sample to room temperature and subsequent re-exposure to CO at 100 K, a faint CO component at 2110 cm^{-1} appeared (black spectrum, Fig. 7.3b). This band is ascribed to CO adsorption on two-dimensional flat gold particles. After 573 K annealing, a sharp absorption band at 2090 cm^{-1} was observed, characteristic of CO on well-faceted Au particles (black spectrum, Fig. 7.3c). In the case of employing MgO_{hi} as the substrate (red spectra, Fig. 7.3), an increased population of positively charged Au-carbonyl species at 2165 cm^{-1} was found after CO adsorption onto the freshly prepared sample at 100 K (Fig. 7.3a). It should be noted that the component at 2120 cm^{-1} was accompanied by a shoulder at 2135 cm^{-1}. Annealing this sample to 300 K produced a pronounced but broad absorption band centered at 2130 cm^{-1} (Fig. 7.3b), which, in contrast to

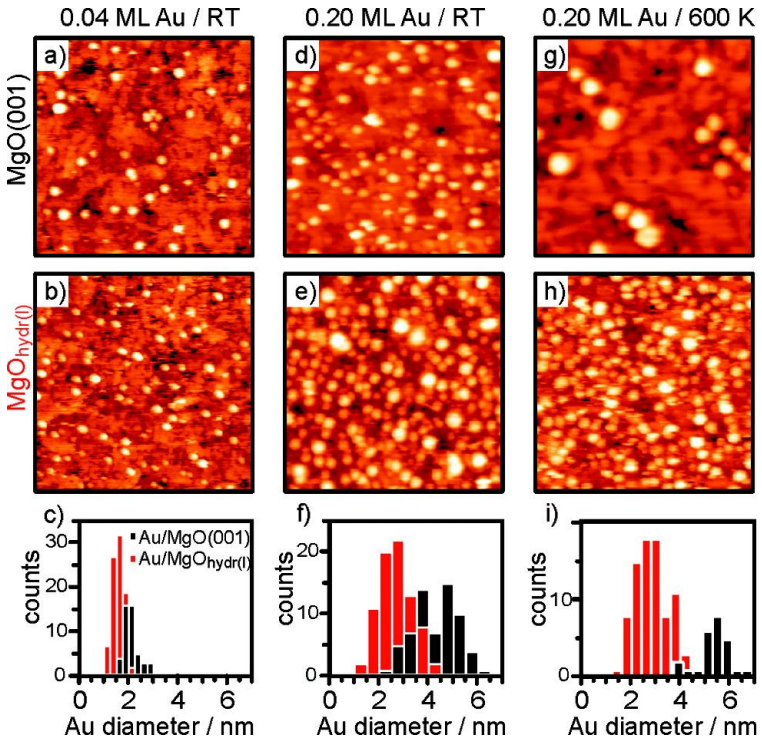

Figure 7.4: STM images (50 nm × 50 nm) of 0.04 (0.2 Å) and 0.20 (1.0 Å) ML Au deposited at room temperature on pristine (a, d) and hydroxylated (b, e) surfaces of 10 ML thick MgO(001)/Mo(001) films, and the 0.2 ML Au samples after annealing to 600 K (g, h). The hydroxylated MgO in panels b and e was covered with approximately 0.4 ML of OH groups, corresponding to MgO_{hi}. The data were taken with a tunneling current of 0.1 nA, and the voltage set to +5–+6 V. The Au particle size distributions appear in panels c, f, and i, respectively [red = Au/MgO(001); black = Au/MgO_{hi}]. With courtesy of X. Shao, F. Stavale, N. Nilius.

Au/MgO(001), indicates the abundance of relatively small $Au^{\sigma+}$ clusters even after annealing to 300 K. Flashing the film to 573 K resulted in the same well-faceted 3D Au particles as observed previously, with the characteristic CO stretching frequency at 2090 cm^{-1} (Fig. 7.3c).

Along with the spectroscopic results presented above, STM studies were carried out in a separate chamber to probe the morphology of Au particles on the hydroxylated surfaces. For technical reasons, 10 ML thin MgO(001)/Mo(001) films were employed as substrate in the STM experiments. The MgO surfaces were hydroxylated by exposure to 0.001 mbar H_2O at room temperature, resulting in a hydroxyl coverage of ∼0.6 ML. STM images were taken for two different Au coverages (0.04 and 0.20 ML). Fig. 7.4 includes: STM images of 0.04 ML Au (Fig. 7.4a and b) and 0.20 ML Au (Fig. 7.4d, e, g and h) deposited on MgO(001) (upper panel) and MgO_{hi} (middle panel), and the corresponding gold particle size distributions (Fig. 7.4c, f and i), respectively. The presence of surface hydroxyls was found to significantly increase the density of Au particles: 0.042 nm^{-2} on MgO_{hi} versus 0.023 nm^{-2} on MgO(001) for 0.04 ML Au, and 0.098 nm^{-2} on MgO_{hi} versus 0.017 nm^{-2} on MgO(001) for 0.20 ML Au. In line with the increased particle density, the diameter of Au particles on MgO_{hi} was smaller than that of

Au/MgO(001): the mean diameter of as-deposited Au particles was 1.5 nm and 2.0 nm for 0.04 ML Au/MgO_{hi} and MgO(001), and 2.5 nm and 4–5 nm for 0.20 ML Au on MgO_{hi} and MgO(001), respectively. The influence of hydroxyls on the size distribution of the Au particles got even more pronounced when the samples were heated. Upon annealing to 600 K, the Au particle density for the 0.04 ML Au/MgO(001) sample decreased from 0.017 to 0.007 cm^{-2}, and the Au particle diameter increased from 4–5 nm to 5–6 nm (see the panels d, f, g and i of Fig. 7.4). By contrast, when the 0.20 ML Au/MgO_{hi} system was annealed at 600 K, the agglomeration of Au particles was found to be strongly suppressed; both the particle density (0.10 nm^{-2}) and the particle diameter (2.6 nm) remained almost the same, although nearly all surface hydroxyl groups were thermally removed from the surface (see Fig. 5.3b). The observed stabilization of small Au particles on MgO_{hi} as well as on the dehydroxylated MgO_{hi} indicates that additional nucleation centers for Au atoms were created on the MgO surface by hydroxylation.

7.2.3 Interactions of Pd with MgO_{hi}

Fig. 7.5 displays Pd 3d XP spectra for Pd/MgO_{hi} (blue spectra) and Pd/MgO(001) (black spectra) at Pd coverages of 0.05 Å (Fig. 7.5a) and 0.3 Å (Fig. 7.5b). Pd deposition was carried out at 100 K, and XP spectra were acquired after annealing to 300, 550 and 650 K.[1] As shown in Fig. 7.5a, a Pd species with a Pd $3d_{5/2}$ binding energy of 337.6 eV appeared for the as-deposited 0.05 Å Pd/MgO(001) sample. Its binding energy dropped to 336.3 eV, accompanied by a reduction of its peak intensity by a factor of 0.7, upon annealing to 300 K. After a further thermal treatment at 650 K, the Pd $3d_{5/2}$ binding energy of this species shifted to 335.7 eV. For 0.05 Å Pd/MgO_{hi}, the as-deposited Pd showed a Pd $3d_{5/2}$ peak at a binding energy of 337.2 eV, accompanied by a second component at 338.5 eV (Fig. 7.5a, top blue trace). Whereas the thermal treatment of Pd/MgO at 300 K caused a negative Pd binding energy shift and a reduction of the peak width, almost no spectral changes were observed for 0.05 Å Pd/MgO_{hi} after annealing to 300 K. These observations are consistent with the view that tiny Pd particles are strongly anchored to surface OD groups. An unexpected observation was the formation of the Pd species with an exceptionally high Pd $3d_{5/2}$ binding energy of 338.5 eV after annealing the sample to 550 K. Even subsequent annealing to 650 K did not totally reduce this highly oxidized Pd species. This species is tentatively assigned to Pd^{4+}.

At a Pd coverage of 0.3 Å (Fig. 7.5b), the freshly deposited Pd particles exhibited a single Pd $3d_{5/2}$ component at 336.5 eV on both the surfaces. Upon subsequent annealing to 300, 550, and 650 K, there was a monotonic decrease of Pd $3d_{5/2}$ binding energy; the Pd $3d_{5/2}$ component on MgO(001) shifted to 335.4 eV, whereas the Pd species on Pd/MgO_{hi} was characterized by a higher Pd $3d_{5/2}$ binding energy of 335.7 eV. The exceptionally highly oxidized Pd species with a binding energy of 338.5 eV was not recognized for 0.3 Å Pd/MgO_{hi}.

[1] Electromagnetic fields created by the Ta wires used for resistive heating are suspected to distort XP spectra, as current and voltage were applied to the samples. Although no clear evidence for this effect was observed, the XP spectra of the samples annealed to temperatures above room temperature have been collected at room temperature to exclude any effects related to the heating.

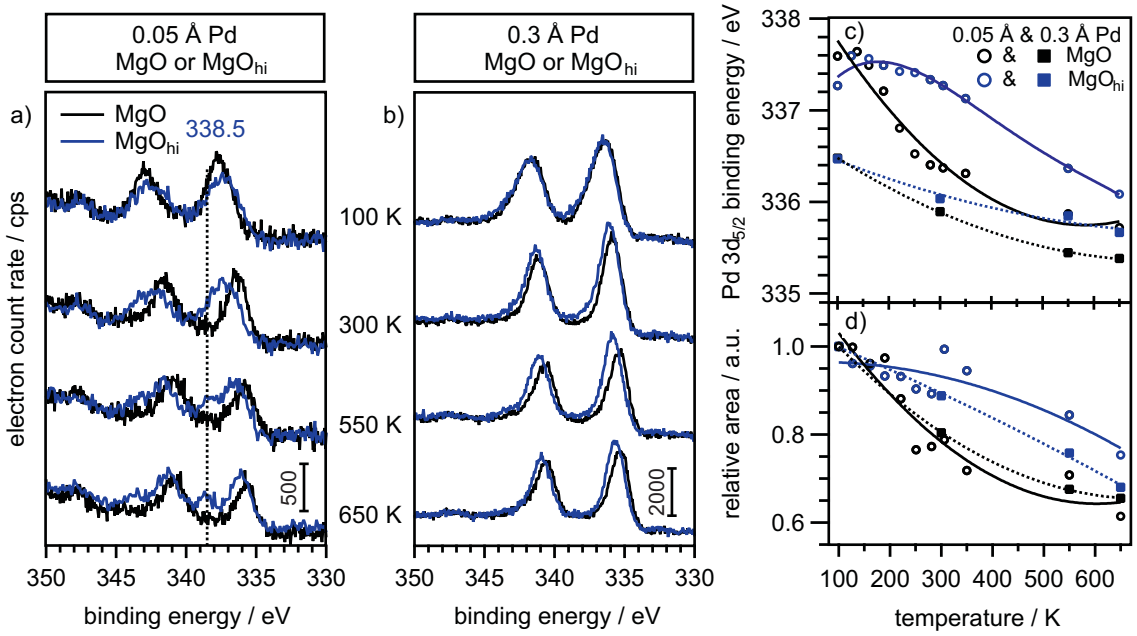

Figure 7.5: Pd 3d XP spectra for a) 0.05 Å and b) 0.3 Å Pd on 20 ML thick MgO or MgO_{hi} films after Pd deposition at 100 K and subsequent annealing to the indicated temperatures. All spectra were collected at room temperature, except for the as-deposited samples. c) The Pd $3d_{5/2}$ binding energy and d) the ratio of the areas to that acquired at 100 K for 0.05 and 0.3 Å Pd supported on MgO and MgO_{hi} surfaces as a function of temperature. Solid and dashed lines in c) and d) show the general trends.

The information obtained by XPS is summarized in panels (c) and (d) of Fig. 7.5, which present the Pd $3d_{5/2}$ binding energies and the Pd 3d peak areas (normalized to those acquired at 100 K) for Pd/MgO(001) and Pd/MgO_{hi} as a function of temperature. These plots show that both the binding energies and the peak areas were consistently higher for Pd/MgO_{hi} compared to Pd/MgO. This trend is particularly pronounced for 0.05 Å Pd in the temperature range of 100–300 K. Initially well-dispersed Pd particles formed on the MgO(001) surface at 100 K are obviously very weakly bound, and few specific trapping sites contributed to their stabilization. The hydroxyl groups present on MgO_{hi} act as additional trapping sites and give rise to an enhancement of the interaction between the Pd particles and the substrate. For 0.3 Å Pd, the substrate effect was clearly less pronounced. This observation is probably related to the limited number of the trapping sites on MgO_{hi}. Nevertheless, even after annealing to 650 K the Pd 3d binding energy of Pd/MgO_{hi} was higher than that of Pd/MgO(001), which indicates that the influence of hydroxylation persisted for the samples with the higher Pd load.

CO-TPD spectra (m/Z = 28) were acquired from Pd/MgO(001) and Pd/MgO_{hi} at Pd coverages of 0.05 and 0.3 Å to provide additional information about the nucleation and sintering of the particles (Fig. 7.6). The freshly prepared samples (Pd deposited at 100 K) were exposed to 2 L CO at 100 K. The 1st TPD spectrum was collected in the temperature range of 100–550 K with a ramp rate of 1 K/s. After cooling to 100 K and re-exposure of 2 L CO, a second TPD

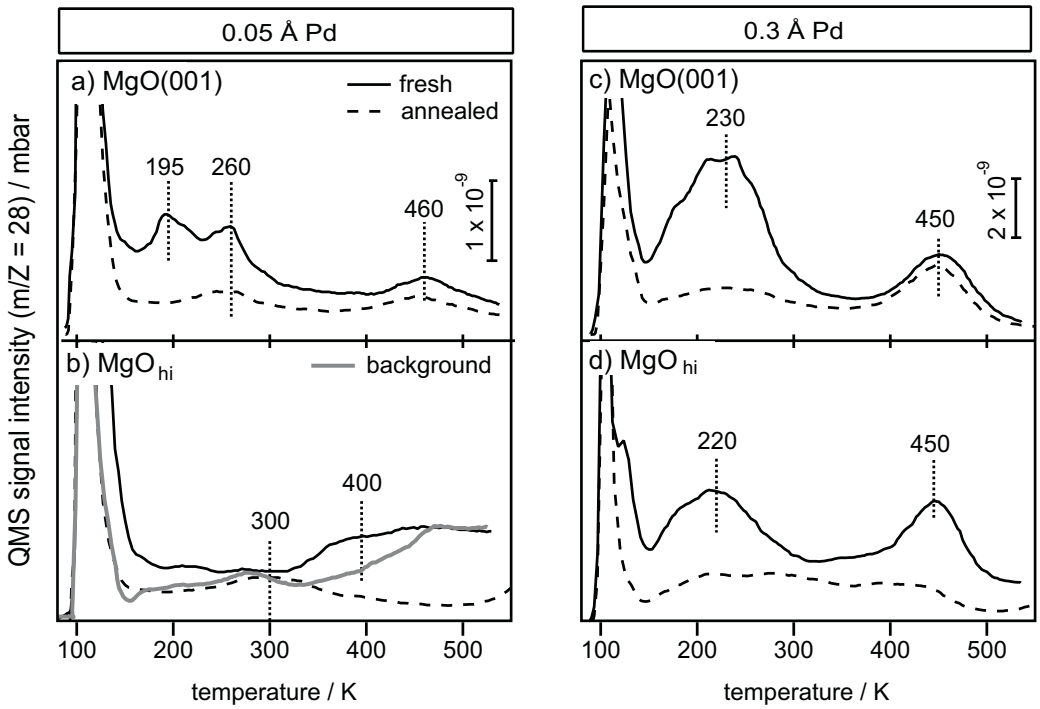

Figure 7.6: CO TPD spectra for 0.05 Å Pd-supported on a) MgO and b) MgO_{hi}, and for 0.3 Å Pd on c) MgO and d) MgO_{hi}. The Pd deposition and 2 L CO dosing were carried out at 100 K. The first and second TPD spectra were acquired in temperature ranges of 100–550 K and 100–650 K, respectively. Ramp rate was 1 K/s.

spectrum was obtained in the range of 100–650 K. The freshly prepared 0.05 Å Pd/MgO(001) exhibited three CO desorption peaks at 195, 260 and 460 K, respectively (Fig. 7.6a). In the 2nd TPD run, this sample showed two quite faint CO desorption peaks at ∼260 K and ∼460 K. The strong reduction of the CO desorption intensity after the first TPD run points to a reduction of the Pd surface area induced by thermal sintering. This conclusion is in agreement with the XPS data shown above (Fig. 7.5d), which showed a reduction of the Pd peak area upon annealing. The increase of Pd loading from 0.05 Å to 0.3 Å on MgO(001) yielded similar CO desorption profiles (Fig. 7.6c) with the only difference that the two distinct CO desorption peaks at 195 and 260 K observed in the first TPD spectrum from the 0.05 Å Pd sample converged into a single broad feature centered at 230 K for 0.3 Å Pd/MgO.

The CO TPD profile from 0.05 Å Pd deposited on MgO_{hi} was distinctly different from the one obtained from 0.05 Å Pd/MgO. Notably, in the 1st TPD run only little CO desorption between 200–300 K, but a broad CO desorption peak above 300 K was observed (Fig. 7.6b). This broad CO desorption was shared by the blank TPD spectrum acquired from MgO_{hi} (gray trace, Fig. 7.6b). This indicates that the decomposition of formates introduced during hydroxylation (see Fig. 5.3) partly contributed to this desorption feature. Taking this into account, the broad desorption between 300–450 K with a maximum at ∼380 K can be assigned to CO desorption from the Pd particles on MgO_{hi}. This desorption peak appears at significantly lower temperature

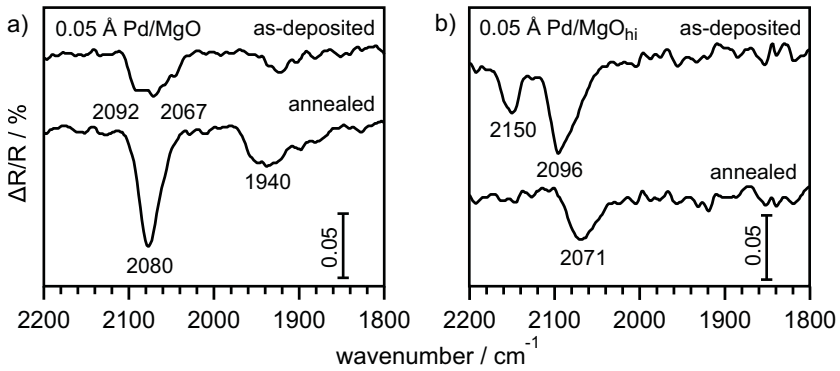

Figure 7.7: IRA spectra of adsorbed CO for 0.05 Å Pd deposited onto a) MgO and b) MgO_{hi} at 100 K (top). After annealing to 500 K, exposure to 2 L CO was performed at 100 K, and IRA spectra were acquired subsequently (bottom).

than that observed for the as-deposited Pd on MgO(001). In the second TPD run, the annealed sample presented a CO desorption peak at 300 K, similar to the annealed Pd/MgO(001) sample. A notable difference was, however, the absence of CO desorption at 460 K for Pd/MgO_{hi}. When the amount of Pd on MgO_{hi} was increased to 0.3 Å, there were two CO desorption peaks at 220 and 450 K, similar to the 0.3 Å Pd/MgO(001) system. Different to Pd/MgO(001), Pd/MgO_{hi} exhibited CO desorption peaks with comparable intensity.

Finally, infrared spectroscopy using CO as a probe molecule was applied to get insight into the surface properties of freshly prepared and annealed 0.05Å Pd/MgO(001) and Pd/MgO_{hi} (Fig. 7.7). All IRA spectra were collected after exposure to 1 L CO at 100 K. The IRA spectra for as-deposited Pd particles on MgO(001) exhibited two CO-IR bands at 2092 and 2067 cm^{-1} (top, Fig. 7.7a), which can be assigned to linearly adsorbed CO on different facets of Pd particles [199]. Thermal treatment at 500 K caused the development of CO signals at 2080 and 1940 cm^{-1} (bottom, Fig. 7.7a), corresponding to CO molecules adsorbed on atop and bridge sites, respectively. The development of these bands is a signature for the formation of well-faceted, small Pd particles [200]. The presence of surface hydroxyl groups results in a different CO absorption profile (top, Fig. 7.7b): as-deposited Pd/MgO_{hi} exhibited CO bands at 2150 and 2096 cm^{-1}. Note that the CO absorption peak at 2150 cm^{-1} appears only for the co-adsorption of CO and atomic oxygen on Pd surfaces [199,201,202]. After the sample experienced the thermal treatment at 500 K, only a single CO signal at 2071 cm^{-1}, corresponding to atop sites on Pd surfaces, remained (bottom, Fig. 7.7b). In contrast to 0.05 Å Pd/MgO, no signal corresponding to CO adsorption on bridge sites was observed for Pd/MgO_{hi}, suggesting the growth of ill-faceted Pd particles on MgO_{hi} [200, 203].

7.3 Discussion

7.3.1 Specific Depletion of Surface Hydroxyls upon Metal Deposition

The MgO_{hi} surface exhibits three OD signals at 2737, 2745, and 2754 cm^{-1} respectively. The results shown in Fig. 7.1 demonstrated that, among these signals, the one at the lowest frequency, 2737 cm^{-1}, was preferentially depleted upon depositing either Au or Pd. This result suggests that the OD group giving rise to this signal is the most reactive on MgO_{hi} in terms of oxidants. This most reactive hydroxyl group is supposed to be more Lewis acidic than any other ODs on MgO_{hi} (see Chapter 5). In light of their oxidation states, these acidic ODs are expected to be more similar to OD· than $OD:^-$. Therefore, this strong Lewis acidity should be the main driving force for the observed strong interaction of the hydroxyl groups with Au and Pd, or even oxidation of the metals, as discussed later. In line with our observation, a recent theoretical study also reported that a radical-like hydroxyl species on a MgO(001) surface is able to oxidize Au atoms by direct charge transfer from atomic Au to the hydroxyl group [204].

From Fig. 7.1 it appears that the ODs exhibiting higher stretching frequencies are more or less unaffected by gold deposition, while in the case of Pd, also these hydroxyls were depleted. The superior resistance of gold to oxidation is ascribed to the higher electronegativity of Au(2.54) compared to Pd(2.2). Furthermore, it is noted that the depletion of all hydroxyl groups upon Pd deposition is not a consequence of the direct metal-redox reaction between Pd and OD at room temperature, but of the formation of stable Pd-OD surface complexes as discussed in Chapter 8.

7.3.2 Chemical States of Au/MgO_{hi}

The most obvious result that demonstrates the influence of hydroxylation on the nucleation and sintering behavior of gold on MgO_{hi} is provided by STM (Fig. 7.4). There are two clear conclusions drawn from the data: (i) the nucleation site density is strongly increased; and (ii) the stability of small Au particles is strongly enhanced on MgO_{hi} as compared to those on MgO(001). Despite the importance of these findings, the STM results do not provide insight into the fundamental interaction giving rise to this effect. This can only be obtained by analyzing the electronic structural information accessed by means of XPS in combination with the CO-IRAS data. It has to be mentioned that the spectroscopic properties of the as-deposited Au species as well as the trend observed upon subsequent annealing, are qualitatively similar among Au/MgO_{hi} and Au/MgO(001) (see Chapter 6 for comparison). However, the details reveal that the chemical nature of the Au species on the two supports is not the same, as discussed below.

For the as-deposited Au/MgO_{hi} sample, the XPS data revealed the presence of an Au species with an Au $4f_{7/2}$ binding energy of 86.4 eV, and the corresponding IRAS spectrum suggests high abundance of Au species that gives rise to a stretching frequency of adsorbed CO at 2165 cm^{-1}. Both of these values strongly deviate from expectations for neutral Au species (84.0 eV and 2100 cm^{-1}). The high binding energy of the Au species falls into the range of binding energies reported for Au_2O_3 and strongly oxidized gold clusters [189, 205]. The simultaneous

disappearance of the high binding energy XPS signal and the CO-IRAS signal at 2165 cm^{-1} upon heating to room temperature suggests a direct relationship between these signals. Note that the large blue-shift of the CO stretching frequency relative to CO adsorbed on neutral Au particles indicates also the presence of positively charged Au [189, 205]. The recorded Au 4f binding energy and the stretching frequency of adsorbed CO on as-deposited Au/MgO_{hi} are similar to the ones obtained for Au/MgO(001), suggesting that the Au species nucleated on these surfaces are of similar cationic nature.

Concerning gold species present on MgO_{hi}, the most notable fact is that there are highly cationic gold species on the MgO(001) surface, as shown in Chapter 6, as well as MgO_{hi}: the Au $4f_{7/2}$ binding energy of 86.4 eV (Fig. 7.2a), accompanied by the corresponding CO frequency of 2165 cm^{-1} observed by IRAS (Fig. 7.3a). The emergence and disappearance of the infrared signals were in parallel to those of XP components, suggesting their relevance. The resemblance of the electronic states of Au and the vibrational frequencies of adsorbed CO among Au/MgO_{hi} and Au/MgO indicates that the Au species nucleated on these surfaces are of similar cationic nature. However, while the formation of cationic Au clusters on MgO(001) could be explained by the presence of specific electron trapping sites (anion vacancies and grain boundaries), it is difficult to imagine that the same trapping sites are also responsible for the formation of cationic Au on MgO_{hi}, since hydroxylation should preferentially deplete these highly reactive sites [189]. Thus, a different interaction should contribute to the formation of cationic gold on MgO_{hi}. Specifically, it is more likely that the cationic nature of the Au species on MgO_{hi} is related to the formation of Au_xO_y species, considering the highly Lewis acidic nature of surface hydroxyl groups on MgO_{hi} as discussed above. The thermal induced simultaneous changes in Au 4f and the absorption of adsorbed CO molecules indicates that these small Au_xO_y moieties are lost either by thermal decomposition [206] or due to agglomeration.

The second Au component with an Au $4f_{7/2}$ binding energy of ∼85 eV was observed for Au/MgO_{hi} in the temperature range of 100—300 K (Fig. 7.2). Being corroborated by the corresponding CO-IRAS spectrum giving rise to a band at ∼2130 cm^{-1}, which is blue-shifted with respect to CO adsorbed on metallic Au particles, this species could be assigned to the slightly positively charged Au-carbonyl species. This CO vibrational species, which was not observed for Au/MgO at room temperature (Fig. 7.3), could discard a possible concern that the presence of smaller Au particles on MgO_{hi} due to the limited sintering causes the upward shift in Au 4f binding energy via increased final state contributions.

After annealing to 573 K, the MgO_{hi} sample exhibited typical characteristics of metallic gold particles: the Au $4f_{7/2}$ binding energy of 84.3 eV and stretching frequency of adsorbed CO at 2090 cm^{-1}. In particular, observing the identical infrared signal of CO adsorbed on the annealed Au/MgO at 573 K indicates the formation of metallic Au particles on both the surfaces. The slightly higher Au $4f_{7/2}$ binding energy of 84.3 eV for Au/MgO_{hi} compared to 84.0 eV for Au/MgO(001) can be ascribed to the limited core-hole screening for smaller gold particles on MgO_{hi}. This conclusion is in agreement with previous TPD data [45] and the STM data reported in Fig. 7.4.

In summary, the correlation of XPS and IRAS results for Au/MgO_{hi} leads to the following conclusions regarding the states of Au at the individual stages of nucleation and sintering. Upon deposition at 100 K, Au interacts with the highly Lewis acidic hydroxyl groups on MgO_{hi} and forms small Au_xO_y aggregates with an Au $4f_{7/2}$ binding energy of 86.4 eV and stretching frequency of adsorbed CO of ∼2165 cm^{-1}. The second Au species with a lower Au $4f_{7/2}$ binding energy (85 eV) and lower CO stretching frequency (2130 cm^{-1}) is ascribed to the formation of partially oxidized Au particles. The former species are decomposed or lost due to the diffusion-induced agglomeration during heating to room temperature, whereas the partially oxidized species is stable at room temperature. Thermal treatment at 573 K leaves only small neutral Au particles on the surfaces. The enhanced sinter stability of gold on MgO_{hi} in comparison to MgO(001) may be explained by the stronger metal/support interaction in the case of MgO_{hi} due to the formation of Au-O interfacial bonds caused by the interaction of Au with the Lewis acidic hydroxyl groups [189].

As a side note, it is mentioned that the electron injection from supported gold into the oxide film should also be observed upon oxidizing Au. This charge transfer is inevitably accompanied by the formation of electron double layers, as evidenced by the band bending. Under this expectation, the positive binding energy shift of the oxide O 1s line observed for Au/MgO_{hi} (Section 7.2.2) suggests that the local charge transfer goes from the supported Au to the MgO_{hi} film (e.g., oxidation of Au) and *vice versa* for Au on either MgO or MgO_{hydr} surfaces, for which a negative O 1s shift has been observed (Appendix C)

7.3.3 Pd on MgO_{hi}

Assignment of the Highly Oxidized Pd Particles Formed on MgO_{hi}

A most noticeable observation is the Pd species with a Pd $3d_{5/2}$ binding energy of 338.5 eV, for the 0.05 Å Pd/MgO_{hi} sample (Fig. 7.5a). This palladium species is expected to be highly oxidized, considering that the Pd $3d_{5/2}$ binding energy of Pd^{2+} species in PdO is 336.5 eV [72, 207]. Very few experimental studies carried out under UHV conditions have reported Pd species with a Pd $3d_{5/2}$ binding energy as high as 338.5 eV. These species were assigned to Pd^{4+} [208, 209]. One study reported that bulk PdO_2 easily decomposed into PdO under UHV conditions [208]. Recently, Pd^{4+} moieties with high thermal stability were produced on a Pd surface using plasma oxidation [210]. These findings support the conclusion that highly oxidized Pd species with high thermal stability are formed on MgO_{hi} (bottom blue spectrum, Fig. 7.5a). The fact that Pd^{2+} species are dominantly observed on Pd catalysts suggests that the special hydroxylation conditions applied to produce MgO_{hi} surfaces could be responsible for the formation of Pd^{4+} species. In analogy to the results for Au on MgO_{hi}, the formation of the highly oxidized Pd species is, therefore, ascribed to the exceptionally strong interaction of deposited Pd atoms with highly Lewis acidic hydroxyl groups present on MgO_{hi}.

It is noted that a thermally stable Pd species with a Pd $3d_{5/2}$ binding energy of 337.9 eV was recently observed via the wet impregnation of $Pd(OH)_2$-like precursors on a MgO(001) model

support when the Pd coverage was below a certain threshold value (≤0.4 ML) [161]. In the case of wet impregnation, this stable species is supposed to result from the partial decomposition of more or less isolated precursor complexes bound to the MgO surface. Due to the nature of the precursor used (Pd-hydroxo complexes), such species are possibly highly abundant on the MgO surface after applying the wet impregnation, which could explain why the highly oxidized Pd species is present at much higher Pd coverages than in the present study (the 338.5 eV component was not observed when the Pd coverage was increased above 0.1 ML, possibly because of agglomeration). Nevertheless, this comparable observation supports the conclusion that the interaction of Pd with hydroxyl groups leads to the formation of the highly oxidized Pd species.

Influence of Hydroxyls on Pd Nucleation

The enhanced stability of gold particles on MgO_{hi} has been evidenced by previous CO-TPD studies [45] as well as the STM and XPS results presented in this chapter. Unfortunately, STM data are not yet available for Pd supported on the MgO_{hi} and MgO(001) surfaces, but information about the morphology and the oxidation state of the supported Pd particles should be reflected in the spectroscopic and spectrometric data.

The discussion starts with an analysis of the electronic structure of Pd particles (Fig. 7.5). At a Pd coverage of 0.05 Å, the freshly prepared (100 K) MgO-supported Pd particles exhibited a very high Pd 3d binding energy comparable to the Pd^{4+} species. This high binding energy is not ascribed to the oxidation of Pd, but to the enormous final state contribution to the binding energy shift due to the limited particle size of Pd [77]. Indeed, it is expected that as-deposited Pd particles at such a low coverage consist of countable number of Pd atoms [186]. Its more rapid decrease in both binding energy and intensity by annealing reflect the low thermal stability of the Pd/MgO(001) species, compared to Pd/MgO_{hi}. The fact that Pd-supported systems at a Pd coverage of 0.3 Å exhibited the same tendency suggests that analogous to gold the presence of hydroxyls also inhibits Pd agglomeration.

Additional information concerning the surface states of Pd particles is first deduced from the CO-IRAS data (Fig. 7.7). There are two notable differences between freshly prepared Pd/MgO and Pd/MgO_{hi}. The first one is the presence of the band at 2150 cm^{-1} for Pd/MgO_{hi}. Noting that this band is typical for CO adsorbed on oxidized Pd or CO coadsorbed with atomic oxygen on Pd surfaces [199, 201, 211], it is conceivable that the collision-induced migration of oxygen on Pd particles occurred upon Pd deposition. This finding corroborates the suggestion that the interaction of Pd with hydroxyl groups on MgO_{hi} leads to the partial oxidation of Pd. Another unshared property is infrared absorption intensity by adsorbed CO molecules: Pd/MgO_{hi} exhibited stronger absorption ascribed to CO adsorbed at atop sites [203]. This clearly indicates that the diffusion of deposited Pd atoms was limited on MgO_{hi}, which results in the formation of smaller Pd particles, i.e., larger total surface areas at the same Pd coverage. Upon annealing to 500 K, in contrast to the freshly prepared ones, drastic changes related to Pd particles were

observed. The multi-coordinated CO molecules in a frequency region of 1900–1980 cm^{-1} were observed for 0.05 Å Pd/MgO(001). This means that this low Pd coverage is enough to form well-faceted three dimensional Pd particles. Furthermore, despite the limited agglomeration of Pd particles on MgO_{hi}, the number of adsorbed CO molecules on Pd/MgO_{hi} sample was fewer. These facts are well explained by a possibility that many Pd surface sites were not accessible to CO molecules due to presence of accommodated oxygen or carbon atoms because of CO and OD dissociation, as previously reported [50, 212–215].

Further information about the morphology of Pd particles was deduced from CO-TPD data (Fig. 7.6). Before going into the details, it needs to be mentioned that, for the present systems, the first TPD spectra inevitably include the information of: (i) as-deposited Pd particles; and (ii) thermal-induced morphological changes of Pd particles such as sintering and rearrangement. The non-negligible involvement of the morphological changes of Pd particles means that these TPD data cannot be straightforwardly compared to the CO-IRAS spectra of the as-prepared samples, which contain only the information of the initial state of the supported systems, unless there is no CO adsorption-induced agglomeration of Pd particles.

As displayed in Fig. 7.6a, the freshly prepared 0.05 Å Pd/MgO(001) sample exhibited two distinct CO desorption peaks below room temperature (195 K and 260 K), as well as a characteristic peak at 460 K due to CO desorption from highly coordinated sites [212]. A CO desorption peak similar to the one at ∼190 K has previously been reported for Pd deposition onto an alumina substrate in a CO atmosphere [216, 217]. These studies assigned the CO desorption peak to the decomposition of Pd-carbonyl compounds, $Pd_m(CO)_n$. It is reasonable to expect that such Pd-carbonyl compounds could formed upon CO adsorption on the highly dispersed Pd species formed at 100 K. Alternatively, the low-temperature CO desorption signal could also be attributed to weakly bound CO at peripheral sites of the Pd clusters and particles, as recently suggested in a study of CO desorption from size-selected Pd clusters deposited on TiO_2(110) [218].

In contrast, the CO TPD spectrum acquired from the freshly prepared 0.05 Å Pd/MgO_{hi} showed that there was little CO desorption below room temperature, accompanied by a distinct CO desorption signal at ∼400 K (Fig. 7.6b). At a glance, this lower CO adsorption capacity observed for Pd/MgO_{hi} than Pd/MgO contradicts with the observation, where CO adsorbed on Pd/MgO_{hi} exhibited the stronger infrared absorption intensity. This, as later closely discussed using Pd/MgO_{hydr} in Chapter 8, seems to be due to the occurrence of CO oxidation reaction by surface hydroxyl groups and/or atomic oxygen on Pd surfaces (CO at 2150 cm^{-1} indicating the CO co-adsorbed with O), for which a part of adsorbed CO molecules desorb not as CO molecules themselves, but as CO_2 above 350 K. The presence of CO molecules adsorbed on small Pd particles, whose dipole moment could be in parallel to the substrate, could provide another explanation for the discrepancy, because the surface selection rule does not allow IRAS to observe this species (see Section 2.3.2).

Different from the 0.05 Å Pd sample, the CO-TPD spectra recorded from as-deposited Pd/MgO as well as Pd/MgO_{hi} at a Pd coverage of 0.3 Å were very similar to each other (panels

(c) and (d) of Fig. 7.6). There were main CO desorption signals at 220–230 K and 450 K. This similarity suggests that a direct chemical interaction between Pd and hydroxyls at low temperature is limited to a few highly reactive surface hydroxyls. Thus, a Pd load of 0.3 Å on MgO_{hi} could saturate this strong interaction, so that the additionally deposited Pd was little affected by the hydroxyls at 100 K, in agreement with the XPS data (Fig. 7.5b).

The supported Pd particles gave rise to different CO desorption profiles after the 1st TPD runs. There was one general tendency: the CO desorption below room temperature was suppressed. Considering that a spectroscopic study has shown that the signal of atop-bound CO on Pd particles disappears between 250 K and 300 K [219], the lack of CO desorption in this temperature range for the annealed Pd/MgO as well as Pd/MgO_{hi} indicates the formation of well-nucleated Pd particles with fractional atop sites. Another notable observation during the 2nd TPD runs was that the suppression of CO desorption at 450 K occurred only for Pd/MgO_{hi}. This loss induced by the thermal interaction of Pd particles with surface hydroxyl groups, again, leads to the conclusion that the large part of highly-coordinated sites of Pd surfaces became blocked by foreign atoms such as C and O during the 1st TPD run, as suggested by infrared spectroscopy. Another hypothesis is that enhanced agglomeration of Pd particles occurred on MgO_{hi}, resulting in reduction of the surface area of Pd particles. However, this is in contradiction with the XPS data.

7.4 Conclusions

The interactions of metals (Pd and Au) with actively hydroxylated MgO surfaces, MgO_{hi}, were investigated using various spectroscopic methods, in combination with STM microscopy. The active hydroxyls at the lowest frequency, 2737 cm^{-1}, selectively reacted with deposited Au. The adsorbed CO on the as-deposited Au on MgO_{hi} gave rather similar absorption profiles to Au/MgO(001), in agreement with the formation of positively charged Au and neutral Au particles on both the surfaces. The MgO_{hi} surface was found to inhibit the agglomeration of Au clusters and particles upon annealing to 300 as well as 600 K. In contrast to Au, Pd deposition onto MgO_{hi} depleted all the surface hydroxyls, after consuming the most reactive ones first. The interaction of Pd with the most active hydroxyls resulted in an exceptionally stable, highly oxidized Pd^{4+} species, with a Pd $3d_{5/2}$ binding energy of 338.5 eV.

Analogous to the Au particles, the presence of surface hydroxyls prevented the agglomeration of Pd and the robust shift of the Pd 3d XP lines to higher binding energy relative to Pd/MgO(001) suggests that also larger Pd particles become partially oxidized. The different properties of Pd on MgO(001) and MgO_{hi} are particularly evident in the CO-IRAS and CO-TPD data recorded from low-coverage samples.

Chapter 8

Metal-Redox and Water-Gas Shift Reaction of Pd with Hydroxyls

This chapter addresses interactions of surface hydroxyls on MgO_{hydr}[1] with Pd particles as well as adsorbed CO molecules. Thermal annealing of Pd/MgO_{hydr} was found to give rise to H_2 formation via the following two processes: the metal-redox process and the Water-gas shift (WGS) reaction. The metal-redox processes occurred as Pd directly interacts with surface hydroxyls at ∼400 K. Evidence for this process was obtained from the perfect correlation of D_2 desorption seen in TPD, and Pd oxidation revealed by XPS and Auger parameter analysis. As Pd particles were covered with CO molecules, the WGS reaction occurred in the temperature range of 400–600 K, as evidenced by the simultaneous desorption of H_2 and CO_2. Variation of the Pd coverage revealed that the WGS activity can mainly be ascribed to the Pd perimeter sites. A comparative study of Au deposited onto MgO_{hydr} highlights the rich chemistry of palladium with hydroxyls.

8.1 Introduction

With growing interest in understanding the contribution of the oxide supports to the reactivity of supported catalysis [61, 220], more effort is required to unravel the role of hydroxyl groups, which are universally present on oxide surfaces [46]. Hydroxyls on oxides can not only alter structural and electronic properties of supported metals, but also react with the particles as well as adsorbed species such as CO. For the present study, attention is focused on two processes that directly or indirectly involve support hydroxyls and supported metals: (i) the metal-redox process proceeding according to Eq. 8.1 [47],

$$Me^0 + \{M^+ - OH^-\} \rightarrow \{M^+O^{2-}\}Me^+ + H_{ad} \tag{8.1}$$

[1] Refer to Chapter 5

where M refers to a metal within the oxide support and Me is a metal atom within the supported metal particles; (ii) the water-gas shift (WGS) reaction [43], reading

$$CO + H_2O \rightarrow CO_2 + H_2 \quad \Delta H = -41 \text{ kJ/mol.} \tag{8.2}$$

Early experimental studies investigating the thermal decomposition of metal-carbonyl complexes adsorbed on hydroxylated oxide surfaces found evidence for a redox pathway leading to the oxidation of the metal upon annealing [221,222]. Following these pioneering works, Libuda et al. were among the first to convincingly show, using a two-dimentional oxide substrate, that the oxidation of Rh atoms occurs upon their direct deposition onto a hydroxylated Al_2O_3 films [47]. This foregoing study has been experimentally followed using other metals such as Co on Al_2O_3 [49]. In line with these experimental investigations, computational efforts have been made to simulate the interactions. In one example it was proposed that Rh particles on a hydroxylated alumina substrate accommodate hydrogen atoms that are released due to the interaction of the particles with surface hydroxyls [53]. Another calculation pointed out the occurrence that the proton accommodation by supported Pt particles on alumina surfaces induces the structural reformation of the Pt particles, with an additional interaction with surface hydroxyls [198]. Despite these experimental and theoretical efforts, the fate of hydrogen from a perspective of chemical reaction has remained elusive.

Another representative reaction to produce hydrogen is the WGS reaction, taking advantage of adsorbed CO as the reducing agent of water molecule to evolve stoichiometric amounts of CO_2 and H_2, in the manners of Eq. 8.2. Studies of the mechanism of the WGS reaction have revealed that it proceeds via either the decomposition of an intermediate species (e.g., formate, carbonate) at the metal-oxide interface [223, 224], or direct oxidation of CO by an oxygen atom embedded on the metal surface, which arise as a consequence of the dissociation of hydroxyls on oxide surfaces (the redox mechanism) [225]. These mechanisms suggest that the oxide surface serves as a reservoir of hydroxyls, while the supported metal particles act as active sites. Since the interaction of hydroxyls with supported metal particles relies critically upon the size of the metal particles [226], effort is required to gain a detailed molecular-level understanding on the size effects and the mechanisms.

Several studies utilizing model systems with a high degree of control over their material composition have been undertaken in order to answer these questions. With Cu particles of different sizes dispersed on $TiO_2(110)$, Rodriguez et al. found the strong interaction between the support and the Cu particles decreased the apparent activation barrier of the WGS reaction. These changes were thought to arise through the energetically favored formation of a OCOH intermediate and its subsequent decomposition into CO_2 and a proton [226]. In the case of $Au/TiO_2(110)$, catalytic performance in the WGS reaction is predominantly related to the abundance of Au corner sites, with which surface hydroxyls or water preferably react [227]. Furthermore, recent investigations demonstrated that activated hydroxyls in the vicinity of atomic Pt or Au particles significantly promote the WGS reaction [11, 228].

In this study, the metal-redox process and the Water-gas shift reaction on the supported

metals (Pd and Au) were investigated with focuses on: (i) the nucleation of the metals on MgO_{hydr}; (ii) their interaction with surface hydroxyls; and (iii) the reaction of metal-bound CO with surface hydroxyls. While Au was found to weakly interact with the hydroxyls on MgO_{hydr}, the deposition of Pd on MgO_{hydr} and subsequent heating gave rise to the evolution of hydrogen, which is indicative of the occurrence of the metal-redox process. Further support for the metal-redox process was provided by observations of the oxidation state changes of Pd particles supported on MgO_{hydr} as quantified by Auger parameter analysis, as explained in Section 2.2.7. The WGS-type reaction between CO adsorbed on Pd particles and support hydroxyls was observed during the heating post-hydroxylated Pd-MgO(001) samples. Mechanistic aspects about the WGS reaction will be discussed in light of the results obtained for different Pd coverages.

8.2 Results

8.2.1 Reactivity of Pd with Surface Hydroxyls on MgO_{hydr}

For the experiments reported in the present chapter, hydroxylated MgO surfaces were prepared by exposing the freshly grown 30 ML MgO(001)/Ag(001) films to 0.05 mbar D_2O for 3 min., resulting in a hydroxyl coverage of ∼0.6 ML (referred to MgO_{hydr}, see Chapter 5). The interaction of Pd with the hydroxyls on MgO_{hydr} was first studied with IRAS by monitoring changes induced by Pd deposition on the OD spectral region around 2750 cm^{-1}. As displayed in Fig. 8.1a, the intensity of the hydroxyls stretching mode of MgO_{hydr} was significantly and non-selectively reduced upon deposition of increasing amounts of Pd. In fact, the bands were almost completely depleted after deposition of 1.0 Å Pd. This observation points to a strong interaction of Pd with the hydroxyls and identifies the hydroxylated sites as preferred metal nucleation sites on MgO_{hydr}.

In order to learn more about the initial interactions of 1.0 Å Pd with surface hydroxyls at room temperature, O 1s XP spectra of pristine MgO_{hydr} and Pd/MgO_{hydr} are presented in the bottom and top panels of Fig. 8.1b, respectively. Fitting of the O 1s components of the Pd/MgO_{hydr} sample is somewhat complicated by the presence of the Pd $2p_{3/2}$ emission in the same binding energy region. Its contribution was estimated by the intensity ratio of Pd 3d/Pd 2p states from a Pd(111) reference sample and recalculating the Pd 2p intensity for the supported samples from its known Pd 3d intensity. The result of the fits shows that the 1.0 Å Pd/MgO_{hydr} sample continues to exhibit a clear shoulder related to hydroxyls. Although its intensity compared to the hydroxyl O 1s peak of MgO_{hydr} dropped by ∼20 %, the similar reduction of intensity of the main O 1s peak ascribed to the oxide support indicates that the loss of the OD signal is entirely related to the attenuation of the photoelectrons by the deposited Pd. This result is in apparent contradiction to the IRAS study, which showed the complete annihilation of the OD signal upon Pd deposition. Interestingly, the OD IRAS signal partly reappeared upon annealing 1 Å Pd/MgO_{hydr} to 373 K (Fig. 8.1a), reflecting the thermally-induced break-up of Pd-OD surface complexes. Therefore, both XPS and IRAS measurements suggest negligible

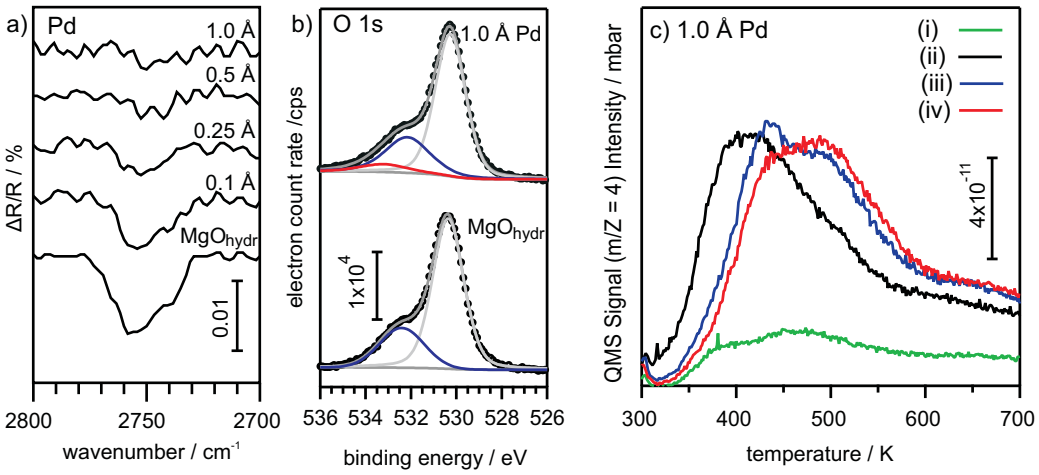

Figure 8.1: a) IRA spectra in the OD stretching region of hydroxylated 30 ML thick MgO(001) films by 0.05 mbar D_2O with subsequent deposition of Pd with a nominal thickness of (i) 0.1, (ii) 0.25, (iii) 0.5 and (iv) 1.0 Å at room temperature. b) XP spectra in the energy regions of O 1s and Pd 3p, of pristine MgO_{hydr}(bottom) and as-deposited 1.0 Å Pd on MgO_{hydr}. c) D_2-TPD spectra of (i) MgO_{hydr}, (ii) 1.0 Å Pd/MgO_{hydr}, (iii) as-deposited Pd/MgO(001), with subsequent hydroxylation by 0.05 mbar D_2O, and (iv) well-faceted Pd particles on MgO(001), which was exposed to 0.05 mbar D_2O prior to the TPD measurements. Ramp rate was 1 K/s. All the XP and IRA data were collected out at room temperature.

hydroxyl consumption, i.e., little if any spontaneous reaction between hydroxyls and Pd at room temperature.

D_2 TPD spectra were acquired in order to explore the reactivity of the samples at elevated temperatures. In Fig. 8.1c, D_2 TPD spectra from the following samples are provided: (i) MgO_{hydr}; (ii) 1.0 Å Pd deposited onto MgO_{hydr}; (iii) well-faceted 1.0 Å Pd/MgO(001) with the subsequent hydroxlylation by 0.05 mbar D_2O for 3 min; and (iv) as-deposited 1.0 Å Pd on MgO(001), which has been hydroxylated by exposure to 0.05 mbar D_2O for 3 min. MgO_{hydr} gave rise to broad D_2 desorption ranging from 350 to 700 K. Strong enhancement of D_2 desorption showing a maximum desorption rate at 400 K was observed for Pd/MgO_{hydr}. Hydroxylating the well-faceted Pd particles supported on MgO(001) shifted the D_2 desorption temperature from 400 to 473 K, accompanied by significant reduction of D_2 desorption below 400 K (spectrum (iii)). In order to study the influence of Pd particle size and the degree of faceting on D_2 evolution, as-deposited 1.0 Å Pd particles on pristine MgO(001) were exposed to water vapor, and a D_2 TPD spectrum was collected (spectrum (iv)). Only minor changes relative to spectrum (iii) were present, suggesting little influence of these parameters at the same Pd coverages.

The distinct D_2 desorption temperatures observed in the spectra (ii) and (iii) are explained in terms of different reaction mechanisms, as deduced from the simultaneously collected D_2, CO and CO_2 desorption signals reported in Fig. 8.2. From Pd/MgO_{hydr}, little CO_2 desorption was observed in the temperature range of 350–550 K (Fig. 8.2a). On the other hand, the

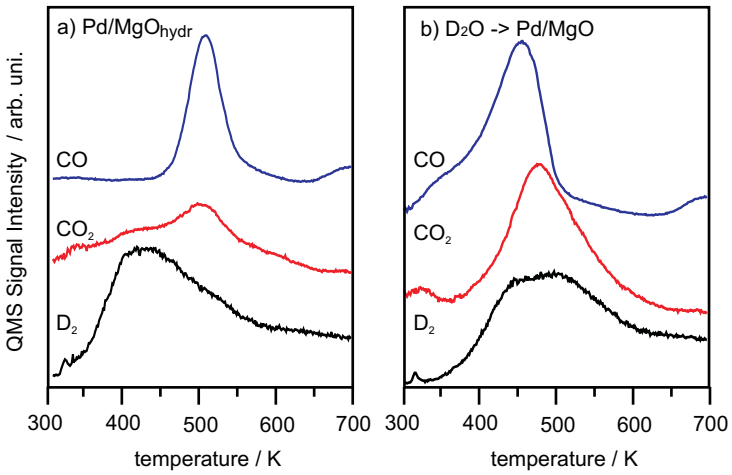

Figure 8.2: TPD spectra of ions corresponding to D_2 ($m/Z = 4$), CO ($m/Z = 28$), and CO_2 ($m/Z = 44$) for a) 1.0 Å Pd deposited onto MgO_{hydr}, and b) well-nucleated 1.0 Å Pd supported on MgO(001) surface, with hydroxylation by 0.05 mbar D_2O before the TPD measurements. Ramp rate was 1 K/s.

post-hydroxylated Pd/MgO had overlapping CO_2 and D_2 desorption peaks between 400–600 K (Fig. 8.2b). Under the present situation, the principles of stoichiometry allows D_2 to be formed only in the presence of a reductant. In the former case, the absence of CO_2 obviously suggests that the supported Pd particles accommodated oxygen atoms, via Eq. 8.1, suggesting the occurrence of a metal-redox process. The simultaneous formation of D_2 and CO_2 on the post-hydroxylated sample indicates that the scenario of the water-gas shift reaction via Eq. 8.2 is likely. More details about the WGS reaction over Pd/MgO_{hydr} will be presented in Section 8.2.3.

8.2.2 Modification of Pd Electronic Structure by Surface Hydroxyls at Elevated Temperatures

The metal-redox chemistry of supported Pd particles with surface hydroxyls is expected to play a crucial role in the surface interactions and reactions as strongly suggested D_2 TPD results presented in the precedent section. According to Eq. 8.1, the electronic structure of Pd should be strongly affected by the metal-redox process. Conventionally, binding energy shifts determined with photoemission spectroscopy allow estimating oxidation states of supported metals [72]. However, as defined by Eq. 2.21, the binding energy shift is the sum of initial and final state contributions. Hence, direct assignment of oxidation states based solely on the determination of binding energy shifts collapses if the final state effect is overwhelming. This circumstance is particularly important in the case of very small particles, where reduced screening of core holes induces upward shifts in binding energies of up to 2.0 eV [77]. Hence, in order to elicit the initial state effect of the Pd particles from the binding energy shifts, the Auger parameter analysis was used to quantitatively probe the reactions of the Pd particles with surface hydroxyls proceeding in the direction of metal oxidation.

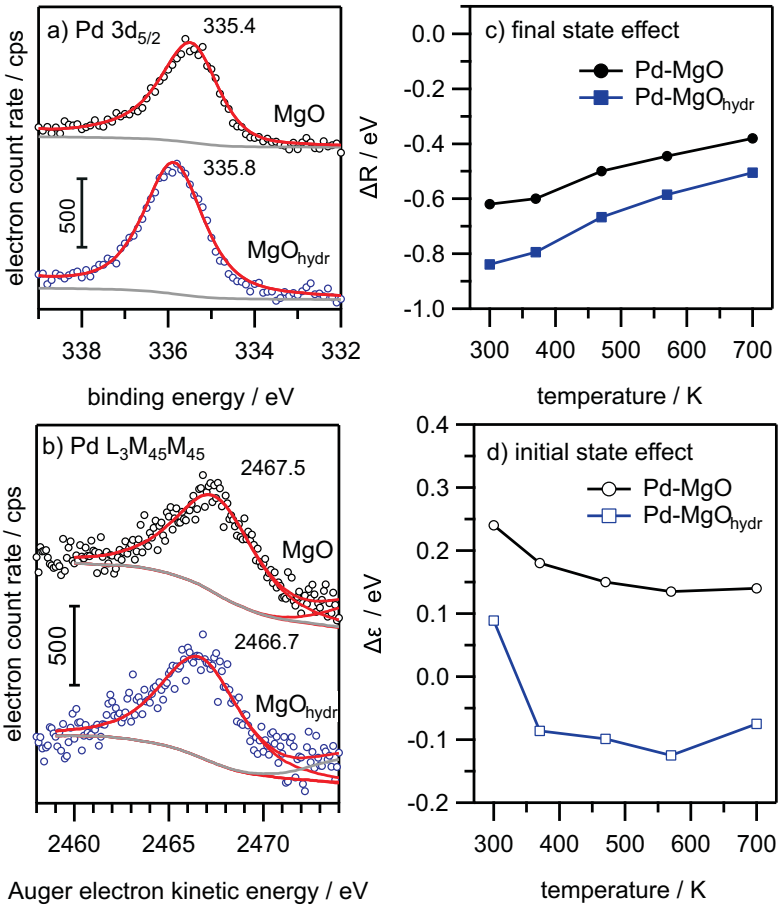

Figure 8.3: a) Pd $3d_{5/2}$ XP spectra and b) Pd $L_3M_{45}M_{45}$ Auger electron spectra taken from 1.0 Å Pd deposited onto the MgO(001) and hydroxylated MgO surfaces, MgO_{hydr}, surfaces at room temperatures. Separated c) final state contribution, ΔR, and d) initial state contribution, $\Delta\varepsilon$, of the supported Pd on both surfaces as a function of temperature.

Pd $3d_{5/2}$ XP spectra (Fig. 8.3a) and Pd $L_3M_{45}M_{45}$ $^1G_4$ Auger electron's kinetic energies (Fig. 8.3b) were acquired for the the as-deposited 1.0 Å Pd supported on MgO(001) as well as MgO_{hydr} at room temperature. The Pd particles on pristine MgO(001) surfaces exhibited a Pd $3d_{5/2}$ binding energy of 335.4 eV, and the corresponding $^1G_4$ Pd $L_3M_{45}M_{45}$ Auger electron had a kinetic energy of 2467.5 eV [229]. The deposition of 1.0 Å Pd onto MgO_{hydr} caused a positive shift of the Pd $3d_{5/2}$ binding energy to 335.8 eV, and a negative shift of the Pd $L_3M_{45}M_{45}$ line to 2466.7 eV.

The separation into initial state, $\Delta\varepsilon$, and final state, ΔR, contributions was carried out for these sets of data, as detailed in Section 2.2.7. The analysis requires the knowledge of the differences in the obtained Pd $3d_{5/2}$ binding energies and Pd $L_3M_{45}M_{45}$ kinetic energies with reference to a standard material. In the present study, a Pd(111) single-crystal reference gave 335.1 eV for the Pd $3d_{5/2}$ binding energy and 2469.1 eV for the Pd $L_3M_{45}M_{45}$ kinetic energy.

For the Pd/MgO as presented in Fig. 8.3a and Fig. 8.3b, ΔBE and ΔKE were calculated to be +0.3 eV and −1.6 eV, respectively. These values and Eq. 2.40 yielded the final state

Table 8.1: Binding energy shifts (eV) of Mg 1s and Mg 2p of the MgO, Mg $KL_{23}L_{23}$ of pristine 30 ML thick MgO(001) films, as-deposited 1.0 Å Pd on the MgO films, and the Pd/MgO sample with annealing at 723 K. All the spectra were taken at room temperature.

Sample	Mg 1s (MgO)	Mg 2p	Mg $KL_{23}L_{23}$
30 ML MgO	1305.0	50.5	1180.6
Pd/MgO @ 300 K	1304.5	50.1	1181.1
Pd/MgO @ 723 K	1304.7	50.2	1181.0

contribution, $\Delta R = -0.65$ eV. The substitution of ΔR into Eq. 2.41 produced the initial state contribution, $\Delta\varepsilon = +0.25$ eV. ΔR of 1.0 Å Pd on the MgO(001) surface was found to be -0.6 eV at the beginning, while ΔR of the Pd/MgO_{hydr} system exhibited a more negative value, -0.84 eV. In the temperature range of 300 and 700 K, the absolute value of ΔR for Pd/MgO was smaller than that for Pd/MgO_{hydr} by ∼0.2 eV. The continuous decrease of ΔR with increasing temperature for the two samples and the constantly higher absolute value of ΔR for Pd/MgO_{hydr} imply: (i) Pd particles on both surfaces grow upon annealing; and (ii) the Pd particle size on MgO_{hydr} is smaller than that on MgO(001) surface.

The initial state effect, $\Delta\varepsilon$, of Pd/MgO appeared at 0.25 eV at room temperature, and readily dropped to 0.15 eV upon annealing to 473 K. For supported metals, a combination of the following factors can account for the binding energy shifts caused by the initial state contribution: (i) original charge states of metals [230]; (ii) charge transfer between substrate and admetals [76]; (iii) surface core-level shift [73]; and (iv) metal-metal bond distance variations [231]. Noting the fact that $\Delta\varepsilon$ is positive for Pd/MgO, i.e., causing a negative shift in the binding energy, the charge transfer into Pd particle [22] and surface core-level shift are expected to be the main factors responsible for the positive $\Delta\varepsilon$ contribution. It is also mentioned that the lattice contraction could lead to a shift in the opposite direction. An indication for the presence of partial charge transfer from the MgO(001) surface to the Pd particles is clearly provided by the fact that the kinetic energies of ejected electrons from the MgO films uniformly increased by ∼0.4 eV upon Pd deposition, as summarized in Tab. 8.1. These universal upward shifts observed for the orbital energies are a characteristic sign for the occurrence of the band bending as a result of the formation of an interfacial dipole layer via the charge transfer to the Pd particles, as discussed in Section 5.3.1. Both the effect of charge transfer and surface core-level shift are expected to become less significant with increasing particle size, which is in agreement with our observation showing that $\Delta\varepsilon$ approaches zero as increasing temperature.

In contrast to Pd/MgO, $\Delta\varepsilon$ of 1.0 Å Pd/MgO_{hydr} shifted abruptly from a positive value (+0.1 eV) to a negative one (-0.1 eV) during the annealing from room temperature to 373 K, and remained negative throughout subsequent annealing to 700 K. The negative $\Delta\varepsilon$ can be accounted for by either (i) charge transfer from the Pd particles to the substrate, or (ii) the oxidation of Pd particles by surface hydroxyls. Charge transfer in the opposite flow direction

as observed for Pd/MgO is hardly feasible, because surface hydroxyls on MgO films make the surface more electron rich and hence not susceptible to accepting further electrons from Pd particles. Therefore, it is highly likely that the oxidation of Pd particles by surface hydroxyl groups, according to Eq. 8.1, is responsible for the 0.2 eV negative shift in $\Delta\varepsilon$ for Pd/MgO_{hydr} upon heating to 373 K. This characterization based on the Pd electronic structure is another proof of the thermal-induced occurrence of the metal-redox process, which leads to simultaneous D_2 evolution (Fig. 8.2a) and Pd oxidation at 400 K.

8.2.3 The Water-Gas Shift Reaction over Various Size Pd Particles on MgO_{hydr}

In order to explore chemical reactions between CO adsorbed on the Pd particles and surface hydroxyls, TPD spectra for D_2 (m/Z = 4), D_2O (m/Z = 20), CO (m/Z) = 28, O_2 (m/Z = 32) and CO_2 (m/Z = 44), from MgO_{hydr} with different amounts of Pd (θ_{Pd} = 0.001–4.0 Å) were recorded (Fig. 8.4a-e). All spectra acquired from Pd/MgO_{hydr} were subtracted from those taken from MgO_{hydr}, and the processed spectra are presented in Fig. 8.4f-j. The dashed lines in Fig. 8.4 indicate that desorption intensity from Pd/MgO_{hydr} and MgO_{hydr} were identical. Fig. 8.4k-o exhibit the total desorption intensity of each ion as a function of Pd coverage in a semilogarithmic graph. For all samples, it is noticeable that simultaneous D_2 and CO_2 desorption occurred in the temperature range of 400–700 K. This is evidence of the occurrence of the WGS reaction. As a function of Pd load, the D_2 desorption intensity increased up to θ_{Pd} = 2.0 Å, and decreased again for θ_{Pd} = 4.0 Å, for which a strong increase of D_2O and CO_2 desorption at a desorption temperature of 400 K is noted (Fig. 8.4f, g, and j). This change is indicative of an alternative reaction path that leads to enhanced D_2O and CO_2 formation, which was opened at high Pd coverages. Up to θ_{Pd} = 1.0 Å, CO desorbed from the Pd particles in the temperature range of 300–500 K. Above this coverage, CO desorption increased in intensity while losing the desorption shoulder centered at 400 K, where CO_2 desorption concurrently became larger.

In order to learn more about possible processes occurring on the surfaces during the TPD runs, the subtracted TPD spectra of D_2, D_2O and CO_2 for Pd/MgO were closely examined. The subtracted TPD spectra are summarized for 0.01 Å Pd/MgO in Fig. 8.5a. For this small Pd coverage, the desorption onset for D_2, D_2O and CO_2 appeared simultaneously at ∼500 K. While the desorption rate for D_2O and CO_2 rapidly decreased after the maximum, D_2 desorption remained rather high up to 700 K. At a higher Pd coverage of 1.0 Å, it is noted the desorption of both D_2 and CO_2 started at ∼400 K, which has been shifted from 500 to 400 K upon increasing the Pd coverage (Fig. 8.5b). In contrast to CO_2, D_2 desorption faded away gradually in the temperature range of 500–700 K, but the desorption maximum was much more pronounced as compared to the sample with the low Pd load.

In addition to the Pd coverage dependence, the effects of varying hydroxyl coverage on the WGS activity of Pd/MgO_{hydr} samples has been examined. To this end, experiments have been performed for samples with two different OD coverages, 0.6 ML and 1.0 ML OD, which were prepared by exposing well-faceted 1.0 Å Pd particles on 30 ML MgO films to either 0.05 mbar

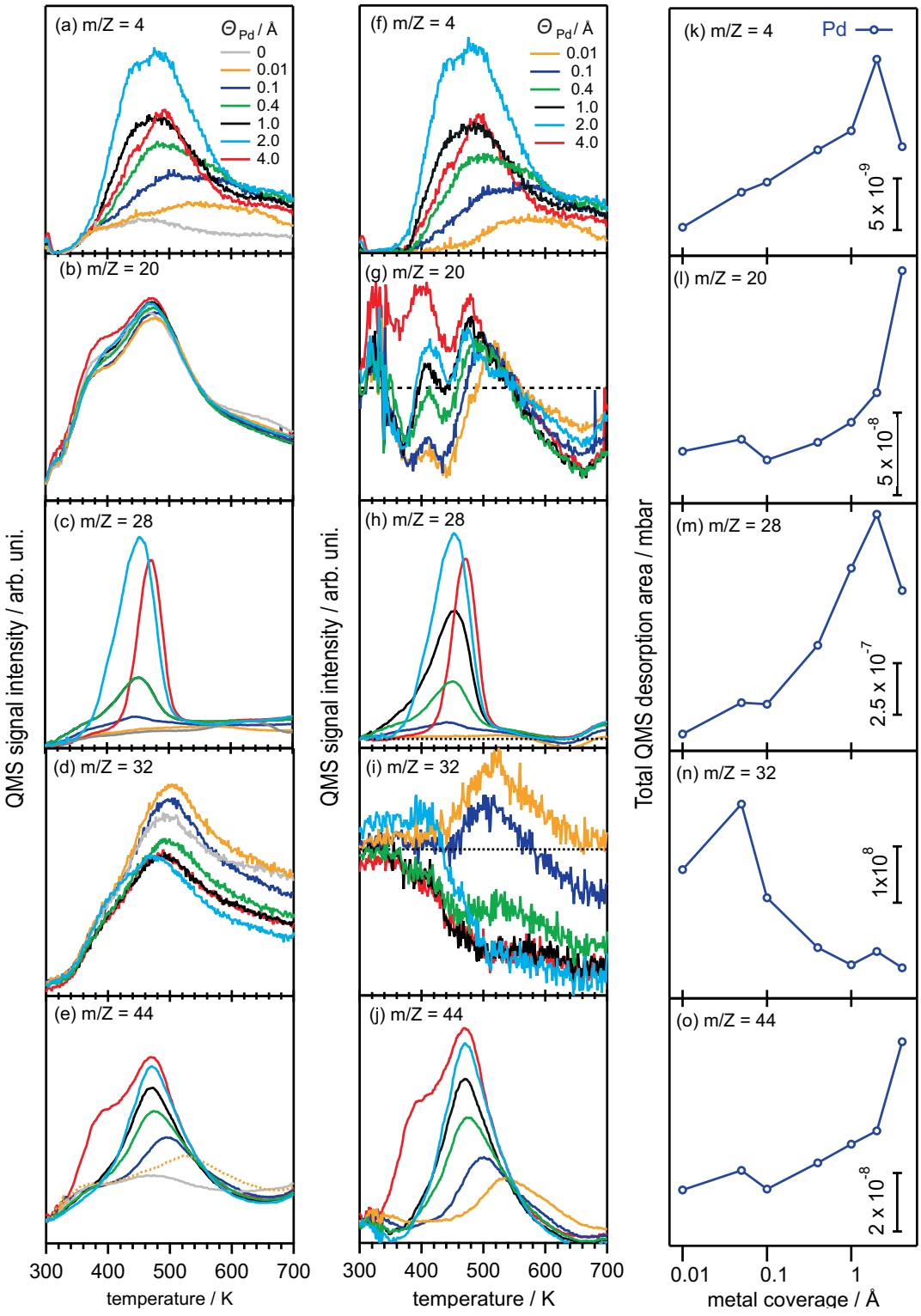

Figure 8.4: TPD spectra corresponding to (a) D_2 (m/Z = 4), (b) D_2O (m/Z = 20), (c) CO (m/Z = 28), (d) O_2 (m/Z = 32) and (e) CO_2 (m/Z = 44) from MgO_{hydr} supporting the indicated amounts of Pd. The corresponding subtracted spectra from reference spectra for MgO_{hydr} are shown in the panel (f)-(j), and each desorption area in (k)-(o), respectively.

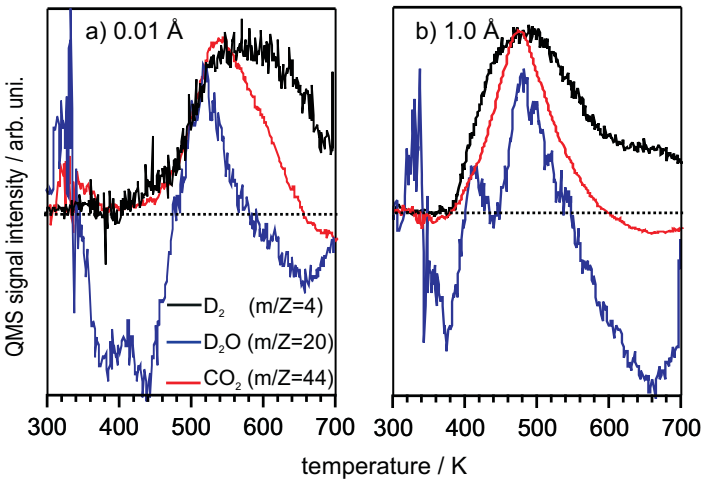

Figure 8.5: Subtracted TPD spectra of D_2, D_2O and CO_2 acquired from a) 0.01 and b) 1.0 Å Pd supported on 30 ML thick MgO film, which have been hydroxylated by 0.05 mbar D_2O at room temperature. Ramp rate was fixed at 1 K/s.

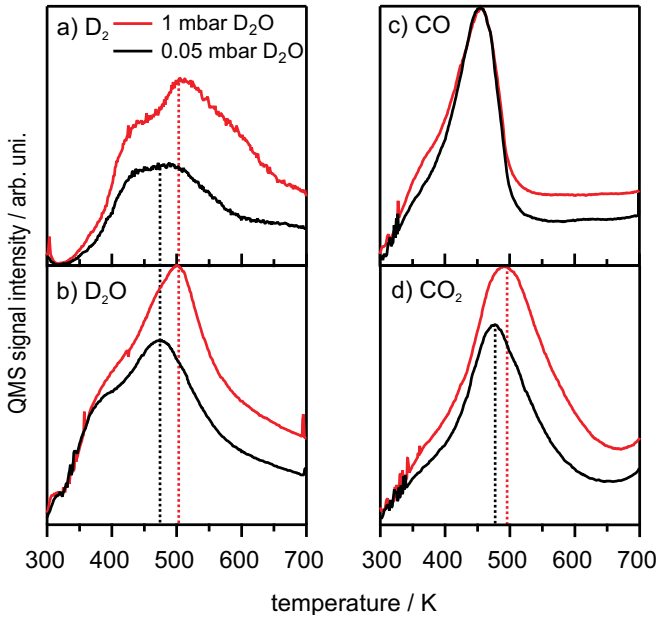

Figure 8.6: TPD spectra of a) D_2, b) D_2O, c) CO and d) CO_2 for well nucleated Pd particles at a coverage of 1.0 Å on a 30 ML thick MgO film, which has been hydroxylated by exposure to either 0.05 mbar D_2O (black) or 1 mbar D_2O (red). Ramp rate was 1 K/s.

or 1 mbar D_2O, respectively. Fig. 8.6 compares the TPD spectra of a) D_2, b) D_2O, c) CO and d) CO_2 for the two samples (black traces: 0.6 ML OD, 0.05 mbar D_2O; red traces: 1 ML OD, 1 mbar D_2O). The two samples shared similar CO desorption profiles. The other masses, however, exhibited different features among the two hydroxylated Pd/MgO samples. First, it was found that heavily hydroxylated Pd/MgO exhibited higher signal intensities of D_2, D_2O and CO_2. Furthermore, desorption maxima of these molecules were shifted uniformly by 30 K to higher

temperature as compared to the sample hydroxylated by 0.05 mbar D_2O.

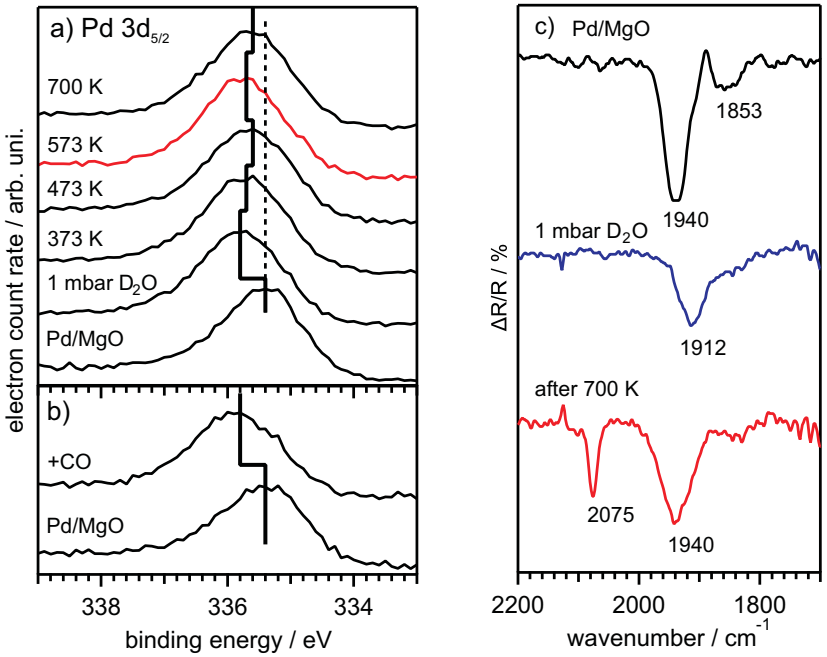

Figure 8.7: Pd $3d_{5/2}$ spectra for a) well-nucleated 1.0 Å Pd particles supported on the MgO(001) surface, which was exposed to 1 mbar D_2O at room temperature with subsequent annealing to the indicated temperatures, and b) 1.0 Å Pd supported on the MgO(001) surface exposed to 2 L CO at room temperature. c) Infrared spectra of adsorbed CO on the well-annealed 1.0 Å Pd particles deposited onto the MgO(001) film (top, black), the hydroxylated 1.0 Å Pd/MgO(001) by exposure to 1 mbar D_2O (middle, blue), and the dehydroxylated 1.0 Å Pd/MgO(001) upon annealing to 700 K (bottom, red). All spectra were taken after exposure to 2 L CO at room temperature.

In order to gain information about changes of the electronic properties of Pd caused by the WGS reaction during the TPD run, Pd $3d_{5/2}$ XP spectra were recorded from the samples consisting of well-faceted 1.0 Å Pd particles on MgO_{hydr}. The freshly prepared 1.0 Å Pd/MgO exhibited a Pd $3d_{5/2}$ binding energy of 335.4 eV, as shown in Fig. 8.7a (bottom). Its hydroxylation by exposure to 1 mbar D_2O at room temperature for 3 min caused a shift of Pd $3d_{5/2}$ binding energy to 335.8 eV. Annealing this hydroxylated sample to 373 K as well as 473 K resulted in the decreases of the binding energy by 0.1 eV, respectively. In contrast, further thermal treatment at 573 K was accompanied by *increasing* the Pd $3d_{5/2}$ binding energy to 335.7 eV. After the removal of all hydroxyls at 700 K, the Pd $3d_{5/2}$ binding energy was eventually stabilized at 335.6 eV.

The influences of hydroxylation/dehydroxylation on the morphology of the well-faceted Pd particles were examined via infrared spectroscopy using CO as a probe molecule. As shown in Fig. 8.7c (top), the pristine Pd particles after exposure to 2 L CO at room temperature exhibited two CO absorption bands at 1940 and 1853 cm^{-1}, which are assigned to CO adsorbed at bridge

and three-fold hollow sites, respectively [200]. These bands are typical for well-nucleated, small supported Pd particles. For comparison, a sample with the same Pd coverage but exposed to 1 mbar D_2O instead of CO exhibited a band at 1912 cm^{-1} of slightly less intensity (Fig. 8.7c, middle). This result confirms that the Pd particles get covered by considerable amounts of CO during the high pressure D_2O dosing. According to the IR data, the CO coverage is slightly below the saturation coverage for the Pd particles (compare top and middle traces in Fig. 8.7c). Another IRA spectrum was collected after the dehydroxylation of this sample via annealing to 700 K and subsequent exposure to 2 L CO at 300 K (Fig. 8.7c, bottom). The dehydroxylated Pd/MgO_{hydr} sample gave rise to an intense band at 2075 cm^{-1}, accompanied by a band at 1940 cm^{-1}, which are assigned to on-top and bridge sites on Pd particles, respectively. The substantial increase of the absorption intensity at 2075 cm^{-1} safely indicates the development of low-coordinated adsorption sites on the Pd particle surfaces.

The spectra shown in Fig. 8.7a confirmed the occurrence of Pd 3d binding energy shift upon hydroxylation and subsequent annealing after the removal of surface hydroxyls from MgO surfaces. In particular, the hydroxylation-induced positive Pd 3d binding energy shift is noted. This positive shift could be interpreted as oxidation of the Pd particles. However, as the infrared spectrum for the hydroxylated Pd/MgO system has proven (Fig. 8.7c, top), the hydroxylation inevitably exposed the sample to CO, which resulted in the CO-covered Pd particles. This concomitant CO adsorption during the hydroxylation could also cause positive binding energy shifts of metals, because molecular adsorption can alter the electronic structure of metals [232–234]. With the aim to clarify the reasons for observing the Pd $3d_{5/2}$ binding energy shift upon hydroxylation, the Pd 3d photoemission spectrum of well-faceted 1.0 Å Pd particles on the 30 ML thick MgO film, which were covered with a saturated amount of CO at room temperature, was acquired (Fig. 8.7b). The CO exposure induced a positive Pd $3d_{5/2}$ binding energy shift from 335.1 eV to 335.8 eV. Note that this shift is comparable to the one observed for Pd/MgO after hydroxylation (Fig. 8.7a). This coincidence indicates that the hydroxylation-induced change can be ascribed to the CO adsorption, because the oxidation of Pd particles at room temperature upon hydroxylation is very unlikely.

The spectroscopic results described above suggest that the WGS reaction occurring during the TPD run leads to irreversible changes of the electronic and morphological properties of the Pd particles, which could in turn affect the reactivity of the sample. This was checked by repeated cycles of hydroxylation by exposure to 0.05 mbar D_2O and subsequent acquisition of TPD spectra of (a) D_2, (b) D_2O, (c) CO and (d) CO_2 for well-nucleated 1.0 Å Pd particles on 30 ML thick MgO film (Fig. 8.8). Essentially, the repeated processes caused the decreases of desorption intensity of each species. It is also noted that during the second cycle, while D_2, CO and CO_2 lost their intensity by 50 % compared to the freshly prepared sample, the D_2O desorption intensity dropped only by 20 %. Furthermore, the repeated cycles of hydroxylation and annealing caused the decrease of all species in intensity, without accompanying changes of the spectral features. This suggests that these processes cause depletion of specific sites, instead of a modification of the surface properties.

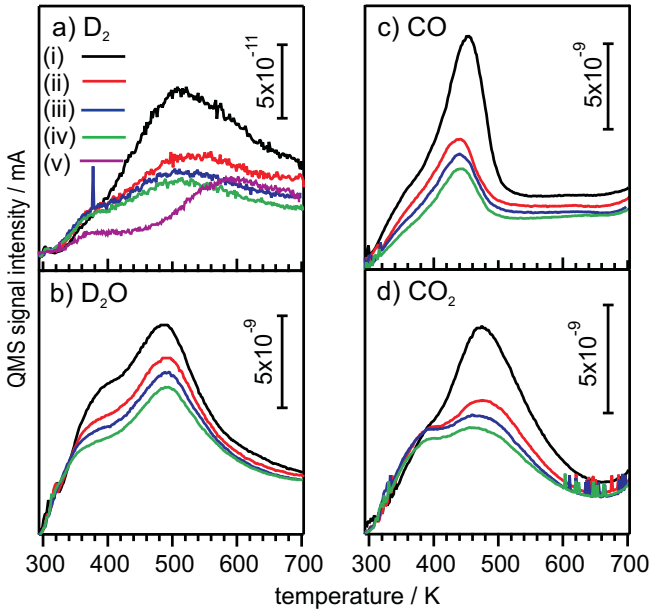

Figure 8.8: TPD spectra of a) D_2, b) D_2O, c) CO, and d) CO_2 acquired from 1.0 Å Pd/MgO(001) after repeated exposure to 0.05 mbar D_2O at room temperature. The numbers (i)-(iv) correspond to the number of the hydroxylation and subsequent TPD measurement. The D_2 desorption spectrum (v) was taken from the sample prepared as follows; well-faceted 1.0 Å Pd particles on 30 ML thick MgO film were oxidized at 423 K in an oxygen atmosphere of 5 mbar for 10 min, and subsequently were exposed to 0.05 mbar D_2O for 3 min at room temperature. Ramp rate was fixed at 1 K/s.

According to the TPD and spectroscopic results presented above, the deactivation is caused by structural and chemical modifications of the Pd particles. Assuming that the deactivation of Pd particles as a catalyst toward the WGS reaction occurs by the oxidation of Pd surfaces, a D_2 desorption spectrum was collected from a sample, where well-faceted 1.0 Å Pd/MgO was oxidized at 423 K in an oxygen atmosphere of 5 mbar for 10 min and subsequently exposed to 0.05 mbar D_2O at room temperature (Fig. 8.8a (v)). These Pd particles were found to be completely oxidized, as evidenced by its Pd $3d_{5/2}$ binding energy of 336.5 eV, which is typical of PdO phase (see Chapter 9) [207]. Compared to the D_2 spectrum (i) taken from the freshly prepared Pd/MgO_{hydr} catalyst, the suppression of D_2 formation between 400–500 K was observed for the PdO/MgO_{hydr} system. This reduction of D_2 evolution reflects either or both the necessity for the presence of metallic Pd particles or/and adsorbed CO molecules on Pd particles supported on MgO_{hydr} for the occurrence of the WGS reaction.

8.2.4 Interactions of Au with MgO_{hydr}

For comparison, the same processes as described above for Pd/MgO_{hydr} were investigated for Au deposited on MgO_{hydr}. In the panels (a) and (b) of Fig. 8.9, the corresponding OD-IRAS and D_2 TPD results are presented. In contrast to Pd (Fig. 8.1a), the deposition of up to 1.0 Å Au onto

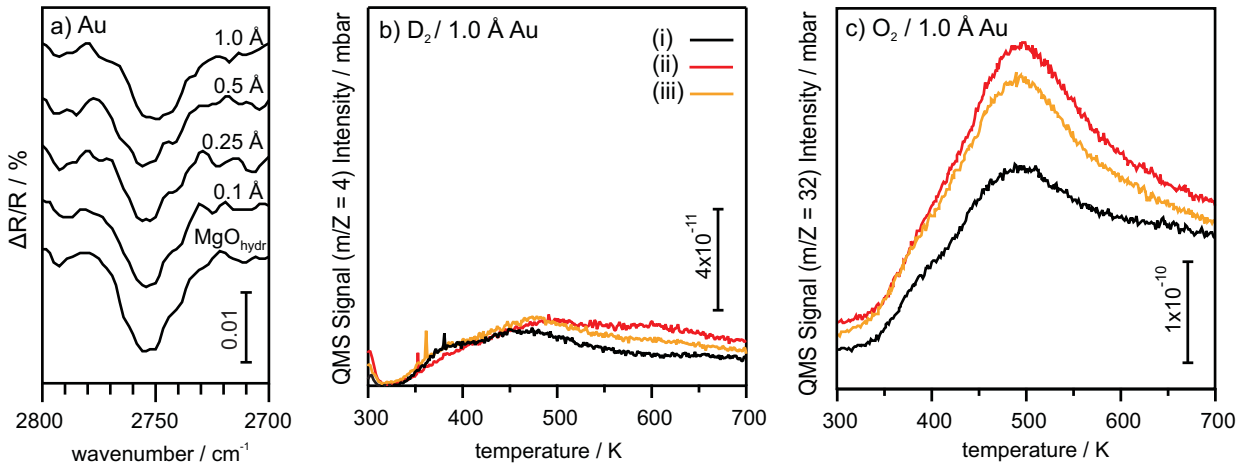

Figure 8.9: a) IRA spectra in the OD stretching region for hydroxylated 30 ML thick MgO(001) films by 0.05 mbar D_2O with subsequent deposition of Au with total nominal thicknesses of 0.1, 0.25, 0.5 and 1.0 Å at room temperature. b) D_2 and c) O_2-TPD spectra acquired from (i) MgO_{hydr}, and (ii) 1.0 Å Au/MgO_{hydr}, and (iii) well-nucleated 1.0 Å Au/MgO(001) exposed to 0.05 mbar D_2O at room temperature for 3 min. Ramp rate was 1 K/s.

MgO_{hydr} did not lead to any significant changes of the OD-IRAS signal of MgO_{hydr}, suggesting that gold does not significantly interact with the hydroxyl groups on MgO_{hydr}. Note that this behavior is different to Au deposited on MgO_{hi}, where the selective depletion of the OD vibration at 2734 cm^{-1} was observed (Fig. 7.1a). In order to check if a chemical reaction between Au and surface hydroxyls occurs at elevated temperature, D_2 TPD spectra were taken from (i) MgO_{hydr}, (ii) 1.0 Å Au deposited onto MgO_{hydr}, and (iii) well-faceted 1.0 Å Au/MgO(001), which has been subsequently hydroxylated by exposure to 0.05 mbar D_2O for 3 min. The presence of 1.0 Å Au contributed to a slight increase of D_2 desorption above 450 K. Different to Pd/MgO_{hydr}, no pronounced D_2 desorption peak developed. Note that the order of hydroxylation and Au deposition gave negligible differences in the D_2 TPD results. The obvious absence of the WGS activity is not surprising because CO will not remain adsorbed on the Au particles under the present experimental conditions. Additionally, the results indicate negligible activity of Au in the metal-redox process at slightly elevated temperatures, in contrast to the results observed for Pd/MgO_{hydr}. Nevertheless, it is noted that the desorption of O_2 from MgO_{hydr} was slightly enhanced by the presence of Au, suggesting that Au could be involved, albeit to a limited extent, in reactions with hydroxyl groups.

The influence of surface hydroxyls on the Au adsorption states was probed by XPS, in combination with the Auger parameter analysis. Fig. 8.10 summarizes the recorded Au $4f_{7/2}$ binding energies,[2] and the kinetic energies corresponding to the $^1I_6$ state of the Au $M_5N_{67}N_{67}$ Auger transition, as well as the corresponding initial and final state contributions, $\Delta\varepsilon$ and ΔR,

[2]Note that the Au $4f_{7/2}$ binding energies reported here are shifted to higher values compared to the ones reported in Chapter 6, which is most likely related to the use of thicker MgO films for the experiments reported in this chapter. Thicker films could lead to reduced screening efficiency.

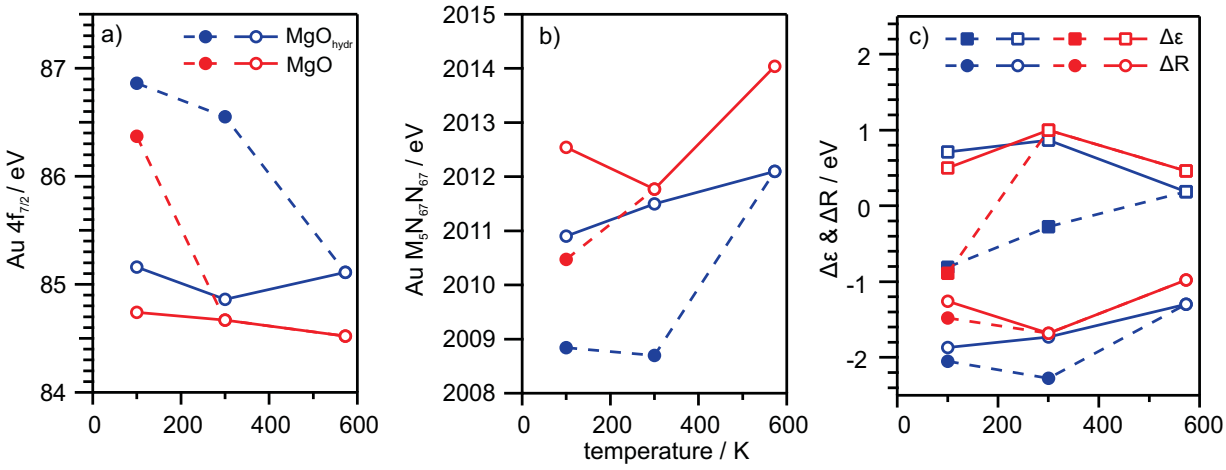

Figure 8.10: a) Au $4f_{7/2}$ binding energies, b) Au $M_5N_{67}N_{67}$–$^1I_6$ state Auger kinetic energies, and c) initial, $\Delta\varepsilon$, and final, ΔR, state contributions for 0.1 Å Au deposited onto MgO(001) and MgO_{hydr} surfaces at 100 K. The solid and open symbols represent different gold components with high and low Au $4f_{7/2}$ binding energies, respectively. All the data were collected at 100 K, after annealing to the indicated temperatures.

for 0.1 Å Au supported on MgO_{hydr} at 100 K and after subsequent annealing to 300 K and 573 K, respectively. For comparison, Fig. 8.10 contains the corresponding data for 0.1 Å Au/MgO.

Similar to Au/MgO, the freshly prepared 0.1 Å Au/MgO_{hydr} exhibited two components with Au $4f_{7/2}$ binding energies of 85.2 and 86.9 eV, respectively. In contrast to the Au/MgO sample, the two Au components survived upon annealing to 300 K. The Au $4f_{7/2}$ binding energies of the two species shifted from 85.2 to 84.9 eV, and 86.9 to 86.6 eV, respectively. After annealing to 573 K, 0.1 Å Au/MgO_{hydr} showed a single Au component at 85.1 eV. The set of Au $M_5N_{67}N_{67}$ kinetic energies for Au/MgO_{hydr} also showed similarly small shifts as a function of annealing temperature (Fig. 8.10b). Upon annealing to 300 K, the Auger line corresponding to the Au component with the higher Au $4f_{7/2}$ binding energy remained almost the same (2008.8 eV at 100 K vs. to 2008.7 eV at 300 K), whereas the other Auger line shifted from 2010.9 to 2011.5 eV. Both peaks converged into a single line at 2012.2 eV after annealing to 573 K. Note that the binding energy shifts and Auger kinetic energy shifts were consistently larger for Au on MgO_{hydr} as compared to Au on MgO(001). The initial and final state contributions are displayed in Fig. 8.10c. $\Delta\varepsilon$s observed for the as-deposited Au/MgO_{hydr} and Au/MgO(001) were rather similar, suggesting that the chemical nature of pristine gold particles was comparable, irrespective of the presence of surface hydroxyl groups. Accordingly, the corresponding ΔRs do also not show much variation. Thermal annealing to 300 K did not cause significant changes in both $\Delta\varepsilon$ and ΔR of Au/MgO_{hydr}, which indicates that neither significant Au agglomeration nor oxidation or reaction between Au atoms and surface hydroxyls occurred. After annealing to 573 K, a small $\Delta\varepsilon$ of +0.2 eV persisted, while ΔR was found still large, −1.3 eV.

Au deposition onto MgO(001) caused the band bending at the interface (see Appendix,

Table 8.2: Binding energy shifts, ΔBE, of O 1s, Mg 1s and Mg 2s states and Mg KL_1L_1 Auger kinetic energy, KE, the initial, $\Delta\varepsilon$, and final, ΔR, state contributions of the Mg ions of 30 ML thick MgO_{hydr} and 0.1 Å Au deposited onto MgO_{hydr} at 100 K. The binding energy differences of Au/MgO_{hydr} with reference to those acquired from clean MgO_{hydr} were also displayed.

condition	O 1s	ΔBE_{O1s}	Mg 1s	ΔBE_{Mg1s}	Mg 2s	ΔBE_{2s}	$KE_{KL_1L_1}$	ΔR	$\Delta\varepsilon$
MgO_{hydr}	530.3		1304.2		88.8		1103.0		
Au/MgO_{hydr} @ 100 K	530.0	−0.31	1303.9	−0.28	88.5	−0.36	1103.25	−0.1	0.5
Au/MgO_{hydr} @ 300 K	529.8	−0.51	1303.7	−0.46	88.3	−0.55	1103.4	−0.1	0.7
Au/MgO_{hydr} @ 570 K	530.1	−0.33	1303.9	−0.23	88.5	−0.37	1103.25	−0.1	0.5

Tab. C1) [133]. To reveal the influence of Au deposition on the band bending at the Au/MgO_{hydr} interface, the binding energies of O 1s, Mg 2s and Mg 1s states and Mg KL_1L_1 Auger kinetic energies of 0.1 Å Au/MgO_{hydr} at 100 K were determined as a function of annealing temperature (Tab. 8.2). Relative to the clean MgO_{hydr} surface, the Au deposition onto MgO_{hydr} induced negative binding energy shifts of the oxide components by 0.3–0.5 eV, accompanied by corresponding positive shifts of the same magnitude of the Mg Auger kinetic energies. The uniformity of the shifts points again to the occurrence of upward band bending in the oxide induced by Au deposition. This conclusion is supported by the fact that the Auger parameter analysis applied to the shifts of the Mg 1s, Mg 2s and Mg KL_1L_1 emissions resulted in almost negligible final state contributions, which means that the shifts have entirely an initial state origin.

8.3 Discussion

8.3.1 Metal-Redox Process of the Pd Particles with Surface Hydroxyls at Elevated Temperatures

The D_2 TPD results (Fig. 8.1c) clearly indicate that the metal-redox process involving Pd particles and hydroxyl groups occurs on MgO_{hydr} at a temperature of 400 K. According to Eq. 2.69, this reaction temperature corresponds to an activation barrier of ∼100 kJ/mol, which is in the same range as the calculated activation barrier for the reaction of Co with hydroxyls on Al_2O_3 surfaces [49]. This barrier prevents the Pd particles from spontaneously reacting with surface hydroxyls at room temperature, as evidenced by the lack of D_2 desorption below 350 K and the negligible consumption of surface hydroxyl groups seen in XPS (Fig. 8.1b). However, the depletion of the OD-IRAS signal upon deposition of 1 Å Pd (Fig. 8.1a) is an indication for a strong interaction between Pd and hydroxyls at room temperature. It is suggested that stable Pd-OD complexes are formed upon Pd deposition at room temperature, which, upon subsequent heating, either decompose (reappearance of OD-IRAS signals after 373 K anneal, Fig. 8.1a), or are involved in the metal-redox process leading to D_2 desorption. By D_2 titration experiments, the amount of hydroxyls contributing to the D_2 desorption centered at 400 K was estimated as

0.05 ML (or about 10 % of hydroxyls present on this surface).

This interpretation is in agreement with the conclusions that are derived from the Auger parameter analysis. At room temperature, $\Delta\varepsilon$ of the Pd on the hydroxylated MgO surface was found at +0.1 eV (Fig. 8.3c). Upon annealing to 400 K, $\Delta\varepsilon$ abruptly decreased to −0.1 eV. Noting that the negative shift in $\Delta\varepsilon$ means a positive binding energy shift and that D_2 evolution occurred in the same temperature range, the relatively small negative shift in $\Delta\varepsilon$ is readily explained by slight oxidation of the Pd particles by surface hydroxyl groups. At the same coverage of Pd, the pristine Pd particles have a Pd 3d $_{5/2}$ binding energy of 335.4 eV, whereas for PdO particles it is 336.5 eV (see Fig. 9.1b). For the latter, Auger parameter analysis revealed that the complete oxidation of the Pd particles brings about a −2.0 eV shift in $\Delta\varepsilon$ (Section 9.2.1). Hence, the extent of oxidation of Pd particles by surface hydroxyls, by which the $\Delta\varepsilon$ was shifted only by 0.2 eV, is expected to be rather small. This is not surprising because i) only a small fraction of surface hydroxyls (∼0.05 ML) was found to react with the Pd particles, and ii) only interfacial PdO is formed during the reaction. This interfacial palladium oxide phase survived even at 723 K, as indicated by the invariance in the $\Delta\varepsilon$.

Information about the thermal agglomeration and sintering of the Pd particles can be obtained from the annealing temperature dependence of ΔR (Fig. 8.3c). The continuous decrease of ΔR with increasing annealing temperature observed for Pd/MgO and Pd/MgO_{hydr} indicates that the Pd particles undergo thermal sintering on these surfaces. The fact that the absolute value of ΔR for Pd/MgO_{hydr} is always larger by 0.2 eV is consistent with the conclusion that Pd preferentially adsorbs on the strongly interacting hydroxyl sites, which diminishes the effects on sintering and results in the formation of smaller particles on MgO_{hydr}. This interpretation is fully in line with previous observations for metal adsorption on hydroxylated oxide surfaces [44, 45].

8.3.2 Mechanistic Insight for the WGS Reaction over Pd/MgO_{hydr}

For the post-hydroxylated Pd/MgO systems, the evolution of D_2 can be accounted for by the occurrence of WGS-type reactions, because: (i) the supported Pd particles were found to be covered with CO molecules (see Fig. 8.7c), which can react with surface hydroxyls on MgO_{hydr}; (ii) the D_2 desorption temperature of 500–600 K was too high for simple recombinative desorption of D atoms from Pd particles [235].

Various reaction mechanisms have been suggested for the WGS reaction. First, the very initial idea proposed decades ago that the reaction proceeds via the formation of formate ($HCOO^-$) and its subsequent decomposition into CO_2 and a hydrogen atom [236]. Panagiotopoulou et al. studied the WGS reaction over precious metals on either reducible or irreducible oxides [237]. They concluded that for metals supported on irreducible oxides, the activation energy is predominantly determined by the nature of the supported metal. This implies that the electronic and morphological characteristics of the interface do not greatly influence the reaction path and kinetics for catalysts with irreducible supports, in contrast to those using reducible oxides (e.g. CeO_2) [224]. Later on, an experimental study in collaboration with DFT calculations has

shown that carboxyl groups are possible intermediates in the WGS reaction [226]. While the studies listed above maintained the formation of reaction intermediates, some studies did propose the so-called redox mechanism, where the surfaces of supported metals are covered with oxygen atoms derived from water to eventually react with CO [225].

By post-hydroxylation of a Pd-MgO model catalyst, a situation has been created in the present study that allows investigating specific WGS-type reactions between CO adsorbed on Pd particles and hydroxyls on the MgO surfaces. Under these conditions, the peripheral Pd sites will be of particular significance. Any reactivity connected with peripheral sites requires the inclusion of the capture zone around the particles. Capture zone refers to the area around the particle, from which molecules captured on the support are able to reach the particle via surface diffusion [238–240]. In the present case, CO is exclusively adsorbed on the surface of the Pd particles, whereas the hydroxyls are exclusively present on the MgO support. If present, capture zone effects will, therefore, mainly concern the diffusion of hydroxyls to the Pd particles. In the following, an analysis of the Pd particle size-dependent reactivity of Pd-MgO model catalysts is presented, which allows concluding that for the systems studied here, and under the given experimental conditions, the WGS reactivity is closely related to the perimeter length of the Pd particles. As shown in Fig. 8.4, there is a linear correlation between the amount of evolved D_2 (and CO_2) and the logarithm of the Pd coverage. For D_2, the corresponding semi-logarithmic function for the Pd coverage range 0.01–1.0 Å can be expressed as:

$$\begin{aligned} I_{D_2} &= (4.6 \times \log_{10}\theta_{Pd} + 12.7) \times 10^{-9} \\ &= 12.7 \times (0.37 \times \log_{10}\theta_{Pd} + 1) \times 10^{-9} \end{aligned} \tag{8.3}$$

where I_{D_2} indicates the subtracted D_2 desorption intensity shown in Fig. 8.4k, and θ_{Pd} is the coverage of Pd in Å. The value of the coefficient is 0.37, which means that the amount of evolved D_2 is roughly proportional to $\theta_{Pd}^{1/3}$. With the assumption that all the particles have the same size at each Pd coverage and the Pd island densities are the same in the entire Pd load, $\theta_{Pd}^{1/3}$ suggests that the catalytic reaction occurs at the periphery of Pd particles. This is because $\theta_{Pd}^{1/3}$ can be simply transformed into r_{Pd}, $\theta_{Pd} = N \times 2\pi r_{Pd}^{3/2}/3$, where N is the number of Pd particles and r_{Pd} is the radius of ideally hemispherical Pd particles. The small positive deviation from the ideal value (0.37 compared to 0.33) might be due to a small additional contribution from capture zone effects, for example the diffusion of OD groups or D atoms to the Pd particles. Computational studies have, however, shown that this is very unlikely [241]. This semi-logarithmic relation fails to correctly describe the D_2 desorption intensity, if the capture zones of individual particles start to overlap. For the present system, this transient seems to be crossed in the Pd load of 2–4 Å. In order to confirm the reliability of this analysis, we checked the multiplier for CO desorption, finding a power factor of 0.58. This value is close to 2/3, as expected for a process that is linearly depend on the surface area.

Next, the desorption profiles of the individual species are more closely examined in order to gain more mechanistic insight into the reactions occurring on the post-hydroxylated Pd-MgO model catalysts. In Fig. 8.6, the TPD spectra obtained for two different hydroxyl coverages, 0.6

ML and 1 ML, are displayed. The increase of D_2O pressure resulted in upward shifts of the D_2, D_2O and CO_2 desorption maximum from 470 K to 500 K. The simultaneous shift of the D_2 and CO_2 desorption maximum is a good indication for the presence of the usual WGS pathway (CO + OD $\rightarrow$ CO_2 + 1/2D_2) in the temperature range of maximum desorption rate. An interesting point to mention is the close correlation between maximum O_2 desorption and maximum D_2 and CO_2 desorption. This observation indicates that an important parameter for the main WGS activity is the activation of surface OD groups. A closer look at the D_2 and CO_2 desorption profiles reveals that, although they exhibit the same maximum desorption temperature, the D_2 desorption profile is significantly broader than the CO_2 one. This suggests that in addition to the usual WGS reaction, other surface processes contribute to D_2 production. More information about possible side reactions is extracted from the Pd coverage dependence.

For Pd/MgO_{hydr} with a low Pd coverage (e.g., 0.01 Å), one finds the following two points (Fig. 8.5a): (i) the CO_2 and D_2 evolution simultaneously started at 500 K; (ii) the D_2 desorption was extended to higher temperature, in which region little CO_2 desorbed. The simultaneous development of CO_2 as well as D_2 signals is safely assigned to the usual WGS reaction via the involvement of both CO and OD in the D_2 formation. By contrast, the high temperature D_2 desorption, which is not accompanied by CO_2 desorption, must be related to a D_2 formation process, in which adsorbed CO molecules are not involved. Considering that increasing the Pd load resulted in the increase of D_2 desorption intensity as well as the decrease in D_2O desorption rate (above 500 K), the occurrence of oxidation of Pd surfaces by surface hydroxyls and subsequent recombination of D atoms is anticipated. Indeed, the reaction-induced oxidation of Pd particles is highly likely, supported by observing upward shifts in Pd 3d binding energy (Fig. 8.7a) and the development of defective Pd particles, which is more closely explained.

8.3.3 Deactivation Mechanisms of Pd Particles in the WGS reaction

The WGS-type interactions lead to strong irreversible deactivation of the Pd-MgO surface, as demonstrated by the repeated water dosing experiments shown in Fig. 8.8. It is notable that in addition to CO, D_2, and CO_2, also the D_2O desorption intensity decreases during repeated cycles of water dosing. The pristine MgO surface is obviously highly reactive toward water dissociation, and repeated annealing and water dosing transforms the MgO surface into a less reactive state. However, the smaller hydroxyl coverage, hence a limited supply of hydroxyl groups, on the MgO surface seems not to be the main factor governing the deactivation of the surface. Quantitative comparison of the TPD data reveals that the loss in CO, CO_2 and D_2 during the cycling is strongly correlated, whereas the D_2O loss shows significant deviation. Therefore, the deactivation must be correlated with changes in the properties of the Pd particles, and in particular their CO adsorption capacity, as the TPD data suggest.

An explanation based solely on the decreased supply of CO holds as long as the microscopic catalytic activity of the Pd particles does not change. However, the catalytic activity of Pd particles should be altered if the morphological and electronic properties of Pd particles are

changed. For instance, it has been pointed out that carbon-covered Pd particles, instead of clean Pd surfaces, exhibit ordinary reactivity [242]. Indeed, the present study confirmed the changes of the surfaces of Pd particles induced by the TPD run. The CO adsorption on the Pd particles probed by infrared spectroscopy shows that the hydroxylation/annealing process increases the population of on-top adsorbed CO, at an expense of multi-coordinated adsorption sites for CO molecules (Fig. 8.7c). This observation could be accounted for either by (i) the reaction-induced development of ill-faceted Pd particles [95], and/or (ii) poisoning of the Pd particle surface by carbon or oxygen atoms, which block multiple-coordinated adsorption sites [50, 243]. One key observation regarding the change of Pd surface states was provided by XPS, by which a positive Pd 3d binding energy shift by ∼0.2 eV was observed after the WGS reaction (Fig. 8.7a). More defective Pd particles than the initially prepared ones are expected to give negative Pd 3d binding energy shifts, according to the surface core-level shift. On the other hand, previous studies investigating PdC [243] and PdO surfaces exhibited shifts of Pd 3d binding energy in the same direction as observed in the present study. From a perspective of Pd chemical shift, the occurrence of poisoning of the Pd particles is likely, although it is not clear which atoms, carbon or oxygen, are responsible for the effects on lowering the activity of the system in the WGS reaction. In summary, either the amount of CO adsorbed on Pd particles or their activity alternations can account for the deactivation of the systems in the WGS reaction.

An earlier work studying the WGS reactivity of Pt/MgO agrees with the importance of hydroxyls in the WGS reaction; there is a positive correlation between the activity of a catalyst in the WGS reaction and the coverage of bridging hydroxyls, suggesting that their direct involvement in the reaction at Pt particles is a key step [244]. Furthermore, they found that this additive Pt prompts hydrogen evolution at ∼550 K, at which temperature the present Pd/MgO_{hydr} system also evolved D_2. These results are in line with the present experiments with different OD coverages (Fig. 8.6). Irrespective of the species causing the deactivation, it is clear that the inefficient accommodation of CO molecules over the supported Pd particles induced by the process could lead to the deactivation of the system. This hypothesis is in agreement with the simultaneous changes of desorption intensity occurring for the other molecules (CO_2 and D_2) to the same extent. It is noted that the change occurred for the Pd particles was induced by the WGS reaction, because the simple adsorption/desorption of CO molecules onto/from the Pd particles induced negligible changes in CO-IRAS spectra (data not shown).

For the Pd/MgO systems with different Pd coverages, the gradual shift of the D_2 desorption peak from 600 to 500 K was observed upon increasing the Pd coverage to 1 Å (Fig. 8.4a). This shift was accompanied by the CO_2 formation starting at 400 K, suggesting that the main path yielding D_2 obeys to the usual scheme for the WGS reaction. While this low temperature D_2 evolution became larger as the coverage increased, D_2 formation above 550 K was still observed for 1.0 Å Pd/MgO_{hydr}. Interestingly, similar to 0.01 Å Pd/MgO_{hydr}, the D_2 evolution at higher temperatures did not, again, require simultaneous CO_2 formation. This observation supports the conclusion about the presence of the two schemes leading to the D_2 evolution, the usual WGS reaction at low temperature and the metal-redox process at higher temperature,

leading to the D_2 evolution. This conclusion is supported by the TPD result for the post-hydroxylated oxidized Pd-MgO sample (Fig. 8.4a, purple trace), where the usual WGS pathway is suppressed because the Pd sites are blocked by oxygen (this gives rise to CO_2 and water formation at 400 K, see Chapter 9), whereas the high-temperature D_2 evolution is unchanged. At higher Pd coverages, the amount of adsorbed CO on Pd/MgO_{hydr} increases so that the D_2 evolution at lower temperature ascribed to the WGS reaction becomes dominant. In addition, it is mentioned that the amount of concomitant formate on the MgO surface did not increase with increasing Pd coverage. This invariance ensures that the WGS activity is unrelated to the formate contamination on the MgO surface.

Lastly, how the decoration of the surfaces of Pd particles have an effect on D_2 evolution is discussed. The complete transformation of Pd particles into PdO phase suppressed D_2 evolution at 500 K observed for pristine Pd/MgO_{hydr} samples, while the tail of D_2 desorption at ∼600 K was preserved well (Fig. 8.7a, trace (v)). The discussion above makes it certain that the prevention of CO adsorption on PdO surfaces was the suppression of D_2 evolution at 500 K. On the other hand, the fact that PdO/MgO_{hydr} did give rise to a comparable amount of D_2 at ∼600 K clearly suggests the presence of another mechanism, such as formate decomposition and the oxidation of Pd surfaces by surface hydroxyl groups at the higher temperature.

8.3.4 Electronic Structure of Au Weakly Interacting with Surface Hydroxyls

At the end of this Chapter, the influence of hydroxyl groups formed on MgO_{hydr} on the properties of deposited Au will be discussed. Distinct from Au/MgO_{hi}, observing the OD signals after the Au deposition is an indication for no, or only very weak interaction between Au and hydroxyl groups on MgO surfaces. Moreover, while the interaction of hydroxyls with Pd gave a noticeable amount of D_2 formation, little enhancement in D_2 formation occurred for Au/MgO_{hydr}. However, the O_2 desorption intensity from 1.0 Å Au deposited onto MgO_{hydr} was found to be much larger than that from Pd/MgO_{hydr} (Fig. 8.4n and Fig. 8.9c). These facts might imply the occurrence of some spontaneous reactions as the evaporated "hot" Au atoms interacted with surface hydroxyls. Indeed, hydrogen atoms weakly interact only very with neutral Au clusters [245]. Hence, the Au deposition onto MgO_{hydr} would lead to a spontaneous reaction with hydroxyls, accompanied by an immediate release of D_2. The remaining oxygen might then act as anchoring sites on the MgO_{hydr} surface and be released at elevated temperatures, possibly due to the instability of adsorbed oxygen atoms on the surfaces of Au particles under UHV environment.

Information about possible effects of hydroxyls on the electronic properties of Au is provided by the XPS and Auger parameter data (Fig. 8.9). Comparing $\Delta\varepsilon$ and ΔR of Au/30 ML MgO to those of Au/MgO_{hydr} revealed that the Au $4f_{7/2}$ binding energy of Au/MgO_{hydr} was slightly higher (∼0.4 eV) than that for Au/MgO at any temperatures. Auger parameter analysis revealed that the main contribution to this upward shift comes from reduced screening effects (Fig. 8.9c). From this data, it is concluded that the Au formed smaller particles on MgO_{hydr} as compared to MgO(001) due to limited agglomeration of gold particles resulting from moderate interactions

of Au adatoms with surface hydroxyl groups or limited diffusion of Au on MgO_{hydr} because of hydroxylation-induced surface roughening (see Chapter 5) [44, 45, 148]. The contribution of hydroxyls in hampering Au agglomeration manifested also in observing little changes in Au $4f_{7/2}$ binding energy, ΔR and $\Delta\varepsilon$ when the Au/MgO_{hydr} sample was heated to 300 K, where no surface hydroxyl groups were thermally removed, in contrast to the behavior of Au observed for Au/MgO (Fig. 8.10).

In addition to the effect of hydroxylation on the Au particles size, oxidation of Au atoms and charge transfer between Au atoms and surface hydroxyls should be considered. Bulk gold tri-oxide, Au_2O_3, has an Au $4f_{7/2}$ binding energy of 85.9 eV [205]. In the present study, the Au $4f_{7/2}$ binding energies of as-deposited Au species were higher than this value. However, both samples (Au/MgO_{hydr} and Au/MgO) exhibited quite comparable $\Delta\varepsilon$, -0.8 eV. The compromise over these observations is that the oxidation of Au by surface hydroxyls was negligibly little, if any. Otherwise, Au deposition onto the MgO(001) surface *coincidently* provided the same Au $4f_{7/2}$ binding energy shift and initial state contributions, as Au/MgO_{hydr}. This is hardly expected. Instead, it is likely that charge transfer between the surface hydroxyls and Au atoms determines the electronic structure of supported Au particles.

In light of charge transfer, the upward shift of Au $4f_{7/2}$ binding energy, accompanied by increasing $\Delta\varepsilon$, observed for Au/MgO_{hydr} is an indication for the presence of strong electron trapping sites, in analogous to MgO(001). Over MgO(001) surfaces, several possible sites with an ability of trapping electrons have been theoretically suggested: the F^{2+}, and grain boundaries [189, 193, 246–248]. The hydroxylation of MgO(001) should preferentially deplete these electron trapping sites, owing to their high activity towards electron donor species such as hydroxyls, water [249]. Despite the depletion of these potential electron trapping sites, the newly formed hydroxyls can also lower the ionization potential of Au (4.06 eV) by a similar amount as, for example, edge sites (4.82 eV) [189]. Note that bulk metallic Au has an ionization potential of 9.22 eV. Furthermore, these surface hydroxyl groups are capable of trapping an electron with a comparable efficiency as F^{2+} centers [248]. Hence, the resemblance of the electronic structure of gold on MgO(001) and MgO_{hydr} surfaces is considered to be caused by: partial charge transfer from Au atoms to (i) F^{2+} centers and grain boundaries on the MgO(001) surface, and to (ii) surface hydroxyl groups over MgO_{hydr}.

A recent theoretical study found that the adsorption energy of an Au_{13} cluster on $Mg(OH)_2$ is $\sim$0.8 eV per one Au-OH bond. The adsorption is accompanied by partial electron transfer from the anchored Au atoms to surface hydroxyl groups on $Mg(OH)_2$ by as much as 0.15|e| [52]. According to Eq. 2.69, the Au_{13}/OH complex should be stable up to $\sim$300 K. The rather high stability and the direction of charge flow are in agreement with the observation made in this study. Although the direct interaction of surface hydroxyls with Au atoms resulted in electron transfer to surface hydroxyls, the opposite charge transfer from hydroxyls to the Au_{13} particle as a whole was also expected to occur [52].

This theoretical model considered only charge density differences between the gas-phase Au cluster and the Au cluster deposited on $Mg(OH)_2$, but not for the Au cluster deposited on

regular MgO(001). According to the present results using Auger parameter analysis, negatively charged Au particles were present on both MgO(001) and MgO_{hydr} at 100 K, in addition to the positively charged particles. No conclusive statement can therefore be made about additional electron transfer processes from the hydroxylated MgO surface to the Au. In summary, the results presented here indicate that positively charged Au species are formed on MgO_{hydr} by interaction of Au with hydroxyls. Similar to the observations made for Au deposited on MgO_{hi}, the hydroxylation appears to favor the stabilization of small Au particles on MgO_{hydr}.

8.4 Conclusions

We have studied the direct interaction of Pd atoms upon their collision with surface hydroxyl groups by means of vibrational spectroscopy, electronic structure determination and thermal desorption. The Pd particles were found to preferentially adsorb to surface hydroxyl groups at room temperature, forming Pd-OD complexes. The metal-redox reaction started at temperatures above 400 K, where the Pd-OD complexes were able to react to yield interfacial Pd oxide and D_2 molecules, in accordance with Eq. 8.1. Furthermore, in the presence of adsorbed CO molecules, the WGS reaction occurred, as evidenced by the simultaneous evolution of D_2 and CO_2 at 500 K. At higher temperature around 600 K, D_2 evolution was accompanied by little CO_2, suggesting that the metal-redox reaction, instead of the WGS reaction, was responsible for the D_2 formation. Furthermore, it was found that the Pd/MgO surface was irreversibly poisoned during the WGS reaction, causing the deactivation of the system.

In contrast to Pd, the interaction of Au with MgO_{hydr} is rather weak. Gold deposition on MgO_{hydr} did not greatly affect the hydroxyl groups, nor was clear evidence for the occurrence of metal-redox processes or WGS-type interactions found. However, the electronic structure methods provided some evidence for the presence of oxidized gold species. Those were probably formed directly during Au deposition. The extent of Au oxidation was smaller for Au/MgO_{hydr} than for Au/MgO_{hi}, which is most likely related to the different chemical properties of the hydroxyls on the two surfaces.

Chapter 9

Oxidation of Pd, and the Reduction with Water

A comprehensive study using IRAS, XPS and TPD, was performed on the reaction of oxidized Pd particles on MgO and oxidized Pd(111) single crystal surfaces with water vapor at near-ambient pressure. Upon exposure to water (D_2O) vapor in the mbar range, only the very surface layers of the oxidized Pd reacted with water molecules to form highly reactive surface hydroxyl species, which readily reacted with concomitant CO to form carbon species such as formate. The hydroxylated (and functionalized) PdO surfaces were found to be thermally less stable than the corresponding "clean" PdO surfaces and hydroxylated/oxidized Pd particles decomposed at slightly lower temperature than the hydroxylated bulk PdO crystal.

9.1 Introduction

The interplay of oxygen and water on metal surfaces has been a central issue of studies in surface chemistry for decades, motivated by, for instance, the desire for control over redox chemistry at the interface which plays a decisive role in interfacial chemical reactions [197, 250, 251]. As a prototypical model, noble metal surfaces (e.g., Pt, Ru) are frequently employed, because of their robust and multi-modal complex chemical activities [2]. In sharp contrast to Pt and Ru, much less attention has been directed at the water/Pd interface, because the fact that Pd is easily corrugated makes its importance low [252]. However, recent development in the materials used in electrochemistry has found that Pd can enhance catalytic activities in, for example, fuel cell, for which detailed knowledge on water/oxygen covered Pd interface is required [253, 254].

The knowledge obtained from the metal/liquid interfaces could be potentially extended to more complex systems, i.e., the oxide/liquid interface. One of the potential fields of interest lies in wet-chemical catalyst preparation, where supported metals react with not only water molecules but also surface hydroxyls upon activation. This key step of catalyst synthesis has been recently vigorously studied using surface science techniques [60, 255, 256]. Indeed, the catalytic performance of supported metal particles for oxidation reaction is greatly tuned by

their transformation from PdO or Pd complexes into metallic Pd [257, 258]. Considering the fact that these preparations are inevitably accompanied by interactions with water molecules as well as surface hydroxyls on the oxide supports, the interactions of supported Pd or PdO particles with water and surface hydroxyls under ambient conditions should help to advance understanding these phenomena.

The behavior of oxygen molecules and atoms on Pd in terms of catalytic reactions, such as CO or methane oxidation, on the Pd(111) surface is well documented [207, 259–265] as well as supported Pd particles [201, 266]. Briefly, the chemisorption of oxygen atoms occurs until saturation coverage (0.25 ML) is achieved with the formation of a p(2×2) phase. Surface palladium oxide is developed by further exposure of Pd surfaces to oxygen, followed by the formation of a stable Pd_5O_4 phase at 600 K. Further increase of oxygen concentration leads to the formation of a subsurface oxide phase. By increasing the oxygen chemical potential, a PdO phase with a thickness of several tens of ML is formed. This was first successfully studied after the development of UHV machinery which could also be used for studies at elevated pressures [267, 268].

A few studies on the interaction of water with oxygen covered Pd surfaces have been performed in the last decades [209, 260, 269–273]. Three early spectroscopic studies found that water interacting below room temperature with surface oxygen on single crystalline Pd surfaces resulted in the formation of two kinds of hydroxyl groups [269–271]. Complex chemistry regarding the coverage of atomic oxygen and hydrogen-bonding upon the formation of surface hydroxyls was also documented [269], and the surface reaction mechanisms for the interaction amongst H, O and OH were inferred [270]. The properties of these systems were further investigated from the perspective of photochemistry [271]. This research found that the fate of adsorbed water on Pd(111) under UV irradiation is determined by surface species; clean Pd(111) surfaces allow water molecules to be photo-dissociated, while the presence of atomic oxygen on Pd(111) switches the reaction path of water to its photo-induced desorption. Regarding the interactions of the mixture of water and oxygen over a Pd surface, which is quite important in terms of suppressing the methane combustion, however, to the best of our knowledge, there is no study on this topic conducted under ambient environments using well-defined models.

In this work, an experimental study of the oxidation and subsequent hydroxylation (D_2O) of supported Pd particles on thick MgO/Ag(001) films and a Pd(111) surface in ambient environments was carried out. A combination of infrared reflection absorption spectroscopy (IRAS), x-ray photoelectron spectroscopy (XPS), and temperature programed desorption (TPD) was employed to investigate the influence of hydroxylation in the mbar range on the chemical composition and stability of the Pd particles and the Pd(111) surface. The results reveal that exposure to water at room temperature results in the hydroxylation of the surface PdO layers, while the inner PdO phase remains intact. The surface hydroxyl groups readily react with concomitantly introduced CO to form d-formate or carbonic acid ions. It is found that the hydroxylated (and functionalized) PdO surfaces are thermally less stable than the corresponding "clean" PdO surfaces and that hydroxylated/oxidized Pd particles decompose at slightly lower temperature than the hydroxylated/oxidized bulk Pd single crystal.

9.2 Results

9.2.1 Oxidation of Pd Particles and Pd(111) Surfaces and Their Hydroxylation

First, information is provided about oxidation of the Pd(111) surface and well-faceted Pd particles with a nominal thickness of 1.0 Å supported on 30 ML thick MgO(001) films grown on an Ag(001) surface by means of XPS acquired at an electron take-off angle of 85 degrees. Pd 3d XP spectra of the pristine Pd(111) surface and the surface oxidized at an oxygen pressure of 5 mbar and a substrate temperature of 673 K for 10 min, denoted PdO_{hev} hereafter, are displayed in Fig. 9.1a. The spectra of the Pd particles and PdO particles produced at the same O_2 pressure and a temperature of 423 K for 10 min are shown in Fig. 9.1b. From the nominal coverage of Pd and on the basis of previous studies [40, 199], it was estimated that the well-faceted pristine Pd particles were estimated to have a diameter of ∼2.5 nm and to be composed of ∼150 Pd atoms (∼50 % Pd atoms belong to the surface layer). The Pd $3d_{5/2}$ binding energy of clean Pd(111) appeared at 335.2 eV, accompanied by a plasmon loss with an excitation energy of 6.5 eV [274]. The asymmetrical feature of the metallic Pd 3d peaks is due to the excitation of electrons at the Fermi edge, which manifests in a tail in the XP spectra at lower kinetic energy [275]. The spin-orbit coupling constant was found to be 5.24 eV [72]. After the oxidation process, a component at a Pd $3d_{5/2}$ binding energy of 336.8 eV developed in intensity in agreement with a previous study [207]. The simultaneous formation of two satellites with energies of 3.7 and 7.5 eV due to interband transitions in the oxide [260], and the simultaneous disappearance of the plasmon loss and the peak asymmetry should also be noted.

A similar tendency was observed for the Pd particles (Fig. 9.1b). The supported metallic Pd particles exhibited a higher binding energy of 335.5 eV due to the limited screening efficiency of core holes (see Fig. 8.3). The oxidation of the supported particles removed most of the signals corresponding to metallic Pd, and yielded a new component at a Pd $3d_{5/2}$ binding energy of 336.6 eV, attributed to PdO [207]. The XP spectra obtained from the supported Pd particles were fitted using two components: metallic Pd at a binding energy of 335.2–335.3 eV and oxidized Pd species above 336.5 eV. The oxidation of the Pd particles left a trace amount of metallic Pd: from the Pd 3d intensity ratio of Pd^{2+}/Pd^0, it can be concluded that ∼90 % of Pd atoms were in the state of Pd^{2+}.

The interaction of water with the PdO surface under ambient conditions was further investigated using IRAS. Fig. 9.1c illustrates the IRA spectra of the PdO particles and PdO_{hev}, and the Pd(111) surface oxidized under the same conditions as the PdO particles, called the PdO_{lig}, to which the subsequent hydroxylation had been applied. PdO_{lig} seemed to be covered with oxygen atoms, without creating any bulk PdO phase [207]. There were two common absorption bands at 2160 and 1400 cm^{-1} among the three samples. The band at 2160 cm^{-1} could be attributed to either the C-D stretching vibration of deuterium formate ($DCOO^-$) [276], or CO adsorption on PdO species [199, 201, 202]. The band at 1880 cm^{-1} observed for the hydroxylated PdO_{lig} is typical for CO molecules on metallic Pd surfaces. This observation indicates that concomitant

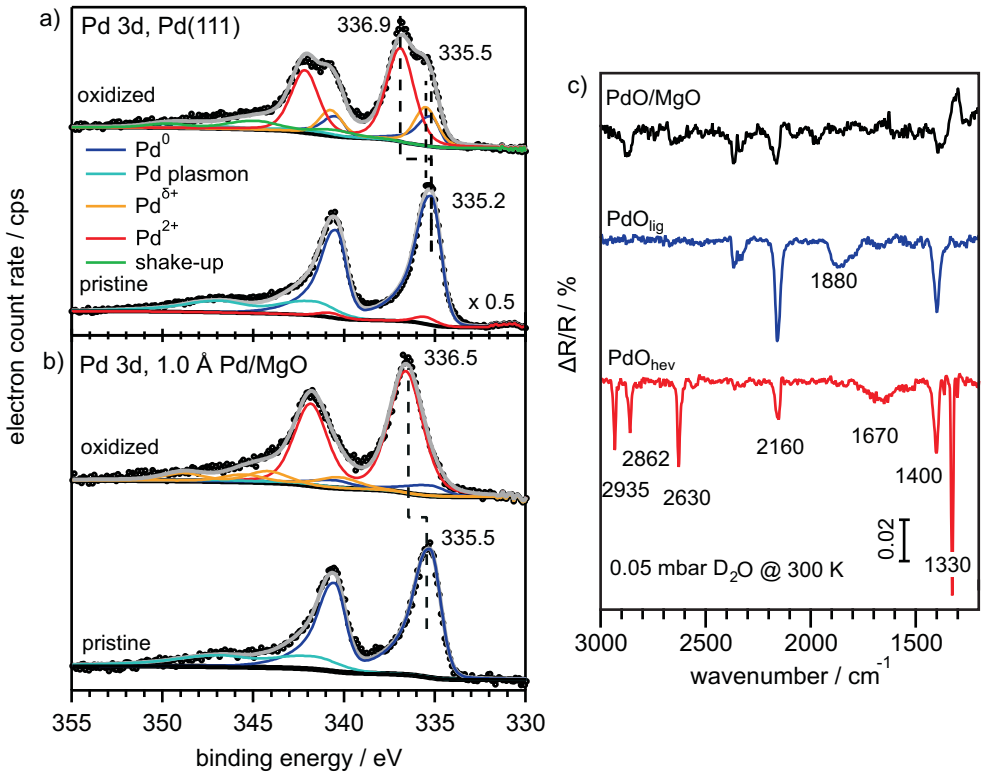

Figure 9.1: Pd 3d XP spectra for a) the Pd(111) surface and b) Pd particles at a coverage of 1.0 Å on MgO films before and after the oxidation carried out at an O_2 pressure of 5 mbar and substrate temperatures of 423 and 673 K for the Pd-MgO system and the Pd(111) surface, respectively. c) IRA spectra taken after the oxidized Pd-MgO system and Pd surfaces (PdO_{hev}) exposed to 5 mbar D_2O vapor. PdO_{lig} referred to the sample that the Pd(111) surface was oxidized under the same conditions as the supported Pd particles with the subsequent hydroxylation.

CO contained in the water vapor adsorbed on the surfaces during the exposure. The absorption at 2630 cm^{-1} was tentatively assigned to the O-D stretching mode. Previous investigations reported that surface hydroxyls on a palladium surface, which could be formed by reaction of water with surface atomic oxygen, are in a frequency range of 2400–2500 cm^{-1} [269–271]. These hydroxyls were, however, unstable above room temperature. Considering that the O-D stretching vibration observed in the present study appeared at higher wavenumber compared to the previous studies, the species corresponding to this band is tentatively assigned to deuterium exchanged carbonic acid ion (DCO_3^-). As documented in Section 9.3, these observations suggest that the PdO surface reacts with both water (D_2O) and CO, resulting in the functionalization of the surface with formate and carbonic acid ions. Furthermore, the adsorption of CO onto metallic Pd sites occurred only for PdO_{lig}, and for the other two samples, PdO_{hev} and the PdO particles, other concurrent components at 2630 and 2862 cm^{-1} were observed. This indicates the similarity between PdO particles and PdO_{hev}, instead of PdO_{lig}. Additionally, it is mentioned that, as theoretically anticipated [272], no water was dissociatively adsorbed on clean Pd(111), excluding any contribution of the non-oxidized Pd surface in the formation of the carbon species

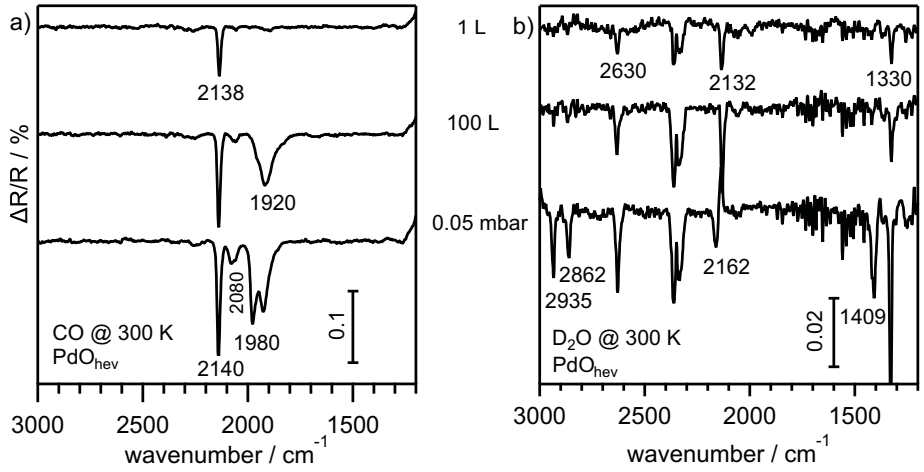

Figure 9.2: IRA spectra of PdO_{hev} after exposures to 1 L, 100 L, and 0.05 mbar (a) CO and (b) D_2O at room temperature. Each spectrum was acquired at room temperature.

under ambient environments (data not shown).

In order to get an idea about the origin of the observed IRAS signals, the interaction of PdO_{hev} with CO and D_2O was investigated over a wide pressure range. Fig. 9.2a displays the infrared spectra of PdO_{hev} after exposure to CO molecules at room temperature. A CO absorption band at 2138 cm^{-1} developed after exposure to 1 L CO, assigned to CO adsorbed with O atoms [199, 201, 202]. An additional signal at 1920 cm^{-1}, typical for CO on metallic Pd surfaces, appeared after subsequent exposure to 100 L CO [95]. Further exposure of PdO_{hev} to 0.05 mbar CO produced a lot of metallic Pd sites characterized by the CO absorption at ∼1980 cm^{-1}, accompanied by a small signal at 2080 cm^{-1} (Fig. 9.2a). Note that there were no signals, which are unusual for CO molecules on Pd surfaces.

1 L D_2O exposure of PdO particles produced bands at 2630, 2132, and 1330 cm^{-1} (Fig. 9.2b, top). Note that the signals are weak compared to CO/PdO_{hev}. Further exposure to 100 L D_2O changed only their absorption intensities, indicative of the absence of changes in the surface properties. The dramatic change occurred at a D_2O pressure of 0.05 mbar, where the band at 2132 cm^{-1} seemed to be blue-shifted to 2162 cm^{-1}, with the simultaneous formation of components at 2935, 2862, and 1409 cm^{-1} (Fig. 9.2b, bottom). Note that there was no CO adsorption ascribed to metallic Pd particles, indicative of the inertness of bulk PdO toward water vapor.

9.2.2 Thermal Reduction of Hydroxylated PdO_{hev} Surfaces

Information on the thermal stability of the hydroxylated and non-hydroxylated PdO_{hev} surfaces was obtained by various methods. A summary of the annealing-temperature dependent surface composition of PdO_{hev}, displayed as the relative portions of the individual Pd components as determined from the XP spectra, is shown in Fig. 9.3a. As already shown in Fig. 9.1a, the freshly prepared PdO_{hev} surface had three components with distinct Pd $3d_{5/2}$ binding energies;

15 % was metal Pd at 335.2 eV, 25 % was surface palladium oxide at 335.5 eV and 60 % was bulk PdO at 336.9 eV. The spectral profile of PdO_{hev} remained identical upon annealing at 573 K. Subsequent annealing to 723 K drastically increased the Pd^0 component, suggesting that the bulk PdO phase was decomposed into molecular oxygen and metallic Pd, as presented in a previous report [277]. Further annealing to 773 K converted more than 90 % PdO into metallic Pd species. XP spectra taken from the PdO_{hev} sample exposed to water vapor at a pressure of 0.05 mbar did not exhibit notable different features from those of non-hydroxylated PdO_{hev} at room temperature. However, thermal annealing revealed that the reduction of the oxidized component started at as low as 473 K for the hydroxylated PdO_{hev}, accompanied by the development of Pd^0 at each temperature. The bulk Pd^{2+} species completely disappeared above 723 K, and, irrespective of the procedures, both samples essentially exhibited the identical metallic Pd component after the thermal treatment.

To gain insight into the thermal processes of the hydroxylated PdO_{hev}, temperature dependent IRAS spectra were acquired (Fig. 9.3b). The hydroxylation of PdO_{hev} caused the IR absorption bands at 2630 and 2160 cm^{-1} to develop in intensity, in addition to the four bands at 2973, 2863, 1403, and 1326 cm^{-1}, as already shown in Fig. 9.2b. The infrared profile exhibited no significant changes upon annealing to 373 K. However, the four components at 1326, 2160, 2863 and 2937 cm^{-1} started to lose intensity at 423 K, with the simultaneous emergence of a new band at 2075 cm^{-1}. This transformation was completed upon annealing to 473 K, leaving a prominent band at 2075 cm^{-1}, accompanied by a component at 1403 cm^{-1}. These bands vanished at 623 K.

The infrared observation suggests the occurrence of decomposition of species present on the surfaces. In order to reveal the surface processes, temperature programmed desorption spectra of c) m/Z = 20 (D_2O), d) m/Z = 32 (O_2), and e) m/Z = 44 (CO_2) for the pristine and the hydroxylated PdO_{hev} surfaces are presented in Fig. 9.3. The trend of the desorption features is divided into two groups based on the desorption temperature. At high temperatures (T > 700 K), both the PdO_{hev} samples exhibited huge O_2 desorption at 767 K due to bulk PdO decomposition. The hydroxylation caused a slight shift in the O_2 desorption from 767 to 761 K, and its intensity got slightly reduced. At low temperatures (T < 600 K), prominent effects of the hydroxylation were observed. While non-hydroxylated PdO_{hev} gave rise to small CO_2 desorption centered at 500 K and D_2O desorption at 350 K, which is attributed to little CO_2 and D_2O contamination during or after the oxidation treatment, the hydroxylated PdO_{hev} sample exhibited a substantial formation of CO_2 at 466 K, following D_2O desorption at 448 K. Comparing the infrared spectra to the TPD spectra shown in Fig. 9.3, one easily finds that the formation of the band at 2075 cm^{-1} occurred concurrently with the desorption of D_2O and CO_2 at 423 K. Given that previous studies assigned the signal at 2075 cm^{-1} to CO adsorption at on-top sites on Pd particles [95, 278], it follows that the initially formed formate and carbonic acid started to be decomposed to give CO_2 and D_2O at 423 K, leaving CO on atop sites of the Pd surface. Furthermore, the signal found at 1403 cm^{-1} seems to be unrelated to any species in the frequency range of 2000–3000 cm^{-1}, because of its unsynchronized behaviors upon annealing.

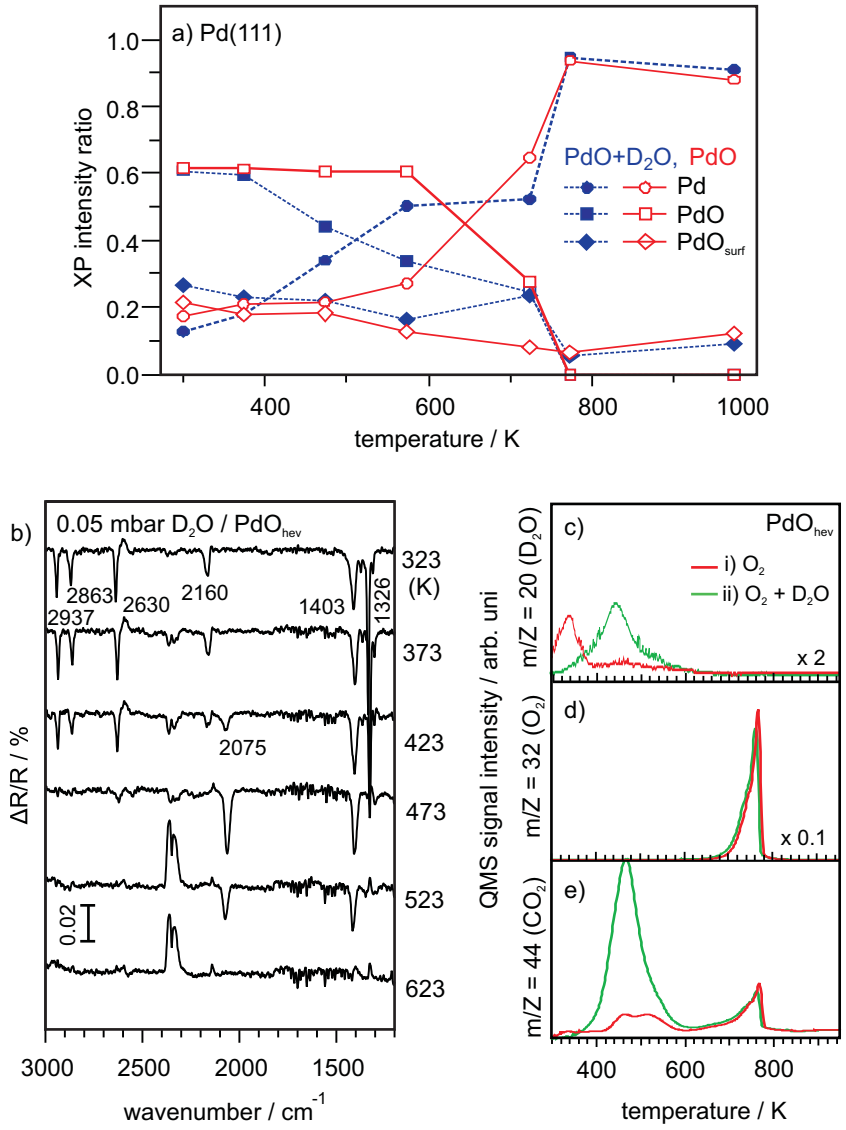

Figure 9.3: a) The temperature dependent intensity ratios of Pd $3d_{5/2}$ peak areas with respect to those taken from the freshly prepared PdO_{hev} samples with or without the post-hydroxylation by D_2O at a pressure of 0.05 mbar and a temperature of 300 K. Each data was taken at room temperature after the subsequent annealing to the indicated temperatures. b) IRA spectra of PdO_{hev} after exposure to 0.05 mbar and subsequent annealing to the indicated temperatures. Data were acquired at room temperature. TPD spectra corresponding to c) D_2O ($m/Z = 20$), d) O_2 ($m/Z = 32$) and e) CO_2 ($m/Z = 44$) were taken from the hydroxylated and unhydroxylated PdO_{hev}, at a ramp rate of 1 K/s.

9.2.3 Thermal Reduction of Hydroxylated PdO-MgO

The hydroxylation-induced changes on the surfaces of PdO particles were first probed by XPS. Comparative Pd $3d_{5/2}$ XPS spectra of the pristine PdO particles and subsequently hydroxylated ones by D_2O exposure at a pressure of 0.05 mbar for 3 min are displayed in Fig. 9.4a. The hydroxylation caused the development of a reduced Pd species having a Pd $3d_{5/2}$ binding energy similar to metallic Pd, at the expense of a portion of the major PdO component at a Pd $3d_{5/2}$ binding energy of 336.5 eV. Although the intensity of the metallic Pd component significantly increased, the XPS result indicates that a major fraction of PdO particles still remained oxidized, suggesting that the hydroxylation affects only the very surfaces of PdO particles.

Thermal reduction of the pristine and the hydroxylated PdO particles was investigated by XPS (Fig. 9.4b), and the results should be compared with those obtained for PdO_{hev} (Fig. 9.3a). The freshly prepared PdO particles exhibited almost only Pd^{2+} at 336.5 eV (∼90 %). The intensity of this PdO component remained the same upon annealing at 573 K, but sharply dropped at 723 K, instead of 773 K observed for PdO_{hev}. Annealing the particles at 723 K for 5 min resulted in the exclusive formation of metallic Pd, indicative of the complete reduction of PdO particles. In contrast to hydroxylated PdO_{hev}, the hydroxylated PdO particles exhibited a much less thermal stability. Indeed, Fig. 9.4b shows that the decrease of the Pd^{2+} component with the simultaneous gain of Pd^0 peak intensity began to occur at as low as 373 K. At 473 K, the ratio of oxidic to metallic Pd was roughly 1:1. At 723 K, the hydroxylated PdO particles left a little PdO peak, indicating almost complete reduction of PdO species. Annealing the sample at 723 K for 5 min left only the metallic Pd component. Note that the decomposition temperature of hydroxylated PdO_{hev} was higher than that of the hydroxylated PdO particles by ∼50 K.

In order to gain insight into the reactions occurring on the hydroxylated PdO/MgO surfaces, a series of TPD spectra corresponding to the ion masses of D_2O, O_2 and CO_2 were, first, collected from the 30 ML thick MgO films with the following three treatments (Fig. 9.4c-e): (i) exposure to D_2O vapor at a pressure of 0.05 mbar and a substrate temperature of 300 K; (ii) oxidation at 5 mbar O_2 and at a substrate temperature of 423 K for 10 min; and (iii) the oxidation and the subsequent hydroxylation using the same parameters. The thick MgO films once exposed to water vapor showed the typical water desorption peak from MgO (Fig. 9.3a, blue trace) [141]. An oxygen desorption peak occurred for the oxidized MgO films at 590 K (Fig. 9.3a, red trace). It is mentioned that powder MgO or single-crystalline MgO(001) surfaces are known to accommodate no O_2 at room temperature without special treatments (e.g., activation by UV irradiation or doping the oxide with alkaline metals [279, 280]). This O_2 desorption peak was assigned to the decomposition of Ag_2O, as discussed later. Broad CO_2 desorption features at ∼375, 485, and 630 K appeared for the oxidized MgO films. The oxidation and hydroxylation of the MgO films provided a slightly larger CO_2 desorption peak at the expense of O_2 and D_2O, compared to those taken from the hydroxylated MgO(001) films.

Fig. 9.4f-h provide, for comparison, the D_2O, O_2 and CO_2 TPD signals acquired from the

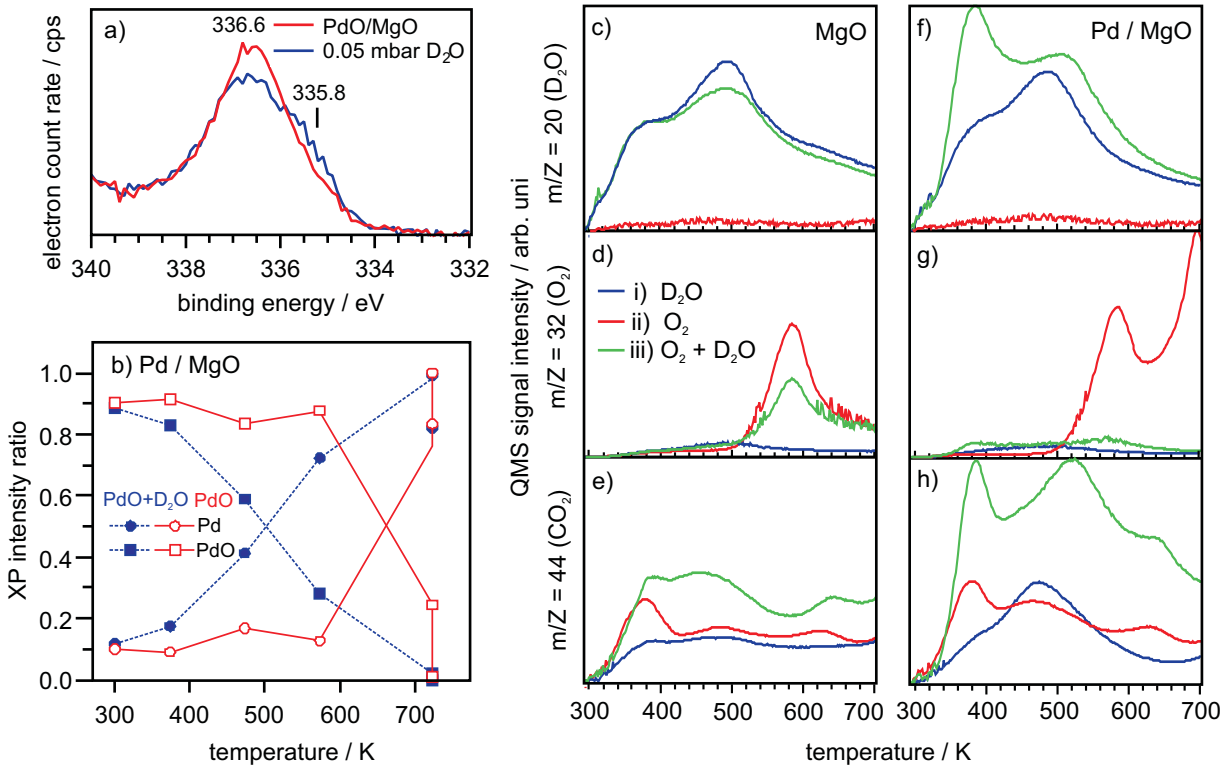

Figure 9.4: a) Pd $3d_{5/2}$ spectra of the PdO particles at a Pd load of 1.0 Å on 30 ML MgO(001) films before and after the hydroxylation by 0.05 mbar D_2O. b) The temperature dependent intensity ratio of Pd $3d_{5/2}$ peak areas with respect to those taken from the freshly prepared PdO/MgO sample with or without the post-hydroxylation by D_2O at a pressure of 0.05 mbar and a substrate temperature of 300 K. Each data was taken at room temperature after the subsequent annealing to the indicated temperatures. TPD spectra corresponding to c) D_2O ($m/Z = 20$), d) O_2 ($m/Z = 32$) and e) CO_2 ($m/Z = 44$) taken from the hydroxylated and unhydroxylated PdO_{hev}. Ramp rate was 1 K/s.

supported Pd particles on the MgO films, to which the same treatments as to the pristine MgO films were applied. Note that the differences in the TPD spectra between the MgO surface and the Pd-MgO sample contain not only the effects of the Pd particles themselves, but also those of the interplay between the particles and the support. The desorption spectra of D_2O and O_2 from the only hydroxylated Pd-MgO sample were rather identical to those acquired from the MgO films, and only the increased CO_2 desorption was noted, which has been discussed in the previous section. For the oxidized Pd/MgO sample, in addition to the O_2 desorption at 590 K observed for the oxidized MgO films, an O_2 desorption peak at 700 K appeared. Note that this desorption temperature corresponds, according to the XPS measurements, to the decomposition of PdO particles (Fig. 9.4b). Except for this O_2 desorption peak, the Pd-MgO system gave no notable differences.

However, the subsequent hydroxylation of the oxidized Pd/MgO sample changed all the desorption profiles. The notable difference was the disappearance of O_2 desorption over the entire

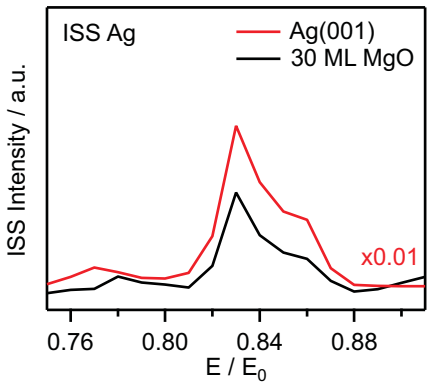

Figure 9.5: ISS measurements, in the region of Ag, of Ag(001) and 30-ML thick MgO(001) films with a thickness of 30 ML grown on Ag(001). Data taken from [156]

temperature range (Fig. 9.4f), suggesting that the surface oxygen species have been consumed by reactions with water or concomitant CO (see Fig. 9.4a and Fig. 9.4b). In agreement with this view, the desorption of D_2O and CO_2 occurs due to the decomposition of the functionalized PdO surfaces, analogous to PdO_{hev} (Fig. 9.3). However, the desorption temperatures of these species dropped by ∼70 K compared to those of hydroxylated PdO_{hev} (380 K vs. 450 K), reflecting the instability of PdO particles. Another distinguishable change of the hydroxylated PdO particles was the broad CO_2 desorption centered at 380 and 500 K with simultaneous D_2O desorption. The hydroxylated PdO_{hev} surface displayed neither of these peaks (Fig. 9.3e), indicating that interplay between the oxidized Pd particles and the functionalized MgO(001) substrate necessarily contributes to their evolution.

In order to determine the origin of species relating to O_2 evolution at ∼590 K observed for the oxidized 30 ML thick MgO(001) films (Fig. 9.4d), He ion scattering spectroscopy (ISS) experiments were performed in another UHV chamber (Fig. 9.5) [161]. A trace amount (∼0.5 %) of Ag was found to be present on the MgO films surface even with a thickness of 30 ML. The decomposition temperature of Ag_2O was previously reported at to be ∼580 K [281], suggesting that the O_2 desorption observed in this work might originate from Ag_2O formed on the sample during the oxidation treatment. It is noted that, under these experimental conditions, no concomitant metal was introduced to the surface even after exposure to O_2 as well as D_2O at ambient pressures.[1]

9.3 Discussion

9.3.1 Activation of PdO by Hydroxylation

The reaction of chemisorbed oxygen with water on Pd surfaces under UHV conditions has previously been investigated and, similar to observations on other noble metal surfaces (e.g., Ag,

[1] Ni contamination easily occurs at sub mbar CO pressures. See Section 3.1.2.

Au or Pt), the formation of hydroxyl groups according to

$$O(ad) + H_2O \rightarrow 2OH(ad) \tag{9.1}$$

has been observed to occur at low temperatures such as 100 K [197, 282]. The hydroxyl layer was found to be unstable at elevated temperatures and recombination of the hydroxyls to release water and leave chemisorbed oxygen on the surface occurs between 170–180 K [273]. According to these studies, hydroxyls are unstable on Pd surfaces at room temperature under UHV conditions.

The present study made an attempt to create a stable hydroxyl layer by reacting heavily oxidized Pd surfaces with water under elevated pressure conditions. The two surfaces investigated and compared here were oxidized single-crystal Pd(111), denoted as PdO_{hev}, and PdO particles supported on MgO(001). It is instructive to start the discussion of the results obtained here for the PdO_{hev} surface when it is exposed to CO (Figure 9.2.a). The band at 2138 cm^{-1} observed for a 1 L dose of CO on PdO_{hev} is typical for CO adsorbed on on-top sites created on oxidized Pd surfaces. Although this infrared band has been observed only at low temperatures [199,201,202], CO-TPD shows that CO molecules are present on the surface even at room temperature [277]. The development of additional bands at 1920, 1980 and 2080 cm^{-1}, which can be attributed to multiple and singly coordinated CO on metallic Pd sites, by increasing the CO dose shows that CO is able to reduce the surface of PdO_{hev} to metallic Pd, due to the CO oxidation reaction [95, 283]. As expected, no stable surface functional groups in addition to adsorbed CO are formed on PdO_{hev}, even after high pressure CO exposure at room temperature. The situation is quite different for the PdO_{hev} surface exposed to D_2O (Fig. 9.2b). The IRAS data provide no support for the formation of a hydroxyl layer on PdO. Instead, surface species with vibrational signatures typical for carbonaceous species are formed already after a 1 L dose of D_2O. The individual bands observed for this system detected by IRAS (Figure 9.2b) are assigned, respectively, to: formate [284]: ν_{sym}(OCO) = 1330 cm^{-1}, ν(CD) = 2140–2160 cm^{-1}, ν(CH) = 2862, 2935 cm^{-1}; carbonate: ν_{sym}(OCO) = 1400 cm^{-1}; carboxyl: ν(OD) = 2630 cm^{-1}. The distinction of the different species according to the vibrational data is supported by literature and the thermal evolution of the various IR bands as discussed below.

The formation of these carbonaceous species must be related to the activation of the PdO surface by interaction with water and its reaction with residual CO molecules in the chamber. It might be conceivable that water interacts with the PdO surface according to Eq. 9.1 and, because of the instability of hydroxyl groups on Pd at room temperature, leaves behind an activated chemisorbed oxygen species, which subsequently interacts with CO to produce CO_2. Such a reaction path is certainly possible, but cannot explain the formation of stable formate or carboxyl species. Another possible mechanism is that water initially breaks up the PdO surface and leads to the formation of active hydroxyl species, the lifetime of which is long enough to interact with coadsorbed or gas-phase CO under the ambient conditions. On the basis of chemical species present on the surfaces, the following reactions are proposed to explain the

formation of the carbonaceous species on the PdO surface:

$$\begin{aligned} O + D_2O &\rightarrow 2OD \\ 2OD + CO &\rightarrow D + OCOOD \\ OD + CO &\rightarrow DCOO \\ OD + CO &\rightarrow COOD \end{aligned}$$

and

$$\begin{aligned} 2OD &\rightarrow O + D_2O \\ 2O + CO &\rightarrow CO_3 \end{aligned}$$

Due to the smaller total surface area of the supported Pd particles as compared to the Pd(111) surface, the abundance of surface species, and therefore the IR intensities, are much smaller for the former (Fig. 9.1c). However, the presence of similar vibrational features suggests that similar events observed for PdO_{hev} occur also on the supported PdO particles. These results show that the interaction of water with PdO results in the activation and subsequent functionalization of oxidized Pd.

A most notable consequence of the surface functionalization of PdO is seen in the thermal behavior of the samples. Consistent with previous studies using Pd(111), Pd(100) and Pd particles supported on SiO_2 surfaces [201,285,286], the PdO phase is stable up to 700 K under UHV conditions, and decomposes at ∼750 K (see XPS and TPD spectra for PdO_{hev} in Fig. 9.3a and 9.3 d. By contrast, reduction of the PdO phase sets in already at around 400 K for hydroxylated PdO. The analysis of the XP spectra points to a continuous reduction of hydroxylated PdO between 400 and 700 K, and complete decomposition above 750 K. This trend is interpreted as low-temperature surface reduction caused by decomposition of the functional groups created during the water exposure, followed by decomposition of bulk PdO at higher temperature. More insight into the molecular processes during the decomposition of hydroxylated PdO is obtained from the IRAS and TPD data. As shown in Fig. 9.3b, the amount of molecular oxygen desorbing from hydroxylated PdO is only slightly smaller than the one from PdO_{hev}, suggesting that the bulk PdO phase remains more or less intact and only the outermost surface layers are affected by the functionalization. Decomposition of the surface species leads to pronounced D_2O and CO_2 desorption signals peaking at 460 K (Fig. 9.3c and 9.3e), perfectly in line with the XPS result, which shows enhanced reduction of the Pd surface layer caused by the exposure to water in this temperature range.

According to the IRAS data presented in Fig. 9.3b, the simultaneous evolution of D_2O and CO_2 can be attributed to the decomposition of surface formate and carboxyl species (disappearance of the corresponding vibrational signals between 423 and 473 K, Fig. 9.3b). The surface carbonate is the thermally most stable species (band at 1403 cm^{-1}, Fig. 9.3b) and disappears only after heating above 523 K. Direct evidence for the surface reduction is provided by the observation of the carbonyl band at 2075 cm^{-1}, which is attributed to CO adsorption on metallic Pd sites. The appearance of this signal goes hand in hand with the disappearance of the

formate and carboxyl contributions, providing a direct link between decomposition of the functional groups and reduction of the PdO surface. The following reactions are proposed to describe the decomposition of the surface functional groups on the hydroxylated PdO surfaces:

$$\begin{aligned} \mathrm{OCOOD + D} &\rightarrow \mathrm{CO_2 + D_2O} \\ \mathrm{DCOO + O + D} &\rightarrow \mathrm{D_2O + CO_2} \\ \mathrm{2DCOO} &\rightarrow \mathrm{D_2O + CO + CO_2} \\ \mathrm{CO_3} &\rightarrow \mathrm{CO_2 + O} \end{aligned}$$

In the case of the MgO-supported PdO particles, similarities as well as differences compared to PdO_{hev} are observed: a notable difference lies in that oxygen of PdO particles gets completely consumed in the case of the hydroxylation (see Fig. 9.4g). Considering the fact that the particles have an average diameter of 2.5 nm and consist of 50 % surface atoms [199], this result indicates that apart from the surface Pd atoms of the particles, which have been functionalized by formate etc., partly remaining PdO core becomes completely reduced during the annealing as well, suggesting that the PdO core of the particles is destabilized by the functionalization and the limited size of PdO particles.

Besides the characteristic oxygen desorption ascribed to the PdO decomposition at ∼700 K, it should be noted that there is another O_2 desorption at 590 K, which is attributed to the decomposition of trace amount (∼0.5 %) of Ag_2O present on top of the MgO films (Fig. 9.5) [281, 287]. Similar to the phenomenon described in the previous paragraph, the hydroxylation also completely suppressed the oxygen desorption due to decomposing Ag_2O; it appears that the presence of Pd is partly responsible for the reduction of Ag_2O (compare Fig. 9.4d and 9.4g), possibly by providing D atoms during the heating. Any contribution of the Ag_2O to the overall reaction scheme cannot be ruled out, but seems to be very unlikely, considering its inertness toward water and concomitant CO [281, 287].

Compared to PdO_{hev}, the CO_2 and water desorption occurs at lower temperature (380 K); there is also a second CO_2 and water desorption at ∼520 K, which is in the temperature range where the CO_2, D_2 desorption occurred in the previous section. The low temperature CO_2-D_2O desorption is attributed to similar decomposition processes as for PdO_{hev} (on the surface of the Pd particles), whereas the higher temperature process could be due to decomposition of C-O species at the periphery of Pd-MgO [214]. Compared to PdO_{hev}, complete decomposition of PdO particles on MgO occurred at ∼700 K. The slightly lower decomposition temperature can be explained by the fact that because of the small particle size, no bulk-like PdO phase survives. The shift of the main CO_2 and D_2O desorption to lower temperature for PdO particles compared to PdO_{hev}, which is equivalent to the more facile decomposition of the surface functional groups and, therefore, the more facile reduction of the PdO particles, is attributed to a particle size effect.

PdO and coexisting Pd/PdO_x are considered to be active catalysts in methane combustion ([288–291] and references therein). Water, which is a by-product of methane combustion, has

been shown to lead to catalyst deactivation. However, no agreement about the mechanism of catalyst deactivation by water has been reached so far. One of the simplest mechanisms causing the deactivation could be the enhanced water-assisted agglomeration of Pd particles. This scenario has, however, been discarded [292]. Considering that water is a possible deactivator, surface hydroxyls formed on the PdO particles might cause the deactivation. Interestingly, in sharp contrast to any surface science studies [269–271] and the present investigation (Fig. 9.2a), the formation of surface hydroxyls on PdO catalysts above room temperature was reported, as PdO/Al_2O_3 was exposed to a mixture of methane and oxygen [288]. However, recent DFT calculations also proposed that the surface hydroxyls on PdO surfaces are unstable [293, 294]. Additionally, it was found that the surface hydroxyls on PdO surfaces, produced by the exposure of the PdO catalyst to H_2, negligibly influenced the catalytic activity [289]. Hence, surface hydroxyls on the surfaces of PdO particles themselves play only a minor role in the deactivation of the Pd catalysts.

The present study proposes two possible mechanisms to explain the deactivation:

a) Given the facts described above, water-assisted formation of carbon-containing species on the surfaces of PdO particles is considered to cause the deactivation of the catalyst. The present study showed that the PdO surfaces were easily contaminated by the formation of carbon-related species at ambient pressures of water. These species were proven to strongly bind to the surfaces, such as that the surface species desorbed in the temperature range of 400–600 K (Fig. 9.4). As such, their adsorption onto the surfaces of PdO particles could prevent the access of gas-molecules such as methane to the particles. If the reactant-induced formation of passive layers on the surfaces of PdO particles causes the deactivation, their removal from the surfaces could immediately lead to the recovery of the reactivity. Indeed, the regeneration of the activity of Pd/Al_2O_3 was achieved upon annealing to 800 K [289]. This observation strongly suggests the idea that the surfaces of PdO particles could be dramatically changed upon annealing. A fundamental point to assert this deactivation and regeneration mechanisms lies in that metallic or under-coordinated PdO phases are catalytically active in methane combustion, which has been well supported by previous theoretical and experimental investigations [290, 295, 296].

b) The results of the present study have shown that the reaction of PdO with water and CO creates surface functional groups, which are thermally less stable than PdO. Since CO is a byproduct of the methane oxidation, similar reactions as observed here could proceed on a catalyst surface under methane oxidation reaction conditions. The consequence would be a more facile decomposition of the PdO phase in the presence of water, leading to a higher fraction of exposed Pd and hence, a lower activity.

9.4 Conclusions

In this study, an experimental investigation of the oxidation and reduction of the Pd(111) surface and supported Pd particles on 30 ML thick MgO films was performed. The oxidation of Pd(111) with subsequent hydroxylation functionalized the surfaces of PdO with formate as well

as carbonic acid ions due to the reaction of concomitant CO or CO_2 and D_2O, while the bulk PdO phase was kept intact. The hydroxylated PdO surface decomposed in the temperature range of 400–600 K. A comparative investigation was conducted using Pd particles supported on 30 ML thick MgO/Ag(001) films. The oxidation of supported Pd particles was achieved at a lower temperature. Upon hydroxylation, the surface layers of PdO particles were similarly decorated by carbonate or formate species, which decomposed at 380 K, as evidenced by the simultaneous desorption of D_2O and CO_2. The facile decomposition of the surface functional groups, hence reduction of the PdO surface to Pd, affected also the stability of the subsurface oxide layers in the case of Pd(111), and the PdO core in the case of supported Pd particles and shifted the Pd oxide decomposition temperature to slightly lower values.

Chapter 10

Interaction of Water with the CaO Films Grown on Mo(001)

This chapter deals with the chemistry of water on calcium oxide (hereafter CaO) films with various thicknesses (5–25 ML) grown on a Mo(001) substrate. In contrast to the MgO(001) films, exposure to water (D_2O) at a pressure of 10^{-8} mbar caused the hydroxylation of the CaO(001) surface. The thinner CaO films were found to be less hydroxylated than thicker ones in the regime of UHV. The exposure of the CaO films to water vapor at a mbar pressure heavily hydrated the CaO films while maintaining its original long-range order. The strongly basic nature of the CaO surface resulted in its hydroxylation even at 110 K. The presence of dissociated water at 110 K indicated the thermal transformation of amorphous solid water (ASW) into crystalline ice (CI) on CaO(001). Comparative discussion of CaO, MgO and MgO_{hydr} is presented regarding hydroxylation as well as the transformation of the ice phases on the surfaces.

10.1 Introduction

The interaction of water with surfaces is of fundamental interest because of its importance in various fields, including astrophysics, electrochemistry, geochemistry, and heterogeneous catalysis. As such, this system has been extensively investigated, as summarized in a number of review papers [197, 249]. Surface science work of water interaction with metal surfaces, in particular with those of the late d-transition metals, is mainly focused on the structure of the water wetting layer at low temperature and its influence on the properties of ice, both in the form of amorphous solid water (ASW) and crystalline ice (CI), grown on top of it [297, 298]. In addition, the formation of a hydroxyl layer by the reaction of water with chemisorbed oxygen has been studied on various metal single-crystal surfaces. For a long time, the water wetting layer on metal surfaces was believed to consist of a water bilayer with ice-like structure. More recent studies have, however, provided evidence that water adsorption on metals is more complicated than anticipated. In fact, the structure and stability of the water wetting layer, which is not a bilayer but a monolayer, was shown to be governed by the subtle balance between water-metal

and water-water (hydrogen bonding) interaction, leading to various forms of wetting layers (only molecular water or mixed molecular/dissociated water), which has consequences for the growth and structure of ice multilayers [297].

In contrast to the water/metal interfaces, detailed atomic-scale information about water/oxide interfaces is much more limited [197]. This arises from the complexity inherent to oxide surfaces. The reactivity of oxide surfaces toward water is expected, and has been shown, to depend on various parameters, such as the ionicity (covalency) of the metal-oxygen bond, the lattice constant, the surface defect structure, and the surface orientation.

MgO(001) is among the most studied oxide surfaces, both experimentally and computationally, with regard to its interaction with water. Various aspects of the water/MgO interaction, such as the structure of the ordered water monolayer formed under UHV conditions/low temperature, the water vapor pressure dependent hydroxylation of MgO, water dissociation on defects, and the dissolution of MgO have been intensively studied [126, 299, 300]. In contrast to MgO, much less fundamental information about its interaction with water is available for the iso-structural, but more basic CaO(001) surface.

CaO vigourously reacts with water in a strongly exothermic reaction to $Ca(OH)_2$ ($CaO + H_2O = Ca(OH)_2$, $\Delta H = -65$ kJ/mol). Calcium hydroxide is of technological relevance, for example in fuel gas desulfurization [301] and cement technology [302]. Key processes in these technologies are the reversible hydroxylation/dehydroxylation of CaO and the reversible phase transformation between CaO and $Ca(OH)_2$. Fundamental studies about water adsorption and hydration/dehydration processes on CaO have in the past been undertaken using powder CaO as well as single-crystal and supported thin film samples [162, 302–306]. The surface science-oriented single-crystal and thin film studies suffered, however, from poorly characterized sample surfaces. Recently, Nilius et al. succeeded in growing well-defined CaO(001) films on a Mo(001)substrate [10]. In addition to demonstrating that thick CaO films have bulk-like properties, these authors showed that doping of the films with Mo, which is an inherent property of thin CaO films or can be achieved by intentional introduction of Mo into thick films, can strongly alter the properties of ad-metals and molecules [10, 307]. CaO/Mo(001) films represent, therefore, a most suitable substrate for further investigations into the adsorption properties of alkaline earth metal oxides.

This chapter presents a spectroscopic investigation using IRAS and XPS on the interactions of water (D_2O) with the surface of CaO(001)/Mo(001) films of various thicknesses. The work focuses on (i) the influence of the hydroxylation conditions (hydroxylation treatments were performed in the UHV regime as well as at elevated pressure and a substrate temperature of 100 or 300 K), (ii) the thermal behavior of ASW on CaO(001) and MgO(001), and (iii) the influence of CaO film thickness on hydroxylation. The results show that water dissociates on CaO(001) at a temperature of as low as 100 K and that the attainable hydroxyl coverage is strongly dependent on the hydroxylation treatment and the film thickness. Moreover, the presence of interfacial hydroxyl groups was found to have consequences for the behavior of multilayer ice.

10.2 Experimental

The Mo(001) specimen was cleaned by repeated cycles of Ar^+ sputtering, annealing to 1300 K in an oxygen atmosphere at a pressure of 1.0×10^{-7} mbar and subsequent flashing to 2300 K via electron bombardment. This initial cleaning step was carried out without the type K thermocouple attached to the sample. The type K thermocouple was mounted onto the specimen after the sample was confirmed to be free of contaminants by XPS and to be well ordered by LEED. The Mo(001) substrate was further cleaned by repeated cycles of Ar^+ sputtering and annealing to 1200 K until a (1×2) LEED pattern with sharp diffraction spots was obtained. CaO films were prepared by evaporating Ca (99.9 %, Goodfellow) via physical vapor deposition onto Mo(001) in an oxygen atmosphere of 5.0×10^{-7} mbar at room temperature. The deposition rate was kept at 1 ML (2.4 Å)/min. Better faceted CaO(001) surfaces were obtained upon annealing to 1200 K for 10 min *in vacuo* [10]. XPS measurements were carried out using a non-monochromatized Al Kα source and the ejected photoelectrons were detected at an emission angle of 60 degrees. IR measurements were performed at grazing incidence, and the resolution was set to 4 cm^{-1}. The IR spectrum of the clean CaO(001) surfaces served as background. Great care was taken during the sample preparation due to the high reactivity of the CaO films toward moisture. Details on this issue are discussed in Section 10.3.1.

10.3 Results

10.3.1 Growth of Thin and Thick CaO Films

The relatively large lattice mismatch of 8 % between Mo(001) and CaO(001) makes the film growth occur in three stages. In the limit of ultra-thin films, mixed Ca-Mo-oxide layers are observed, whose formation is driven by Mo diffusion from the substrate into the CaO rock-salt structure [10]. The second growth regime starts at a film thickness of about 5 ML, when the Mo diffusion into CaO stops and the lattice mismatch between the mixed-oxide layers and the CaO layers growing on-top of them is still large enough to yield a three-dimensional CaO(001) growth mode. For CaO films thicker than 15 ML, well-coalesced CaO(001) films with low defect concentration and bulk-like structural, electronic and optical properties have been obtained.

Fig. 10.1a-c present LEED patterns of CaO(001) films with various thicknesses (5, 10, and 25 ML) grown on the Mo(001) substrate in this study. Reasonable agreement with the previous study was reached for CaO(001) films with thicknesses of 5 and 25 ML [308]. However, the CaO films with a thickness of 10 ML prepared in the present study exhibited a noticeable discrepancy; the absence of the (2 × 2) diffraction spots corresponding the mixed-oxide interface layer. Instead, analysis of this LEED pattern suggested its similarity to the reported CaO films with a thickness of 20 ML. The absence of (2 × 2) spots in the LEED image for the 10 ML CaO film indicates the growth of well-coalesced CaO(001) films in this study. As already mentioned in Section 10.2, the preparation of CaO(001) films over Mo(001) required scrupulous attention to the following conditions:

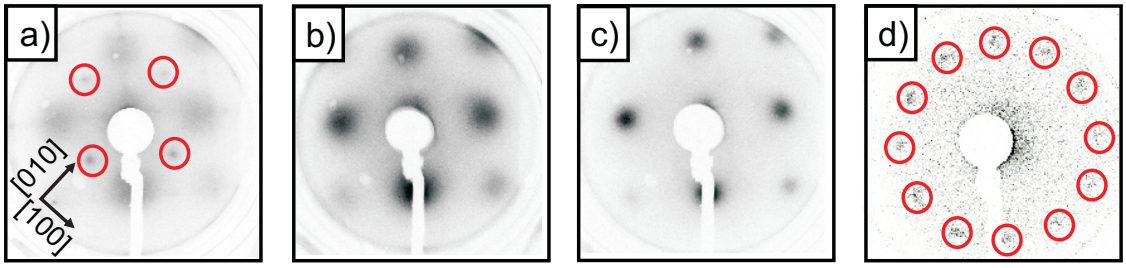

Figure 10.1: LEED images of a) 5 ML CaO(001), b) 10 ML CaO(001), c) 25 ML CaO(001), and d) 20 ML CaO(111) films, taken with an electron kinetic energy of 70 eV.

1. The background pressure must be kept as low as possible ($\sim 2\times10^{-10}$ mbar), because remaining water can vigorously react with as-deposited amorphous CaO to form a CaO(111) phase upon annealing.

2. One gas line was exclusively used to introduce oxygen gas from an O_2 bottle to the UHV chamber via a leak valve. Before the introduction of oxygen, both the gas line and the chamber were baked with the variable leak valve open. This treatment assures the UHV-quality of the gas line (see Section 3.1.2).

3. Thick CaO films cannot be prepared in one step onto the Mo(001) substrate. Instead, thin CaO(001) films needed to be grown first as a *template* for thick CaO films. In the experimental set-up used in this study, physical vapor deposition of CaO, corresponding to 10 or 20 ML, onto well-ordered 5 ML thick CaO(001) films produced well-faceted thick CaO(001) films after subsequent annealing to 1100 K for 10 min.

All the above-mentioned conditions must have been upheld. Otherwise, a LEED pattern with 12 concentric spots appeared, indicating the formation of CaO(111) facets (Fig. 10.1d).

10.3.2 Characterization of CaO(001) Interacting with Water

O 1s XP spectra for 25 ML thick CaO(001) films were collected after exposure to a) 2 L D_2O at 300 K, b) 5 L D_2O at 110 K, and c) 0.05 mbar D_2O at 300 K for 3 min (Fig. 10.2).[1] As shown in Fig. 10.2a, the hydroxylated CaO(001) films exhibited an additional O 1s component at 533.9 eV, which could be assigned to hydroxyls, with the oxide component at 530.1 eV (hereafter CaO_{hydr}). Thermal annealing of CaO_{hydr} above 400 K caused a decrease in the peak area of the hydroxyl signal, and upon annealing to 800 K, a negligible amount of hydroxyls was observed.

In case of the D_2O exposure at 110 K, the O 1s XP spectrum exhibited three peaks at 535.0, 532.5 and 530.1 eV (Fig. 10.2b). The presence of hydroxyl groups with an O 1s binding energy of 532.5 eV indicates that water dissociation readily occurs on CaO(001) even at 100 K. The O 1s component with the highest O 1s binding energy, 535.0 eV, can be attributed to amorphous

[1] Sample irradiation to x-ray was restricted as much as possible, in order to prevent photo-induced dissociation of water on the CaO surfaces and damage of the CaO film [162].

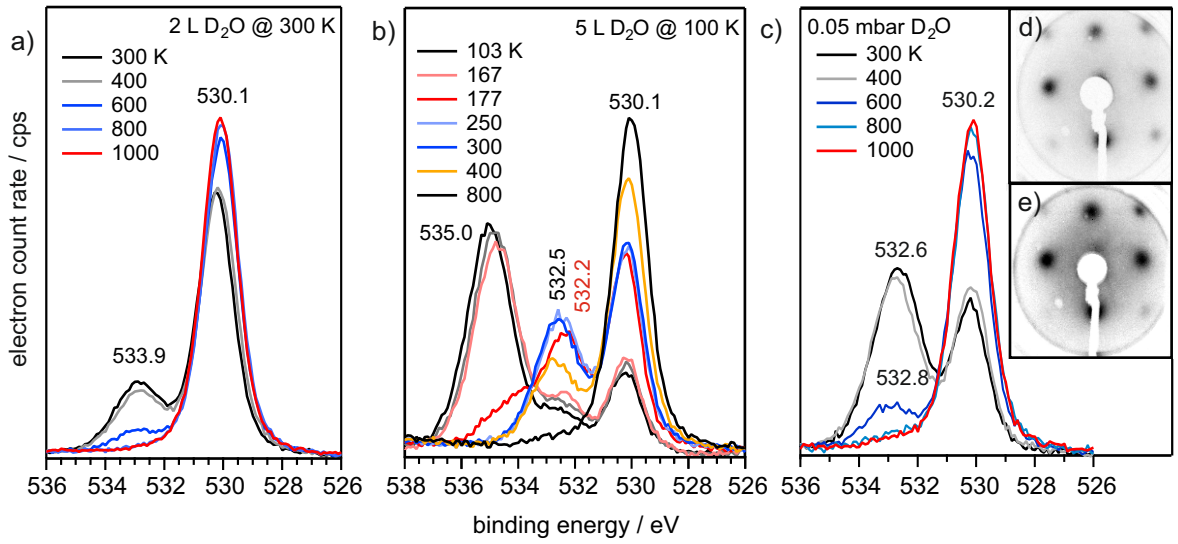

Figure 10.2: O 1s XP spectra for 25 ML thick CaO(001) films after exposures to a) 2 L D_2O at 300 K, b) 5 L D_2O at 110 K, and c) 0.05 mbar D_2O at 300 K for 3 min. LEED patterns for d) a clean 25 ML thick CaO(001) film and e) the CaO(001) film exposed to 0.05 mbar D_2O at 300 K. All the measurements were conducted at 300 K, after annealing to the indicated temperature above 300 K. Samples below 300 K were measured at the indicated temperatures.

solid water [197]. Thermal annealing of these ice layers to 167 K caused only little spectral changes. A large fraction of molecular water has desorbed by 177 K and further annealing to 250 K led to complete disappearance of the corresponding O 1s signal. The remaining O 1s signals of the hydroxyls and the oxide did not change between 250–300 K, showing that the fully hydroxylated CaO surface is stable in this temperature regime. The intensity of the hydroxyl O 1s signal decreased in intensity upon heating to 400 K, which was different from CaO_{hydr}, where almost no change occurred during this heating step. Complete dehydroxylation of the substrate did proceed upon annealing to 800 K, as already observed for CaO_{hydr}.

The coverage of hydroxyl groups on these surfaces by applying a methodology described previously [162]. This methodology is applicable only when the outermost surface is hydroxylated. With the assumption that the IMFP of O 1s electrons ejected from the CaO films is 2.6 nm [69], the coverage of surface hydroxyl groups present at 300 K is calculated to be 0.6 ML for CaO_{hydr}, and 1.0 ML for the CaO surface prepared by annealing ice layers to 300 K. Upon annealing to 400 K, the coverage of hydroxyl groups was 0.55 ML on CaO_{hydr}, while for the surface prepared by adsorbing water at 100 K the coverage dropped from 1.0 ML to 0.6 ML. This result indicates that a part of surface hydroxyl groups produced by the prolonged contact of water molecules to the CaO(001) surface at 100 K have a lower activation barrier for desorption than those on CaO_{hydr} in the temperature range of 300–400 K. The remaining surface hydroxyls at 400 K share the same nature with those present on CaO_{hydr}.

Fig. 10.2c displays a series of O 1s XP spectra of a 25 ML thick CaO(001) which has been exposed to 0.05 mbar D_2O at 300 K, as a function of annealing temperature. Additionally, the

LEED patterns for a clean 25 ML thick CaO film and the hydrated one are shown in Fig. 10.2d and Fig. 10.2e, respectively. The CaO(001) surface exposed to the water vapor exhibited the same LEED patterns as the pristine CaO(001) surface. However, the observation of enhanced background scattering and broadened diffraction spots points to more structural disorder on the surface of the water-exposed sample [302, 305]. It is mentioned that the LEED pattern presented in Fig. 10.2e appeared only after the sample had been exposed to the electron beam of the LEED gun for several seconds, pointing to the presence of some weakly adsorbed water species, which can easily be removed by electron-stimulated desorption. The O 1s XP spectrum of CaO exposed to 0.05 mbar D_2O exhibited in addition to the oxide component at 530.2 eV, a strong signal due to hydroxyls at 532.6 eV. Indeed, the hydroxyl signal intensity of this sample is significantly larger than the one obtained from the fully hydroxylated CaO surface (Fig. 10.2d), which suggests that the hydroxylation affected not only the surface of the samples, but extended deeper into the bulk. This result is in agreement with previous studies [141,152,303] and is most likely related to the transformation of the CaO surface and subsurface layers into a metastable brucite-type pseudolattice (see Section 10.4.1). Upon annealing to 400 K, the hydroxyl O 1s signal slightly decreased in intensity and its binding energy shifted from 532.5 eV to 532.9 eV. A strong decrease in the hydroxyl signal intensity was observed after annealing at 600 K.

The interaction of water with the surface of a pristine 25 ML CaO(001) film was additionally monitored with infrared spectroscopy. Fig. 10.3a presents a series of IRA spectra after successive exposures of the CaO(001) films to D_2O vapor (0.15, 0.3, 1.0, 2.0 L) at room temperature. Three absorption bands at 2740, 2723 and 2600 cm^{-1} simultaneously appeared after a minimum amount of exposure to D_2O. The repeated exposure to D_2O led to the apparent saturation of these hydroxyl signals. Note that no additional absorption features appeared in the OD region. In accordance with the XPS results (Fig. 10.2a), the three infrared bands should correspond to surface hydroxyl groups formed by water dissociation.

A series of infrared spectra for the CaO(001) surface were taken at 110 K, after dosing sub-monolayer to multilayer coverages of D_2O (Fig. 10.3b). Exposure of the CaO surface to 0.15 L D_2O at 110 K yielded one sharp band at 2745 cm^{-1}, accompanied by a small shoulder at 2725 cm^{-1}. These bands developed in intensity with the formation of another band centered at 2600 cm^{-1} after an additional exposure to 0.15 L D_2O. Further condensation of D_2O onto the film (total 5.0 L) produced a typical spectrum corresponding to ASW: a single sharp band centered at 2730 cm^{-1} and a broad ν_{OD} centered at 2545 cm^{-1} [197].

In the next place, Fig. 10.3c displays the thermal development of CaO_{hydr} in the temperature range of 300–1000 K. The IRA spectra show the total disappearance of ν_{OD} in the frequency region of 2650–2500 cm^{-1} with the simultaneous depletion of the sharp ν_{OD} at 2742 cm^{-1} upon annealing at 600 K. Instead, a new absorption at 2730 cm^{-1} was observed. These remaining surface hydroxyl groups virtually vanished upon heating to 800 K.

Fig. 10.3d shows the dehydroxylation of the hydroxylated CaO films after the removal of the ice layers by heating to 300 K (see Fig. 10.2b). At 300 K, this ice-free surface exhibited a strong ν_{OD} at 2719 cm^{-1}, accompanied by a broad signal at 2680 cm^{-1}. Upon annealing to 500 K, the

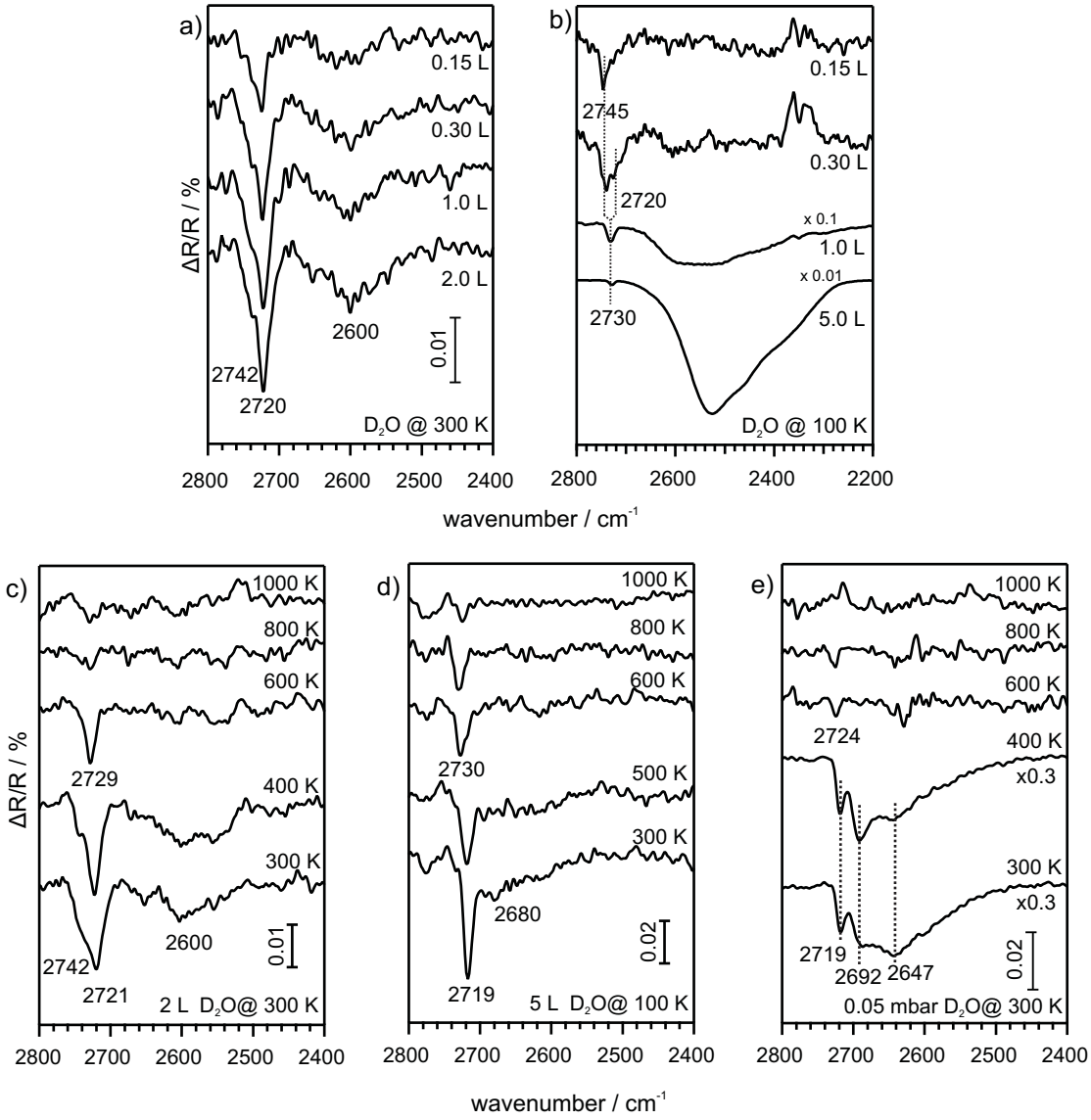

Figure 10.3: IRA spectra for 25 ML thick CaO(001) film after a) D_2O exposures (0.15, 0.3, 1.0 and 2.0 L) at 300 K, and b) 0.15, 0.3, 1.0 and 5.0 L D_2O exposures at 110 K. Temperature programmed IRA spectra (c) and (d) corresponding to the samples (a) and (b) upon annealing to the indicated temperatures. IRA spectra in the panel (e) for a CaO(001) film exposed to 0.05 mbar D_2O at 300 K for 3 min with subsequent annealing to the temperatures. All the measurements were done at 300 K for the samples except for the data shown in the panel (b). IRA spectra shown in the panel (b) were acquired at 110 K.

signal intensity dropped. Upon annealing to 600 K, the broad signal with the lower frequency disappeared, and the sharp ν_{OD} shifted from 2719 cm^{-1} to 2730 cm^{-1}. The signal at 2730 cm^{-1} was still present at 800 K and faded away at 1000 K.

The dehydration of the hydrated CaO films was also monitored by IRAS (Fig. 10.3e). The freshly hydrated sample was characterized by two broad ν_{OD}s at 2692 and 2647 cm^{-1}, respectively, as well as a sharp one at 2719 cm^{-1}. Note that a similar spectral profile was obtained

for hydrated CaO powder [303]. After annealing to 400 K, the two ν_{OD}s at 2692 and 2719 cm^{-1} gained intensity at the expense of the broad ν_{OD} centered at 2645 cm^{-1}. It is again notable that similar thermal developments have been documented using CaO powder [303]. At a sample temperature of 800 K, only the band at 2713 cm^{-1} was detectable. There was no detectable absorption band after heating to 1000 K.

10.3.3 Ice Desorption and its Phase Transition over CaO(001)

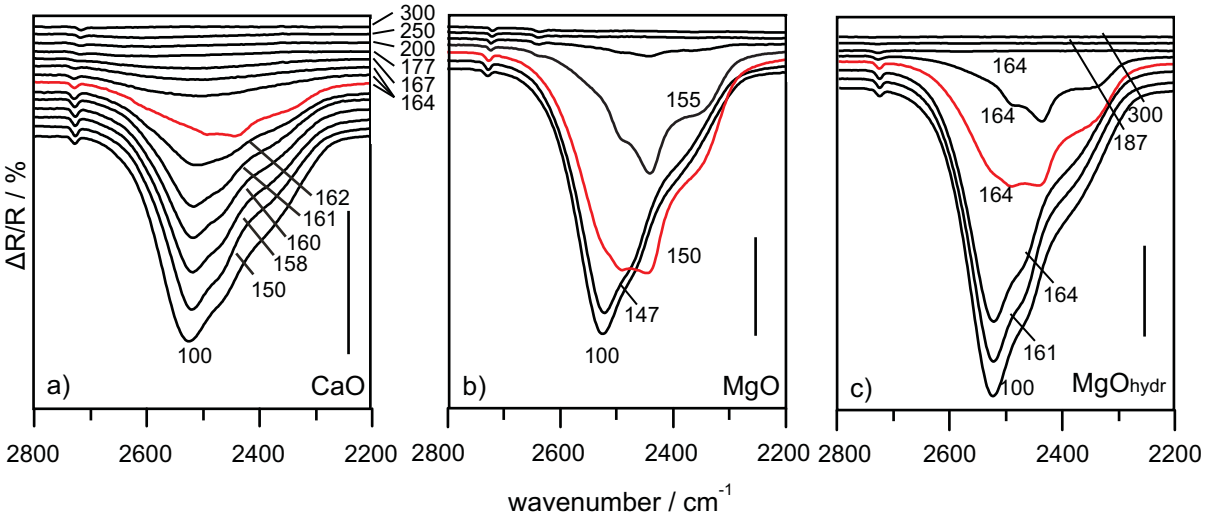

Figure 10.4: IRA spectra for a) 25 ML CaO/Mo(001), b) 2 ML MgO/Ag(001), and c) 30 ML MgO_{hydr} after dosing 5 L D_2O at 100 K. Spectra were acquired at the indicated temperatures.

In the previous section, both O 1s XP (Fig. 10.2b) and IRA spectra (Fig. 10.3b) demonstrated the presence of ASW at 110 K for the CaO(001) surface exposed to 5 L D_2O at 110 K. In order to acquire better knowledge concerning the thermal behavior of ASW on CaO(001), infrared spectroscopy was applied. Particular attention was paid to the observation of the phase transition from ASW to CI. The 25 ML CaO film was exposed to 5 L D_2O at 100 K to form thick ASW layers, and IRA spectra were acquired after annealing to elevated temperatures (Fig. 10.4a). As already shown in Fig. 10.3b, ASW exhibits a typical infrared spectrum with two peaks at 2730 and 2525 cm^{-1}. Heating up to 162 K caused only water desorption, but no change in the spectral profile. However, upon annealing to 164 K, the phase transition from ASW to CI was observed, as evidenced by the emergence of the sharp ν_{OD} at 2440 cm^{-1} (red spectrum) [197]. This feature disappeared during isothermal desorption at 164 K and the water remaining on the CaO surface exhibited ASW-like character (broad, featureless absorption centered at 2500 cm^{-1}). Upon annealing the sample to 250 K, observed were a red-shift of the ν_{OD} from 2732 cm^{-1} to 2719 cm^{-1} and a blue-shift of the broad feature to 2600 cm^{-1}.

For comparison, similar experiments were carried out with MgO and MgO_{hydr} surfaces, and the results are shown in Fig. 10.4b and Fig. 10.4c, respectively. At 100 K, the ice layers on the pristine MgO(001) film exhibited the typical ASW feature. The occurrence of the ASW→CI

transition was observed at 150 K as evidenced by the appearance of the absorption centered at 2440 cm^{-1} [309]. Note the fact that the ASW→CI transition temperature observed for the MgO(001) surface was much lower than that for CaO(001). For MgO_{hydr} exposed to 5 L D_2O at 100 K, the infrared feature corresponding to ASW remained up to 164 K. Keeping the sample at 164 K for 5 min, however, allowed the ASW phase to be transformed into CI (see red spectrum). Comparing the three surfaces investigated here suggests that the occurrence of the ASW→CI transition and the transition temperature, which is higher by 15 K for CaO and MgO_{hydr} than for MgO(001), depend on the properties of the interfacial layer. Both the CaO and the MgO_{hydr} surfaces exhibit stable hydroxyl groups that interact with the ice layers, whereas a less stable, mixed molecular/dissociated water later is formed on the MgO(001) surface. As discussed later, this result is analogous to an earlier experimental work, which observed a similar dependence of the ASW→CI transition on the presence of hydroxyl groups on functionalized self-assembled monolayer (SAM)s [310].

10.3.4 Effect of Film Thickness on Hydroxyls

In order to get an insight into effects of film thickness on hydroxylation, we carried out O 1s XPS measurements for CaO films of various thicknesses (5, 10 and 25 ML) after the following treatments: exposure to 2 L D_2O at 300 K (Fig. 10.5a); exposure to 5 L D_2O at 100 K and subsequent annealing to 300 K (Fig. 10.5b); exposure to 0.05 mbar D_2O at 300 K for 3 min (Fig. 10.5c). The CaO films exposed to 2 L D_2O at room temperature were found to be covered with surface hydroxyls. The corresponding hydroxyl O 1s binding energy shifted to higher values as the film thickness increased: 532.0 eV for 5 ML thick CaO, 532.5 eV for 10 ML thick CaO, and 532.9 eV for 25 ML CaO films. Additionally, the hydroxyl O 1s signal intensity and, thus, the hydroxyl coverage increased with increasing film thickness.

Similar trends were observed for the CaO films hydroxylated using ice (Fig. 10.5b) and for the hydrated CaO films (Fig. 10.5c). In either case, the hydroxyl coverage increased and its O 1s binding energy shifted to higher values with increasing film thickness.

The results of the XPS measurements are summarized in Fig. 10.5d, which displays the hydroxyl O 1s peak intensities as a function of film thickness. This plot shows that the maximum achievable hydroxylation level drops by 50 % irrespective of the hydroxylation treatment applied, if the film thickness is reduced from 25 ML to 5 ML.

In order to learn if the nature of surface hydroxyls is influenced by the oxide-film thickness, IRA spectra of CaO(001) films with thicknesses of 5, 10 and 25 ML were collected after exposure to 2 L D_2O at room temperature (Fig. 10.5e). The observed strong reduction of the OD signal intensities with decreasing film thickness is in accordance with the XPS results presented above. Even though the comparison of absolute intensities in IRAS is not always straightforward and valid, the trend observed here agrees very well with the conclusion of a strongly reduced hydroxyl coverage on thin CaO films. In addition, some characteristic differences in the IRAS spectra of the hydroxylated thick and thin CaO films can be made out: The branched narrow OD bands

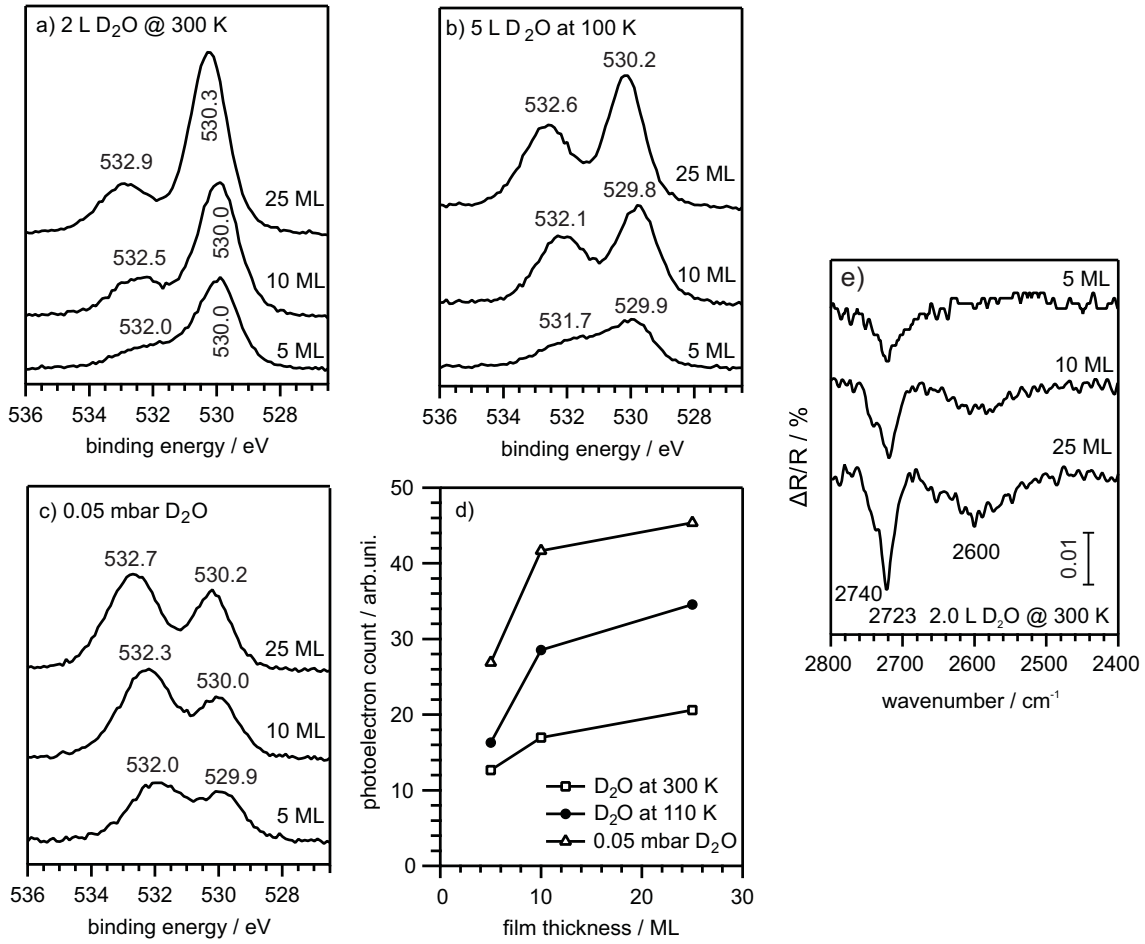

Figure 10.5: O 1s XP spectra for CaO films at thicknesses of 5, 10 and 25 ML after: a) exposure to 2 L D_2O at 300 K; b) exposure to 5 L D_2O at 100 K and subsequent annealing to 300 K; and c) exposure to 0.05 mbar D_2O at 300 K for 3 min. d) O 1s peak intensity corresponding to hydroxyl groups for the samples shown inthe panels (a)-(c). e) IRA spectra after exposing the CaO(001) films with various thicknesses (5, 10, and 25 ML) to 2 L D_2O at room temperature.

present on the 25 ML CaO film above 2700 cm^{-1} are reduced to a single absorption at 2720 cm^{-1} on the thin film. Moreover, the broad absorption centered at 2600 cm^{-1} is completely absent on the 5 ML CaO film.

10.4 Discussion

10.4.1 Characterization of Surface Hydroxyl Groups

Prior to providing detailed insight into the results of the present study, findings of previous work related to the hydroxylation of CaO are summarized. There have not been many studies published to date that deal with the fundamental understanding of hydroxylation of the CaO surface [162,302–306,311–313]. The one closest to the present work was published by Low et al., the results of which are reproduced in Fig. 10.6 and summarized in Tab. 10.1 [303]. In this work,

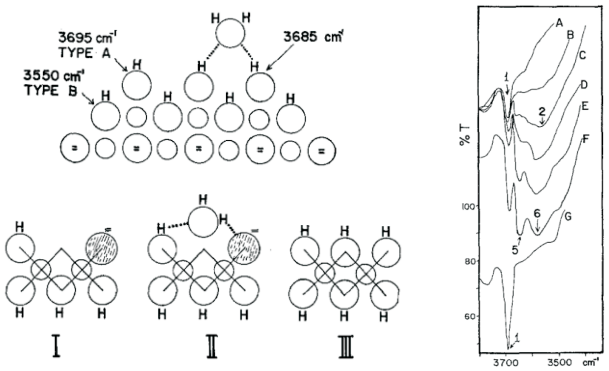

Figure 10.6: Goodsel's model of incomplete hydration of CaO into pseudo $Ca(OH)_2$ [303]

$Ca(OH)_2$ powder was initially dehydrated and dehydroxylated at a temperature of 973 K. The IR spectrum of the resultant material (CaO) is shown in Fig. 10.6, Spectrum A. The presence of a sharp OH signal at 3695 cm^{-1} points to incomplete dehydroxylation or fast re-hydroxylation of the CaO surface in this experiment. Spectra B–E in Fig. 10.6 were acquired after dosing increasing amounts of water (up to 1 ml normal temperature and pressure (NTP)), and spectra F and G represent the states of the surface after subsequent heating to 373 K and 773 K, respectively. The band position and assignment of the signals marked in Fig. 10.6 are given in Tab. 10.1 and the proposed structural models are shown on the left side of Fig. 10.6. Signals 1 and 2 (Type A and B hydroxyls) have been assigned to "regular" single and multiple coordinated hydroxyls on the CaO surface, while signals 5 and 6, which developed only after the largest water doses, were attributed to bulk $Ca(OH)_2$-like hydroxyls. It is noted that pure $Ca(OH)_2$ lacks of any hydrogen-bond interaction between the hydroxyl groups and gives rise to only a single sharp OH stretch signal at 3640 cm^{-1} (or 2680 cm^{-1} for $Ca(OD)_2$) [311]. Low et al. concluded from their experimental result, which shows that a substantial degree of hydrogen-bond interaction between the hydroxyls exists even after the largest water doses, that the transformation of CaO into $Ca(OH)_2$ was incomplete. Therefore, they assigned the signals 5 and 6 to hydroxyls in a $Ca(OH)_2$ pseudo-lattice (see schematic representation in Fig. 10.6, bottom left; Scheme II contains the physisorbed water, signal 6, and the hydroxyl, signal 5 (perturbed Type C), to which it is hydrogen-bonded). In addition, they note that unperturbed Type C hydroxyls of the pseudo-lattice (signal 3 in Tab. 10.1) are present after incomplete decomposition of $Ca(OH)_2$.

For comparison with the results of Low et al. using CaO powder, Tab. 10.2 provides a summary of the most relevant IR observations in the present study on CaO thin films. According to the quantitative XPS analysis presented above, the hydroxylation of the CaO surface leads to two different states: Surface-only hydroxylation occurs for all hydroxylation treatments performed in the low-pressure regime (hydroxylation procedures a and b, Fig. 10.2), whereas surface plus partial bulk hydroxylation occurs when hydroxylation was performed at a near ambient vapor pressure (hydroxylation procedure c, Fig. 10.2). As concerns the surface hydroxylation state, the IR experiments present some very characteristic features depending on the hydroxyl cov-

Table 10.1: Results of Goodsel for hydration of CaO powder [303]

Band No.	3	1	4	5	6	2	7
OH/cm^{-1}	3707	3695	3655	3638	3580	3550	3520
OD/cm^{-1}	2734	2719	2690	2678	2636	2625	2595
type	Type C: OH^- pseudolattice	Type A: free OH^-	chemisorbed water, pseudolattice	perturbed Type C	Physisorbed water	Type B: bound OH^-	Pysisorbed water

Table 10.2: Observable surface OD groups as a function of water exposure for 25 ML CaO films.

Band No.	1a	3	1b	1	5	6	2,7
OD / cm^{-1}	2745	2730	2725	2719	2690	2643	2600(b)
0.15 L D_2O, 100K	◯						
0.3 L D_2O, 100K	◯		◯				◯
0.15–2 L D_2O, 300K	◯		◯				◯
anneal 600 K		◯					
1 L D_2O, 100 K → 300 K				◯			◯
0.05 mbar D_2O, 300 K				◯	◯	◯	◯

erage. For small doses of water at a sample temperature of 110 K, an OD band with ν_{OD} = 2745 cm^{-1}, which is not accompanied by any additional OD contribution at lower frequency, has been observed. In the experiments reported here, this band has reached saturation already after the first water dose, and subsequent water adsorption/dissociation on the CaO surface at 110 K leads to the formation of an additional hydroxyl band with ν_{OD} = 2725 cm^{-1}, and contributions at 2600 cm^{-1}. It is noted that water dosing at 300 K yielded hydroxyl groups with the same vibrational frequencies, however slightly different abundance. The hydroxylated CaO surface prepared by adsorption of ice at low temperature followed by annealing to 300 K, which yields an OD coverage of 1 ML, exhibits only one sharp OD band at 2719 cm^{-1}, which is accompanied by a broad and featureless signal at lower frequencies ranging from 2700–2600 cm^{-1}. For the CaO surface exposed to 0.05 mbar D_2O, where hydroxylation extends partially into the bulk of the material, three distinct signals at 2719 cm^{-1}, 2690 cm^{-1}, and 2643 cm^{-1}, respectively, appear in addition to the broad contribution centered at 2600 cm^{-1}.

In Tab. 10.2, the signals observed on hydroxylated CaO thin films that have similar frequencies as those detected on CaO powders have been labeled according to the numbering given in Tab. 10.1 [303]. It is noted that for the strongly hydrated state (exposure to 0.05 mbar D_2O at 300 K) in particular, the two experimental results match well, suggesting that similar hydrated surface states were obtained after hydroxylation at near ambient conditions. However, regarding the situation where surface-only hydroxylation prevails, the results obtained in the present study are more rich in information, mainly because the UHV-based preparation allowed the CaO films to be maintained sufficiently clean for hours. Comparing now the initial IR spectrum of the CaO powder with those obtained from the films in UHV suggests that the surface of the former was already fully hydroxylated at the beginning of the experiment (ν(OD) = 2719 cm^{-1}, band No. 1, corresponds to the state identified to exhibit 1 ML OD coverage). The bands labeled in

Tab. 10.2 as 1a and 1b (2745 and 2725 cm^{-1}) can, therefore, be assigned to adsorbed hydroxyls in adsorption structures corresponding to sub-monolayer coverage.

A lot of information about hydroxylation in the sub-monolayer regime has in the past been generated for MgO(001) (see Chapter 5). Because MgO is iso-structural to CaO, this information might serve as a starting point to discuss possible adsorption sites for dissociative water chemisorption based on characteristic shifts of the hydroxyl stretching vibration [314,315]. However, because of the low reactivity of regular MgO(001) facets, information is available mainly for hydroxyls adsorbed at defect sites of the MgO surface. Since CaO is much more reactive toward water dissociation due to its exothermic reaction, hydroxylation of regular CaO(001) terraces additionally needs to be taken into account as well. Indeed, information about CaO-water interaction from calculations is mainly available for the CaO(001) terraces, while defects have rarely been considered [312].

Fig. 10.7 summarizes results of recent computational studies concerned with water adsorption on CaO(001). For water monomer adsorption, DFT calculations predict the minimum energy structure to be a tight H–OH ion pair, with the OH group adsorbed in bridge position between two Ca ions, and the proton transferred to the adjacent oxygen ion [313]. Molecular dynamics simulations suggest that the proton is pinned while the OH group is mobile around the proton (Fig. 10.7 left). In the middle of Fig. 10.7 the results of a reactive force field molecular dynamics simulation of the hydration of CaO(001) is presented [312]. The topmost figure presents the positions of the hydroxyl groups during the time of the simulation for 0.25 ML water coverage at 300 K, showing that the ion pairs stay intact at this coverage. The bottom three side views are snapshots from the simulation for 0.25 ML, 0.75 ML and 1.5 ML water coverages, exhibiting increasing disorder of the CaO surface with increasing water coverages, as well as hydroxylation of the second layer in the case of the highest coverage considered. The most recent experimental and computational results for water interaction with CaO(001) are shown in Fig. 10.7, right. STM images have been acquired from a 10 ML thick CaO(001) thin film sample and show the formation of 1-dimensional water structures (chains) on the surface at room temperature after exposure to 0.02 and 0.2 L water. Atomistic models for these 1-dimensional structures corresponding to water coverages of about 0.5 ML (5 and 6 water molecules in a 3×4 unit cell), together with the calculated vibrational spectra for the 5 water molecules in the (3×4) unit cell are presented below the STM images. It should be mentioned that the models for the 1-dimensional water structures have been obtained within the framework of DFT including dispersion interaction correction using FHI-aims [316] (unpublished data by X. Zhao and S. Levchenko), whereas the reactive force field study did not yield any ordered structures [312]. Analysis of the calculated vibrational spectrum reveals that the band at the highest frequency corresponds to the stretching vibration of adsorbed OD groups resulting from water dissociation and the one at around 2600 cm^{-1} is from the surface OD group (transferred proton) located in the “square” feature. The low frequency vibration results from the surface OD groups of the “linker” element. At an elevated temperature, 300 K, in addition to thermal broadening, coupling of the two surface OD groups of the “linker” element leads to splitting

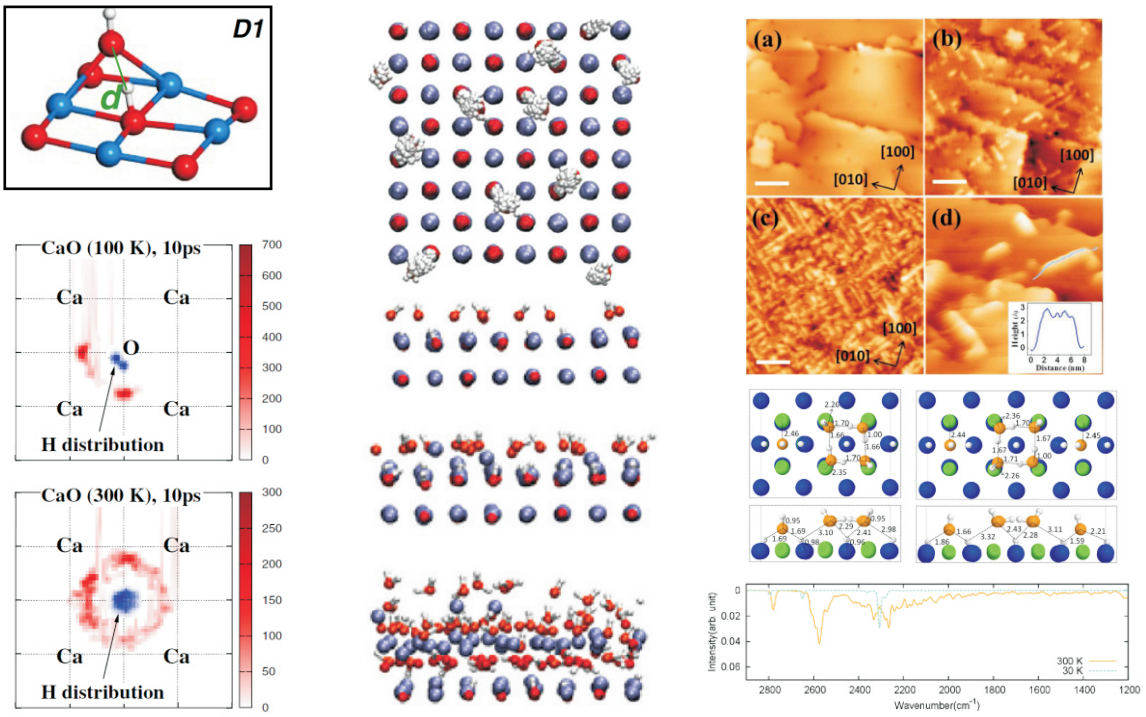

Figure 10.7: (left) H-OH ion pair on CaO(001) (top) and MD simulation at 100 and 300 K showing the rotation of the OH group at the center of a H-O_s group, according to Ref. [313]; (middle) Results of reactive force field simulations of Manzano et al. [312]: top: top view of 0.25 ML water coverage on CaO(001); bottom: side views of simulation results for 0.25, 0.75 and 1.5 ML water coverages on CaO(001), according to a prior study; (right, top) STM images of a 10 ML CaO(001) films before (a) and after exposed to about 0.02 L (b) and 0.2 L (c) of water vapor at room temperature. (d) shows an enlarged images of the water stripes. Scale bar 10 nm. With courtesy of X. Shao, Y. Cui and N. Nilius (unpublished data). (right, down) Top and side views of CaO(001) surfaces with 5 or 6 water molecules, and corresponding infrared spectra at 0 and 300 K, according to DFT calculations performed by X. Zhao and S. Levchenko (unpublished data).

into the symmetric and asymmetric stretching vibrations. Further STM studies, which are not presented here, have shown that small doses of water at adsorption temperatures below RT lead to point-like features, resulting most probably from single water molecules, and water clusters. On the other hand, large doses of water at RT resulted in substantial roughening of the surface due to the strong interaction of water with CaO(001).

With the information from the computational studies and the STM investigations, the findings of the present work are interpreted as follows:

a) Low-temperature, low-coverage regime: The sharp band at 2745 cm^{-1} observed initially after small doses of water at 110 K can most likely be attributed to the OD vibration of the tight ion pair proposed by calculations. The contributions at the low frequency side of this band, that grow in after increasing the water dose then correspond to the OD vibrations of

larger water/hydroxyl aggregates (dimers, trimers, tetramers), which also give rise to vibrations in the 2600 cm^{-1} region.

b) Room-temperature, low coverage regime (up to 0.6 ML OD): For the smallest water coverage (0.15 ML), the band with the most spectral weight appears at 2725 cm^{-1}, which is accompanied by smaller OD contributions at higher frequencies as well as a broad signal at 2600 cm^{-1}. According to the STM investigations, water/hydroxyl chains as well as smaller aggregates are present on the surface under these conditions, and the signals are assigned accordingly. The observation of the 2725 cm^{-1} and 2600 cm^{-1} components would very well fit with the computational results. However, the calculated broad signal at low frequencies of $\sim$2300 cm^{-1} according to the "linker" OD's could never be clearly seen in the experimental IR data. On the one hand, this could leave a possibility of the presence of discrepancy between the theoretical and experimental models in details. On the other hand, it could also mean that no chain-like structures were present on the sample in the IR experiments. Since those signals are subjected to strong broadening, which could be enhanced further by the presence of different chain configurations, the absence, or difficulty for detection of this signal is not entirely unreasonable. With increasing coverage, the OD signal in the 2720 cm^{-1} region increases and broadens towards the low-frequency side (hard to see in Fig. 10.3a), and the 2600 cm^{-1} signal increases as well in intensity. This most likely reflects the transition from the ordered, low-coverage phases, to the disordered, high coverage state, where hydrogen-bonding network affects greatly decreases the wavenumber of hydroxyl's stretching mode (this would be consistent with STM observations).

c) Room-temperature, high coverage regime: Upon water dosing at 110 K and subsequent heating to 300 K, a hydroxylation state corresponding to full monolayer coverage of water/hydroxyls could be stabilized. The study of the thermal stability, however, showed that upon heating to 400 K, the water/hydroxyl coverage drops significantly and reaches a value equal to the one that is obtained after heating the room-temperature-dosed sample to 400 K. The surface prepared by this procedure obviously contains weakly bound water/hydroxyls that are stabilized on the hydroylated CaO surface due to the long and intimate contact at low temperature.

d) Hydrated surface (after mbar exposure): The IR spectra taken from this preparation exhibit similar features as the one in the procedure c) (sharp 2719 cm^{-1} band and broad 2600 cm^{-1} signal), and in addition new contributions at 2690 cm^{-1} and 2643 cm^{-1}. The former ones are attributed to the water/hydroxyl species of a fully hydroxylated surface, and the latter ones correspond to $Ca(OD)_2$-like structures, as suggested by the work of Low et al. ($Ca(OH)_2$ pseudolattice [303]).

10.4.2 Mechanisms behind Hydroxylation and the Effect of Films Thickness

Very few experimental studies were performed with an aim to reveal the effects of oxide-film thickness on hydroxylation of the oxide-film surfaces [112]. Thin oxide films grown on metal substrates could be either charged or doped. CaO films on a Mo(001) substrate correspond to

the latter [308]. The spectroscopic data presented in this chapter found thinner CaO/Mo(001) films to be difficult to be hydroxylated (Section 10.3.4), which agrees with a cooperative STM investigation (data not shown). As already described, for CaO(001)/Mo(001) systems, this Mo-doping induces even the formation of Ca_3MoO_4 phase when the films are quite thin such as 2–4 ML in order to relax the lattice mismatch [10].

Considering the atomic composition of thin CaO/Mo(001) films, a plausible reason why the hydroxylation is not favored on the thin CaO films lies in the presence of Mo species on the surface, because, instead of molybdenum oxide, pure molybdenum species are not hydroxylated at all. This indicates that the effective surface area with an ability of binding hydroxyls drops as the CaO/Mo film thickness decreases. In addition to this geometric mechanism, changes in the electronic structure provide another explanation. The previous studies using LT-STM claimed that the Mo dopants in the films donate electrons to either the Mo(001) substrate or supported admetals [10,308]. This results in the formation of highly cationic Mo species such as Mo^{3+}. Thus, the CaO films with Mo dopants are classified as an *p*-type semiconductor, i.e., the formation of a new vacant state occurs. As concerns effects of highly cationic dopants, recent DFT calculations reveal that the doped-oxides become hydrophobic due to the charge transfer from adsorbed water molecules to highly cationic dopants, by which the amounts of electrons able to be spent for the formation of chemical bond between the oxide surfaces and water molecules decrease [168]. Theoretically, this was evidenced by the shrinking of HOMO of water molecule upon adsorption onto oxide surfaces. In agreement with this result, a calorimetric study of water adsorption and absorption found the decrease of adsorption energy of water as the concentration of highly cationic dopants increases for CaO powder [317]. As mentioned in this investigation, less hydrophilic surfaces present on the doped-oxides have less hydrogen-bonding network, due to the decrease of surface polarity. Our observation of the simultaneous disappearance of the infrared bands at 2600 and 2740 cm^{-1} agrees well with this proposal.

10.4.3 ASW → CI Transition and Surface Hydroxyls

The influence of the wettability of interfaces on the ASW → CI transformation and ice desorption was studied two decades ago, using mixed SAMs consisting of alkanethiols with either -CH_3 or -OH termination as substrates [310]. This study revealed that both the transition and the desorption temperature of ice strongly depend on the substrate functionality, with clear inhibition of ASW → CI transformation and increase of ice desorption temperature on the more hydrophilic (-OH terminated) interfaces. This effect was explained in terms of the stronger hydrogen-bond interaction between ice and the OH-terminated interface as compared to the hydrophobic (-CH_3 terminated) interface. In the present study, a similar approach has been used to alter the properties of ice at interfaces. However, instead of functionalizing the substrate with foreign molecules exhibiting different functionality, here the intrinsic reactivity of the oxide surface toward water could be used as a tuning factor. As shown by the results for water adsorption on the CaO(001) films, this surface gets hydroxylated already under UHV conditions

at temperatures as low as 100 K, providing a favorable situation for hydrogen-bond interaction with water molecules in the ice layers. By contrast, hydroxylation of MgO(001) is unfavorable under UHV conditions and water adsorption at low temperatures leads to the formation of an ordered water monolayer. While this ordered phase contains both undissociated and dissociated water molecules, its interaction with subsequent ice layers has previously been shown to be weak [309, 314]. In the present study, the previously published thermal behavior of ASW grown on MgO(001) at 100 K has been confirmed: Upon heating, the ASW layer transforms into CI at around 150 K, which is accompanied by ice dewetting but only little water desorption. Further heating to 155 K leads to complete desorption of CI [112, 309]. A different behavior was observed for ice on CaO(001): during heating, the ASW layer remains stable and only water desorption from ASW is observed up to 162 K. Only when almost all water was desorbed at 164 K a clear transition from ASW to CI occurred. The critical temperature for the ASW → CI transition was 10 K higher on CaO(001) compared to that on the pristine MgO(001) surface [112, 309]. The test experiment with hydroxylated MgO(001) confirmed a primary role of surface hydroxyls in the inhibition. Therefore, the present results confirmed the conclusions of previous studies for ice on SAMs by showing the inhibition of the ASW → CI transition by the presence of interfacial hydroxyl groups, which allow the multilayer ice to be strongly attached to the interface by formation of an intermolecular H-bonding network.

10.5 Conclusions

Comprehensive understanding of the interactions of water with CaO/Mo(001) films at UHV and elevated pressures was obtained, using various spectroscopic methods. Adsorption of water at room temperature produced hydroxylated CaO surfaces with a maximum hydroxyl coverage of 0.6 ML. At ambient pressures of water, the oxide films were partially transformed into a brucite-type $Ca(OD)_2$ pseudo-lattice. Exposure of the CaO(001) surfaces to water at 110 K resulted in the formation of H-OH pair at low coverages and the growth of ASW by further water dosing. On the CaO(001) surfaces, the critical temperature for the ASW → CI phase transition was found to be 164 K. The surface hydroxyls formed on CaO(001) surfaces at low temperatures were shown to inhibit the transition and increase the critical temperature by ∼10 K, compared to MgO(001). The CaO film thickness dependence experiments revealed that the hydroxyl coverage decreased with decreasing CaO film thickness, an effect that can be relating to the presence of Mo dopants in the ultra-thin CaO films. This hydrophobic surface was shown to let weak hydrogen-bonded hydroxyl be formed. Finally, surface hydroxyls with different vibrational frequencies on CaO films were closely characterized.

Chapter 11

Conclusions and Outlook

The goal of the present work was to provide detailed understanding of the interaction between supported metal particles and oxide surfaces using thin, single-crystalline oxide films as model substrates and X-ray based electronic structure determination methods, infrared probe spectroscopy and thermal desorption spectroscopy as main analysis techniques. The elucidation of the effect of oxide surface functionalization by hydroxyls on the nucleation and sinter behavior of metal atoms and metal particles was the main focus of this thesis. Additionally, related topics such as the nucleation and sinter behavior of metals on clean oxide surfaces, the reactivity of clean and oxidized metal single-crystal surfaces, and a comparison of water interaction with different oxide surfaces, were addressed. The main results of this thesis are summarized in the following.

The Effect of Oxide Film Thickness on the Interaction between Metals and Oxide Surfaces

To reveal the effect of oxide film thickness on metal nucleation, gold was deposited on Ag(001)-supported MgO films of different thickness (from 2 to 20 ML) and the charge state and the identity of the resulting supported gold species was analyzed with XPS, Auger parameter analysis, and CO-IRAS. The analysis of the spectroscopic results revealed the formation of neutral Au clusters and of positively and negatively charged Au species upon Au deposition on ultrathin MgO films. Whereas the formation of negatively charged Au via charge transfer through the thin oxide film was expected based on previous findings, the observation of cationic Au indicated the presence of particular defects with high electron affinity on the films. In collaboration with DFT, anion vacancies and grain boundaries were suggested as possible adsorption sites giving rise to cationic Au. CO-IRAS was furthermore used to probe the MgO film thickness-dependent variation of the defect distribution, whereas XPS in combination with Auger parameter analysis was applied to provide direct spectroscopic information about the different charge states of Au species formed on ultrathin and thick MgO films.

Interactions of Water with Oxide Surfaces

Studies about the interaction of water with oxide surfaces were performed with MgO(001) and CaO(001) thin films and encompassed detailed investigations of surface hydroxylation, ice crystallization, and film thickness effects.

A stable hydroxylated MgO(001) surface could only be obtained by exposing the MgO(001) surface to water vapor at elevated pressure conditions. In this thesis, two routes for surface hydroxylation were applied: an electron-assisted route, where the ion gauge inside the hydroxylation cell was left on, and a normal route, where the ion gauge was switched off. The surface hydroxyl coverage obtained via the two routes was roughly the same and did not vary as a function of MgO film thickness. However, according to infrared characterization, the hydroxyls obtained via the electron-assisted route are more Lewis acidic than those obtained via the normal route.

In contrast to MgO(001), stable hydroxyl groups were formed on CaO(001) by water exposure at UHV conditions and low temperature (100 K). While surface hydroxylation prevailed for any surface hydroxylation treatment in UHV, partial bulk hydroxylation and the transformation of CaO(001) into a pseudo-$Ca(OH)_2$ phase occurred upon water exposure at near ambient conditions. The presence of hydroxyl groups on CaO(001) and their strong interaction with second layer water molecules was found to inhibit the crystallization of ice on CaO(001) and to shift the ice desorption to higher temperature by 10 K compared to MgO(001). On ultrathin CaO(001) films, a reduction of the hydroxylation level by almost 50 % compared to thick, bulk-like CaO(001) films was noticed after identical hydroxylation treatments. This effect could be attributed to the presence of Mo dopants in the ultrathin films.

Interactions and Reactions between Metals and Surface Hydroxyls on Oxide Surfaces

To gain insight into surface processes involving hydroxyl groups on MgO(001), their interaction with metals, Au and Pd, was studied. Deposition of these metals onto surfaces containing the more acidic hydroxyl groups created via the electron-assisted hydroxylation route led to the formation of small, cationic metal clusters. In addition, it was found that the hydroxylation treatment inhibited, either because of enhanced metal-support interaction or due to hydroxylation-induced roughening of the surface, the thermal sintering of the metal particles. More details about the chemical interaction between the hydroxyl groups and Pd particles, as well as CO adsorbed on Pd particles, were obtained from combined IRAS, Auger parameter analysis, and TPD experiments conducted with hydroxylated MgO obtained via the normal hydroxylation route. Deposition of Pd atoms onto the hydroxylated MgO surface at room temperature led to the formation of strongly interacting Pd-OH complexes. Upon heating, the evolution of hydrogen molecules and simultaneous oxidation of the Pd particles was detected between 380 and 450 K, indicating the occurrence of a redox interaction between Pd and OH. Hydrogen evolved also at around 500 K in the presence of CO molecules adsorbed on Pd particles. The observation of

simultaneous CO_2 and D_2 desorption provided evidence for the occurrence of the water-gas shift reaction. Under the experimental conditions employed in this study, the WGS-type interactions were found to occur mainly at the peripheral sites of the Pd particles. In addition, the Pd coverage-dependent results indicated that D_2 formation occurs via different mechanisms (usual WGS-type interactions with COOH intermediates at low temperature and a metal-redox process involving hydroxyls at the periphery of the Pd particles at high temperature). Gold exhibited little interaction and reactivity toward normal surface hydroxyls.

Interaction of Water with Oxidized Metals

The reaction of water with oxidized metals was studied using MgO-supported PdO particles and oxidized Pd(111). The strongly oxidized Pd surfaces obtained by oxidation at elevated temperature and oxygen pressure were found to readily react with water and concomitant CO to yield formate and carbonate species. This functionalization affected only the very surface layers, while the sub-surface layers in the case of Pd(111), and the particle core in the case of Pd nanoparticles, remained oxidized. The functionalized surfaces were found to be thermally less stable than the pure oxidic phases, leading to the evolution of water and carbon dioxide at temperatures much lower than the decomposition temperature of Pd-oxide, and generally to a destabilization of the oxide phases, hence a more facile reduction to metallic Pd.

General Outlook & Concluding Remarks

A step toward a better understanding of the properties of surface hydroxyls on oxide surfaces and their interactions with supported metals has been undertaken in this thesis. Here, surface hydroxyls on the non-polar MgO(001) surface were examined, and few environmental effects were included except for the pressure effects. Information relevant to more realistic events could be accessed in the future. One of the top priority aspects to study might be the effect of surface polarity. The hydroxylation and hydration of MgO surfaces inevitably leads to the growth of 111 facets. This polar surface, which in most cases is stabilized by adsorption of foreign species, can be a dominantly present surface phase on real catalysts. Therefore, an interesting point to be addressed in the future would be the study of the properties of metal particles and adsorbates on MgO(111) surfaces. The second subject concerns the elucidation of the effects of electron-donor or acceptor dopants. The possible role of dopants in the activation of supported catalysts have been mentioned over decades, but mechanistic details about their influence on adsorbates or supported metals on oxide surfaces have rarely been considered. The surface hydroxyls on doped oxide surfaces could be used as sample adsorbates, in order to understand how the electronic structure and the reactions of surface functional groups are controlled by dopants.

It is hoped that further work on the interplay of hydroxyls on oxide surfaces under more realistic conditions could help to illuminate the essence of catalytic reactions, and trigger novel ideas in chemical reactions.

Abbreviations

Acronym	Full Name
AES	Auger Electron Spectroscopy
AFM	Atomic Force Microscopy
CVD	Chemical Vapor Deposition
DFT	Density Functional Theory
EPR	Electron Paramagnetic Resonance
EXAFS	Extended X-ray Absorption Fine Structure
FT-IR	Fourier Transform Infrared
HREELS	High Resolution Electron Energy Loss Spectroscopy
IR(R)AS	Infrared Reflection Absorption Spectroscopy
ISS	Ion Scattering Spectroscopy
LEED	Low-Energy Electron Diffraction
ML	Monolayer
NEXAFS	Near-Edge X-ray Adsorption Fine Structure
PES	Photoelectron Spectroscopy
PM-IR(R)AS	Polarization-Modulation Infrared Reflection Absorption Spectroscopy
PVD	Physical Vapor Deposition
QMS	Quadrupole Mass Spectrometer
RHEED	Reflection High Energy Electron Diffraction
TOF	Turn Over Frequency
TPD	Temperature Programmed Desorption
SAM	Self Assembled Monolayer
SCLS	Surface Core Level Shift
SEXAFS	Surface Extended X-ray Absorption Fine Structure
SIMS	Secondary Ion Mass Spectroscopy
STM	Scanning Tunneling Microscopy
TEM	Transmission Electron Spectroscopy
UHV	Ultra-high Vacuum
UPS	Ultraviolet Photoelectron Spectroscopy
XAFS	X-ray Adsorption Fine Structure
XPS	X-ray Photoelectron Spectroscopy

Appendix

A Infrared Spectra of CO Adsorbed on Supported Au under Various Conditions

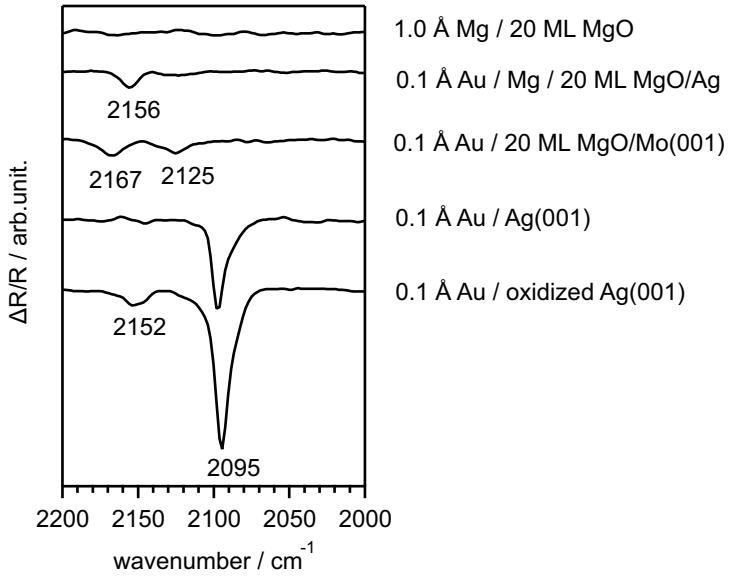

Figure A1: IRA spectra of adsorbed CO at 100 K for 1.0 Å Mg/20 ML MgO, 0.1 Å Au/1.0 Å Mg/20 ML MgO, 0.1 Å Au/Ag(001), 0.1 Å Au/oxidized Ag(001) and 0.1 Å Au on 20 ML MgO/Mo(001) (from top to bottom).

In order to support the conclusions presented in Chapter 6, infrared spectra of CO adsorbed at 100 K on Au deposited on clean and modified Ag(001) and MgO(001)/Ag(001) thin film surfaces have been acquired. The spectrum (i) was obtained for 1.0 Å Mg deposited on 20 ML MgO(001) films. The absence of any CO IR signals means that neither Mg^{2+} ions on the surface nor the Mg ions trapped by F^{2+} centers contributes to CO adsorption. The spectrum (ii) corresponds to 0.1 Å Au deposited on the Mg/MgO surface. The consequence of the Mg pre-deposition was the absence of the IR band at 2170 cm^{-1}, which indicates that the nucleation sites for gold leading to this particular CO stretching frequency have been occupied by Mg. Mg trapping at special surface sites has been reported in a recent EPR study [196]. The spectrum (iii) was acquired for 0.1 Å Au on MgO(001) films with the same thickness, 20 ML, on a different support, Mo(001). The MgO/Mo(001) films were prepared according to a well-

known recipe [318]. Adsorbed CO on Au/MgO/Mo(001) gave bands at 2167 and 2125 cm^{-1}, similar to the observations made for CO adsorbed on Au/MgO/Ag(001) as presented in Fig. 6.1. This similarity suggests that the properties of thick MgO films are hardly affected by the different substrates. Additionally, the following interactions are possible for Au/MgO/Ag(001) system: (a) Au contacting with metallic or oxidized Ag surfaces. The spectrum (iv) and (v) correspond to the two situations, respectively. The deposition of Au onto Ag surfaces produces a CO adsorption signal at 2095 cm^{-1}, suggesting that the Au particles are metallic [99]. CO adsorbed on Au/AgO_x gave an additional component at ~2152 cm^{-1}. This observation implies the possible contribution of oxygen to the formation of the positively charged Au clusters on thin MgO/Ag(001) films. However, Au/MgO/Mo(001) gave an analogous absorption band, confirming that AgO_x patches are not necessarily responsible for the formation of positively charged Au-carbonyl clusters.

B O_2 Adsorption on Ultra-Thin MgO/Mo(001) Films

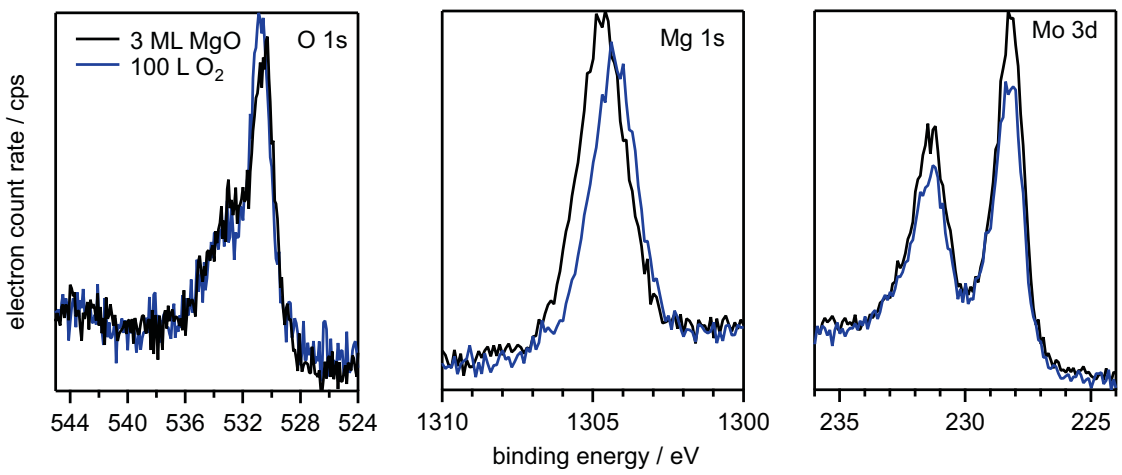

Figure B1: O 1s, Mg 1s, and Mo 3d XP spectra for pristine 3 ML MgO/Mo(001) films, and the MgO films after exposure to 100 L O_2 at 100 K. XP spectra were acquired at an electron emission angle of 85 degrees.

Recently, the formation of O_2^- species on ultra-thin MgO/Mo(001) films, which might be active species in catalytic CO oxidation, was theoretically predicted and confirmed experimentally by EPR spectroscopy [21, 169, 319]. To add another proof for this phenomenon, the adsorption of O_2 on ultra-thin MgO/Mo(001) films was studied using XPS. The preparation of the MgO films was carried out according to a well-established recipe [318]. Fig. B1 displays the O 1s, Mg 1s and Mo 3d XP spectra at an electron emission angle of 85 degrees for the 3 ML thick MgO/Mo(001) films before and after exposure to 100 L O_2 at 100 K. The oxygen exposure induced the development of a new constituent in the O 1s region at a binding energy of 532.8 eV, accompanied by negative binding energy shifts of 0.3 eV of the main O 1s signal and 0.4 eV of the Mg 1s emission. The negative binding energy shifts indicate that band bending occurred

by the adsorption of O_2, in agreement with the formation of a negatively charged adsorbate. Furthermore, the intensities of the Mo 3d and Mg 1s peaks got slightly reduced upon oxygen exposure, whereas the O 1s signal intensity increased by 6 %, which is close to the O_2^- coverage quantified by EPR [21]. Eq. 2.17 with a mean free path of 8 Å for photoelectrons from the Mg 1s orbital supported the presence of adsorbates at a coverage of 0.06 ML [320]. Neither vibrational spectroscopic nor mass-spectrometric characterization of this adsorbate was performed. The reactivity of the adsorbates toward CO molecules was investigated at 100 K. Negligible consumption of adsorbed O_2 species occurred, even after 100 L CO exposure of the oxygen covered ultra-thin MgO films (data not shown). Instead, the exposure to CO induced a slight increase in the O 1s peak at a binding energy of ∼533.0 eV.

C Auger Parameter Analysis for Au/MgO

Electronic Structure of MgO Films and Supported Au Particles

To promote a better understanding of the electronic structure of supported systems using thin oxide films as already investigated by various techniques (see Chapter 6), Auger parameter analysis has been applied to gold particles supported on MgO(001)/Ag(001) thin films. The MgO films were prepared according to the procedure described in a Ref. [321]. As for 0.1 Å Au deposited on 2 ML and 30 ML thick MgO films at 100 K, Tab. C1 summarizes the binding energies of Mg 1s, Mg 2s, and the kinetic energies of the Mg KL_1L_1 Auger transition upon annealing to 100 (as-deposited), 300 and 573 K.

In general, the deposition of Au onto the MgO films induced negative binding energy shifts of the oxide components by several hundreds meV. On the other hand, the KL_1L_1 Auger kinetic

Table C1: Binding energy shifts (eV) of Mg 1s and Mg 2s, and kinetic energy of the Mg KL_1L_1 Auger transition for 2 ML and 30 ML thick MgO/Ag(001) films upon depositing 0.1 Å Au at 100 K. The corresponding initial, $\Delta\varepsilon$, and final, ΔR, state effects of Mg were calculated. Spectra were collected at an electron emission angle of 60 degrees.

condition	Mg 1s	Mg 2s	Mg KL_1L_1	ΔR	$\Delta\varepsilon$
2 ML MgO	1303.85	88.77	1103.12		
Au/MgO @ 100 K	1303.63	88.43	1103.49	−0.05	0.39
Au/MgO @ 300 K	1303.63	88.41	1103.5	−0.05	0.42
Au/MgO @ 573 K	1303.72	88.55	1103.4	−0.02	0.24
30 ML MgO	1304.13	89.26	1102.09		
Au/MgO @ 100 K	1303.63	88.67	1102.7	−0.04	0.63
Au/MgO @ 300 K	1303.62	88.58	1102.72	−0.1	0.51
Au/MgO @ 573 K	1303.83	88.89	1102.4	−0.06	0.43

energies exhibited upward shifts as Au was deposited on the MgO films. No changes occurred in ΔR for the Au/MgO/Ag systems, which indicate that the binding energy shifts caused by Au deposition can purely be ascribed to band bending. The extent of band bending is contained in $\Delta\varepsilon$. Au deposition on 2 ML MgO films caused ∼0.4 eV band bending, whereas for the thick films the effect was larger by 0.2 eV. This is not surprising given that the thin films are strongly influenced by the Ag substrate. Upon annealing to 300 K, no changes of the electronic structure of the MgO films were observed, suggesting that the degree of band bending remained identical. Considering the fact that flat Au islands were produced upon annealing to 300 K, the contact area of Au particles to the MgO films seems to govern the degree of the band bending. Further annealing to 573 K resulted in the decrease of the degree of the band bending by ∼0.2 eV, as evidenced by the decrease of $\Delta\varepsilon$ for both the Au/MgO systems.

Electronic States of the Supported Au Particles

How the film thickness of MgO films and the band bending affect the electronic states of supported Au particles remains unanswered. To directly elucidate electronic states of supported gold, the Au particles supported on the MgO films as well as on the clean Ag(001) surface were investigated using XPS and the Auger parameter analysis. All measurements were carried out at a substrate temperature of 100 K and a background pressure better than 4.0×10^{-10} mbar to avoid any molecular adsorption of water and CO, which could induce the binding energy shifts [234]. Additionally, Au 4f XP and Au $M_5N_{67}N_{67}$ AE spectra were collected within 1.5

Table C2: Binding energy shifts (eV) of Au $4f_{7/2}$ and kinetic energy of the Au $M_5N_{67}N_{67}$ $^1I_6$ Auger transition for 2 ML and 30 ML thick MgO/Ag(001) films with a gold coverage of 0.1 Å deposited at 100 K. The corresponding initial, $\Delta\varepsilon$, and final, ΔR, state effects of Au were calculated. Spectra were acquired at an electron emission angle of 60 degrees.

condition	Au $4f_{7/2}$	Au $M_5N_{67}N_{67}$	ΔR	$\Delta\varepsilon$
Au/Ag(001) @ 100 K	83.8	2015.5	−0.26	0.46
Au/Ag(001) @ 300 K	84.0	2015.7	−0.05	0.05
Au/2 ML MgO @ 100 K	85.75	2011.6	−1.23	−0.53
Au/MgO @ 100 K	84.26	2014.16	−0.7	0.43
Au/MgO @ 300 K	84.25	2014.26	−0.65	0.4
Au/MgO @ 573 K	84.15	2014.6	−0.53	0.38
Au/30 ML MgO @ 100 K	86.55	2011.0	−1.15	−1.41
Au/MgO @ 100 K	84.73	2014.1	−0.49	−0.25
Au/MgO @ 300 K	84.59	2013.4	−0.91	0.32
Au/MgO @ 573 K	84.35	2014.5	−0.46	0.11

hours. For fitting, the Au 4f spin-orbit splitting of 3.67 ev was used, and the intensity ratio of the two 4f components was set to the theoretical value of 3:4 [72]. For the Auger parameter analysis, the Au(111) surface was used as a reference. Its Au $4f_{7/2}$ binding energy was measured to be 84.0 eV [72]. The Au $M_5N_{67}N_{67}$ Auger transition consists of three micro-states. Of those, the $^1I_6$ line (two holes in the 4f orbitals with the angular momentum $l = +3$) with an electron kinetic energy of 2015.8 eV was used for the analysis [322]. The corresponding data for 0.1 Å Au supported on MgO/Ag(001) films at thicknesses of 2 ML and 30 ML are summarized in Tab. C2.

We start to discuss the result of Au/Ag(001) (Tab. C2, top). The freshly prepared Au particles on the Ag(001) substrate exhibited an Au $4f_{7/2}$ binding energy of 83.8 eV. The corresponding Au Auger electrons had a kinetic energy of 2015.5 eV. The Auger parameter gives slightly negative ΔR, −0.26 eV, and positive $\Delta\varepsilon$, 0.46 eV. The rather small final state contribution is good indicative of the growth of medium size Au particles on conductive materials. The positive $\Delta\varepsilon$, +0.46 eV, is a strong indication of the occurrence of surface core level shift (SCLS), which essentially occurs for small Au particles due to the efficient 6s → 5d intra-atomic charge transfer at less coordinated Au atoms [73]. Another possible explanation is the reduction of Au caused by the large difference in electronegativity between Au (2.54) and Ag (1.93) (*cf.* [323]). However, the result in Fig. A1 indicates the presence of metallic Au on Ag(001). Thus, this positive $\Delta\varepsilon$ should be ascribed to the occurrence of SCLS. Upon annealing to room temperature, the supported Au particles exhibited almost the same properties as bulk metallic gold has, suggesting that rather large metallic Au particles were formed.

In the middle of Tab. C2, the results for Au supported on the 2 ML thick MgO/Ag film are presented. As already shown in Chapter 6, gold at sub-monolayer coverages on thin and thick MgO films exhibits various chemical states, such as positively charged [189] and negatively charged ones [22]. Therefore, the obtained Au 4f signals were fitted using two components. Careful fitting was carried out for the freshly prepared Au/2 ML MgO sample. There was one component with an Au $4f_{7/2}$ binding energy of 85.75 eV, and the other one appeared at 84.26 eV. Corresponding Auger signals were fitted with the constraint that the peak area ratio of the two components must be the same as that of the two Au 4f components. The Au species with the higher Au $4f_{7/2}$ binding energy gave an Au $M_5N_{67}N_{67}$ Auger signal with an electron kinetic energy of 2011.6 eV, while the other component yielded an electron kinetic energy of 2014.16 eV. Consequently, the former species gave ΔR of −1.23 eV, and $\Delta\varepsilon$ appeared at −0.53 eV, while the latter species gave ΔR of −0.7 eV and $\Delta\varepsilon$ of 0.43 eV. Upon annealing to 300 K, the decrease in FWHM of the Au 4f signal indicates formation of a single gold species with a binding energy of 84.25 eV. Infrared data revealed that flat Au islands are formed upon annealing to 300 K (see Chapter 6), which agrees with the presence of one component inferred by the fitting. This species exhibits similar initial state and final state contributions to the binding energy shift as the Au component with the lower Au 4f binding energy at 100 K ($\Delta R = -0.65$ eV and $\Delta\varepsilon = 0.4$ eV). Further annealing to 573 K results in the formation of large metallic Au particles with $\Delta R = -0.53$ eV and $\Delta\varepsilon = 0.38$ eV.

For 0.1 Å Au supported on 30 ML thick MgO/Ag(001) films, the broad Au 4f signal was again fitted with two Au components. There was a gold species with an Au $4f_{7/2}$ binding energy of 86.55 eV and an Au $M_5N_{67}N_{67}$ Auger electron emission with a kinetic energy of 2010.0 eV, accompanied by another species with an Au 4f binding energy of 84.73 eV and an Au Auger electron kinetic energy of 2014.1 eV. The former species exhibited a large negative $\Delta\varepsilon$, −1.41 eV, in contrast to the latter one ($\Delta\varepsilon = -0.25$ eV). Interestingly, upon annealing to 300 K, we observed only one gold species with $\Delta\varepsilon = 0.32$ eV and $\Delta R = -0.91$ eV. At 573 K, in agreement with the results presented in Chapter 6, there was only one metallic Au component with $\Delta\varepsilon =$ 0.11 eV and $\Delta R = -0.46$ eV.

Here, short discussion about the results for Au supported on the Ag (001) surface as well as the MgO films is provided. The first issue concerns the final state contributions. Positive core-level binding energy shifts are frequently observed for well-dispersed gold particles [189]. However, Torelli et al. maintained that atomically dispersed Au particles should intrinsically exhibit a *negative* binding energy shift due to SCLS [76]. The present study shows that, for atomically dispersed Au particles on the Ag(001) surface, the negative Au 4f binding energy shift was composed of a positive $\Delta\varepsilon = 0.4$ eV, which is partially counterbalanced by the screening effect (−0.26 eV) (Tab. C2). Our demonstration of the positive initial state effect, causing a negative shift in the binding energy, of well-dispersed Au particles on the silver surface is in excellent agreement with their proposal. Analogously, the non-negligible final state contributions due to ill-conductive supports were found to become notable for the MgO-supported Au particles. Furthermore, irrespective of film thickness, atomically dispersed Au particles exhibited a pronounced final state contribution of more than 0.4 eV, because of the lack of surrounding gold atoms. As a consequence of the non-negligible final state contributions, *a-priori* evaluation of binding energies of supported systems can be easily erroneous.

Now, effects of MgO film thickness on electronic properties of the deposited Au particles are discussed. Compared to Au/30 ML MgO, the as-deposited Au/2 ML MgO exhibited both positive and negative shifts of $\Delta\varepsilon$: −0.53 and 0.43 eV (Tab. C2). Both positive and negative $\Delta\varepsilon$ for Au/2 ML MgO films should appear in accordance with earlier studies; some small Au particles on thin MgO films are anionic due to charge transfer from the substrate to Au particles [22, 324], and the other Au particles trapped at defect sites such as F^{2+} could become positively charged [189]. The Auger analysis of the Au/30 ML MgO system yielded a negative $\Delta\varepsilon$ of −1.41 and −0.25 eV for the two Au components. Considering the fact that there are Au species with at least three different charged states (positive, negative and neutral) according to the CO-IRAS study (Chapter 6), fitting the Au 4f and Au Auger spectra by only two components could be ambiguous and yield unreasonable results. This possible erroneous assumption might cause the exceptionally small final state contribution (−0.49 eV) for the slightly positively charged species with $\Delta\varepsilon$ of −0.25 eV. Nevertheless, the results of the Auger parameter analysis for Au on the thin and thick MgO films are in very good agreement with previous data [22, 325], showing that positively charged Au clusters are present on thin and thick MgO films upon Au deposition at 100 K, and that on thin films negatively charged Au species are formed in addition.

The thermal development of gold particles on MgO films is also very well captured by Auger parameter analysis. Upon annealing to 300 K, the Au 4f spectra became significantly narrowed. This indicates the agglomeration-induced convergence of different Au species into one species. Alongside, $\Delta\varepsilon$ of Au appeared at slightly positive values of $\sim$ 0.3 eV, irrespective of the film thickness. This noteworthy similarity agreed with that Au/4 ML MgO exhibited an identical absorption spectra (data not shown) to Au/20 ML MgO after annealing to 300 K, as displayed in Fig. 6.2b. Additionally, the gold species on MgO(001) surfaces at room temperature are expected to form flat islands [189,326]. This explains well why $\Delta\varepsilon$ is positive: the occurrence of SCSL. Indeed, the positive $\Delta\varepsilon$ of +0.3 eV is in the range of reported SCLS for Au surfaces [73]. Furthermore, Au on 2 ML MgO films, in contrast to Au on thick films, is considered to be more negatively charged and to be less affected by the screening due to the partial charge transfer to the particles and the small MgO film thickness. The results of the Auger parameter analysis fully supports this assumption. The agglomeration of Au particles to an average size of $\sim$3 nm occurred upon annealing Au/MgO(001) to 573 K (Fig. 7.4). These nucleated neutral Au particles exhibited a slightly positive $\Delta\varepsilon$, with a significantly reduced contribution of ΔR.

It should be mentioned that some ambiguity in the fitting results for the Au 4f XP and the Au Auger spectra might arise from: (i) the presence of multiple components; (ii) poor S/N ratio of the Auger lines. Nevertheless, the Auger parameter basically succeeded in grasping the primary properties of the systems. For example, conventional analysis based only on the binding energy shift could assign the Au particles on 2 ML MgO(001) film to being cationic, instead of anionic (Tab. C2). Therefore, the present research demonstrated the utility of the Auger parameter analysis to understand "meaningful" data for supported metals at sub-monolayer coverages.

In summary, electronic structure of gold deposited onto MgO films with a thickness of 2 and 30 ML was probed by photoemission spectroscopy and Auger parameter analysis. Gold deposition caused the band bending of MgO films by $\sim$0.5 eV. A correlation between the degree of band bending and the contact area of Au particles was found. Supported Au particles on the Ag(001) surface exhibited a negative initial state contribution, indicative of SCLS, which is partly counterbalanced by the effect of reduced screening. This behavior is in perfect agreement with a prior study by Torelli et al. [76]. As for well-dispersed Au particles on 2 ML thick MgO films, there were negatively charged Au particles, as previously proven by LT-STM and EPR [22, 327]. For freshly prepared gold particles on a thicker MgO film (30 ML), there was a clear tendency of gold to be more positively charged. At 300 K, while no change in the degrees of band bending was observed, flat gold islands appeared, in agreement with a previous observation [22, 325].

References

[1] Handbook of Heterogeneous Catalysis, 2nd ed., edited by G. Ertl, H. Knözinger, F. Schüth, and J. Weitkamp (Wiley-VCH Verlag GmbH, Weinheim, 2008).

[2] G. Ertl, *Angew. Chem. Int. Ed.* **47**, 3524 (2008).

[3] M. Appl, Ullmann's Encyclopedia of Industrial Chemistry., 2nd ed. (Wiley-VCH Verlag GmbH, Weinheim, 2006), pp. 1–143.

[4] G. Ertl, *Catal. Rev. -Sci. Eng.* **21**, 201 (1980).

[5] G. C. Bond and D. T. Thompson, *Gold Bulletin* **33**, 41 (2000).

[6] M. M. Schubert, S. Hackenberg, A. C. van Veen, M. Muhler, V. Plzak, and R. J. Behm, *J. Catal.* **197**, 113 (2001).

[7] V. Henrich and P. Cox, The Surface Science of Metal-oxides (Cambridge University Press, Cambridge, 1994).

[8] S. Arndt, G. Laugel, S. Levchenko, R. Horn, M. Baerns, M. Scheffler, R. Schlögl, and R. Schomäcker, *Catal. Rev.* **53**, 424 (2011).

[9] J. H. Lunsford, *Angew. Chem. Int. Ed.* **34**, 970 (1995).

[10] X. Shao, S. Prada, L. Giordano, G. Pacchioni, N. Nilius, and H.-J. Freund, *Angew. Chem. Int. Ed.* **50**, 11525 (2011).

[11] Y. Zhai, D. Pierre, R. Si, W. Deng, P. Ferrin, A. U. Nilekar, G. Peng, J. A. Herron, D. C. Bell, H. Saltsburg, M. Mavrikakis, and M. Flytzani-Stephanopoulos, *Science* **329**, 1633 (2010).

[12] G. Ertl, D. Prigge, R. Schloegl, and M. Weiss, *J. Catal.* **79**, 359 (1983).

[13] K. K. Kolasinski, Surface Science: Foundations of Catalysis and Nanoscience, 3rd ed. (John Wiley & Sons, Inc., West Sussex, United Kingdom, 2012), p. 574.

[14] H.-J. Freund, M. Bäumer, and H. Kuhlenbeck, *Adv. Catal.* **45**, 333 (2000).

[15] H.-J. Freund and E. Umbach, Adsorption on Ordered Surfaces of Ionic Solids and Thin Films, 1st ed. (Springer-Verlag, Berlin, 1993).

[16] U. Diebold, *Surf. Sci. Rep.* **48**, 53 (2003).

[17] G. H. Vurens, M. Salmeron, and G. A. Somorjai, *Surf. Sci.* **201**, 129 (1988).

[18] M.-C. Wu, J. S. Comeille, C. A. Estrada, J.-W. He, and D. W. Goodman, *Chem. Phys. Lett.* **182**, 472 (1991).

[19] J. Libuda, F. Winkelmann, M. Bäumer, H.-J. Freund, T. Bertrams, H. Neddermeyer, and K. Muller, *Surf. Sci.* **318**, 61 (1994).

[20] H.-J. Freund, *Angew. Chem. Int. Ed.* **36**, 452 (1997).

[21] A. Gonchar, T. Risse, H.-J. Freund, L. Giordano, C. Di Valentin, and G. Pacchioni, *Angew. Chem. Int. Ed.* **50**, 2635 (2011).

[22] M. Sterrer, T. Risse, U. M. Pozzoni, L. Giordano, M. Heyde, H.-P. Rust, G. Pacchioni, and H.-J. Freund, *Phys. Rev. Lett.* **98**, 096107 (2007).

[23] F. F. Vo'lkenshtein, *Russ. Chem. Rev.* **35**, 537 (1966).

[24] S. J. Tauster, S. C. Fung, and R. L. Garten, *J. Am. Chem. Soc.* **100**, 170 (1978).

[25] Y.-N. Sun, L. Giordano, J. Goniakowski, M. Lewandowski, Z.-H. Qin, C. Noguera, S. Shaikhutdinov, G. Pacchioni, and H.-J. Freund, *Angew. Chem. Int. Ed.* **49**, 4418 (2010).

[26] S. Böcklein, S. Günther, and J. Wintterlin, *Angew. Chem. Int. Ed.* **52**, 5518 (2013).

[27] A. C. Yang and W. Garland, *J. Phys. Chem.* **61**, 1504 (1957).

[28] D. Yates, L. Murrell, and E. Prestridge, *J. Catal.* **57**, 41 (1979).

[29] H. F. J. van't Blik, J. B. A. D. van Zon, T. Huzinaga, J. C. Vis, D. C. Koningsberger, and R. Prins, *J. Am. Chem. Soc.* **107**, 3139 (1985).

[30] D. E. Starr, Z. Liu, M. Hävecker, A. Knop-Gericke, and H. Bluhm, *Chem. Soc. Rev.* **42**, 5833 (2013).

[31] T. Masuda, H. Yoshikawa, H. Noguchi, T. Kawasaki, M. Kobata, K. Kobayashi, and K. Uosaki, *Appl. Phys. Lett.* **103**, 111605 (2013).

[32] G. Rupprechter, *Annu. Rep. Prog. Chem. Sect. C* **100**, 237 (2004).

[33] P. Guyot-Sionnest, J. Hunt, and Y. Shen, *Phys. Rev. Lett.* **59**, 1597 (1987).

[34] L. Velarde, X.-Y. Zhang, Z. Lu, A. G. Joly, Z. Wang, and H.-F. Wang, *J. Chem. Phys.* **135**, 241102 (2011).

[35] E. D. Crozier, *Nucl. Iinstrum. Meth. B* **133**, 134 (1997).

[36] R. Sonnenfeld and P. Hansma, *Science* **232**, 211 (1986).

[37] G. A. Somorjai, R. L. York, D. Butcher, and J. Y. Park, *Phys. Chem. Chem. Phys.* **9**, 3500 (2007).

[38] T. Fukuma, K. Kobayashi, K. Matsushige, and H. Yamada, *Appl. Phys. Lett.* **87**, 034101 (2005).

[39] H. Imada, K. Kimura, and H. Onishi, *Chem. Phys.* **419**, 193 (2013).

[40] G. Renaud, C. Revenant, A. Barbier, M. Noblet, O. Ulrich, J. Jupille, Y. Borensztein, C. R. Henry, J.-P. Deville, F. Scheurer, J. Mane-Mane, and O. Fruchart, *Science* **300**, 1416 (2009).

[41] H. Hashimoto, T. Naiki, T. Eto, and K. Fujiwara, *Jpn. J. Appl. Phys.* **7**, 946 (1968).

[42] H. Yoshida, Y. Kuwauchi, J. R. Jinschek, K. Sun, S. Tanaka, M. Kohyama, S. Shimada, M. Haruta, and S. Takeda, *Science* **335**, 317 (2012).

[43] C. Ratnasamy and J. P. Wagner, *Catal. Rev.* **51**, 325 (2009).

[44] D. Cunningham, W. Vogel, H. Kageyama, S. Tsubota, and M. Haruta, *J. Catal.* **177**, 1 (1998).

[45] M. A. Brown, E. Carrasco, M. Sterrer, and H.-J. Freund, *J. Am. Chem. Soc.* **132**, 4064 (2010).

[46] M. Sterrer and H.-J. Freund, *Catal. Lett.* **143**, 375 (2013).

[47] J. Libuda, M. Frank, A. Sandell, S. Andersson, P. A. Brühwiler, M. Bäumer, N. Martensson, and H.-J. Freund, *Surf. Sci.* **384**, 106 (1997).

[48] J. Kelber, C. Niu, K. Shepherd, D. Jennison, and A. Bogicevic, *Surf. Sci.* **446**, 76 (2000).

[49] S. Chambers, T. Droubay, D. Jennison, and T. Mattsson, *Science* **297**, 827 (2002).

[50] F. Mittendorfer, N. Seriani, O. Dubay, and G. Kresse, *Phys. Rev. B* **76**, 233413 (2007).

[51] D. Matthey, J. Wang, S. Wendt, M. J, R. Schaub, E. Lagsgaard, B. Hammer, and F. Besenbacher, *Science* **315**, 1692 (2007).

[52] D.-e. Jiang, S. H. Overbury, and S. Dai, *J. Phys. Chem. Lett.* **2**, 1211 (2011).

[53] G. N. Vayssilov, B. C. Gates, and N. Rösch, *Angew. Chem. Int. Ed.* **42**, 1391 (2003).

[54] J. P. Fitts, T. P. Trainor, D. Grolimund, J. R. Bargar, G. A. Parks, and G. E. Brown, *J. Synchrotron Radiat.* **6**, 627 (1999).

[55] C. L. Pang, H. Raza, S. A. Haycock, and G. Thornton, *Surf. Sci.* **460**, L510 (2000).

[56] Q. Fu, T. Wagner, and M. Rühle, *Surf. Sci.* **600**, 4870 (2006).

[57] J. Wang and B. Hammer, *Phys. Rev. Lett.* **97**, 136107 (2006).

[58] T. Wu, W. E. Kaden, and S. L. Anderson, *J. Phys. Chem. C* **112**, 9006 (2008).

[59] M. C. R. Jensen, K. Venkataramani, S. Helveg, B. S. Clausen, M. Reichling, F. Besenbacher, and J. V. Lauritsen, *J. Phys. Chem. C* **112**, 16953 (2008).

[60] H.-F. Wang, H. Ariga, R. Dowler, M. Sterrer, and H.-J. Freund, *J. Catal.* **286**, 1 (2012).

[61] C. T. Campbell and J. Sauer, *Chem. Rev.* **113**, 3859 (2013).

[62] Surface crystallography by LEED : theory, computation and structural results, 1st ed., edited by M. A. VanHove and S. Y. Tong (Springer-Verlag, Berlin, 1979), p. 671.

[63] N. W. Ashcroft and N. D. Mermin, Solid State Physics (Thomson Learning, Inc., ADDRESS, 1976).

[64] K. Siegbahn, *J. Electron Spectrosc. Relat. Phenom.* **5**, 3 (1974).

[65] K. Siegbahn, *Rev. Mod. Phys.* **54**, 709 (1982).

[66] C. Fadley, in Electron Spectroscopy, Theory, Techniques, and Applications, edited by C. R. Brundle and A. D. Baker (Pergamon Press Ltd., Oxford, 1978), Chap. 1, pp. 1–156.

[67] H. Gonska, H. Freund, and G. Hohlneicher, *J. Electron Spectrosc. Relat. Phenom.* **12**, 435 (1977).

[68] S. Evans, *Chem. Phys. Lett.* **23**, 134 (1973).

[69] M. Seah and W. Dench, *Surf. Interface Anal.* **1**, 2 (1979).

[70] S. Tanuma, C. Powell, and D. Penn, *Surf. Interface Anal.* **17**, 911 (1991).

[71] P. S. Bagus, E. S. Ilton, and C. J. Nelin, *Surf. Sci. Rep.* **68**, 273 (2013).

[72] J. F. Moulder, W. F. Stickle, P. E. Sobol, and K. D. Bomben, in Surface and Interface Analysis, edited by J. Chastain (Perkin-Elmer Corporation, Eden Prairie, 1992), No. 4.

[73] P. Citrin and G. Wertheim, *Phys. Rev. B* **27**, 3176 (1983).

[74] P. S. Bagus, G. Pacchioni, and F. Parmigiani, *Phys. Rev. B* **43**, 5172 (1991).

[75] S. Peters, S. Peredkov, M. Neeb, W. Eberhardt, and M. Al-Hada, *Surf. Sci.* **608**, 129 (2013).

[76] P. Torelli, L. Giordano, S. Benedetti, P. Luches, E. Annese, S. Valeri, and G. Pacchioni, *J. Phys. Chem. C* **113**, 19957 (2009).

[77] D. M. Woord, *Phys. Rev. Lett.* **46**, 749 (1981).

[78] J. M. Smith, *AIAA Journal* **3**, 648 (1965).

[79] G. Wertheim and S. DiCenzo, *Phys. Rev. B* **37**, 844 (1988).

[80] H. Hövel, B. Grimm, M. Pollmann, and B. Reihl, *Phys. Rev. Lett.* **81**, 4608 (1998).

[81] A. Messiah, Quantum Mechanics (Dover Publications, Mineola, New York, 2012), p. 1152.

[82] P. Zhang and T. Sham, *Phys. Rev. Lett.* **90**, 245502 (2003).

[83] W. Egelhoff, *Surf. Sci. Rep.* **6**, 253 (1987).

[84] M. Sterrer, T. Risse, M. Heyde, H.-P. Rust, and H.-J. Freund, *Phys. Rev. Lett.* **98**, 206103 (2007).

[85] Electronic States and Optical Transitions in Solids, 1st ed., edited by G. F. Bassani, P. Parravicinim G, and R. Ballinger (Pergamon Press Ltd., Oxford, 1975), pp. 149–176.

[86] S. A. Chambers, *Surf. Sci. Rep.* **39**, 105 (2000).

[87] S. Hüfner and G. K. Wertheim, *Phys. Lett.* **51A**, 299 (1975).

[88] L. A. Feldkamp and L. C. Davis, *Phys. Rev. B* **22**, 3644 (1980).

[89] C. Wagner, *Faraday Discussion* **60**, 291 (1975).

[90] D. A. Shirley, *Phys. Rev. B* **5**, 4709 (1972).

[91] N. Lang and A. Williams, *Phys. Rev. B* **20**, 1369 (1979).

[92] G. Hohlneicher, H. Pulm, and H.-J. Freund, *J. Electron Spectrosc. Relat. Phenom.* **37**, 209 (1985).

[93] C. Wagner, *J. Electron Spectrosc. Relat. Phenom.* **47**, 283 (1988).

[94] A. E. Siegman, Lasers, 1st ed. (University Science Books, Mill Valley, California, 1986).

[95] F. M. Hoffmann, *Surf. Sci. Rep.* **3**, 107 (1983).

[96] G. C. Schatz and M. A. Ratner, Quantum Mechanics in Chemistry, 2nd ed. (Dover Publications, New York, 2002), p. 384.

[97] G. Pacchioni, G. Cogliandro, and P. S. Bagus, *Surf. Sci.* **255**, 344 (1991).

[98] G. Blyholder, *J. Phys. Chem.* **68**, 2772 (1964).

[99] M. Mihaylov, H. Knözinger, K. Hadjiivanov, and B. C. Gates, *Chem. Ing. Tech.* **79**, 795 (2007).

[100] M. Sterrer, M. Yulikov, T. Risse, H.-J. Freund, J. Carrasco, F. Illas, C. Di Valentin, L. Giordano, and G. Pacchioni, *Angew. Chem. Int. Ed.* **45**, 2633 (2006).

[101] J. Bardeen, *Phys. Rev.* **71**, 717 (1947).

[102] R. Bracewell, The Fourier Transform and Its Applications (McGraw-Hill Book Company, New York, 1965), p. 381.

[103] I. Langmuir, *J. Am. Chem. Soc.* **40**, 1361 (1918).

[104] J. E. Lennard-Jones, *Proc. R. Soc. Lond. A* **106**, 463 (1924).

[105] D. A. King, *Surf. Sci.* **47**, 384 (1975).

[106] P. Redhead, *Vacuum* **12**, 203 (1962).

[107] R. I. Masel, Principles of adsorption and reaction on solid surfaces (John Wilez & Sons, Inc., Newyork, Chichester, Brisbane, Toronto, Singapore, 1996).

[108] S. Günther, T. Mentes, M. Nino, A. Locatelli, S. Böcklein, and J. Wintterlin, *Nat. Comm.* **5**, 3853 (2014).

[109] K. A. Fichthorn and W. Weinberg, *J. Chem. Phys.* **95**, 1090 (1991).

[110] P. Zeitoum, G. Faivre, S. Sebban, T. Mocek, A. Hallou, M. Fajardo, D. Aubert, P. Balcou, F. Burgy, D. Douillet, S. Kazamias, G. de Lachéze-Murel, T. Lefrou, S. le Pape, P. Mercére, H. Merdji, A. S. Morlens, J. P. Rousseau, and C. Valentin, *Nature* **431**, 426 (2004).

[111] P. E. Miller and M. B. Denton, *J. Chem. Educ.* **63**, 617 (1986).

[112] E. Carrasco, M. A. Brown, M. Sterrer, H.-J. Freund, K. Kwapien, M. Sierka, and J. Sauer, *J. Phys. Chem. C* **114**, 18207 (2010).

[113] F. Ringleb, Y. Fujimori, H.-F. Wang, H. Ariga, E. Carrasco, M. Sterrer, H.-J. Freund, L. Giordano, G. Pacchioni, and J. Goniakowski, *J. Phys. Chem. C* **115**, 19328 (2011).

[114] P. J. Linstrom, NIST Chemistry WebBook, http://webbook.nist.gov/chemistry/, 2014.

[115] V. E. Henrich, G. Dresselhaus, and H. Zeiger, *Phys. Rev. B* **22**, 4764 (1980).

[116] D. Fritsch, H. Schmidt, and M. Grundmann, *Appl. Phys. Lett.* **88**, 134104 (2006).

[117] C. Satoko, M. Tsukada, and H. Adachi, *J. Phys. Soc. Jpn.* **45**, 1333 (1978).

[118] O. Robach, G. Renaud, and A. Barbier, *Surf. Sci.* **401**, 227 (1998).

[119] V. E. Henrich, G. Dresselhaus, and H. Zeiger, *Phys. Rev. Lett.* **36**, 158 (1976).

[120] R. Gomer and C. Smith, Structure and Properties of Solid Surfaces (University of Chicago Press, Chicago, 1952).

[121] A. Zangwill, Physics at Surfaces (Cambridge University Press, Cambridge, 1988).

[122] L. Murr, Interfacial Phenomena in Metals and Alloys (Addison-Wesley, Reading, MA, 1975), p. 132.

[123] T. König, G. H. Simon, H.-P. Rust, G. Pacchioni, M. Heyde, and H.-J. Freund, *J. Am. Chem. Soc.* **131**, 17544 (2009).

[124] M. Kiguchi, S. Entani, K. Saiki, T. Goto, and A. Koma, *Phys. Rev. B* **68**, 115402 (2003).

[125] F. Finocchi, A. Barbier, J. Jupille, and C. Noguera, *Phys. Rev. Lett.* **92**, 136101 (2004).

[126] R. Hacquart and J. Jupille, *Chem. Phys. Lett.* **439**, 91 (2007).

[127] B. E. Gaddy, E. A. Paisley, J.-P. Maria, and D. L. Irving, *Phys. Rev. B* **90**, 125403 (2014).

[128] J. Wollschläger, J. Viernow, C. Tegenkamp, D. Erdös, K. Schröder, and H. Pfnür, *Appl. Surf. Sci.* **142**, 129 (1999).

[129] H. Meyerheim, R. Popescu, J. Kirschner, N. Jedrecy, M. Sauvage-Simkin, B. Heinrich, and R. Pinchaux, *Phys. Rev. Lett.* **87**, 076102 (2001).

[130] C. Giovanardi, A. di Bona, T. S. Moia, S. Valeri, C. Pisani, M. Sgroi, and M. Busso, *Surf. Sci.* **505**, L209 (2002).

[131] N. Lopez and S. Valeri, *Phys. Rev. B* **70**, 125428 (2004).

[132] S. Altieri, L. Tjeng, and G. Sawatzky, *Phys. Rev. B* **61**, 948 (2000).

[133] W. Mönch, Semiconductor Surfaces and Interfaces (Springer-Verlag, Berlin, Heidelberg, New York, 1993).

[134] S. Altieri, L. Tjeng, F. Voogt, T. Hibma, and G. Sawatzky, *Phys. Rev. B* **59**, R2517 (1999).

[135] S. Schintke, S. Messerli, M. Pivetta, F. Patthey, L. Libioulle, M. Stengel, A. De Vita, and W.-D. Schneider, *Phys. Rev. Lett.* **87**, 276801 (2001).

[136] L. Giordano, M. Baistrocchi, and G. Pacchioni, *Phys. Rev. B* **94**, 115403 (2005).

[137] Y.-N. Sun, Ph.D. thesis, Freie Universität Berlin, 2010.

[138] Z. Wang, M. Saito, K. P. McKenna, L. Gu, S. Tsukimoto, A. L. Shluger, and Y. Ikuhara, *Nature* **479**, 380 (2011).

[139] S. Gregg and R. Razouk, *J. Chem. Soc.* S36 (1947).

[140] E. Knözinger, K. Jacob, S. Singh, and P. Hofmann, *Surf. Sci.* **290**, 388 (1993).

[141] H. Duúski, W. K. Jóźwiak, and H. Sugier, *J. Catal.* **146**, 166 (1994).

[142] Y. D. Kim, J. Stultz, and D. W. Goodman, *J. Phys. Chem. B* **106**, 22 (2002).

[143] C. Chizallet, G. Costentin, M. Che, F. Delbecq, and P. Sautet, *J. Am. Chem. Soc.* **129**, 6442 (2007).

[144] C. Chizallet, G. Constentin, H. Lauron-Pernot, M. Che, C. Bonhomme, J. Maquet, F. Delbecq, and P. Sautet, *J. Phys. Chem. C* **111**, 18279 (2007).

[145] N. Jiang, D. Su, and J. C. H. Spence, *Ultramicroscopy* **109**, 122 (2008).

[146] K. Honkala, A. Hellman, and H. Grönbeck, *J. Phys. Chem. C* **114**, 7070 (2010).

[147] R. I. Razouk and R. S. H. Mikhail, *J. Phys. Chem.* **62**, 920 (1958).

[148] W. Langel and M. Parrinello, *Phys. Rev. Lett.* **73**, 504 (1994).

[149] H.-J. Shin, J. Jung, K. Motobayashi, S. Yanagisawa, Y. Morikawa, Y. Kim, and M. Kawai, *Nat. Mater.* **9**, 442 (2010).

[150] P. Liu, T. Kendelewicz, and G. E. Brown Jr., *Surf. Sci.* **413**, 315 (1998).

[151] O. Diwald, M. Sterrer, and E. Knözinger, *Phys. Chem. Chem. Phys.* **4**, 2811 (2002).

[152] P. Liu, T. Kendelewicz, G. E. Brown Jr., and G. A. Parks, *Surf. Sci.* **412/413**, 287 (1998).

[153] L. O. Paz-borbo, A. Hellman, and H. Grönbeck, *J. Phys. Chem. C* **116**, 3545 (2012).

[154] J. T. Newberg, D. E. Starr, S. Yamamoto, S. Kaya, T. Kendelewicz, E. R. Mysak, S. Porsgaard, M. B. Salmeron, G. E. Brown, A. Nilsson, and H. Bluhm, *J. Phys. Chem. C* **115**, 12864 (2011).

[155] P. J. Cumpson and M. P. Seah, *Surf. Interface Anal.* **25**, 430 (1997).

[156] F. Ringleb, Y. Fujimori, M. A. Brown, W. E. Kaden, F. Calaza, H. Kuhlenbeck, M. Sterrer, and H.-J. Freund, *Catal. Today* **240**, 206 (2014).

[157] A. Ouvrard, J. Niebauer, A. Ghalgaoui, C. Barth, C. R. Henry, and B. Bourguignon, *J. Phys. Chem. C* **115**, 8034 (2011).

[158] M. W. Cole and M. H. Cohen, *Phys. Rev. Lett.* **23**, 1967 (1969).

[159] V. Shikin, *Soviet Physics JETP* **31**, 940 (1970).

[160] C. J. Nelin, F. Uhl, V. Staemmler, P. S. Bagus, Y. Fujimori, M. Sterrer, H. Kuhlenbeck, and H.-J. Freund, *Phys. Chem. Chem. Phys.* **16**, 21953 (2014).

[161] F. Ringleb, Ph.D. thesis, Freie Universität Berlin, 2013.

[162] P. Liu, T. Kendelewicz, G. E. Brown Jr., G. A. Parks, and P. Pianetta, *Surf. Sci.* **416**, 326 (1998).

[163] E. Knözinger, K.-H. Jacob, and P. Hofmann, *J. Chem. Soc., Faraday Trans.* **89**, 1101 (1993).

[164] Z. Zhang and J. T. Yates, *Chem. Rev.* **112**, 5520 (2012).

[165] H. P. Boehm and H. Knözinger, in Catalysis Science and Technology, 4th ed., edited by J. R. Anderson and M. Boudart (Springer-Verlag, Berlin, 1983), p. 39.

[166] G. D. Christian, Analytical Chemistry, 6th ed. (John Wiley & Sons, Inc., Hoboken, New Jersey, 2004).

[167] O. Diwald, P. Hofmann, and E. Knözinger, *Phys. Chem. Chem. Phys.* **1**, 713 (1999).

[168] H. Kwak and S. Chaudhuri, *J. Alloys Compd.* **509**, 8189 (2011).

[169] G. Pacchioni, L. Giordano, and M. Baistrocchi, *Phys. Rev. Lett.* **94**, 226104 (2005).

[170] A. Filippetti and V. Fiorentini, *Phys. Rev. B* **72**, 035128 (2005).

[171] M. Haruta, S. Tsubota, T. Kobazashi, H. Kagezama, M. J. Genet, and B. Delmon, *J. Catal.* **144**, 175 (1993).

[172] M. Sterrer, M. Yulikov, E. Fischbach, M. Heyde, H.-P. Rust, G. Pacchioni, T. Risse, and H.-J. Freund, *Angew. Chem. Int. Ed.* **45**, 2630 (2006).

[173] L. Giordano, J. Carrasco, C. Di Valentin, F. Illas, and G. Pacchioni, *J. Chem. Phys.* **124**, 174709 (2006).

[174] G. Pacchioni and H. Freund, *Chem. Rev.* **113**, 4035 (2013).

[175] C. Lemire, R. Meyer, S. Shaikhutdinov, and H.-J. Freund, *Surf. Sci.* **552**, 27 (2004).

[176] H.-J. Freund and G. Pacchioni, *Chem. Soc. Rev.* **37**, 2224 (2008).

[177] P. S. Bagus and G. Pacchioni, *J. Phys.: Conf. Ser.* **117**, 012003 (2008).

[178] R. Meyer, C. Lemire, S. K. Shaikhutdinov, and H.-J. Freund, *Gold Bulletin* **37**, 72 (2004).

[179] E. Escalona-Platero, D. Scarano, G. Spoto, and A. Zecchina, *Faraday Discuss. Chem. Soc.* **80**, 183 (1985).

[180] M. I. Zaki and H. Knözinger, *J. Catal.* **321**, 311 (1989).

[181] M. Sterrer, T. Risse, and H.-J. Freund, *Surf. Sci.* **596**, 222 (2005).

[182] S. Sicolo, L. Giordano, and G. Pacchioni, *J. Phys. Chem. C* **113**, 10256 (2009).

[183] X. Lin, B. Yang, H.-M. Benia, P. Myrach, M. Yulikov, A. Aumer, M. A. Brown, M. Sterrer, O. Bondarchuk, E. Kieseritzky, J. Rocker, T. Risse, H.-J. Gao, N. Nilius, and H.-J. Freund, *J. Am. Chem. Soc.* **132**, 7745 (2010).

[184] K. Naya, R. Ishikawa, and K.-I. Fukui, *J. Phys. Chem. C* **2**, 10726 (2009).

[185] K. T. Rim, D. Eom, L. Liu, E. Stolyarova, J. M. Raitano, S.-W. Chan, M. Flytzani-Stephanopoulos, and G. W. Flynn, *J. Phys. Chem. C* **113**, 10198 (2009).

[186] M. Sterrer, T. Risse, L. Giordano, M. Heyde, N. Nilius, H.-P. Rust, G. Pacchioni, and H.-J. Freund, *Angew. Chem. Int. Ed.* **46**, 8703 (2007).

[187] L. Giordano, U. Martinez, S. Sicolo, and G. Pacchioni, *J. Chem. Phys.* **127**, 144713 (2007).

[188] C. Lee, W. Yang, and R. G. Parr, *Phys. Rev. B* **37**, 785 (1988).

[189] M. A. Brown, F. Ringleb, Y. Fujimori, M. Sterrer, H.-J. Freund, G. Preda, and G. Pacchioni, *J. Phys. Chem. C* **115**, 10114 (2011).

[190] M. Neumaier, F. Weigend, O. Hampe, and M. M. Kappes, *J. Chem. Phys.* **122**, 104702 (2005).

[191] A. Fielicke, G. von Helden, G. Meijer, B. Simard, and D. M. Rayner, *J. Phys. Chem. B* **109**, 23935 (2005).

[192] A. S. Wörz, U. Heiz, F. Cinquini, and G. Pacchioni, *J. Phys. Chem. B* **109**, 18418 (2005).

[193] K. P. McKenna and A. L. Shluger, *Nat. Mater.* **7**, 859 (2008).

[194] H.-M. Benia, P. Myrach, A. Gonchar, T. Risse, N. Nilius, and H.-J. Freund, *Phys. Rev. B* **81**, 241415 (2010).

[195] L. Giordano, U. Martinez, G. Pacchioni, V. R. Cozzi, M. Watkins, and A. L. Shluger, *J. Phys. Chem. C* **112**, 3857 (2008).

[196] A. Gonchar, T. Risse, E. Giamello, and H.-J. Freund, *Phys. Chem. Chem. Phys.* **12**, 12520 (2010).

[197] M. A. Henderson, *Surf. Sci. Rep.* **46**, 1 (2002).

[198] C. Hao, C. Chizallet, C. Mager-Maury, M. Corral-Valero, P. Sautet, H. Toulhoat, and P. Raybaud, *J. Catal.* **274**, 99 (2010).

[199] T. Schalow, B. Brandt, D. E. Starr, M. Laurin, S. K. Shaikhutdinov, S. Schauermann, J. Libuda, and H.-J. Freund, *Phys. Chem. Chem. Phys.* **9**, 1347 (2007).

[200] T. Schalow, B. Brandt, M. Laurin, S. Guimond, D. E. Starr, S. K. Shaikhutdinov, S. Schauermann, J. Libuda, and H.-J. Freund, *Top. Catal.* **42-43**, 387 (2007).

[201] X. Xu and D. W. Goodman, *J. Phys. Chem.* **97**, 7711 (1993).

[202] N. M. Martin, M. V. D. Bossche, H. Gro, C. Hakanoglu, F. Zhang, T. Li, J. Gustafson, J. F. Weaver, and E. Lundgren, *J. Phys. Chem. C* **118**, 1118 (2014).

[203] A. M. Bradshaw and F. M. Hoffmann, *Surf. Sci.* **72**, 513 (1978).

[204] J. Jeon, A. Soon, J.-N. Yeo, J. Park, S. Hong, K. Cho, and B. D. Yu, *J. Phys. Soc. Jpn.* **81**, 054601 (2012).

[205] J. Pireaux, J. Ghijsen, J. W. McGowan, J. Verbist, and R. Caudano, *Surf. Sci.* **80**, 488 (1979).

[206] L. K. Ono and B. R. Cuenya, *J. Phys. Chem. C* **112**, 4676 (2008).

[207] G. Ketteler, D. F. Ogletree, H. Bluhm, H. Liu, E. L. Hebenstreit, and M. Salmeron, *J. Am. Chem. Soc.* **127**, 18269 (2005).

[208] K. S. Kim, A. F. Gossmann, and N. Winograd, *Anal. Chem.* **46**, 197 (1974).

[209] T. L. Barr, *J. Phys. Chem.* **82**, 1801 (1978).

[210] L. S. Kibis, A. I. Stadnichenko, S. V. Koscheev, V. I. Zaikovskii, and A. I. Boronin, *J. Phys. Chem. C* **116**, 19342 (2012).

[211] F. Gao, Y. Wang, Y. Cai, D. W. Goodman, K. K. Gath, M. S. Chen, and Q. L. Guo, *J. Phys. Chem. C* **113**, 174 (2009).

[212] X. Guo and J. T. Yates, *J. Chem. Phys.* **90**, 6761 (1989).

[213] V. Matolin and E. Gillet, *Surf. Sci.* **238**, 75 (1990).

[214] I. Stara and V. Matolin, *Surf. Sci.* **313**, 99 (1994).

[215] S. L. Tait, L. T. Ngo, Q. Yu, S. C. Fain, and C. T. Campbell, *J. Chem. Phys.* **122**, 064712 (2005).

[216] J. Libuda, A. Sandell, M. Bäumer, and H.-J. Freund, *Chem. Phys. Lett.* **240**, 429 (1995).

[217] A. Sandell, J. Libuda, M. Bäumer, and H.-J. Freund, *Surf. Sci.* **346**, 108 (1996).

[218] W. E. Kaden, W. A. Kunkel, F. S. Roberts, M. Kane, and S. L. Anderson, *Surf. Sci.* **621**, 40 (2014).

[219] K. Wolter, O. Seiferth, J. Libuda, H. Kuhlenbeck, M. Bäumer, and H.-J. Freund, *Surf. Sci.* **402-404**, 428 (1998).

[220] E. W. McFarland and H. Metiu, *Chem. Rev.* **113**, 4391 (2013).

[221] R. L. Burwell and A. Brenner, *J. Mol. Catal.* **1**, 77 (1976).

[222] A. Brenner and D. A. Hucul, *Inorg. Chem.* **18**, 2836 (1979).

[223] T. Shido and Y. Iwasawa, *J. Catal.* **141**, 71 (1993).

[224] C. M. Kalamaras, S. Americanou, and A. M. Efstathiou, *J. Catal.* **279**, 287 (2011).

[225] T. Bunluesin, R. Gottea, and G. Grahamb, *Appl. Catal. B* **15**, 107 (1998).

[226] J. A. Rodriguez, J. Evans, J. Graciani, J.-B. Park, P. Liu, J. Hrbek, and J. F. Sanz, *J. Phys. Chem. C* **2**, 7364 (2009).

[227] M. Shekhar, J. Wang, W.-S. Lee, W. D. Williams, S. M. Kim, E. A. Stach, J. T. Miller, W. N. Delgass, and F. H. Ribeiro, *J. Am. Chem. Soc.* **134**, 4700 (2012).

[228] M. Yang, L. F. Allard, and M. Flytzani-Stephanopoulos, *J. Am. Chem. Soc.* **135**, 3768 (2013).

[229] G. Kleiman, R. Landers, P. Nascente, and S. de Castro, *Phys. Rev. B* **46**, 4450 (1992).

[230] H. Pulm, G. Hohlneicher, H.-J. Freund, H.-U. Schuster, J. Drews, and U. Eberz, *J. Less-Common Met.* **115**, 127 (1986).

[231] B. Richter, H. Kuhlenbeck, H.-J. Freund, and P. S. Bagus, *Phys. Rev. Lett.* **93**, 026805 (2004).

[232] E. W. Plummer, W. R. Salaneck, and J. S. Miller, *Phys. Rev. B* **18**, 1673 (1978).

[233] G. Comelli, M. Sastry, G. Paolucci, and K. C. Prince, *Phys. Rev. B* **43**, 14385 (1991).

[234] A. Sandell, A. Beutler, R. Nyholm, J. Andersen, S. Andersson, P. Brühwiler, N. Mårtensson, J. Libuda, K. Wolter, O. Seiferth, M. Bäumer, H. Kuhlenbeck, and H.-J. Freund, *Phys. Rev. B* **57**, 13199 (1998).

[235] M. Wilde, K. Fukutani, M. Naschitzki, and H.-J. Freund, *Phys. Rev. B* **77**, 113412 (2008).

[236] T. Shido, K. Asakura, and Y. Iwasawa, *J. Catal.* **122**, 55 (1990).

[237] P. Panagiotopoulou and D. I. Kondarides, *Catal. Today* **112**, 49 (2006).

[238] E. Gillet, S. Channakhone, V. Matolin, and M. Gillet, *Surf. Sci.* **152/153**, 603 (1985).

[239] I. Stara, V. Nehasil, and V. Matolin, *Surf. Sci.* **365**, 69 (1996).

[240] C. Becker and C. R. Henry, *Surf. Sci.* **352-354**, 457 (1996).

[241] R. Prins, V. K. Palfi, and M. Reiher, *J. Phys. Chem. C* **116**, 14274 (2012).

[242] M. Che and C. O. Bennett, in Advances in Catalysis, edited by D. Eley., H. Pines, and P. B. Weisz (Academic Press. Inc., Waltham, Massachusetts, 1989), p. 55.

[243] D. Teschner, Z. Révay, J. Borsodi, M. Hävecker, A. Knop-Gericke, R. Schlögl, D. Milroy, S. D. Jackson, D. Torres, and P. Sautet, *Angew. Chem. Int. Ed.* **47**, 9274 (2008).

[244] E. Chenu, G. Jacobs, A. C. Crawford, R. A. Keogh, P. M. Patterson, D. E. Sparks, and B. H. Davis, *Appl. Catal. B* **59**, 45 (2005).

[245] N. S. Phala, G. Klatt, and E. V. Steen, *Chem. Phys. Lett.* **395**, 33 (2004).

[246] P. V. Sushko, J. L. Gavartin, and A. L. Shluger, *J. Phys. Chem. B* **106**, 2269 (2002).

[247] D. Ricci, A. Bongiorno, G. Pacchioni, and U. Landman, *Phys. Rev. Lett.* **97**, 036106 (2006).

[248] F. Napoli, M. Chiesa, E. Giamello, E. Finazzi, C. D. Valentin, and G. Pacchioni, *J. Am. Chem. Soc.* **129**, 10575 (2007).

[249] P. A. Thiel and T. E. Madey, *Surf. Sci. Rep.* **7**, 211 (1987).

[250] S. Maier, I. Stass, T. Mitsui, P. J. Feibelman, K. Thürmer, and M. Salmeron, *Phys. Rev. B* **85**, 155434 (2012).

[251] P. J. Feibelman, *Science* **295**, 99 (2002).

[252] H. Liu, C. Song, L. Zhang, J. Zhang, H. Wang, and D. P. Wilkinson, *J. Power Sources* **155**, 95 (2006).

[253] G. Michal, M. Lukaszewski, G. Jerkiewicz, and A. Czerwiski, *Electrochim. Acta* **53**, 7583 (2008).

[254] B. Lim, M. Jiang, P. H. C. Camargo, E. C. Cho, J. Tao, X. Lu, Y. Zhu, and Y. Xia, *Science* **324**, 1302 (2009).

[255] A. Tougerti, I. Llorens, F. D'Acapito, E. Fonda, J.-L. Hazemann, Y. Joly, D. Thiaudi, M. Che, and X. Carrier, *Angew. Chem. Int. Ed.* **51**, 7697 (2012).

[256] H.-F. Wang, W. E. Kaden, R. Dowler, M. Sterrer, and H.-J. Freund, *Phys. Chem. Chem. Phys.* **14**, 11525 (2012).

[257] J. G. McCarty, *Catal. Today* **26**, 283 (1995).

[258] M. Lyubovsky and L. Pfefferle, *Catal. Today* **47**, 29 (1999).

[259] R. Imbihl and G. Ertl, *Chem. Rev.* **95**, 697 (1995).

[260] G. B. Hoflund, H. A. Hagelin, J. F. Weaver, and G. N. Salaita, *Appl. Surf. Sci.* **205**, 102 (2003).

[261] F. Gao, T. E. Wood, and D. W. Goodman, *Catal. Lett.* **134**, 9 (2009).

[262] F. Gao and D. W. Goodman, *Langmuir* **26**, 16540 (2010).

[263] D. Zemlyanov, B. Aszalos-Kiss, E. Kleimenov, D. Teschner, S. Zafeiratos, M. Hävecker, A. Knop-Gericke, R. Schlögl, H. Gabasch, W. Unterberger, K. Hayek, and B. Klötzer, *Surf. Sci.* **600**, 983 (2006).

[264] R. Toyoshima, M. Yoshida, Y. Monya, Y. Kousa, K. Suzuki, H. Abe, B. S. Mun, K. Mase, K. Amemiya, and H. Kondoh, *J. Phys. Chem. C* **116**, 18691 (2012).

[265] C. Hakanoglu and J. F. Weaver, *Surf. Sci.* **611**, 40 (2013).

[266] S. Penner, P. Bera, S. Pedersen, L. Ngo, J. Harris, and C. T. Campbell, *J. Phys. Chem. B* **110**, 24577 (2006).

[267] S. Yamamoto, H. Bluhm, K. Andersson, G. Ketteler, H. Ogasawara, M. Salmeron, and A. Nilsson, *J. Phys.: Condens. Matter* **20**, 184025 (2008).

[268] M. Salmeron, H. Bluhm, M. Tatarkhanov, G. Ketteler, T. Shimizu, A. Murarza, X. Deng, T. Terranz, S. Yamamoto, and A. Nilsson, *Faraday Discuss.* **141**, 221 (2009).

[269] E. Stuve, S. Jorgensen, and R. Madix, *Surf. Sci.* **146**, 179 (1984).

[270] C. Nyberg and C. Tengstak, *J. Chem. Phys.* **80**, 3463 (1984).

[271] X.-Y. Zhu, J. White, M. Wolf, E. Hasselbrink, and G. Ertl, *J. Phys. Chem.* **95**, 8393 (1991).

[272] Y. Cao and Z.-X. Chen, *Surf. Sci.* **600**, 4572 (2006).

[273] M. Gladys, A. Zein, A. Mikkelsen, J. Andersen, and G. Held, *Surf. Sci.* **602**, 3540 (2008).

[274] H. A. E. Hagelin, J. F. Weaver, G. B. Hoflund, and G. N. Salaita, *J. Electron Spectrosc. Relat. Phenom.* **124**, 1 (2002).

[275] CRC Press, 2nd ed., edited by J. C. Riviere and S. Myhra (Taylor & Francois, Boca Raton, London, New York, 2009), p. 671.

[276] T. Ohtani, J. Kubota, A. Wada, J. N. Kondo, K. Domen, and C. Hirose, *Surf. Sci.* **368**, 270 (1996).

[277] J. A. Hinojosa, H. H. Kan, and J. F. Weaver, *J. Phys. Chem. C* **101**, 8324 (2008).

[278] D. R. Rainer, C. Xu, P. M. Holmblad, and D. W. Goodman, *J. Vac. Sci. Technol., A* **15**, 1653 (1997).

[279] H. Huang, X. Jiang, Z. Zou, G. Xu, W. Dai, K. Fan, and J. Deng, *Surf. Sci.* **398**, 203 (1998).

[280] T. Ito, M. Kato, K. Toi, T. Shirawaka, I. Ikemoto, and T. Tokuda, *J. Chem. Soc., Faraday Trans. 1* **81**, 2835 (1985).

[281] A. Michaelides, M. Bocquet, P. Sautet, A. Alavi, and D. A. King, *Chem. Phys. Lett.* **367**, 344 (2003).

[282] C. Sachs, M. Hildebrand, S. Volkening, J. Wintterlin, and G. Ertl, *Science* **293**, 1635 (2001).

[283] F. Gao, M. Lundwall, and D. Goodman, *J. Phys. Chem. C* **112**, 6057 (2008).

[284] W. S. Sim, P. Gardner, and D. A. King, *J. Phys. Chem.* **100**, 12509 (1996).

[285] E. Stuve, R. Madix, and C. Brundle, *Surf. Sci.* **146**, 155 (1984).

[286] B. A. Banse and B. E. Koel, *Surf. Sci.* **232**, 275 (1990).

[287] G. Rovida, F. Pratesi, M. Maglietta, and E. Ferroni, *Surf. Sci.* **43**, 230 (1974).

[288] D. Ciuparu, E. Perkins, and L. Pfefferle, *Appl. Catal. A* **263**, 145 (2004).

[289] K. Persson, L. D. Pfefferle, W. Schwartz, A. Ersson, and S. G. Järås, *Appl. Catal. B* **74**, 242 (2007).

[290] R. Felici, R. V. Rijn, J. W. M. Frenken, J. N. Andersen, E. Lundgren, and H. Grönbeck, *J. Phys. Chem. Lett.* **3**, 678 (2012).

[291] A. Dianat, N. Seriani, L. C. Ciacchi, M. Bobeth, and G. Cuniberti, *Chem. Phys.* **443**, 53 (2014).

[292] P. Araya, S. Guerrero, J. Robertson, and F. Gracia, *Appl. Catal. A* **283**, 225 (2005).

[293] M. Blanco-Rey, D. Wales, and S. Jenkins, *J. Phys. Chem. C* **113**, 16757 (2009).

[294] H. H. Kan, R. J. Colmyer, A. Asthagiri, and J. F. Weaver, *J. Phys. Chem. C* **113**, 1495 (2009).

[295] J. N. Carstens, S. C. Su, and A. T. Bell, *J. Catal.* **142**, 136 (1998).

[296] Y.-H. C. Chin, C. Buda, M. Neurock, and E. Iglesia, *J. Am. Chem. Soc.* **135**, 15425 (2013).

[297] A. Hodgson and S. Haq, *Surf. Sci. Rep.* **64**, 381 (2009).

[298] J. Carrasco, A. Hodgson, and M. Michaelides, *Nat. Mat.* **11**, 667 (2012).

[299] M. Odelius, *Phys. Rev. Lett.* **82**, 3919 (1999).

[300] I. Giner, O. Ozcan, and G. Grundmeier, *Corros. Sci.* **87**, 51 (2014).

[301] M. Sakai, C. Su, and E. Sasaoka, *Ind. Eng. Chem. Res.* **41**, 5029 (2002).

[302] M. Ghiasi and A. Malekzadeh, *Crys. Res. Technol.* **47**, 471 (2012).

[303] M. Low, N. Takezawa, and A. Goodsel, *J. Colloid Interface Sci.* **37**, 422 (1971).

[304] J.-M. Krafft, M. Che, and H. Petitjean, *Phys. Chem. Chem. Phys.* **12**, 14740 (2010).

[305] J. P. Allen, A. Marmier, and S. C. Parker, *J. Phys. Chem. C* **116**, 13240 (2012).

[306] F. Bebensee, F. Voigts, and W. Maus-Friedrichs, *Surf. Sci.* **602**, 1622 (2008).

[307] Y. Cui, X. Shao, M. Baldofski, J. Sauer, N. Nilius, and H.-J. Freund, *Angew. Chem. Int. Ed.* **52**, 11385 (2013).

[308] X. Shao, P. Myrach, N. Nilius, and H.-J. Freund, *J. Phys. Chem. C* **115**, 8784 (2011).

[309] E. Carrasco, A. Aumer, J. F. Gomes, Y. Fujimori, and M. Sterrer, *Chem. Commun.* **49**, 4355 (2013).

[310] I. Engquist, I. Lundstrom, and B. Liedberg, *J. Phys. Chem.* **99**, 12257 (1995).

[311] H. Lutz, H. Moeller, and M. Schmidt, *J. Mol. Struct.* **328**, 121 (1994).

[312] H. Manzano, R. J. M. Pellenq, F.-J. Ulm, M. J. Buehler, and A. C. T. van Duin, *Langmuir* **28**, 4187 (2012).

[313] J. Carrasco, F. Illas, and N. Lopez, *Phys. Rev. Lett.* **100**, 016101 (2008).

[314] R. Wzodarczyk, M. Sierka, K. Kwapie, J. Sauer, E. Carrasco, A. Aumer, J. F. Gomes, M. Sterrer, and H.-J. Freund, *J. Phys. Chem. C* **115**, 6764 (2011).

[315] C. Chizallet, G. Costentin, H. Lauron-Pernot, J.-M. Krafft, M. Che, F. Delbecq, and P. Sautet, *J. Phys. Chem. C* **112**, 16629 (2008).

[316] V. Blum, R. Gehrke, F. Hanke, P. Havu, V. Havu, X. Ren, K. Reuter, and M. Scheffler, *Comput. Phys. Commun.* **180**, 2175 (2009).

[317] B. Fubini, V. Bolis, M. Bailes, and S. S. Frank, *Solid State Ionics* **32/33**, 258 (1989).

[318] S. Benedetti, H. Benia, N. Nilius, S. Valeri, and H. Freund, *Chem. Phys. Lett.* **430**, 330 (2006).

[319] A. Hellman, S. Klacar, and H. Grönbeck, *J. Am. Chem. Soc.* **131**, 16636 (2009).

[320] C. M. Kwei, Y. F. Chen, C. Tung, and J. P. Wang, *Surf. Sci.* **293**, 202 (1993).

[321] J. Pal, M. Smerieri, E. Celasco, L. Savio, L. Vattuone, and M. Rocca, *Phys. Rev. Lett.* **112**, 126102 (2014).

[322] I. Chorkendorff and J. Onsgaard, *Phys. Rev. B* **33**, 937 (1986).

[323] F. Chen and R. L. Johnston, *Acta Mater.* **56**, 2374 (2008).

[324] M. Sterrer, T. Risse, and H.-J. Freund, *Appl. Catal. A* **307**, 58 (2006).

[325] M. A. Brown, M. Faubel, and B. Winter, *Annu. Rep. Prog. Chem. Sect. C* **105**, 174 (2009).

[326] V. Simic-Milosevic, M. Heyde, X. Lin, T. König, H.-P. Rust, M. Sterrer, T. Risse, N. Nilius, H.-J. Freund, L. Giordano, and G. Pacchioni, *Phys. Rev. B* **78**, 235429 (2008).

[327] M. Yulikov, M. Sterrer, M. Heyde, H.-P. Rust, T. Risse, H.-J. Freund, G. Pacchioni, and A. Scagnelli, *Phys. Rev. Lett.* **96**, 146804 (2006).